THEORETICAL
AND MATHEMATICAL PHYSICS

Modeling the Electrical Characteristics
of Periodic Dielectric Media

Yu. P. Emets

Institute of Electrodynamics, National Academy of Sciences of Ukraine, Kiev 03680, Ukraine
e-mail: emets@irpen.kiev.ua
Received March 16, 2004

Abstract—The dispersion of the effective permittivities of two inhomogeneous matrix systems with unidirectional fiber inclusions with a square cross section is studied. Interpolation formulas for the effective permittivity as a function of the frequency are obtained, whose range of applicability is determined through physical modeling and comparison with known systems of equations admitting exact solutions. It is established that the effective loss factor exhibits anomalous behavior in the vicinity of the critical concentration of inclusions. © 2004 MAIK "Nauka/Interperiodica".

INTRODUCTION

This paper addresses the dispersion of permittivity of two-dimensional piecewise homogeneous media with ultimately high concentrations of fiber inclusions, whose properties significantly differ from those of the matrix. Materials with the critical parameters undergo dielectric–metal transitions. Using the methods of dielectric spectroscopy, it is possible to establish distinguishing features inherent in the effective permittivity of inhomogeneous systems in the region of critical parameters and, thereby, to provide for a correct interpretation of the experimental data.

Investigations usually assume that exact analytical expressions for the effective permittivity of inhomogeneous structures with a variable composition (up to the ultimate possible values) are known. Unfortunately, the number of systems admitting such solutions is small. Among these, the most thoroughly studied are matrix media with a double-periodic distribution of unidirectional cylindrical fibers (see, e.g., [1–3]). However, the expressions obtained for the effective permittivity are very cumbersome and lose physical transparency at high inclusion concentrations. If permittivities are complex-valued, the computational burden multiply increases. These difficulties can sometimes be overcome using approximations based on interpolation formulas. This approach is employed in the present study. It is shown that the interpolation formulas proposed for the systems under consideration are simple and can easily be applied in spectral analysis, while providing acceptable accuracy in calculations of the effective parameters.

The interpolation formulas are derived based on a discrete representation of the inhomogeneous structures. To this end, the fundamental periodic domain is divided into small cells, which, being electrically coupled, form systems with serial, parallel, and mixed connections and can be easily analyzed by numerical methods. Thus obtained expressions for the effective permittivity meet commonly accepted requirements. In fact, they satisfy reciprocity relationships (Keller's theorem) and other conditions of the theory of effective parameters of inhomogeneous media. They also coincide with all the known exact solutions. The results of modeling in conducting paper corroborate validity of the interpolation formulas in a wide range of parameters. The limitations imposed on the interpolation formulas naturally follow from the procedure used to derive them. They give only discrete values of the effective permittivity, these points being separated by relatively wide intervals (in terms of the concentration) at small inclusion concentrations. However, as the inclusion concentration increases, the intervals between these points decrease and tend to zero in the limit as the critical point is approached. It should also be noted that the method used to derive the interpolation formulas is not rigorous; therefore, the region where they are valid is not clearly defined. It is believed that this drawback will gradually be removed with increasing the number of problems solved analytically.

We study two matrix systems with double-periodic arrays of square unidirectional fibers arranged in (i) square and (ii) checkerboard grids. The systems have different critical compositions: in the first case, the medium becomes homogeneous due to properties of the inclusions; in the second case, the two phases at the critical point occupy equal volumes (equal cross-sectional areas). The differences between the structures of these systems lead to different behavior of the effective permittivity in the neighborhood of the critical point, which, as will be shown, is manifested in the dielectric spectrum of the inhomogeneous materials under consideration.

SYSTEM WITH SQUARE ARRANGEMENT OF INCLUSIONS

A fragment of a spatially infinite system of this type is shown in Fig. 1. The matrix with the permittivity ε_1 contains a double-periodic array of unidirectional square fibers with permittivity ε_2. In the plane normal to the fiber axes, the system is two-dimensional and, upon averaging, has to be described in terms of isotropic properties. As the fiber cross section increases, the relative concentration s of inclusions in the system grows and in the limit acquires the critical value $s_c = 1$, at which the two-component material becomes a single-phase material with the permittivity ε_2.

To write an expression for the effective permittivity of this inhomogeneous medium, it is necessary to study the periodic cell of the system, which is outlined by a dashed line in Fig. 1. This cell is a square, which contains one inclusion. Being subjected to transformations
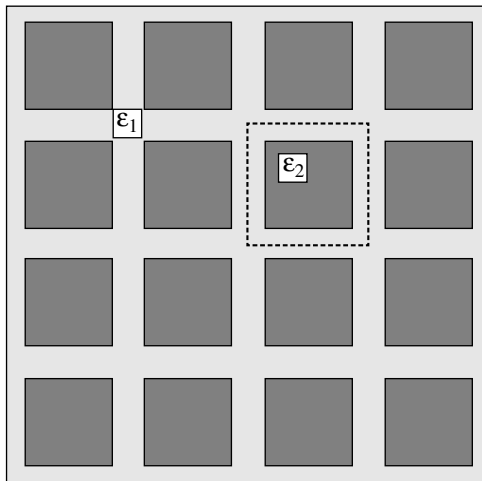

Fig. 1. Fragment of the cross section of a composite dielectric material with the square arrangement of long fibers with a square cross section. The dotted line shows the cell being analyzed.
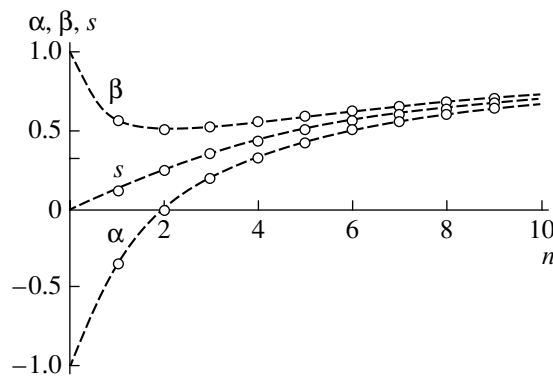

Fig. 2. Plots of the $\alpha(n)$, $\beta(n)$, and concentration of inclusions vs. initial values of n.

of translation in the axes of Cartesian coordinates, the cell completely covers the plane without spaces.

Let us superimpose a mesh of small squares on the periodic cell so that only one layer of the squares is between the inclusion and the cell boundary. This condition determines the scale of the small squares. We assume that the inclusion is divided into an integer number of small squares. It is clear that, the larger the dimensions of the inclusion and, consequently, the higher the concentration of the additional phase, the smaller the squares of the mesh that divides the periodic cell.

On the whole, the fundamental periodic cell is divided into $(n + 2)^2$ squares and the inclusion contains n^2 squares, where n is an integer number ($n = 0, 1, 2, \ldots$). At $n = 0$, there is no inclusion; if $n \longrightarrow \infty$, the inclusion entirely fills the cell and the medium becomes homogeneous with permittivity ε_2. The relative concentration of the inclusions is given by the formula

$$s = \left(\frac{n}{n+2}\right)^2 \quad (0 \leq s \leq s_c), \tag{1}$$

where s_c is the critical inclusion concentration ($s_c = 1$).

According to formula (1), the inclusion concentration takes on discrete values separated by different intervals whose lengths tend to zero with increasing n.

Calculations using a procedure briefly described at the end of this section give the following expression for the effective permittivity of the inhomogeneous system under consideration:

$$\varepsilon_{\text{eff}} = \varepsilon_1 \left[\frac{1 - \alpha\Delta}{1 + \alpha\Delta}\frac{1 - \beta\Delta}{1 + \beta\Delta}\right]^{1/2}. \tag{2}$$

Here, α and β are the functions of n defined as

$$\alpha = \frac{n-2}{n+2}, \quad \beta = \frac{n^2+4}{(n+2)^2} \quad (n = 0, 1, 2, \ldots) \tag{3}$$

and Δ is the relative permittivity,

$$\Delta = \frac{\varepsilon_1 - \varepsilon_2}{\varepsilon_1 + \varepsilon_2} \quad (-1 \leq \Delta \leq 1). \tag{4}$$

The functions α, β, and s are interrelated through the algebraic equations

$$\alpha^2 - 2\beta + 1 = 0, \quad s = \frac{1}{2}(\alpha + \beta). \tag{5}$$

Figure 2 plots functions $\alpha(n)$, $\beta(n)$, and $s(n)$ for the first ten values of n. As can be seen, the function $\beta(n)$ has a minimum of $\beta_{\min} = 1/2$ at $n = 2$; at this point, $\alpha = 0$ and $s = 1/4$. As n grows to infinity, all three functions $\alpha(n)$, $\beta(n)$, and $s(n)$ tend to the same limit,

$$\alpha, \beta, s \longrightarrow 1, \tag{6}$$

asymptotically as

$$\alpha, \beta, s \approx 1 - \frac{4}{n}, \quad n \longrightarrow \infty. \qquad (7)$$

Note some of the main features of expression (2) for the effective permittivity.

(i) Expression (2) meets the reciprocity relationship (Keller's theorem)

$$\varepsilon_{\text{eff}}(\Delta)\varepsilon_{\text{eff}}(-\Delta) = \varepsilon_1^2. \qquad (8)$$

(ii) The first-order homogeneity condition

$$\varepsilon_{\text{eff}}(k\varepsilon_1, k\varepsilon_2) = k\varepsilon_{\text{eff}}(\varepsilon_1, \varepsilon_2), \qquad (9)$$

where k is an arbitrary constant, is satisfied. This relationship is a consequence of the linearity of the electric field equations.

(iii) As follows from multipole expansions, expressions for effective permittivity must satisfy the differential relationship

$$\frac{d}{d\Delta}\left(\frac{\varepsilon_{\text{eff}}}{\varepsilon_1}\right)\bigg|_{\Delta = 0} = -2s. \qquad (10)$$

This condition is also satisfied.

(iv) If the concentration of inclusions takes on the values $s = 0$ ($n = 0$, $\alpha = -1$, $\beta = 1$) or $s = s_c = 1$ ($n \longrightarrow \infty$, $\alpha = \beta = 1$), the medium becomes homogeneous with permittivity ε_1 or ε_2, respectively.

(v) At the inclusion concentration $s = 1/4$ ($\alpha = 0$, $\beta = 1/2$), expression (2) for the effective permittivity becomes simpler, taking the form

$$\varepsilon_{\text{eff}} = \varepsilon_1 \sqrt{\frac{2 - \Delta}{2 + \Delta}}. \qquad (11)$$

This formula was obtained by Obnosov [4] from an exact solution to the boundary-value problem. It can be seen that formula (11) has the simplest form among all its possible meaningful representations. Therefore, it is not surprising that this particular case admits an exact expression for the effective parameter. To the best of the author's knowledge, efforts to obtain other exact solutions for the studied system were not as successful. Numerical results for the given system with the concentration of $s = 1/4$, provided by Bakhvalov and Panasenko [5, p. 132, Fig. 11b] for $\varepsilon_1 = 1$ and $\varepsilon_2 = 10$ ($\Delta = -9/11$), show that $\varepsilon_{\text{eff}} = 1.548$. Calculations using formula (11) give $\varepsilon_{\text{eff}} = 1.5442$, which testifies to extremely good agreement between the results of analytical and numerical calculations.

(vi) When the concentration of inclusions is close to the critical value $s \longrightarrow s_c$ ($n \longrightarrow \infty$), then, in accordance with asymptotic formulas (7), expression (2) can be represented as

$$\varepsilon_{\text{eff}} \approx \varepsilon_1 \frac{1 - s\Delta}{1 + s\Delta}. \qquad (12)$$

Formula (12) was obtained by Andrianov *et al.* [6] using a substantially different method (in terms of the theory of heat conduction; the boundary problem was solved by the perturbation technique using the two-point Padé's approximation). Experiments show that formula (12) provides for a quite high accuracy for all s at $\Delta = -1$ [7].

(vii) The values of the effective permittivity given by expression (2) are corroborated experimentally by physical modeling of the system under consideration in electrically conducting paper. The modeling relied on the well-known analogy between the electrostatic field and electric fields of stationary currents in a conducting medium. The results of these experiments are plotted in Fig. 3.

The solid curve in Fig. 3 plots the function $\varepsilon_{\text{eff}*}^{-1}(s) = \varepsilon_{\text{eff}}^{-1}(s)/\varepsilon_1$ calculated using formula (2) for a perfectly conducting inclusion, $\varepsilon_2 \longrightarrow \infty$ ($\Delta = -1$) (the asterisk symbol, which indicates that the values of the function are relative, is omitted). The experimental data are shown by open squares. Also, the triangles in Fig. 3 show experimental data for the same conditions borrowed from [6] (reproduced from [7]). On the whole, calculations using interpolation formula (2) are in good agreement with the experimental data. The greatest differences between the experimental and theoretical values of the effective permittivity are observed at small concentrations of inclusions ($s < 0.2$).

The dashed line in Fig. 3 is calculated under the same conditions using the exact solution obtained in [8]. The exact solution involves hypergeometric functions, which were calculated approximately by the quadrature method with the series truncated beyond
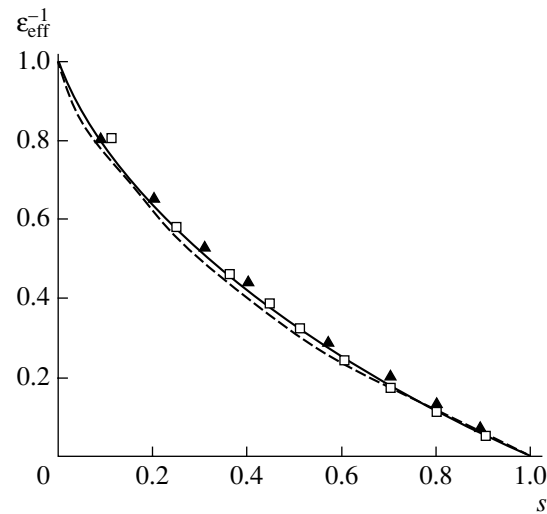

Fig. 3. Function $\varepsilon_{\text{eff}}^{-1}(s)$ calculated for the system illustrated in Fig. 1 at $\Delta = -1$ using (solid line) formula (2) and (dashed line) the exact solution [8]. Open squares and filled triangles show the results of two different experiments.

three terms, which proved to be insufficient. At higher degrees of approximation, the exact solution fits the experimental results obtained in models in the entire range of inclusion concentration.

Interpolation formula (2) is relatively simple, especially at high inclusion concentrations (see asymptotic representation (12)); therefore, this formula is convenient to use for investigation of the permittivity dispersion in strongly inhomogeneous media.

The purely algebraic method of deriving formula (2) employs the following procedure. The fundamental periodic cell of the system is divided into elementary square blocks as described in the beginning of this section. The square elements combined in series to form layers connected in parallel. Two such schemes can be obtained for the two cases, in which the external electric field in the periodic cell is parallel to (i) the horizontal axis x or (ii) the vertical axis y. As a result, we obtain two expressions for the effective permittivities $\varepsilon_e'(\varepsilon_1, \varepsilon_2)$ and $\varepsilon_e''(\varepsilon_1, \varepsilon_2)$. The effective permittivity of the cell can be represented by a symmetric tensor with the diagonal elements $\varepsilon_e'(\varepsilon_1, \varepsilon_2)$ and $\varepsilon_e''(\varepsilon_1, \varepsilon_2)$. The second variant of the tensor (its determinant) $I_2 = \varepsilon_e'(\varepsilon_1, \varepsilon_2)\varepsilon_e''(\varepsilon_1, \varepsilon_2)$ allows us to define the effective permittivity as a geometric mean of the two equivalent permittivities [8]. This approach to determining the effective permittivity, while not claiming to be rigorous, allows us to obtain the well-known exact solutions by simple calculations and satisfies all conditions imposed by general postulates of the theory of inhomogeneous media.

In the general case, when the components have arbitrary properties and the dimensions of inclusions are not fixed, calculation of the electric field in this system encounters insurmountable difficulties.
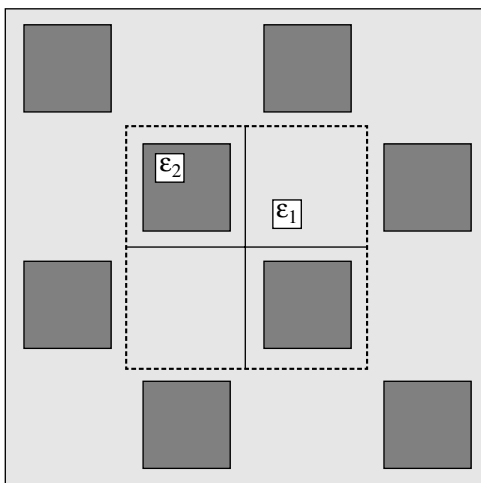
Fig. 4. Fragment of the cross section of a composite dielectric material with the checkerboard arrangement of long fibers with a square cross section. The dotted line shows the cell being analyzed.

SYSTEM WITH CHECKERBOARD ARRANGEMENT OF INCLUSIONS

The structure of this system is illustrated in Fig. 4. It differs from the system shown in Fig. 1 in that the inclusions are packed less densely. If the inclusions increase to their maximum size, the two-component system acquires a checkerboard structure.

As in the previous case, the matrix and inclusion permittivities are denoted as ε_1 and ε_2, respectively. The fundamental periodic cell outlined by the dotted line in Fig. 4 contains two inclusions. The cell is selected on the conditions that (i) being translated in the axes of Cartesian coordinates, it covers the entire plane completely (without gaps) by elements of the same type, and (ii) the elementary cell has the minimum possible dimensions.

The periodic cell outlined in Fig. 4 in turn consists of four smaller cells of two types: with inclusions and without them (in Fig. 4, they are separated by solid lines). In this respect, the system as a whole can be represented as a checkerboard-structure system with the two values of permittivity conventionally designated as ε_a (cell with inclusion) and ε_b (cell without inclusion). Consequently, the system permittivity can be defined by the well-known formula

$$\varepsilon_{\text{eff}} = \sqrt{\varepsilon_a \varepsilon_b}. \tag{13}$$

In the system considered in the previous section, the cell with inclusion was the fundamental periodic cell and was used in calculations of the effective permittivity; therefore, we can take expression (2) as ε_a. For the inclusion-free cell, it is natural to take permittivity ε_1 of the matrix as ε_b. Then, formula (13) takes the following final form:

$$\varepsilon_{\text{eff}} = \varepsilon_1 \left[\frac{1 - \alpha\Delta}{1 + \alpha\Delta} \frac{1 - \beta\Delta}{1 + \beta\Delta} \right]^{1/4}. \tag{14}$$

This is the interpolation formula for the inhomogeneous system with the checkerboard inclusion arrangement. Formula (14) differs from the corresponding expression (2) for the square inclusion arrangement in the power of the root and in the concentration, which is twice as small in this case. Below, to indicate the latter difference in the inclusion concentration in the system with the checkerboard inclusion arrangement, we introduce the notation s_μ. We thus obtain

$$s_\mu = \frac{s}{2} = \frac{1}{2}\left(\frac{n}{n+2}\right)^2 \quad (0 \le s_\mu \le s_{\mu c}), \tag{15}$$

where $s_{\mu c}$ is the critical inclusion concentration, $s_{\mu c} = 1/2$; the remaining notations are the same as in the previous section.

Expression (14) for the effective permittivity exhibits the following characteristic properties.

(i) Expression (14) can easily by shown to satisfy conditions (i–iii) (relationships (8)–(10)) of the previous section.

(ii) At $s_\mu = 0$ ($n = 0$, $\alpha = -1$, $\beta = 1$), the medium is homogeneous with the permittivity ε_1. When $s_\mu = s_{\mu c} = 1/2$ ($n \longrightarrow \infty$, $\alpha = \beta = 1$), the system has the structure of a standard two-component checkerboard with the effective permittivity

$$\varepsilon_{\text{eff}} = \varepsilon_1 \sqrt{\frac{1-\Delta}{1+\Delta}}. \tag{16}$$

(iii) In the particular case of $s_\mu = 1/8$ ($n = 2$, $\alpha = 0$, $\beta = 1/2$), expression (14) takes the simplest form,

$$\varepsilon_{\text{eff}} = \varepsilon_1 \left(\frac{2-\Delta}{2+\Delta}\right)^{1/4}. \tag{17}$$

Regarding inclusion concentration as a small parameter, formula (17) can approximately be written as

$$\varepsilon_{\text{eff}} \approx \varepsilon_1 \frac{1-\Delta/8}{1+\Delta/8} \quad (s_\mu = 1/8). \tag{18}$$

Expression (18) coincides with formula (12), which was extended to the entire range of inclusion concentration through Padé's approximation, and with the formula for the effective permittivity of a system with small concentration of unidirectional cylindrical filaments with a circular cross section [1, 9]. The latter circumstance reflects the well-known theoretical statement: the lower the concentration, the smaller the effect of the inclusion shape on the expression of effective parameters of the medium, which is on average isotropic.

(iv) The applicability area of interpolation formula (14) can be outlined by comparing it with the exact solution obtained for the dielectric medium containing perfectly conducting square inclusions arranged in the checkerboard manner: $\varepsilon_2 \longrightarrow \infty$ ($\Delta = -1$) [8] (strictly speaking, the solution is constructed in terms of conducting media with perfect dielectric inclusions, which is insignificant due to the electrostatic analogy).

The corresponding solution is [8]

$$\varepsilon_{\text{eff}} = \varepsilon_1 \frac{K(k)}{K(k')}, \tag{19}$$

where $K(\cdot)$ is the complete elliptic integral of the first kind and k and k' are the moduli of elliptic integrals:

$$k = \sqrt{\frac{1-g}{2}}, \quad k' = \sqrt{\frac{1+g}{2}} \quad (0 \leq g \leq 1). \tag{20}$$

The parameter g is related to the concentration s_μ as

follows:

$$s_\mu = g \left[\frac{B\left(\frac{1}{2}, \frac{3}{4}\right) F\left(\frac{1}{2}, \frac{1}{2}; \frac{5}{4}; g^2\right)}{B\left(\frac{1}{2}, \frac{1}{4}\right) F\left(\frac{1}{4}, \frac{1}{4}; \frac{3}{4}; g^2\right)} \right]^2, \tag{21}$$

where $B(\cdot)$ is the beta function and $F(\cdot)$ is the hypergeometric function.

At certain particular values of their parameters, formulas (19)–(21) become somewhat simpler. For example, at $g = 1/\sqrt{2}$, the hypergeometric functions that enter into relationship (21) reduce to [10]

$$F\left(\frac{1}{2}, \frac{1}{2}; \frac{5}{4}; \frac{1}{2}\right) = \frac{1}{(2)^{1/4}} \frac{\Gamma(1/2)\Gamma(5/4)}{[\Gamma(7/8)]^2},$$
$$F\left(\frac{1}{4}, \frac{1}{4}; \frac{3}{4}; \frac{1}{2}\right) = \frac{\Gamma(1/2)\Gamma(3/4)}{[\Gamma(5/8)]^2}, \tag{22}$$

where $\Gamma(\cdot)$ is the gamma function.

As a result, formula (21) yields

$$s_\mu = \frac{\pi^2}{4} \left[\sin^2\left(\frac{5\pi}{8}\right) \Gamma\left(\frac{1}{4}\right) \Gamma\left(\frac{3}{4}\right) \right]^{-2} = 0.171573. \tag{23}$$

Using tables of elliptic integrals [11], we obtain the effective permittivity $\varepsilon_{\text{eff}} = 1.4684\varepsilon_1$. At the same concentration (23), interpolation formula (14) yields $\varepsilon_{\text{eff}} = 1.44948\varepsilon_1$. Parameters ε_{eff} calculated from the exact and interpolation formulas give close values; the difference is on the order of 1%.

Another example that allows us to estimate the accuracy of interpolation formula (14) is when elliptic integrals in expression (19) satisfy the relationship [10]

$$K'\left(\frac{\sqrt{2}-1}{\sqrt{2}+1}\right) = 2K\left(\frac{\sqrt{2}-1}{\sqrt{2}+1}\right). \tag{24}$$

Expressions (19)–(21) then yield

$$\varepsilon_{\text{eff}} = 2\varepsilon_1, \quad g = 0.941, \quad s_\mu = 0.305. \tag{25}$$

At the concentration specified in (25), interpolation formula (14) gives $\varepsilon_{\text{eff}} = 2.0408\varepsilon_1$, which differs from the exact value by about 2%.

(v) The system under consideration, like the previous one, was modeled in conducting paper. The experimental results are shown in Fig. 5. The solid curve plots here the function $\varepsilon_{\text{eff}*}^{-1}(s_\mu) = \varepsilon_{\text{eff}}^{-1}(s_\mu)/\varepsilon_1$, which, like the similar curve for the system with square inclusions, is calculated for the case when the dispersion phase is perfectly conducting: $\varepsilon_2 \longrightarrow \infty$ ($\Delta = -1$). Experimental results are shown in the figure by open squares. As follows from these plots, the experimental results and the data obtained using formula (14) agree at small and medium inclusion concentrations ($s_\mu < 0.3$). At higher concentrations ($s_\mu > 0.3$), agreement between the exper-
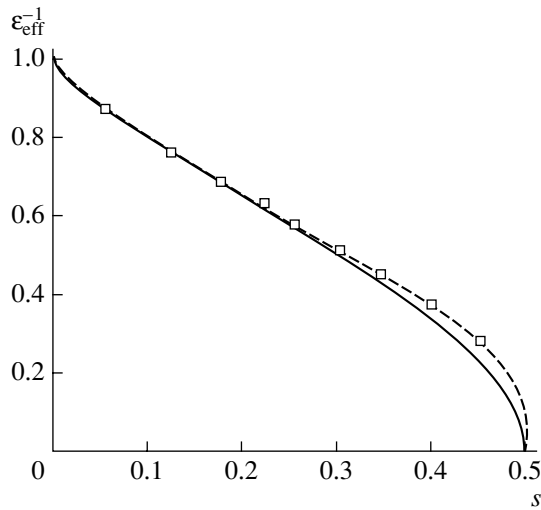
Fig. 5. Function $\varepsilon_{eff}^{-1}(s)$ calculated for the system illustrated in Fig. 4 at $\Delta = -1$ using (solid line) formula (14) and (dashed line) the exact solution [8]. Open squares show the experimental results.

imental data and effective permittivity calculated from formula (14) can be regarded as qualitative. As can be seen, the dashed line calculated using exact formulas (19)–(21) coincides with the experimental results at all inclusion concentrations and exhibits a more rapid variation near the critical point.

DISPERSION OF PERMITTIVITY

In the general case, real dielectric materials exhibit nonzero, albeit small, conductivity. The properties of such materials in an alternating electric field are described using a complex permittivity. The matrix composite materials can conventionally be classified in terms of the characteristic features of their dielectric spectrum into (i) dielectric materials whose matrix is conducting and, consequently, exhibit through conductivity and (ii) dielectric materials in which only inclusions are conducting and, hence, through conducticity appears only at the critical concentration, when the inclusions touch each other. At low frequencies, the permittivity dispersion in these two types of composite materials is significantly different. For materials of the first type, the effective steady-state permittivity and the loss factor exhibit unlimited growth as the frequency tends to zero. For materials of the second type, these characteristics are finite, the effective loss factor tending to zero. This issue was studied in [12, 13] in the cases when the inclusion concentration is small or takes certain fixed values. If the metal–dielectric transition is possible in the system, that is, it actually converts from the first type to the second, the dielectric spectrum abruptly changes. The behavior of the system on the passage from one type of dielectric spectrum to another is of independent theoretical interest. This problem is

still poorly studied, because the known exact solutions have a highly complicated form, which hinders analytical study on the complex plane. This difficulty is easily overcome with the help of interpolation formulas (2) and (14). Though the result obtained in this manner gives only an approximate solution to the problem (due to limitations imposed in the course of derivation of formulas (2) and (14)), this is nevertheless a very simple way to establish the main features of the frequency dependence of the permittivity for a system approaching the critical point.

Below, the permittivity dispersion is considered under the usual assumptions. The nonstationary electrical processes are described by the electromagnetic field equations in the quasi-stationary approximation, under which the wavelength of the external harmonic field is much longer than the characteristic dimension of the system. The main polarization mechanism in the inhomogeneous dielectric is the Maxwell–Wagner polarization. This is an orientation polarization type that can be studied in terms of the Debye theory describing the relaxation of charges in an alternating electric field. Accordingly, the Coal–Coal diagram can be constructed.

Under these assumptions, the effective permittivity of the systems under consideration is determined by relationships (2) and (14) with complex permittivities.

1. System with Square Arrangement of Inclusions

In this case, relationship (2) with the complex effective permittivity

$$\hat{\varepsilon}_{eff}(\omega) = \varepsilon'_{eff}(\omega) - i\varepsilon''_{eff}(\omega), \tag{26}$$

takes the form

$$\hat{\varepsilon}_{eff}(\omega) = \varepsilon_1 \left[\frac{1 - \alpha\hat{\Delta}(\omega)}{1 + \alpha\hat{\Delta}(\omega)} \frac{1 - \beta\hat{\Delta}(\omega)}{1 + \beta\hat{\Delta}(\omega)} \right]^{1/2}. \tag{27}$$

Here, $\hat{\Delta}(\omega) = \Delta'(w) + i\Delta''(\omega)$ is a complex parameter whose real and imaginary parts are

$$\Delta'(\omega) = \frac{4\Delta - \Gamma^2(\omega)(1 - \Delta)^2}{4 + \Gamma^2(\omega)(1 - \Delta)^2},$$

$$\Delta''(\omega) = \frac{2\Gamma(\omega)(1 - \Delta)^2}{4 + \Gamma^2(\omega)(1 - \Delta)^2}, \tag{28}$$

where $\Gamma(\omega)$ is the frequency parameter defined as a ratio of the Maxwell frequency ω_0 to the circular frequency ω of the external electric field:

$$\Gamma(\omega) = \frac{\omega_0}{\omega} = \frac{\sigma_2}{\varepsilon_0 \varepsilon_2 \omega}, \tag{29}$$

where ε_0 is the permittivity of free space and σ_2 and ε_2 are the conductivity and permittivity of inclusions, respectively. The matrix is assumed to be nonconducting.

As the variable, it is convenient to use the relative frequency

$$\Delta_\omega = \frac{\omega_0}{\omega_0 + \omega} \quad (0 \le \Delta_\omega \le 1). \tag{30}$$

At high inclusion concentrations, when the relationship $\alpha \approx \beta \approx s$ is valid, expression (27) can be simplified. In this case, we obtain

$$\hat{\varepsilon}_{eff}(\omega) \approx \varepsilon_1 \left[\frac{1 - s\hat{\Delta}(\omega)}{1 + s\hat{\Delta}(\omega)} \right]. \tag{31}$$

This formula can also be derived from expression (12) by passing to complex variables. The real and imaginary parts of the effective complex permittivity are

$$\varepsilon'_{eff}(\omega) \approx \varepsilon_1 \left[\frac{1 - s^2(\Delta'^2(\omega) + \Delta''^2(\omega))}{(1 + s\Delta'(\omega))^2 + (s\Delta''(\omega))^2} \right],$$

$$\varepsilon''_{eff}(\omega) \approx \frac{2s\varepsilon_1\Delta''^2(\omega)}{(1 + s\Delta'(\omega))^2 + (s\Delta''(\omega))^2}. \tag{32}$$

When $\omega \longrightarrow 0$ ($\Gamma(\omega) \longrightarrow \infty$, $\Delta_\omega \longrightarrow 0$), the effective electrostatic quantities $\varepsilon'_{eff}(0)$ and $\varepsilon''_{eff}(0)$ are given by the expressions

$$\varepsilon'_{eff}(0) \approx \varepsilon_1 \frac{1 + s}{1 - s}, \quad \varepsilon''_{eff}(0) = 0. \tag{33}$$

In another limiting case, at high frequencies $\omega \longrightarrow \infty$ ($\Gamma(\omega) \longrightarrow 0$, $\Delta_\omega \longrightarrow 1$), the optical values of the effective permittivity $\varepsilon'_{eff}(\infty)$ and the effective loss factor $\varepsilon''_{eff}(\infty)$ are determined as

$$\varepsilon'_{eff}(\infty) \approx \varepsilon_1 \frac{1 - s\Delta}{1 + s\Delta}, \quad \varepsilon''_{eff}(\infty) = 0. \tag{34}$$

According to the first relationship in (33), as $s \longrightarrow s_c = 1$, the effective electrostatic permittivity grows without limit as $\varepsilon'_{eff}(0) \sim 1/(1 - s)$. The effective loss factor $\varepsilon''_{eff}(\omega)$ reaches a maximum at a frequency that depends in a complex manner on the relation between parameters of the material the concentration and conductivity of inclusions and the difference between permittivities of the matrix and inclusion (i.e., the parameter Δ). The value of the function $\varepsilon''_{eff}(\omega)$ at its extremal frequency depends on the same parameters. According to the second expression in (32), as $\Delta = -1$, the frequency of the maximum moves toward the Maxwell frequency ($\omega_{max} \longrightarrow \omega_0$) and the value of the function $\varepsilon''_{eff}(\omega)$ decreases. If the inclusion concentration increases, the position of the maximum moves toward lower frequencies and the function $\varepsilon''_{eff}(\omega)$ increases. When the inclusion concentration reaches its critical value of $s = s_c = 1$, the loss factor changes stepwise when $\omega \longrightarrow 0$, taking in this case an infinite value. To illustrate the above analysis, Fig. 6 plots the frequency
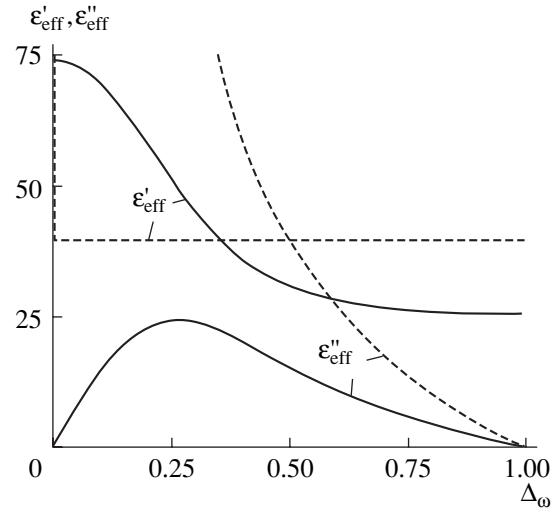
Fig. 6. Plots of the effective permittivity and the effective loss factor vs. relative frequency for the system illustrated in Fig. 1 at $\Delta = -0.95$ and (solid lines) $s = 0.9733$ and (dashed lines) $s = s_c = 1$.

dependences $\varepsilon'_{eff}(\omega)$ and $\varepsilon''_{eff}(\omega)$ for the system with $\Delta = -0.95$ at (solid lines) $s = 0.9733$. The dashed lines in this figure refer to the limiting case of $s = s_c = 1$ and $\Delta = -0.95$. The Coal–Coal diagram has the form of a semicircle, which complies with the classical Debye charge relaxation theory; for the above limiting parameters, the semicircle has an infinite radius.

2. System with Checkerboard Arrangement of Inclusions

In this case, under the same conditions as those taken in the analysis of the previous structure, the complex effective permittivity has the form

$$\hat{\varepsilon}_{eff}(\omega) = \varepsilon_1 \left[\frac{1 - \alpha\hat{\Delta}(\omega)}{1 + \alpha\hat{\Delta}(\omega)} \frac{1 - \beta\hat{\Delta}(\omega)}{1 + \beta\hat{\Delta}(\omega)} \right]^{1/4}. \tag{35}$$
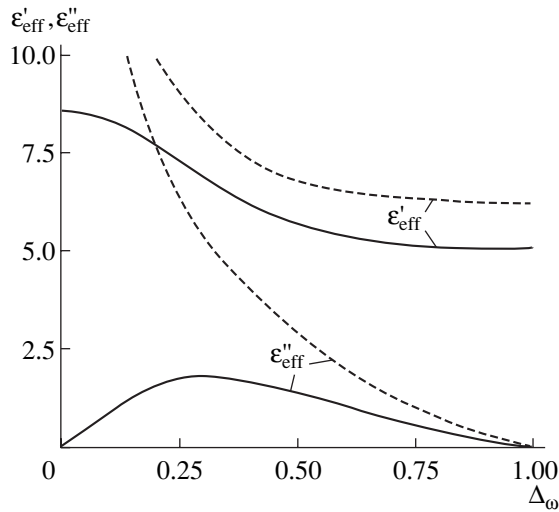
The inclusion concentration s_μ now varies within $0 \le s_\mu \le 1/2$ with $2s_\mu = s$ (15). If the inclusion concentration is high, the relationship $\alpha \approx \beta \approx 2s_\mu$ is valid and expression (35) can approximately be written as

$$\hat{\varepsilon}_{eff}(\omega) \approx \varepsilon_1 \sqrt{\frac{1 - 2s_\mu\hat{\Delta}(\omega)}{1 + 2s_\mu\hat{\Delta}(\omega)}}. \tag{36}$$

It should be recalled that the critical concentration for the system under study is $s_{\mu c} = 1/2$.

Separating expression (36) into real and imaginary parts yields

$$\varepsilon'_{eff}(\omega) \approx \frac{\varepsilon_1}{\sqrt{2}} \sqrt{\sqrt{u^2(\omega) + v^2(\omega)} + u(\omega)},$$

$$\varepsilon''_{eff}(\omega) \approx \frac{\varepsilon_1}{\sqrt{2}} \sqrt{\sqrt{u^2(\omega) + v^2(\omega)} - u(\omega)}, \tag{37}$$

Fig. 7. Plots of the effective permittivity and the effective loss factor vs. relative frequency for the system illustrated in Fig. 4 with $\Delta = -0.95$ at (solid lines) $s_\mu = 0.4865$ and (dashed lines) $s_\mu = s_{\mu c} = 1/2$.
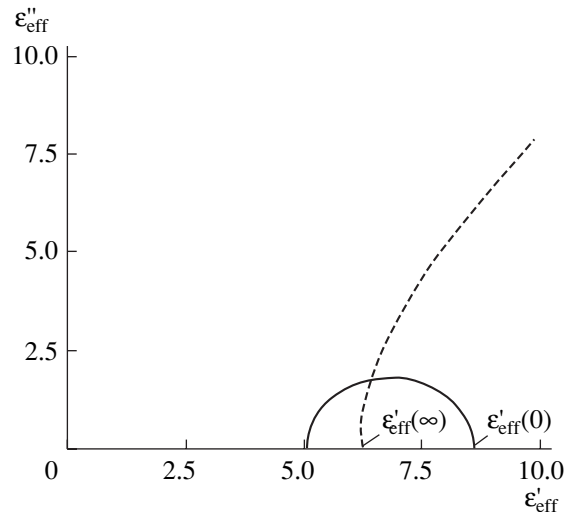
Fig. 8. Diagram of the effective complex permittivity for the system with the same parameters as in Fig. 7.

where

$$u(\omega) = \frac{1 - 4s_\mu^2(\Delta'^2(\omega) + \Delta''^2(\omega))}{(1 + 2s_\mu\Delta'(\omega))^2 + (2s_\mu\Delta''(\omega))^2},$$

$$v(\omega) = \frac{2s_\mu\Delta''(\omega)}{(1 + 2s_\mu\Delta'(\omega))^2 + (2s_\mu\Delta''(\omega))^2}. \tag{38}$$

When $\omega \longrightarrow 0$ ($\Gamma(\omega) \longrightarrow \infty$, $\Delta_\omega \longrightarrow 0$), the effective electrostatic permittivity $\varepsilon'_{\text{eff}}(0)$ and the effective electrostatic loss factor $\varepsilon''_{\text{eff}}(0)$ are given by the expressions

$$\varepsilon'_{\text{eff}}(0) \approx \varepsilon_1 \sqrt{\frac{1 + 2s_\mu}{1 - 2s_\mu}}, \quad \varepsilon''_{\text{eff}}(0) = 0. \tag{39}$$

At high frequencies, when $\omega \longrightarrow \infty$ ($\Gamma(\omega) \longrightarrow 0$, $\Delta_\omega \longrightarrow 1$), the optical values of the effective permittivity $\varepsilon'_{\text{eff}}(\infty)$ and effective loss factor $\varepsilon''_{\text{eff}}(\infty)$ are determined as follows:

$$\varepsilon'_{\text{eff}}(\infty) \approx \varepsilon_1 \sqrt{\frac{1 - 2s_\mu\Delta}{1 + 2s_\mu\Delta}}, \quad \varepsilon''_{\text{eff}}(\infty) = 0. \tag{40}$$

In the general case, the frequency dependence of the effective complex permittivity of the checkerboard structure is the same as that for the system with the square arrangement of inclusions (with a correction for the root dependence); accordingly, when the inclusion concentration approaches its critical value $s \longrightarrow s_c = 1/2$, the effective electrostatic permittivity of this system follows the square root law: $\varepsilon'_{\text{eff}}(0) \sim 1/\sqrt{1 - 2s_\mu}$. To compare the frequency dependence of the effective complex permittivity of the two systems, Fig. 7 plots

(solid lines) $\varepsilon'_{\text{eff}}(\omega)$ and $\varepsilon''_{\text{eff}}(\omega)$ for the system with $\Delta = -0.95$ at $s_\mu = s/2 = 0.48665$. The complex diagram is shown in Fig. 8. The dashed lines in Figs. 7 and 8 plot the functions for the limiting case of $s_\mu = s_{\mu c} = 1/2$ at $\Delta = -0.95$.

CONCLUSIONS

The permittivity dispersion in strongly inhomogeneous matrix dielectric materials can be exhaustively studied using interpolation formulas, which are simple and convenient for analytical calculations. They coincide with the well-known exact solutions and, what is most importantly, are corroborated by experimental data in a wide range of the inclusion concentrations. However, the interpolation formulas are not free of some disadvantages: they have no rigorous substantiation based on solutions to boundary-value problems and yield discrete values of the effective permittivity. The latter circumstance is significant only at small inclusion concentrations. In this case, it is better to use different models.

REFERENCES

1. W. T. Perrins, D. R. McKensie, and R. C. McPedran, Proc. R. Soc. London, Ser. A **369**, 207 (1979).

2. R. D. Manteufel and N. E. Todreas, Int. J. Heat Mass Transf. **37**, 647 (1994).

3. B. Ya. Balagurov and V. A. Kashin, Zh. Éksp. Teor. Fiz. **117**, 978 (2000) [JETP **90**, 850 (2000)].

4. Yu. V. Obnosov, SIAM J. Appl. Math. **59**, 1267 (1999).

5. N. S. Bakhvalov and G. P. Panasenko, *Averaging of Processes in Periodic Media* (Nauka, Moscow, 1984) [in Russian].

6. I. V. Andrianov *et al.*, Proc. R. Soc. London, Ser. A **455**, 3401 (1999).

7. K. S. Cole, Ch. Li, and A. F. Bak, Exp. Neurol. **24**, 459 (1969).

8. Yu. P. Emets, *Electrical Performance of Composites* (Naukova Dumka, Kiev, 1986) [in Russian].

9. Yu. P. Emets, Zh. Éksp. Teor. Fiz. **114**, 1121 (1998) [JETP **87**, 612 (1998)].

10. *Higher Transcendental Functions (Bateman Manuscript Project)*, Vols. 1–3, Ed. by A. Erdelyi (McGraw-Hill, New York, 1955; Nauka, Moscow, 1967).

11. N. I. Akhiezer, *Theoretical Grounds of Elliptic Functions* (Nauka, Moscow, 1970) [in Russian].

12. Yu. P. Emets, Zh. Éksp. Teor. Fiz. **121**, 1339 (2002) [JETP **94**, 1149 (2002)].

13. Yu. P. Emets, Zh. Tekh. Fiz. **73** (3), 42 (2003) [Tech. Phys. **48**, 317 (2003)].

Translated by A. Khzmalyan

THEORETICAL
AND MATHEMATICAL PHYSICS

Equation of State in the Quasi-Classical Approximation

V. V. Prut

Russian Research Center Kurchatov Institute, pl. Kurchatova 1, Moscow, 123182 Russia
e-mail: prut@nfi.kiae.ru
Received July 7, 2003; in final form, April 29, 2004

Abstract—An approximate equation of state is considered that contains a correction for electron-gas inhomogeneity in the exchange-correlation and kinetic energies in the quasi-classical approximation. The problem of finding the model parameters satisfying the condition $P = 0$ has been solved for metals at a normal density. The results of numerical solution of the model equations are presented for degrees of compression. The values of the quasi-classical parameter determining the approximation accuracy are found. The results are illustrated by the dependences on the degree of compression plotted in the range $\rho/\rho_0 = 1–10^6$ and by the spatial dependences. Our approach to construction of the equation of state provides for a quite simple but sufficiently accurate approach to the experimental values of the model parameters. Moreover, the proposed model gives much more self-consistent information as compared to conventional approximations. In particular, the ionicity is calculated for an increase in the density. The model equation can also be used instead of the well-known effective bound-electron potential approximation. © *2004 MAIK "Nauka/Interperiodica"*.

INTRODUCTION

The Thomas–Fermi equation can be obtained using a variational method through minimization with respect to the electron density of a functional constructed for the quasi-classical electron energy [1]. The Thomas–Fermi equation can also be derived from the Hartree–Fock equation in the quasi-classical approximation with allowance for the quantum second- and fourth-order $\hbar$ corrections [2–4]. Kohn and Sham [5] reduced the problem of minimization of the functional to solving the Schrödinger equation with an effective potential in which the exchange-correlation energy has to be explicitly taken into account. The local density approximation is mainly used when the functional depends only on the density and is independent of its derivatives. This is substantially due to the fact that the conditions of applicability of the first gradient expansion are invalid in the real systems under consideration. The quantum and exchange corrections to the energy and the chemical potential of the Thomas–Fermi atom and the numerical calculations of thermodynamic quantities were reported by Kalitkin [6].

However, there are no solutions for the functionals that can also take into account the second derivatives—the so-called $\hbar^4$ approximation [4]. This is likely to be related both to certain mathematical difficulties and to the fact that taking into account higher approximations can lead to ambiguities and can even deteriorate the agreement with experimental results.

The Thomas–Fermi approximation can be applied so as to take into account the electron shell structure of an atom [7–9]. The electron structure can be taken into account more consistently using the Hartree–Fock model [10]. The band structure was approximately taken into account in terms of the quasi-band model [11], quasi-classical model of the equation of state [12], and self-consistent field model [13].

Various modifications of the Thomas–Fermi method are used at arbitrary temperatures. The results of calculations in a broad range of densities and temperatures are presented in [14, 15].

A disadvantage of the approximations mentioned above is, for example, the fact that the condition $P(V_0) = 0$ is not satisfied at a normal experimental density. For copper, the characteristic value of this deviation is ~1 Mbar. Of course, for problems at high pressures ($P > 1$ a.u. (300 Mbar)), this value can be neglected, which is common practice. However, in many problems, the equation of state at normal densities and megabar pressures is also of significant interest. Using any perfect modern model, it is evidently impossible to perform an exact *ab initio* calculation of all the required parameters that are measured experimentally. Of course, this is also impossible within the framework of the quasi-classical approximation. Therefore, solving the problem at normal densities requires fitting parameters similar to those introduced, for example, in the pseudopotential method.

In order to correctly introduce a free parameter and to retain the terms of the Thomas–Fermi–Dirac equation adopted in the local approximation, we will use the quasi-classical approximation so as to qualitatively take into account the first gradient correction for the electron gas inhomogeneity in the exchange-correlation energy.

Such a model can describe metals at all densities to a reasonable accuracy, and, at a high density (when outer-shell electrons begin to form a continuous spectrum), the model can adequately describe all substances. The problem of determining the parameters of model satisfying the condition $P(V_0) = 0$ has been solved numerically.

Because of the limited volume of this article, some illustrations are presented elsewhere [16].

THOMAS–FERMI–DIRAC– WEIZSÄCKER EQUATION

The functional, from which the Thomas–Fermi–Dirac–Weizsäcker equation can be derived (hereafter, referred to as the Weizsäcker equation or model) for a Wigner–Seitz cell of volume V at a temperature of $T = 0$, has the following form:

$$
E[n] = \frac{3}{5}k_k\int_V n^{5/3}dv - \frac{3}{4}k_x\int_V n^{4/3}dv
$$
$$
+ k_g\int_V \frac{1}{n}(\nabla n)^2 dv + \int_V\left(-\varphi_i + \frac{1}{2}\varphi_e\right)n dv, \tag{1}
$$

where the coefficients are $k_k = (3\pi^2)^{2/3}/2$ and $k_x = (3/\pi)^{1/3}$, $k_g = 1/72$ [3, 4]; all the notations are as commonly accepted: n is the electron density; φ_i and φ_e are the nuclear and electron potentials, respectively; p is the momentum; P is the pressure; and the system of units is atomic, unless otherwise specified.

The condition of conservation of charge is

$$
\int_V n dv = Z, \tag{2}
$$

where Z is the nuclear charge.

The potential $\varphi = \varphi_i - \varphi_e$ satisfies Poisson's equation

$$
\Delta\varphi = 4\pi n. \tag{3}
$$

The minimization of functional (1) with respect to the density under condition (2) leads to the equation

$$
k_k n^{2/3} - k_x n^{2/3} + k_g\frac{1}{n^2}(\nabla n)^2 - 2k_g\frac{1}{n}\Delta n - \varphi = \mu,
$$

where μ is the Fermi energy (chemical potential, Lagrangian multiplier).

First, let us introduce the correlation energy into this equation.

CORRELATION ENERGY

The correlation energy was calculated in many papers (e.g., see the reviews [17–20]), where analytical expansions were obtained at high densities [21, 22] and low densities [23] and numerical results were obtained in the intermediate region (see the above reviews and

[24–27]). Various approximations were proposed to describe the correlation interaction over a wide density range (see, e.g., [18, 28, 29]); however, a universal, generally accepted, and convenient formula has not been derived. Therefore, let us approximate the correlation energy using asymptotic expressions obtained in the high- and low-density limits and introduce one free parameter to be determined by comparison with the numerical calculations performed at intermediate densities.

At high densities ($r_s \ll 1$), the well-known classical asymptotic Gell-Mann–Brueckner dependence is valid [21]:

$$
e_c = c_0\ln(r_s) - c_1. \tag{4}
$$

Another approximation is the Carr–Maradidin formula [22]

$$
e_c = c_0\ln(r_s) - c_1 + c_2 r_s\ln(r_s) - c_3 r_s, \tag{5}
$$

where the coefficients are taken to be $c_0 = 0.031091$, $c_1 = 0.04664$, $c_2 = 0.00664$, and $c_3 = 0.01043$.

At low densities ($r_s \gg 1$), Wigner [17] assumed that electrons form a body-centered cubic lattice in space, and Carr *et al.* [23] obtained the expansion

$$
e_c = -\frac{a_0}{r_s} + \frac{a_1}{r_s^{3/2}} - \frac{a_2}{r_s^2} - \frac{a_3}{r_s^{5/2}} + O\left(\frac{1}{r_s^3}\right). \tag{6}
$$

Here, the coefficient $a_0 = 0.89593$ specifies the electrostatic energy of the lattice, the coefficient $a_1 = 1.325$ specifies the zero-oscillation energy, and the terms $a_2 = 0.365$ and $a_3 = 0.4$ represent the anharmonic corrections.

We adopt the following interpolation (immediately writing the dependences on n rather than on r_s, which is a common practice):

$$
e_c(n) = -\frac{c}{\beta}\ln\left(1 + \frac{a\beta n^{1/3}}{1 + dn^{1/6}} + (bn)^\beta\right). \tag{7}
$$

Let us determine the coefficients a, b, c, and d from the following conditions. The two coefficients (c_0, c_1) of the expansion at high densities (see (4)) and the two coefficients (a_0, a_1) of the expansion at low densities (see (6)) should be satisfied identically. The term $(bn)^\beta$ in (7) dominates at high densities; therefore, the coefficients c and b are determined from Eq. (4). The second term under the logarithm dominates at low densities; therefore, a and d are determined from Eq. (6). Then, we have $c = c_0/3$, $b = q\exp(3c_1/c_0)$, $a = 3q^{1/3}a_0/c_0$, and $d = q^{1/6}a_1/a_0$; here, $q = 4\pi/3$.

The only free parameter β is specified through minimization of the function determining the error,

$$
F(\beta) = \sum_{i=1}\left(\frac{e_i - \varepsilon_i}{\delta\varepsilon_i}\right)^2.
$$

$-e_c$, mRy
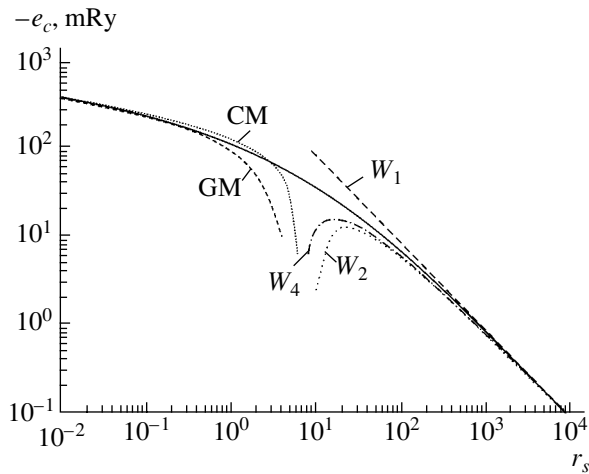
Fig. 1. Plots of the correlation energy vs. r_s^*: (GM) the Gell-Mann–Brueckner dependence [21], Eq. (4); (CM) the Carr–Maradidin approximation [22], Eq. (5); (W_1, W_2, W_3) the Wigner approximation, Eq. (6) with one, two, and four terms, respectively.

Here, ε_i is the energy calculated at $r_s = 1, 2, 5, 10, 50,$ and 100 [24] and $\delta\varepsilon_i$ is the absolute calculation error of ε_i.

The numerical minimization gives the value $\beta = 0.544$ with a relative error $<3 \times 10^{-2}$ over the whole range. The transition from one asymptotic case to another occurs at $r_s \sim 1$. The energy at the top of the Fermi distribution is determined from the relation $e_{cF} = (de_c n)/(dn)$, and the pressure is

$$P_c = n^2 \frac{de_c}{dn}.$$

Figure 1 shows the constructed approximation and asymptotic dependences. These asymptotic dependences are inapplicable in the interval $\sim 1 < r_s < \sim 10^2$, which extends over six orders of magnitude in density (including the normal densities of all elements). The dependence obtained agrees well with the results reported not only in [24] but also in [25–27] at normal and near-normal densities.

QUANTUM CORRECTIONS TO THE EXCHANGE-CORRELATION ENERGY

The condition of applicability of the quasi-classical approximation is known to be [30]

$$\xi = \left|\frac{d\lambda}{dx}\right| \ll 1, \tag{8}$$

where λ is the quasi-classical de Broglie electron wavelength; this approximation is inapplicable when this condition is unsatisfied.

A quantum correction, namely, the gradient term in Eq. (1), can qualitatively be obtained as follows. We

have

$$\lambda = \frac{1}{p}, \quad \xi = \frac{1}{p^2}\left|\frac{dp}{dx}\right|$$

(in dimensional quantities, $\xi = \frac{\hbar}{p^2}\left|\frac{dp}{dx}\right|$; therefore, expansion in terms of ξ is the expansion in terms of $\hbar$). In the quasi-classical approximation, we obtain $p_F = (3\pi^2)^{1/2}n^{1/3}$. Then, we have

$$\xi = \frac{1}{3(3\pi^2)^{1/3}} \frac{1}{n^{4/3}} \frac{dn}{dx}.$$

The influence of quantum effects is specified by the parameter ξ^2, since, when physical quantities are expanded in a series about $\hbar$, odd-order terms are canceled out identically [30]. Therefore, a change in the quasi-classical kinetic energy $e_k = \frac{3}{5} k_k n^{5/3}$ is

$$\delta e_k = e_k \nu_k \xi^2, \tag{9}$$

where the coefficient ν_k should generally be ~ 1.

A comparison of Eq. (9) with the exact first approximation [3] indicates that $\nu_k = 5/12$; then, Eq. (9) can be reduced to

$$\delta e_k = \frac{1}{72} \frac{1}{n} \left(\frac{dn}{dr}\right)^2.$$

Let us assume that the same functional holds for a relative change in the exchange-correlation energy. For

$$e_x = \frac{3}{4} k_x n^{4/3}$$

we obtain

$$\delta e_x = e_x \nu_x \xi^2$$

or

$$\delta e_x = \frac{1}{36} \frac{3^{2/3}}{\pi^{5/3}} \frac{\nu_x}{n^{4/3}} \left(\frac{dn}{dr}\right)^2.$$

Gradient corrections to the exchange-correlation energy were studied in [31–34], since the authors tried to go beyond the limits of the local approximation in the density functional method. The functional dependence of the first gradient correction has the same form; therefore, their comparison gives $\nu_x = 5/18$. For transformations and numerical calculations, the last equation can conveniently be written as

$$\delta e_x = \frac{c_x}{12} \frac{1}{n^{4/3}} \left(\frac{dn}{dr}\right)^2,$$

where

$$c_x = \frac{2 \times 3^{2/3}}{\pi^{5/3}}.$$

For the correlation energy, we can write

$$\delta e_c = \frac{c_x}{72} \frac{c_c e_c}{n^{5/3}} \left(\frac{dn}{dr}\right)^2,$$

where

$$c_c = \frac{4}{3}\left(\frac{\pi}{3}\right)^{1/3}.$$

The effective degree of the density dependence of the correlation energy (at a normal density) is

$$\alpha_c = \frac{d \ln e_c}{d \ln n} \approx \frac{1}{6}.$$

Therefore, when the density decreases, the correlation energy depends mainly on the density gradient.

By collecting all the gradient terms for the kinetic energy and the exchange-correlation energy, we can write

$$\delta e_{kxc} = \frac{g}{72n}\left(\frac{dn}{dr}\right)^2,$$

where

$$g(n) = c_k + \frac{c_x}{n^{1/3}}\left(1 + \frac{c_c e_c}{n^{1/3}}\right).$$

The attempt to go beyond the limits of the first gradient correction (which is valid in the limit of slowly changing density) without consideration of higher-order corrections led to the formulation of the so-called generalized gradient approximation [31–34]. Actually, the function $g(n, \nabla n)$ is assumed to depend not only on the density but also on its gradient. The function $g(n, \nabla n)$ cannot be chosen only theoretically, and this choice is insufficiently substantiated (as can be clearly seen in [34]). Therefore, in this study, we will restrict our consideration to finding the parameters c_k and c_x of the $g(n)$ function for $c_x = 1$. Let us assume that these parameters (c_k or c_x) can be determined from the condition $P(V_0) = 0$. The variation of these parameters is justified to a certain extent by the fact that the $\hbar^2$ approximation cannot be used in a certain radial region and higher approximations are not taken into account.

The unknown functional is assumed to have the following form:

$$E[n] = \frac{3}{5}k_k\int_V n^{5/3}dv - \frac{3}{4}k_x\int_V n^{4/3}dv - \int_V e_c n dv$$
$$+ k_g\int_V \frac{g}{n}(\nabla n)^2 dv + \int_V \left(-\varphi_i + \frac{1}{2}\varphi_e\right)n dv. \tag{10}$$

The minimization of functional (10) under condition (2) with respect to the density n leads to the equation

$$2k_g\frac{g}{n}\Delta n + k_g\frac{d}{dn}\left(\frac{g}{n}\right)(\nabla n)^2$$
$$- k_k n^{2/3} + k_x n^{1/3} + e_c + \varphi + \mu = 0. \tag{11}$$

By substituting

$$\varphi + \mu = \frac{u}{r}, \tag{12}$$

we transform Eq. (11) into

$$2k_g\frac{g}{n}\frac{1}{r^2}\frac{d}{dr}r^2\frac{dn}{dr} + k_g\frac{d}{dn}\left(\frac{g}{n}\right)\left(\frac{dn}{dr}\right)^2$$
$$- k_k n^{2/3} + k_x n^{1/3} + e_c + \frac{u}{r} = 0, \tag{13}$$

and Poisson's equation into

$$\frac{d^2 u}{dr^2} = 4\pi r n. \tag{14}$$

For Eq. (13), the left boundary condition (at $r = 0$) can be obtained as follows. If n is supposed to be limited at $r = 0$, the solution to Eq. (13) can be represented as the power series

$$n = n_0(1 + a_1 r + a_2 r^2 + \ldots),$$
$$u = Z(1 + b_1 r + b_2 r^2 + \ldots). \tag{15}$$

Substitution of expressions (15) into Eq. (13) yields the boundary condition

$$\frac{dn}{dr} = -18Zn. \tag{16}$$

The right boundary condition (at $r = R$, which is the Wigner–Seitz cell radius) is $dn/dr = 0$.

For Eq. (14), the left boundary condition is $u = Z$. Its right boundary condition, $R(du/dr) = u$, is determined from a condition for the electric field strength: $d\varphi/dr = 0$.

The bound and free electron densities are determined on the condition that the total energy is $e(r) = 0$. The bound electron density n_b is obtained by solving the equation

$$2k_g\frac{g}{n_b}\frac{1}{r^2}\frac{d}{dr}r^2\frac{dn_b}{dr} + k_g\frac{d}{dn_b}\left(\frac{g}{n_b}\right)\left(\frac{dn_b}{dr}\right)^2$$
$$- k_k n_b^{2/3} + k_x n_b^{1/3} + e_c(n_b) + \varphi = 0. \tag{17}$$

The free electron density is found from the relation $n_f = n - n_b$. The total number of free electrons (the ion-

icity) is determined as

$$Z_f = \int_0^R n_f 4\pi r^2 dr.$$

The boundary conditions for Eq. (17) are identical to those for Eq. (13).

NUMERICAL SOLUTION

Upon substitution $y = n^{1/2}$, Eq. (13) this equation reduces to

$$4k_g \frac{g}{r^2} \frac{d}{dr} r^2 \frac{dy}{dr} + 2k_g \frac{dg}{dy} \left(\frac{dy}{dr}\right)^2$$
$$- k_k y^{7/3} + k_x y^{5/3} + e_c y + \frac{u}{r} y = 0. \tag{18}$$

This equation was linearized with respect to dy/dr and y and then approximated. Let us introduce a lattice with respect to r according to the relation $x = r^{1/2}$, where the x lattice is uniform, subscript i runs within $o \le i \le I$, and the r steps are dr_i and $dr_{i+1/2}$. Then, the difference scheme for Eq. (13) is

$$4k_g \frac{g_i^k}{r_i^2} \frac{1}{dr_i} \left(r_{i+1/2}^2 \frac{y_{i+1}^{k+1} - y_i^{k+1}}{dr_{i+1/2}} - r_{i-1/2}^2 \frac{y_i^{k+1} - y_{i-1}^{k+1}}{dr_{i-1/2}}\right)$$
$$+ 2k_g \frac{d^k g}{dy_i} \left(\frac{y_{i+1}^{k+1} - y_{i-1}^{k+1}}{2dr_i} 2 \frac{y_{i+1}^k - y_{i-1}^k}{2dr_i}\right.$$
$$\left. - \left(\frac{y_{i+1}^k - y_{i-1}^k}{2dr_i}\right)^2\right) - k_k \left(\frac{7}{3} y_i^{k+1} y_i^{k4/3} - \frac{4}{3} y_i^{k7/3}\right)$$
$$+ k_x \left(\frac{5}{3} y_i^{k+1} y_i^{k2/3} - \frac{2}{3} y_i^{k5/3}\right) + e_c y_i + \frac{u_i}{r_i} y_i = 0. \tag{19}$$

The superscript k is the number of the iteration step. For the particular case $g \equiv 1$, the substitution $w = rn^{1/2}$ is known to reduce Eq. (13) to

$$\frac{1}{18} \frac{d^2 w}{dr^2} - k_k \frac{w^{7/3}}{r^{4/3}} + k_x \frac{w^{5/3}}{r^{2/3}} + e_c w + uw = 0. \tag{20}$$

The equation is seen to have no term with the first derivative and to have the second derivative instead of the Laplacian. The difference scheme is analogous to that for Eq. (13).

The difference scheme of Eq. (14) is

$$\frac{1}{dr_i} \left(\frac{u_{i+1}^{k+1} - u_i^{k+1}}{dr_{i+1/2}} - \frac{u_i^{k+1} - u_{i-1}^{k+1}}{dr_{i-1/2}}\right) = 4\pi r_i y_i^2. \tag{21}$$

Both schemes (19) and (20) have the second order of smallness with respect to r.

The boundary conditions for Eqs. (13) and (14) were approximated to within the second order of accu-

racy; otherwise, the required solution accuracy could not be achieved and the convergence sharply degraded.

The left boundary condition (at $r = 0$) for Eq. (14) is $u = Z$, and the right boundary condition (at $r = R$) is

$$R \frac{du}{dr} = u.$$

The derivative du/dr can be calculated in the second order with regard to the Taylor expansion and Eq. (14):

$$u_{I-1} = u_I - dr_{I-1/2} \left(\frac{du}{dr}\right)_I + \frac{dr_{I-1/2}^2}{2} \left(\frac{d^2 u}{dr^2}\right)_I.$$

Whence it follows that

$$-\frac{u_{I-1}}{dr_{I-1/2}} + \frac{u_I}{dr_{I-1/2}} - \frac{u_I}{R} = -2\pi n_I R dr_{I-1/2}.$$

For Eq. (13), the left boundary condition is $dy/dr = -9Zy$ and the right boundary condition is $dy/dr = 0$. Both conditions were approximated by difference relationships to within the second order of accuracy:

$$3 \frac{y_1 - y_0}{dr_{1/2}} - \frac{y_2 - y_1}{dr_{3/2}} = -18Z y_0,$$

$$-\frac{y_{I-1} - y_{I-2}}{dr_{I-3/2}} + 3 \frac{y_I - y_{I-1}}{dr_{I-1/2}} = 0.$$

The left boundary condition for Eq. (20) reduces to

$$\frac{dw}{dr} = 0. \tag{22}$$

The left boundary condition for Eq. (13) imposes a rigid condition on the r step because of a very large derivative. Condition (22) lifts this restriction and makes it possible to calculate Eq. (19) at any r step. Equation (20) was mainly used to debug and check results, as well as to calculate c_k at $c_x = 0$.

The gradient pressure in the Weizsäcker model was determined as [3]

$$P = -\frac{1}{36} \left(\frac{d^2 n}{dr^2}\right)_R.$$

In our model (with an arbitrary g function), the pressure (and its components) was determined as [35]

$$P = -\frac{g}{36} \left(\frac{d^2 n}{dr^2}\right)_R.$$

The second derivative for calculating the pressure, or the Laplacian for calculating energy (18), can be found by two methods: either directly from Eq. (13) or "by definition" at a calculated density.

The difference equations were solved by the standard sweep method. The initial density and its derivatives were found from the solution to the Thomas–Fermi–Dirac equation with correlation energy (7). The calculation results were obtained using 1000 points

over the radius. The condition of iteration termination was $\max|du|, |dn| < 10^{-8}$. The parameters c_k and c_x of the function g were found with an accuracy of 10^{-8} by solving the relation $P(c) = 0$ using the Newton method with restrictions involved in the method of interval bisection.

CALCULATION RESULTS

We present the results of calculations for copper ($Z = 29$). Copper is known to have the best combination of parameters, which makes it a convenient standard material. The zero pressure was calculated in the Debye approximation: $P = 9/8 \times R\Theta\Gamma/V_0$, where R is the gas constant, Θ is the Debye temperature, Γ is the Grüneisen parameter, and V_0 is the specific volume.

Figure 2 mainly illustrates the possibility of reaching the goal of this study, namely, to obtain $P(V_0) = 0$ through the calculation of the model parameters: $c_k = 3.14$ at $c_x = 0$ or $c_x = 0.466$ at $c_k = 1$. The proposed method of introducing the form of a dependence that approximates the functional allows us to rather simply and accurately approach the actual values of the parameters under consideration. Like the correlation energy, accumulating all the disadvantages of the Hartree–Fock model, the dependence found and its parameters accumulate all the errors of the model proposed. In the region of inapplicability of the $\hbar^2$ local approximation, the approximating dependence can be chosen so that it would provide the maximum compensation both for the errors of higher and nonlocal approximations not taken into account and for the model errors.

Of course, other equations, such as equations for the bulk compression modulus $B(c) = B_0$, the Fermi energy, the ionization energy, or the total energy, can be solved jointly with the equation $P(c) = 0$. However, this procedure significantly increases the amount of calculations, apart from bringing uncertainty in the approximation of the gradient corrections and in the choice of priority of additional conditions. Naturally, the thus-obtained equation of state cannot be directly used in hydrodynamic calculations. It should preliminarily be transformed into a tabular form or approximated by analytical functions (see, e.g., [36, 37]). Nevertheless, it can serve as an additional criterion of the validity of such approximations. Moreover, the approximation proposed provides much more information on the microscopic level. In particular, it allows one to calculate the ionicity for an increase in the density. It can also be used instead of the well-known effective bound-electron potential approximation, in which coefficients are adjusted so as to reach the best agreement with experimental data.

At a normal density, the pressure is 3.16 Mbar in the Thomas–Fermi model, 2.05 Mbar in the Thomas–Fermi–Dirac model, and 1.2 Mbar in the Weizsäcker model. The differences in the pressures for the different
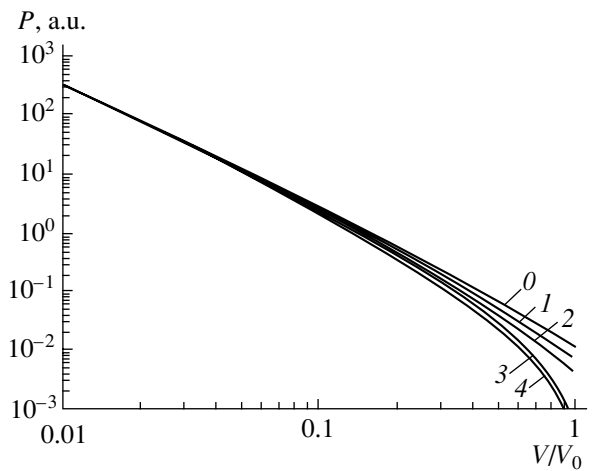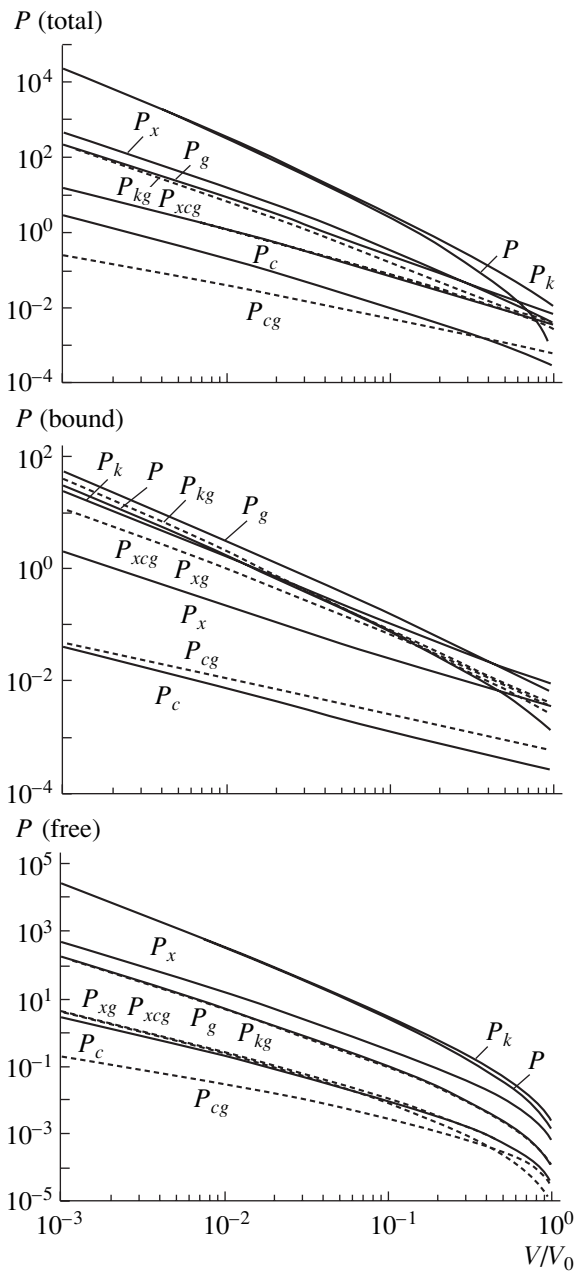

Fig. 2. Plots of the pressure vs. specific-volume: (*0*) the Thomas–Fermi equation; (*1*) the Thomas–Fermi–Dirac equation with correlation energy (7); (*2*) Eq. (13) with $c_k = 1$ and $c_x = 0$; (*3*) Eq. (13) with $c_k = 3.14$ and $c_x = 0$; (*4*) Eq. (13) with $c_k = 1$ and $c_x = 0.446$.

models vanish only upon ~10–100-fold compression, which corresponds to a pressure higher than 1–100 Gbar.

Figure 3 shows the pressure components for the total electron density and for the free and bound electrons. The pressure component are as follows: P_k is the kinetic pressure; P_x is the exchange pressure; P_c is the correlation pressure; and P_{kg}, P_{xg}, and P_{cg} are their gradient components ($P_{xcg} = P_{xg} + P_{cg}$). The subscript g indicates the gradient pressure. As can be seen from Fig. 3, all the pressure components retain their signs. Only the kinetic pressure is positive, whereas the other (exchange, correlation) components and all the gradient components are negative. Because of the logarithmic scale in Fig. 3, the signs of the negative components are changed; moreover, we imply their absolute magnitudes in the estimations given below.
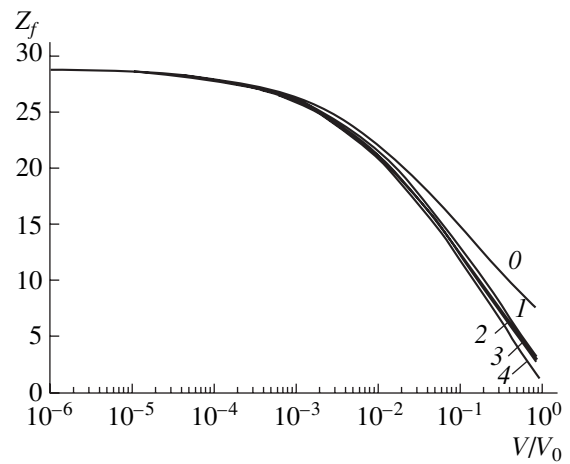
The main contribution to the total pressure is naturally made by the kinetic pressure; the exchange pressure is an order of magnitude smaller (in the density range under consideration). Then, these pressures diverge according to the $\rho^{5/3}$ and $\rho^{4/3}$ laws. The correlation pressure is even smaller (by ~1.5 orders of magnitude); at a normal density, it is 100 kbar and cannot compensate for the model drawbacks. The gradient pressures in the Weizsäcker model and the proposed model are noticeably different and converge only at a ~100-fold compression. The total gradient pressure at compressions <~3 is even higher than the local exchange pressure. Actually, it is this substantial increase in the gradient pressure that allows us to satisfy the condition $P(V_0) = 0$. This fact also indicates that the local density approximation in the quasi-classical approximation cannot provide for an acceptable calculation accuracy. At a normal density, we have $P_{kg} \approx P_{xcg}$,

Fig. 3. Pressure components for the total electron density, bound electrons, and free electrons.

Fig. 4. Plots of the total number of free electrons vs. specific-volume. Curve numbers are the same as in Fig. 2.

sity, the gradient correlation pressure exceeds the gradient exchange pressure.

For bound electrons, these relations are mostly invalid. First, the total pressure P is always negative (in Fig. 3, the sign is changed). This is related to the fact that the gradient densities for bound electrons are always high and the total gradient pressure P_g significantly exceeds P_k. All the pressures of bound electrons upon compression are significantly lower than the corresponding values for free electrons. At a normal density, the bound-electron pressure is −300 kbar and the free-electron pressure is +310 kbar. The ~10-kbar difference is related to the pressure of zero-point oscillations. In the range of relative compressions under study, $P_{cg} > P_c$ and $P_{xg} > P_x$; however, the kinetic gradient pressure is $P_k > P_{kg}$ at compressions below ~70, but $P_k < P_{kg}$ upon further increase in compression.

Figure 4 shows the dependence of the total number of free electrons Z_f on the specific volume. At a normal density, the Thomas–Fermi model gives a strongly overestimated value ($Z_f \approx 7$), the Thomas–Fermi–Dirac model gives $Z_f \approx 2.5$, the Weizsäcker model gives $Z_f \approx 2.4$, the Weizsäcker model with $c_k = 3.14$ ($P = 0$) gives $Z_f \approx 2.1$, and Eq. (13) gives $Z_f \approx 0.9$. Upon compression, the total number of free electrons first sharply increases: to $Z_f \approx 12$ at about a tenfold compression (at a pressure $P \approx 10^9$ bar) and to $Z_f \approx 21$ at about a hundredfold compression (at a pressure $P \approx 10^{12}$ bar). However, all electrons are completely forced into a continuous spectrum only at $V/V_0 \approx 10^{-5}$ (at a pressure $P \approx 10^{17}$ bar).

Figure 5 shows the dependences of the energies on the specific volume for the total electron density and separately for the free and bound electrons. The total energy is $E = E_k - E_x - E_c + E_g - E_u$, where E_k is the kinetic energy, E_x is the exchange energy, E_c is the correlation energy, E_g is the gradient energy, and E_u is the

which seems rather unexpected. However, the pressure is determined by the limiting density, which is always significantly greater than the average density, and the component P_{xcg} increases with decreasing density. Then (upon compression), P_{kg} becomes the most important contribution. The correlation pressure and its gradient component are always the smallest, and $P_{cg} > P_c$ at a normal density.

For free electrons, these relations hold true to a large measure. The only exception is that, at a normal den-

potential energy. The signs of these components are constant except for the total energy. In order to show the total energy in Fig. 4 in the logarithmic scale, we shifted it by the value of the minimum. At a normal density, the total energy is 1732.0, while the Weizsäcker model yields 1737.4 and experiment gives 1652.7. A comparison of these values indicates that the gradient correction to the exchange-correlation energy affects the energy to a significantly lower extent than does the pressure. This is related to the fact that, unlike the energy, the pressure is determined by the density at the boundary, which is substantially lower than the average density. The gradient correction increases with decreasing density. Moreover, this behavior can serve as indirect evidence of the fact that the solution to $P(c) = 0$ obtained here is not obvious a priori.

Expected power dependences for free electrons are likely to be only E, E_k, E_u, E_x, and E_c, with allowance for $Z_f(\rho)$. For bound electrons, they decrease with increasing density because of decreasing $Z_b(\rho)$. For the total electron density upon compression <100, the energies E_k, E_u, E_x, and E_c (apart from E) change only weakly, since they are determined by strongly bound electrons. An increase in the total energy depends on free electrons; therefore, this energy exhibits approximately a power dependence, except for the region of nearly normal densities (where exponential decrease is likely to occur). For the total electron density, the energies E, E_k, E_u, and E_x exhibit power asymptotic behavior upon compression at to $\rho/\rho_0 \approx 10^3$ (the energy E_c becomes logarithmic). For the total electron density and the bound-electron density, the gradient energies decrease monotonically upon compression due to decreasing density gradients. For free electrons, the gradient energy is nonmonotonic: E_g first increases (at $\rho/\rho_0 < 10^4$) because of an increase in the number of free electrons Z_f and then (when almost all the shells are crushed) decreases because of increasing homogeneity.
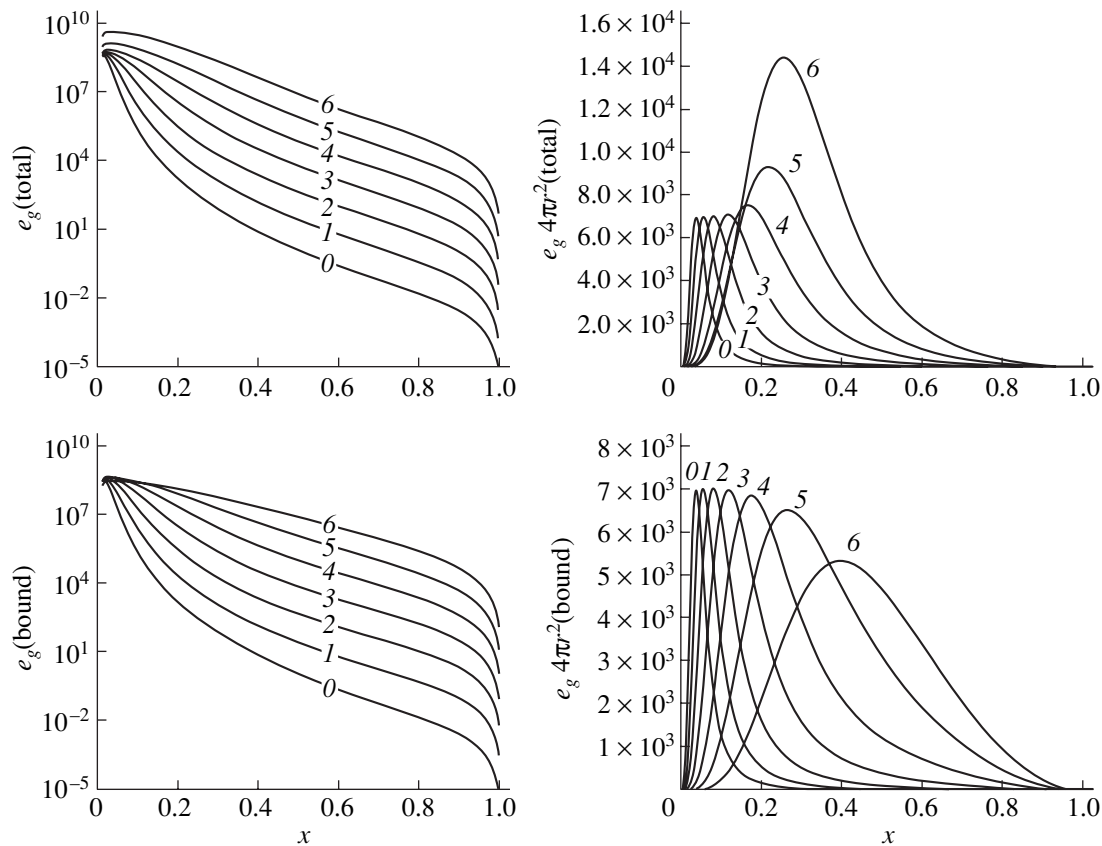
Figure 6 shows the radial profiles of the gradient energy densities at various compressions for the total electron density and the bound-electron density $e_g = e_{kg} + e_{xg} + e_{cg}$ and the corresponding dependences of $e_g \times 4\pi r^2$. At the center, the densities are rather close to each other ($\sim 10^9$) at all degrees of compression; at the boundary, the densities are obviously equal to zero; and at $r \approx 0.5$, e_g drops by about an order of magnitude for each order of magnitude of ρ/ρ_0 upon compression. The characteristic features in the behavior of $e_g \times 4\pi r^2$ are virtually the same values at all degrees of compression and a monotonic increase in the radius corresponding to the maximum.

The calculation of the radial profiles of the quantities $q_x = e_{xg}/e_{kg}$ and $q_c = e_{cg}/e_{kg}$, where e_{xg} and e_{cg} are the gradient energy densities determining the relative contribution to the gradient energies of the exchange and correlation components, shows that the exchange energy contribution to the gradient energy is greater
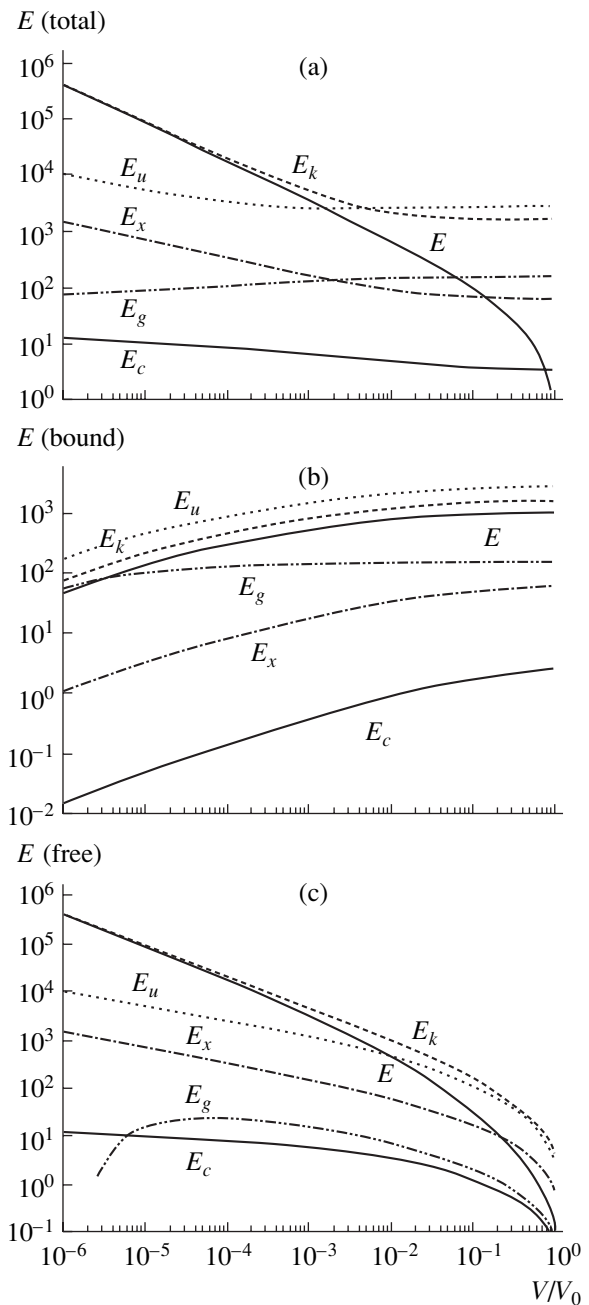
Fig. 5. Plots of the energies vs. specific-volume for (a) the total (free and bound) electron density, (b) bound electrons, and (c) free electrons: E is the total energy, E_k is the kinetic energy, E_x is the exchange energy, E_c is the correlation energy, E_g is the gradient energy, and E_u is the potential energy.

than the kinetic energy contribution near the cell boundary at a normal density upon several fold compression. The correlation energy contribution to the gradient energy is always smaller. Upon strong compression, the relative contribution of the gradient kinetic energy is always (at any degrees of compression) and everywhere (at any radius) greater. The total

Fig. 6. Radial profiles of the gradient energy densities. Figures at the curves indicate the degree of compression $\rho/\rho_0 = 10^k$.

(radius-averaged) gradient kinetic energy is always greater than the gradient exchange-correlation energy for both free and bound electrons.

An increase in the degree of homogeneity with increasing compression is illustrated by Fig. 7, which shows the radial ($x = (r/R)^{1/2}$) profiles of the total electron density, the bound-electron density, and the free-electron density. Note that, in this density range, the actual radii vary by a factor of 100. At a normal density, the total electron density changes by more than six orders of magnitude; however, as the average density ρ/ρ_0 increases by an order of magnitude, the boundary density (at $r = R$) also increases by about an order of magnitude, while the density at the center varies only weakly. The bound-electron density exhibits a similar dependence. Only at the center the density begins to decrease at large compressions ($\rho/\rho_0 = 10^6$) due to a decrease in the total number of bound electrons. The bound-electron density is always inhomogeneous, whereas, upon compression, the free-electron density increases by about an order of magnitude at the boundary and to a slightly extent at the center, thus gradually becoming homogeneous.

Figure 7 also illustrates the radial profiles of $B = 4\pi r^2 n$ for the total electron density, the bound-electron density, and the free-electron density. The plots are normalized to maxima to be simultaneously presented on a linear scale. The shapes of the curves for free electrons are almost the same. The maximum values of N are always (at any degrees of compression) located at the boundary. For bound electrons, the situation is radically different. At a normal density, N exhibits a maximum near the center (at $r/R \approx 0.04$). As the compression increases, the maximum shifts gradually toward the boundary, and, at a large compression ($\rho/\rho_0 = 10^6$), the maximum is at the boundary. Naturally, the $N(r)$ dependence for the total electron density first corresponds to bound electrons, but then its shape becomes analogous to that of free electrons.

At the top of the Fermi distribution, electrons become relativistic under the condition $p_F = mc$, or $(3\pi^2)^{1/3} n^{1/3} = 137$ and $n = 0.87 \times 10^5$. At $\rho/\rho_0 \leq 10^4$, electrons become relativistic only near the nucleus. At large compressions ($\rho/\rho_0 \geq 10^5$), electrons with a momentum $p \approx p_F$ become relativistic over the whole range. At $\rho/\rho_0 \geq 10^6$, electrons become ultrarelativistic also over the whole range. Bound electrons never become ultrarelativistic, since, at weak compression, they are weakly relativistic only near the nucleus; at large com-
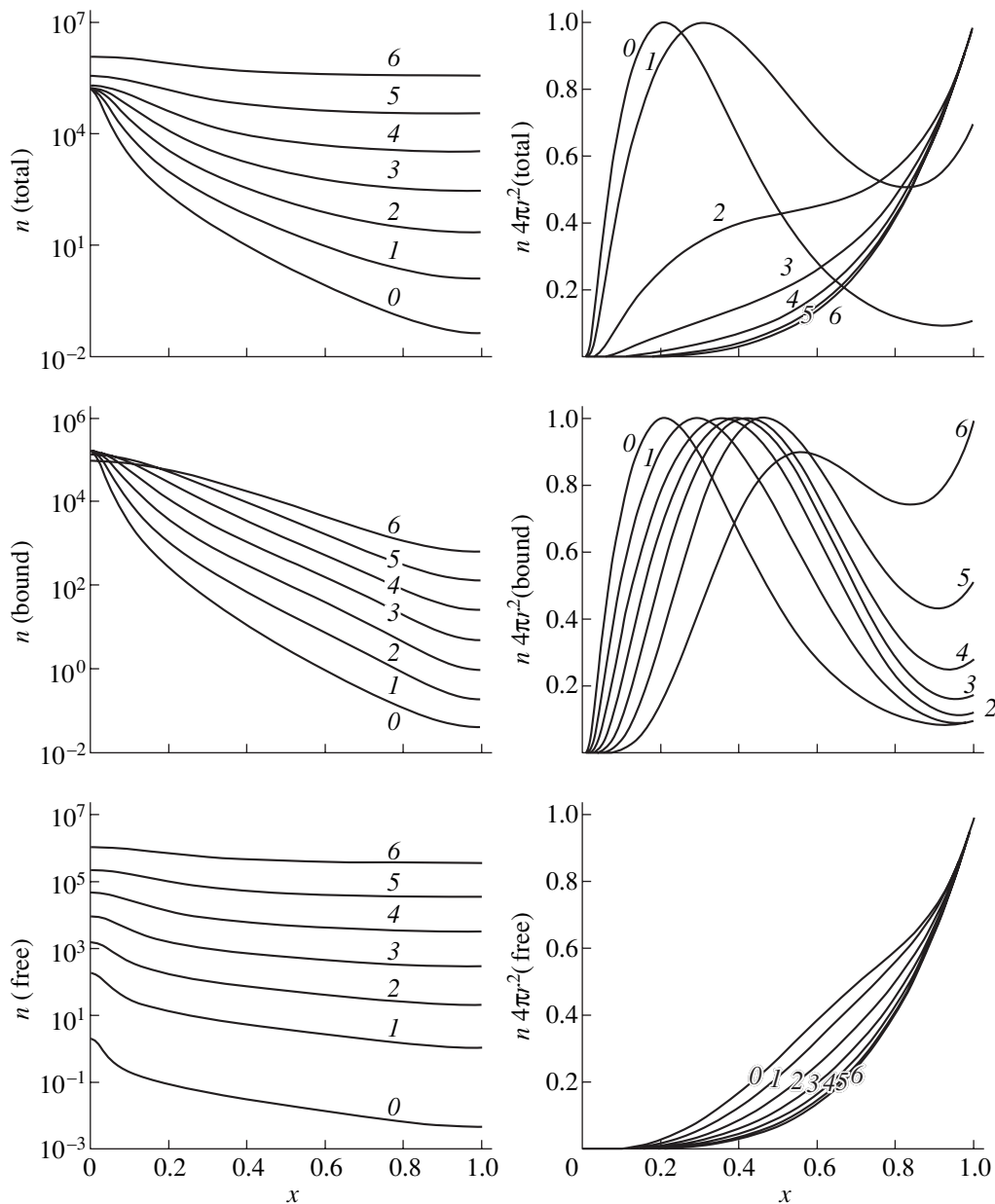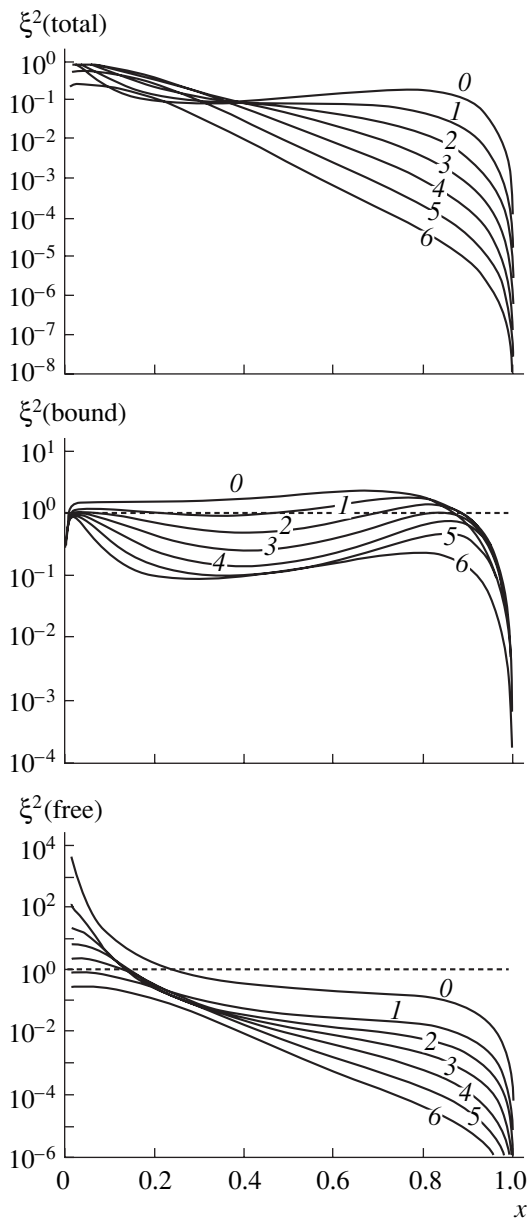
Fig. 7. Radial profiles of the total electron density and $N = 4\pi r^2 n$ and the analogous dependences for the bound-electron density and the free-electron density. Figures at the curves indicate the degree of compression $\rho/\rho_0 = 10^k$ (same as in Fig. 6).

pressions, the number of the electrons is small and they are located at the bottom of the Fermi distribution.

The shape of the total potential changes weakly with increasing compression. Apparently, it is this specific feature that allows one to approximate the potential as $\varphi = (1 + ax)^{-2}$ [3]. The ion (nucleus with bound electrons) potential can be calculated as follows. Poisson's equation was solved for the obtained free-electron density and the boundary condition $\varphi = z/R$; then, the free-electron potential was subtracted from the total potential. The shape of the ion potential is determined by the screening effect of free electrons.

Since all the quasi-classical models under consideration are based on the smallness of the quasi-classical parameter ξ^2, it is interesting to calculate this parameter and to determine the boundaries of the validity of expansion in terms of $\hbar^2$. Figure 8 shows the radial profiles of the quasi-classical parameter ξ^2 for the total electron density, the bound-electron density, and the free-electron density. Near the center, $\xi^2 \sim 1$ for the total electron density and $\xi^2 > 1$ for free electrons. Depending on the degree of compression, a region where $\xi^2 < 1$ always exists (since the boundary condition $(dn/dr)_{r=R} = 0$, then $\xi^2_{r=R} = 0$). As the compression

Fig. 8. Radial profiles of the quasi-classical parameter ξ^2 for the total electron density, the bound-electron density, and the free-electron density. Figures at the curves indicate the degree of compression $\rho/\rho_0 = 10^k$ (same as in Fig. 6).

increases, Ξ^2 decreases for the total density and increases for bound electrons.

REFERENCES

1. P. Gambás, *The Statistical Theory of Atoms and Its Applications* (Die Statistische Theorie des Atoms und Ihre Anwendungen) (Springer-Verlag, Vienna, 1949; Inostrannaya Literatura, Moscow, 1951).

2. C. F. von Weizsacker, Z. Phys. **96**, 431 (1935).

3. A. S. Kompaneets and E. S. Pavlovskiǐ, Zh. Éksp. Teor. Fiz. **31** (3), 115 (1956).

4. D. A. Kirzhnits, Zh. Éksp. Teor. Fiz. **32** (1), 115 (1957) [Sov. Phys. JETP **5**, 64 (1957)].

5. W. Kohn and J. Sham, Phys. Rev. **140**, A1133 (1965).

6. N. N. Kalitkin, Zh. Éksp. Teor. Fiz. **38**, 1534 (1960) [Sov. Phys. JETP **11**, 1106 (1960)].

7. J. W. Zink, Phys. Rev. **176**, 279 (1968).

8. B. F. Rozsnyai, Phys. Rev. A **5**, 1137 (1972).

9. D. A. Kirzhnits, Yu. E. Lozovik, and G. V. Shpatakovskaya, Usp. Fiz. Nauk **117**, 3 (1975) [Sov. Phys. Usp. **18**, 649 (1975)].

10. A. F. Nikiforov, V. G. Novikov, and V. B. Uvarov, *Quantum Statistical Models of High-Temperature Plasma* (Fizmatlit, Moscow, 2000) [in Russian].

11. N. N. Kalitkin, Mat. Model. **1**, 64 (1989).

12. A. V. Andriyash and V. A. Simonenko, Fiz. Plazmy **14**, 1201 (1988) [Sov. J. Plasma Phys. **14**, 703 (1988)].

13. G. V. Sin'ko, Teplofiz. Vys. Temp. **21**, 1041 (1983).

14. N. N. Kalitkin and L. V. Kuz'mina, Fiz. Plazmy **2**, 858 (1976) [Sov. J. Plasma Phys. **2**, 478 (1976)].

15. F. Perrot and M. W. C. Dharma-Wardana, Phys. Rev. E **52**, 5352 (1995).

16. V. V. Prut, Preprint No. 6465/9, IAE (Kurchatov Institute of Atomic Energy, Moscow, 2003).

17. D. Pines and P. Noziéres, *The Theory of Quantum Liquids* (Benjamin, New York, 1966; Mir, Moscow, 1967).

18. S. H. Vosko, L. Wilk, and M. Nusair, Can. J. Phys. **58**, 1200 (1980).

19. K. S. Singwi and M. P. Tosi, Solid State Phys. **36**, 177 (1981).

20. S. Ichimaru, Rev. Mod. Phys. **54**, 1017 (1982).

21. M. Gell-Mann and K. A. Brueckner, Phys. Rev. **106**, 364 (1957).

22. W. J. Carr and A. A. Maradudin, Phys. Rev. **133**, A371 (1964).

23. W. J. Carr, R. A. Coldwell-Horsfall, and A. E. Fein, Phys. Rev. **124**, 747 (1961).

24. D. M. Ceperly and B. J. Alder, Phys. Rev. Lett. **45**, 566 (1980).

25. J. G. Zabolitzky, Phys. Rev. B **22**, 2353 (1980).

26. P. Vashishta and K. S. Singwi, Phys. Rev. B **6**, 875 (1972).

27. L. J. Lantto, Phys. Rev. B **22**, 1380 (1980).

28. J. P. Perdew and A. Zunger, Phys. Rev. B **23**, 5048 (1981).

increases, the parameter ξ^2 decreases because of decreasing density gradients. To estimate this condition integrally with respect to r, the parameter ξ^2 can be represented as $\Xi^2 = E_g/E_k$, depending on the compression degree. The parameter Ξ^2 for free electrons is always small, which is a consequence of the fact that free electrons are mainly located at the boundary (where $\xi^2 = 0$). For bound electrons and the total density, $\Xi^2 = 0.1$ at a compression of $\rho/\rho_0 \leq 10^2$. As the compression

29. T. Endo, M. Horiuchi, Y. Takada, and H. Yasuhara, Phys. Rev. B **59**, 7367 (1999).

30. L. D. Landau and E. M. Lifshitz, *Course of Theoretical Physics*, Vol. 3: *Quantum Mechanics: Non-Relativistic Theory* (Nauka, Moscow, 1989, 4th ed.; Pergamon, New York, 1977, 3rd ed.).

31. J. P. Perdew, J. A. Chevary, S. H. Vosko, *et al.*, Phys. Rev. B **46**, 6671 (1992).

32. J. F. Dobson, J. Wang, and T. Gould, Phys. Rev. B **66**, 081108 (2002).

33. E. Engel and S. H. Vosko, Phys. Rev. B **50**, 10498 (1994).

34. J. P. Perdew, K. Burke, and M. Ernzerhof, Phys. Rev. Lett. **77**, 3865 (1996).

35. P. Fromy, C. Deutch, and G. Maynard, Phys. Plasmas **3**, 714 (1996).

36. E. N. Avrorin, B. K. Vodolaga, V. A. Simonenko, and V. E. Fortov, Usp. Fiz. Nauk **163**, 1 (1993) [Phys. Usp. **36**, 337 (1993)].

37. V. V. Prut, Preprint No. 6464/9, IAE (Kurchatov Institute of Atomic Energy, Moscow, 2003).

Translated by K. Shakhlevich

Electron Transitions as a Result of Interaction between a Heavy Ion and an Ultrashort Electromagnetic Pulse

V. I. Matveev and I. N. Pashev

Lomonosov Pomor State University, Arkhangel'sk, 163006 Russia
e-mail: matveev.victor@pomorsu.ru
Received February 26, 2004; in final form, May 25, 2004

Abstract—The electron transitions arising when a heavy relativistic ion interacts with a spatially nonuniform ultrashort electromagnetic pulse are studied by solving the Dirac equation, and expressions for the excitation and ionization probabilities are derived. One-electron inelastic processes that accompany the interaction between the ultrashort pulses and hydrogen-like atoms are considered by way of example. The approach developed in this article makes it possible to accurately include the spatial nonuniformity of the ultrashort pulse field. © 2004 MAIK "Nauka/Interperiodica".

INTRODUCTION

In many cases of practical importance, perturbations are relatively small and the perturbation theory cannot be applied (see, e.g., [1–9]). If, however, the time of action of perturbation is much shorter than the characteristic atomic times, the related problem can be solved analytically without restricting the amount of perturbation. An example is the interaction of atoms with ultrashort electromagnetic pulses, which is today becoming the object of experimental and theoretical research. In this article, by ultrashort pulses, we mean those the duration of which is much shorter than the characteristic time periods for a target atom, which may be either in the ground state or in the excited (including in the highly excited, i.e., Rydberg) state. The generation of such pulses is the subject of heated discussion in the literature. Their nature may be different [10–13]. Specifically, they may be fields of relativistic or ultrarelativistic heavy ions [14–17]. In the latter case, the perturbation theory is inapplicable to the fields of multiply charged ions, however high their energy is [18, 19]. It should be noted that, in essence, collision experiments still remain the only real way of simulating ultrashort pulses of duration $\tau \leq 10^{-17}$ s (which is comparable to, or shorter than, the characteristic atomic time $\tau_a \sim 10^{-17}$ s) in spite of recent advances in high-power laser technology and ultrashort pulse generation. For example, in the experiments conducted in [15] (see also [16]), the double and single ionization of a helium atom colliding with a U^{92+} atom of energy 1 GeV/nucleon was studied and an ultra-high-intensity pulse ($I > 10^{19}$ W/cm^2) of duration ~10^{-18} s was simulated.

Additionally, collision experiments give the chance to directly observe the interaction of atoms with an ultrashort electromagnetic pulse. In recent observations of the multiphonon generation of pairs by an ultrarela-tivistic electron with a relativistic factor $\gamma \sim 10^5$ that moved through an ultra-high-intensity laser field [20], the frequency of the laser field and its strength increased γ times in the electron rest system. Theoretical works [21, 22] consider the multiphonon generation of pairs when bare ultrarelativistic nuclei collide with an intense laser beam. Their results indicate the feasibility of related experiments with modern accelerators. Thus, when a target atom or a partially stripped atom with a number of electrons on its shells (structural ion) moving with a relativistic velocity collides (interacts) with an ultrashort electromagnetic pulse of duration τ, collision time τ_c in the atom (ion) rest system decreases by a factor of γ; that is, $\tau_c \sim \tau/\gamma$. Let us estimate the time of observation of inelastic processes (which this article is devoted to) in such experiments for a relativistic factor $\gamma \sim 10^4$ currently attainable in heavy particle accelerators, which effectively decreases the pulse duration by four orders [1], and characteristic (femtosecond) times $\tau \sim 10^{-15}$ s. Estimates will be made for relativistic problems, where $\Delta E \sim mc^2$ (m is the electron mass and c is the velocity of light) and the corresponding characteristic frequency $\omega_a = mc^2/\hbar$ ($\hbar$ is the Planck constant). Accordingly, the characteristic time of a target atom at rest is $\tau_a = 2\pi/\omega_a \simeq 8.1 \times 10^{-21} \approx 10^{-20}$ s and $\tau_c \sim \tau/\gamma \sim 10^{-19}$ s. Thus, for the relativistic effects considered in this article to be observed directly, it is necessary to cut the pulse duration by one order (or to correspondingly increase γ), which keeps pace with present-day experimental trends.

This and similar problems can be naturally solved in terms of the sudden perturbation approximation [2, 9], which is closely related to the eikonal approximation [4]. As far as we know, the sudden perturbation approximation was earlier applied to only nonrelativistic problems. These are the excitation or ionization of atoms as

a result of nuclear reactions [9], e.g., β decay, where the escape of a fast β electron is perceived by atom electrons as a sudden change in the nuclear charge; neutron–nucleus collisions, where abrupt momentum transfer to the nucleus takes place; etc. The sudden perturbation approximation is used in considering electron transitions in many-electron atoms, where the transitions in the inner shells are perceived as sudden events by slow outer-shell electrons (see, e.g., [3, 6]). The inelastic processes resulting from collisions between fast multiply charged particles and atoms [4–6], as well as between charged particles and highly excited atoms [7], are also viewed as the sudden perturbation effects. The generalization of the sudden perturbation approximation has led to the development of a relativistic theory [23, 24] that describes electron transitions and atom radiation when the atom interacts with a spatially non-uniform ultrashort electromagnetic pulse. Based on this theory, expressions for the excitation and ionization probabilities were derived and the spectra and cross sections of the reradiation of such a pulse by the atom were found.

In this work, the sudden perturbation approximation is applied to solve relativistic problems in terms of the Dirac equation. Based on a solution to the Dirac equation, the electron transitions resulting from the interaction of a heavy relativistic ion with a spatially nonuniform (over the target atom size) ultrashort electromagnetic pulse are considered and the excitation and ionization probabilities are found.

GENERAL

In terms of work [2], a perturbation related to the field of an ultrashort pulse is similar to scattering-type shaking. In this case, the sudden perturbation approximation is best illustrated with a formal solution to the Schrödinger equation (hereafter, atomic units are used)

$$i\dot{\Psi} = (H_0 + U(t))\Psi, \qquad (1)$$

where sudden perturbation $U(t)$ acts for a time much shorter than the characteristic time periods of an unperturbed system that is described by Hamiltonian H_0.

Then, when solving Eq. (1), one can ignore (for the time of action of perturbation $U(t)$) the evolution of the wave function due to intrinsic Hamiltonian H_0 and solve the equation $i\dot{\Psi} = U(t)\Psi$. Eventually, we have

$$\Psi(t) = \exp\left\{-i\int_{t_0}^{t} U(t)dt\right\}\Psi(t_0). \qquad (2)$$

The amplitude of transition of a nonrelativistic atom from state $|i\rangle$ to state $|f\rangle$ as a result of sudden perturba-

tion $U(t)$ has the form [2]

$$a_{if} = \left\langle f\left|\exp\left\{-i\int_{-\infty}^{+\infty} U(t)dt\right\}\right|i\right\rangle. \qquad (3)$$

It is easy to see that the result will be the same if Eq. (1) includes δ-like potential $\tilde{U}(t)$ that is related to potential $U(t)$ as

$$\tilde{U}(t) = U_0\delta(t), \quad U_0 = \int_{-\infty}^{+\infty} U(t)dt. \qquad (4)$$

It is this circumstance that allows us to solve the Dirac equation in the sudden perturbation approximation.

The behavior of an electron of a hydrogen-like atom (the only condition imposed on atomic charge Z_a is the applicability of the Dirac equation [25]) in an external field $(\mathbf{A}, \varphi)$ is described by the Dirac equation (the electron charge equals 1 a.u.)

$$i\dot{\Psi} = \left\{c\boldsymbol{\alpha}\left(\hat{\mathbf{p}} + \frac{1}{c}\mathbf{A}\right) - \frac{Z_a}{r} - \varphi - \beta c^2\right\}\Psi. \qquad (5)$$

Here, the set of terms $c\boldsymbol{\alpha}\hat{\mathbf{p}} - \beta c^2 - Z_a/r$ represents the Hamiltonian H_0 of an isolated atom, the interaction of an atom electron with the external field is given by $U(t) = U(\mathbf{r}, t) = \boldsymbol{\alpha}\mathbf{A} - \varphi$, $\hat{\mathbf{p}}$ is the momentum operator, $\boldsymbol{\alpha}$ and β are the Dirac matrices, c is the velocity of light, and $\mathbf{r}$ are the atom electron coordinates.

We take a potential gauge such that scalar potential φ equals zero and assume that vector potential $\mathbf{A}$ depends on coordinates $\mathbf{r}$ and time t as follows: $\mathbf{A} = \mathbf{A}(\mathbf{r}, t) = \mathbf{A}(\eta)$, where $\eta = \omega_0 t - \mathbf{k}_0 \cdot \mathbf{r}$ is the phase of the electromagnetic wave. Wavevector $\mathbf{k}_0$ obeys the relationship $|\mathbf{k}_0| = \omega_0/c$, where ω_0 is the circular frequency. Let us perform the gauge transformation [19]

$$\mathbf{A}' = \mathbf{A} + \nabla f, \quad \varphi' = \varphi - \frac{1}{c}\frac{\partial f}{\partial t},$$

where $f = \mathbf{A} \cdot \mathbf{r}$.

Eventually, we have $\mathbf{A}' = -\mathbf{k}_0(\mathbf{r} \cdot d\mathbf{A}/d\eta)$ and $\varphi' = -(\mathbf{E} \cdot \mathbf{r})$, where $\mathbf{E} = \mathbf{E}(\mathbf{r}, t) = -|\mathbf{k}_0|d\mathbf{A}/d\eta$; therefore, the vector and scalar potentials in the new gauge are related as $\mathbf{A}' = (\mathbf{k}_0/|\mathbf{k}_0|)\varphi'$. Let the Z axis be aligned with $\mathbf{k}_0$. In this case, the interaction of the atom electron with the external field in Eq. (5) is given by

$$U(t) = \boldsymbol{\alpha}\mathbf{A}' - \varphi' = -\left(1 - \frac{\boldsymbol{\alpha}\mathbf{k}_0}{|\mathbf{k}_0|}\right)\varphi' = -(1 - \alpha_z)\varphi'. \qquad (6)$$

Below, we will use the new gauge and omit the primes. To solve Dirac equation (5) in terms of the sudden perturbation approximation, we write it in the form

$i\dot{\Psi} = (H_0 + U(t))\Psi$ and take advantage of substitution (4), introducing the relationships

$$\tilde{\varphi} = -\varphi_0\delta(ct - z), \quad \varphi_0 = c\int_{-\infty}^{+\infty}\varphi(ct - z)dt. \quad (7)$$

Accordingly, $U(t)$ from formula (6) is replaced by $\tilde{U}(t) = -(1 - \alpha_z)\tilde{\varphi}$ or by

$$\tilde{U}(t) = U_0\delta(ct - z), \quad (8)$$

where

$$U_0 = c\int_{-\infty}^{+\infty}U(t)dt = -(1 - \alpha_z)\varphi_0. \quad (9)$$

Eventually, Eq. (5) takes the form

$$i\dot{\Psi} = \left\{c\boldsymbol{\alpha}\hat{\mathbf{p}} - \frac{Z_a}{r} - \beta c^2 - (1 - \alpha_z)\tilde{\varphi}\right\}\Psi. \quad (10)$$

To exactly solve the Dirac equation with such a potential, we expand $\Psi = \Psi(\mathbf{r}, t)$ in the eigenfunctions $\phi_k(r)$ (with energies E_k) of unperturbed atomic Hamiltonian $H_0 = c\boldsymbol{\alpha}\hat{\mathbf{p}} - \beta c^2 - Z_a/r$:

$$\Psi(\mathbf{r}, t) = \sum_k a_k(t)\phi_k(\mathbf{r})e^{-iE_kt}.$$

Substituting this expansion into the left of the equation $i\dot{\Psi} = (H_0 + \tilde{U}(t))\Psi$, integrating, and multiplying the left of the equation by some state ϕ_f, we get, in view of the orthogonality of states ϕ_k,

$$\frac{da_f(t)}{dt} = -ie^{iE_ft}\langle\phi_f|\tilde{U}(t)|\Psi(\mathbf{r}, t)\rangle. \quad (11)$$

Let the atom be in state ϕ_j before collision; then,

$$\Psi(\mathbf{r}, t = -\infty) = e^{-E_jt}\phi_j(\mathbf{r}), \quad (12)$$

$$a_f(t = -\infty) = \delta_{fj}, \quad (13)$$

where δ_{fj} is the Kronecker symbol.

To solve Eq. (11), it will suffice to know the values of $\Psi(\mathbf{r}, t)$ only for $z = ct$, since $\tilde{U}(t) = U_0\delta(ct - z)$. These values are found from Eq. (10) as follows. Passing to the light cone variables

$$z^- = (ct - z),$$
$$z^+ = (ct + z) \quad (14)$$

and leaving only the derivatives with respect to z^- and singular potential $-(1 - \alpha_z)\tilde{\varphi}$ in the small neighborhood

of $z^- = 0$, we arrive at the equation

$$ic(1 - \alpha_z)\frac{\partial\Psi}{\partial z^-} = -(1 - \alpha_z)\tilde{\varphi}\Psi. \quad (15)$$

Since $\tilde{\varphi} = -\varphi_0\delta(z^-)$ and

$$\frac{d}{dx}\theta(x) = \delta(x), \quad \frac{d}{dx}\exp(\theta(x)) = \delta(x)\exp(\theta(x)), (16)$$

where $\theta(x) = 0$ for $x < 0$ and $\theta(x) = 1$ for $x > 0$, we find a solution to Eq. (15):

$$(1 - \alpha_z)\Psi(z^- + 0)$$
$$= (1 - \alpha_z)\exp\left[-i\frac{\varphi_0}{c}\theta(z^{-1})\right]\Psi(z^- - 0). \quad (17)$$

Now, returning to time t, we find a solution that is valid for $t < z/c$ and near $t = z/c$ (i.e., $t = z/c + \varepsilon$, where ε is small and >0):

$$(1 - \alpha_z)\Psi(\mathbf{r}, t) = (1 - \alpha_z)\exp\left[-i\theta(ct - z)\frac{\varphi_0}{c}\right] \quad (18)$$
$$\times \exp[-iE_jt]\phi_j(\mathbf{r}).$$

Substituting (18) into the right of (11) and integrating over t subject to initial conditions (13), we get

$$a_{fj} = a_f(t = +\infty) = \delta_{fj} - i\int_{-\infty}^{+\infty}dt e^{i(E_f - E_j)t} \quad (19)$$
$$\times\left\langle\phi_f\left|\delta(z - ct)(1 - \alpha_z)\exp\left[-i\theta(ct - z)\frac{\varphi_0}{c}\right]\right|\phi_j\right\rangle.$$

Using relationships (16), we find

$$a_{fj} = \delta_{fj}$$
$$+ \left\langle\phi_f\left|(1 - \alpha_z)e^{i(E_f - E_j)z/c}\left[\exp\left(-i\frac{\varphi_0}{c}\right) - 1\right]\right|\phi_j\right\rangle. \quad (20)$$

This is the desired exact (cf. [1]) solution to the Dirac equation with potential $\tilde{U}(t) = U_0\delta(ct - z)$. It includes potential (6) in the sudden perturbation approximation. The expression derived can be recast in a more convenient form using the easy-to-check relationship

$$\left\langle\phi_f\left|(1 - \alpha_z)e^{i(E_f - E_j)z/c}\right|\phi_j\right\rangle = \delta_{fj}. \quad (21)$$

Eventually,

$$a_{fj} = \left\langle\phi_f\left|(1 - \alpha_z)e^{i(E_f - E_j)z/c}\exp\left(-i\frac{\varphi_0}{c}\right)\right|\phi_j\right\rangle. \quad (22)$$

For the interaction of an atom electron with a Gaussian electromagnetic pulse (of effective duration $\sim\lambda^{-1}$),

we have

$$\mathbf{E}(\mathbf{r}, t) = \mathbf{E}_0 \exp\left(-\lambda^2\left(t - \frac{\mathbf{k}_0 \cdot \mathbf{r}}{\omega_0}\right)^2\right)\cos(\omega_0 t - \mathbf{k}_0 \cdot \mathbf{r}),$$

$$\varphi = \mathbf{r} \cdot \mathbf{E}(r, t), \quad \varphi_0 = -c\mathbf{q} \cdot \mathbf{r}, \tag{23}$$

where

$$\mathbf{q} = \int_{-\infty}^{+\infty} dt \mathbf{E}(\mathbf{r}, t) = \mathbf{E}_0 \frac{\sqrt{\pi}}{\lambda}\exp\left(-\frac{\omega_0^2}{4\lambda^2}\right). \tag{24}$$

Taking into account that $\alpha_z = \boldsymbol{\alpha}\mathbf{k}_0/k_0$ and introducing vector $\mathbf{Q} = (Q_x, Q_y, Q_z) = (q, 0, \Omega_{fj}/c)$, where $\Omega_{fj} = E_f - E_j$, we can recast a_{fj} from (22) in the form

$$a_{fj} = \left\langle \phi_f\left|\left(1 - \frac{\boldsymbol{\alpha}\mathbf{k}_0}{k_0}\right)e^{i\mathbf{QR}}\right|\phi_j\right\rangle. \tag{25}$$

Now we align the Z axis with $\mathbf{Q}$ to get

$$a_{fj} = \langle\phi_f|(1 - \alpha_z\cos\theta)e^{iQz}|\phi_j\rangle$$
$$- \langle\phi_f|(1 - \alpha_x\sin\theta)e^{iQz}|\phi_j\rangle, \tag{26}$$
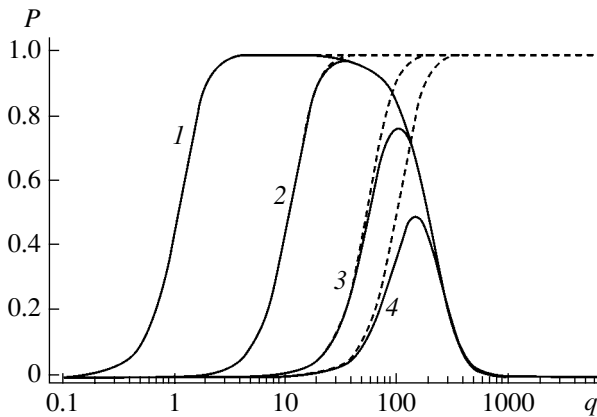
where

$$Q = \sqrt{q^2 + \Omega_{fj}^2/c^2}, \quad \cos\theta = \Omega_{fj}/\sqrt{c^2 q^2 + \Omega_{fj}^2},$$

$$\sin\theta = q/\sqrt{q^2 + \Omega_{fj}^2/c^2}.$$

Thus, if the atom was in state ϕ_j with energy E_j prior to interaction with the ultrashort pulse (i.e., at $t = -\infty$), the probability that the atom will be in state ϕ_j with energy E_j after the interaction (i.e., at $t = +\infty$) is given by

$$|a_{fj}|^2 = \frac{q^2}{Q^2}\left(\frac{q^2}{Q^2}|F^{fj}|^2 + |G_x^{fj}|^2\right). \tag{27}$$

Ionization (K vacancy generation) probabilities P for hydrogen-like atoms with different nuclear charge Z_a vs. transferred momentum $q = |\mathbf{q}|$ (see (24)) (atomic units). Continuous curves, relativistic calculation by formula (27); dashed curves, nonrelativistic calculation by formula (27) at $c \longrightarrow \infty$ [18, 19]. $Z_a =$ (*1*) 1, (*2*) 10, (*3*) 50, and (*4*) 92.

Here, we, following [26], used the well-known expressions for inelastic atomic form factors:

$$F^{fj} = \langle\phi_f|e^{iQz}|\phi_j\rangle = \frac{Q_c}{\Omega_{fj}}\langle\phi_f|\alpha_z e^{iQz}|\phi_j\rangle,$$

$$G_x^{fj} = \langle\phi_f|\alpha_x e^{iQz}|\phi_j\rangle.$$

The above formulas allow one to calculate the probabilities of excitation or ionization of an atom by an ultrashort electromagnetic pulse. The figure shows the ionization probabilities (the probabilities of K vacancy generation) for hydrogen-like atoms with different nuclear charge Z_a. In the calculations, we used the quasi-relativistic Darwin functions [25, 28, 29] as the wave functions of the initial and final states (see [26, 27]). Such an approach makes it possible to calculate the form factors analytically. Strictly speaking, the quasi-relativistic functions are valid if $Z_a \ll c$ and $q \ll c$. Otherwise, the calculation satisfactorily illustrates the behavior of the total ionization cross sections on the qualitative basis [29].

ACKNOWLEDGMENTS

REFERENCES

1. A. J. Baltz, Phys. Rev. Lett. **78**, 1231 (1997).

2. A. M. Dykhne and G. L. Yudin, Usp. Fiz. Nauk **125**, 377 (1978) [Sov. Phys. Usp. **21**, 549 (1978)].

3. V. I. Matveev and É. S. Parilis, Usp. Fiz. Nauk **138**, 583 (1982) [Sov. Phys. Usp. **25**, 881 (1982)].

4. J. Eichler, Phys. Rev. A **15**, 1856 (1977).

5. G. L. Yudin, Zh. Éksp. Teor. Fiz. **80**, 1026 (1981) [Sov. Phys. JETP **53**, 523 (1981)].

6. V. I. Matveev, Fiz. Élem. Chastits At. Yadra **26**, 780 (1995).

7. I. C. Percival, in *Atoms in Astrophysics*, Ed. by P. G. Burke, W. B. Eissner, D. G. Hammer, and I. C. Percival (Plenum, New York, 1983; Mir, Moscow, 1988), p. 87.

8. V. I. Matveev, Zh. Éksp. Teor. Fiz. **121**, 260 (2002) [JETP **94**, 217 (2002)].

9. A. B. Migdal, *Qualitative Methods in Quantum Theory* (Nauka, Moscow, 1975; Benjamin, Reading, 1977).

10. S. E. Harris and A. V. Sokolov, Phys. Rev. Lett. **81**, 2894 (1998).

11. I. P. Christov, M. M. Murnane, and H. C. Kapteyn, Opt. Commun. **148**, 75 (1998).

12. A. V. Sokolov, D. D. Yavuz, and S. E. Harris, Opt. Lett. **24**, 557 (1999).

13. A. E. Kaplan and P. L. Shkolnikov, Phys. Rev. Lett. **88**, 074 801 (2002).

14. A. J. Baltz, Phys. Rev. A **52**, 4970 (1995).

15. R. Moshammer, W. Schmitt, J. Ullrich, *et al.*, Phys. Rev. Lett. **79**, 3621 (1997).

16. A. V. Selin, A. M. Ermolaev, and C. J. Joachain, Phys. Rev. A **67**, 012709 (2003).

17. A. B. Voitkiv, B. Najjari, and J. Ullrich, J. Phys. B **36**, 2325 (2003).

18. J. Eichler, Phys. Rev. A **15**, 1856 (1977).

19. J. Eichler, Phys. Rep. **193**, 165 (1990).

20. C. Bamber *et al.*, Phys. Rev. D **60**, 092004 (1999).

21. C. Muller, A. B. Voitkiv, and N. Grun, Phys. Rev. A **67**, 063 407 (2003).

22. C. Muller, A. B. Voitkiv, and N. Grun, Nucl. Instrum. Methods Phys. Res. B **205**, 306 (2003).

23. V. I. Matveev, Zh. Tekh. Fiz. **73** (6), 17 (2003) [Tech. Phys. **48**, 677 (2003)].

24. V. I. Matveev, Zh. Éksp. Teor. Fiz. **124**, 1023 (2003) [JETP **97**, 915 (2003)].

25. V. B. Berestetskii, E. M. Lifshitz, and L. P. Pitaevskii, *Course of Theoretical Physics*, Vol. 4: *Quantum Electrodynamics* (Nauka, Moscow, 1989; Pergamon, New York, 1982).

26. R. Anholt, Phys. Rev. A **19**, 1004 (1979).

27. D. M. Davidovic, B. L. Moiseivitsch, and P. H. Norrington, J. Phys. B **11**, 847 (1978).

28. C. G. Darwin, Proc. R. Soc. London, Ser. A **118**, 654 (1928).

29. J. Eichler and W. E. Meyrhoft, *Relativistic Atomic Collisions* (Academic, New York, 1995).

Translated by V. Isaakyan

THEORETICAL
AND MATHEMATICAL PHYSICS

Model Problem of Wave Refraction by a Periodically Nonuniform Boundary of the Solar Plasma

A. A. Aleksandrova and Yu. N. Aleksandrov

Kharkov Military University, Kharkov, 61043 Ukraine
Kharkov National University of Radioelectronics, Kharkov, 61726 Ukraine
Received April 22, 2004

Abstract—The problem of the diffraction of Alfvén and magnetosonic waves by a boundary between two media in the form of a plane interface modulated by a running sinusoidal wave is considered in the linear approximation on the basis of the mathematical apparatus of integral equations of solar magnetohydrodynamics. The results obtained are analyzed and discussed. © *2004 MAIK "Nauka/Interperiodica".*

Because of its high dynamic activity, the sun is always subject to various waves. The activity of the sun is attributed to the continual motions of its individual structural elements that occur on very different spatial and time scales. Thus, in the plasma forming the solar atmosphere, there are usually four modes of wave motion driven by different restoring forces. The magnetic tension force and Coriolis force give rise to Alfvén and inertial waves. The magnetic pressure force, plasma pressure force, and gravity force can act separately from one another, thereby generating Alfvén compression waves, magnetosonic waves, and internal gravitational waves, respectively. However, when these three forces act together, they bring about only two magnetosonic–gravitational modes (MSG waves). In the absence of the gravity force, these two modes are fast or slow magnetosonic waves and, in the absence of a magnetic field, they are sonic–gravitational waves (gravitational sound).

According to Priest [1], Alfvén waves exist in the upper chromosphere of the sun and in the solar corona, accelerated MSG waves are observed to occur in the running wave of the penumbra of a sunspot and a Moretone coronal wave that is excited after a solar flare is nothing more than an accelerated magnetosonic wave. In addition, the small-scale wave motions occurring outside sunspots are standing sonic waves, and MHD waves themselves are always present in the solar wind. The common view is that sonic waves heat the lower chromosphere, while magnetic waves (or magnetic dissipation) can heat the upper chromosphere and the corona. In other words, the wave motions in question and the solar plasma, which generates them, are inseparably interrelated.

The basic aspects of the theory of the above wave perturbations in a homogeneous medium whose density varies on a characteristic spatial scale much longer than the perturbation wavelength have been investigated fairly well [2]. Since, in this case, the partial differential equations for the perturbing quantities reduce to the well-studied algebraic equations, the assumption that the medium is homogeneous makes these equations much easier to analyze mathematically. Perturbations in an inhomogeneous medium have a different structure, and their study is complicated by the fact that they can exhibit both a discrete and a continuous mode spectrum.

For instance, the main factors responsible for the inhomogeneity of the sun are the gravity force and magnetic field. The gravity force increases the pressure in the direction toward the Sun's center, while the magnetic field and the associated Lorentz force often increase the pressure in the direction normal to the magnetic field in regions far from those where the magnetic flux is concentrated. These and some other factors lead to the appearance of interfaces between inhomogeneous media (or inhomogeneities), the most typical of which are magnetic flux tubes and plane-parallel stratified layers. At such interfaces, the physical quantities describing the field perturbations in the solar plasma, as well as their derivatives, suffer sharp discontinuities. Significant jumps in the quantities and in their derivatives at the discontinuity surfaces are determined from integral conservation laws or integral balance equations. In the physics of wave processes, new effects may arise, such as those associated with the enhancement of the wave, with changes in the character of its propagation (i.e., in one region, the perturbation may behave as a propagation wave, while, in another region, it may be nonpropagating), with the onset of the surface modes that are damped away from the interface, etc.

It is only recently that the problem of long-wavelength perturbations in the inhomogeneous solar atmosphere has attracted attention and, being very important, it will undoubtedly receive considerable study in the future. This is why we will consider one of the simplest model problems of the scattering of a packet of

solar plasma waves by a boundary between two plasma media in the form of a plane interface modulated by a running sinusoidal wave. An interface of this kind can originate from spatially periodic magnetic fields or spatially periodic fluxes of charged particles.

As the mathematical apparatus, we chose the method of integral equations, which has been applied successfully in electrodynamics [3] and linear magnetohydrodynamics [4]. As compared to the differential equations, the integral equations underlying the method can be supplemented with boundary and initial conditions in a more natural way and, physically, they are more illustrative; this makes it possible to substantially simplify the construction of an algorithm for solving a boundary-value problem.

We consider the boundary-value problem in a formulation that leads to integral equations for linear field perturbation in solar magnetohydrodynamics.

Let a certain region (inhomogeneity) within which all the parameters are assumed to be homogeneous be characterized by unperturbed magnetic field $\mathbf{B}_2$; Alfvén and magnetosonic speeds V_{A2} and V_{S2}, respectively; and density ρ_2. Let the inhomogeneity have a volume $V(t)$ and its boundary vary over time. We assume that, before being perturbed by an incident field determined by the state vector $\mathbf{\Psi}_0(\mathbf{r}, t) = \{\mathbf{u}_0(\mathbf{r}, t)\mathbf{b}_0(\mathbf{r}, t), \rho_0(\mathbf{r}, t), p_0(\mathbf{r}, t)\}$, the infinite medium surrounding the inhomogeneity is characterized by the parameters $\mathbf{B}_1$, V_{A1}, V_{S1}, and ρ_1. The components of the MHD state vector $\mathbf{\Psi}(\mathbf{r}, t) = \{\mathbf{u}(\mathbf{r}, t)\mathbf{b}(\mathbf{r}, t), \rho(\mathbf{r}, t), p(\mathbf{r}, t)\}$ are the deviations of the perturbed quantities, namely, the velocity $\mathbf{u}(\mathbf{r}, t)$, magnetic field $\mathbf{b}(\mathbf{r}, t)$, density $\rho(\mathbf{r}, t)$, and pressure $p(\mathbf{r}, t)$, from their equilibrium values, characterizing the MHD state of the solar plasma.

The derivation of the integral equations in operator form with nonlocal boundary conditions in solar magnetohydrodynamics was discussed in an earlier paper by [5]. We do not repeat this derivation and immediately write out the equations in the laboratory frame of reference:

$$\mathbf{\Psi}(\mathbf{r}, t) = \mathbf{\Psi}_0(\mathbf{r}, t)$$
$$+ \hat{G}_{\mathbf{r}, t} \int_{-\infty}^{\infty} dt' \int_{V(t')} d\mathbf{r}' \mathbf{\Psi}(\mathbf{r}', t') I(\mathbf{r} - \mathbf{r}', t - t'). \tag{1}$$

Here, the differential operator $\hat{G} = \|G_{ij}\|_{i, j = 1, 2, 3}$ is a matrix relative to a specially chosen basis and the Green's function, which depends on the spatial variables, $\mathbf{r} - \mathbf{r}'$, and on the time variable $t - t'$, is given in

terms of the Fourier–Laplace transform,

$$I(\mathbf{r} - \mathbf{r}', t - t') = \int_{-\infty + i\sigma_0}^{\infty + i\sigma_0} \exp[-iq(t - t')]dq$$
$$\times \iiint_{\infty} \frac{\exp[i\mathbf{p} \cdot (\mathbf{r} - \mathbf{r}')]}{\delta(q, \mathbf{p})\Delta(q, \mathbf{p})\tau(q, \mathbf{p})}d\mathbf{p}. \tag{2}$$

The structure of the integral representation of Green's function (2) implies that each integral is taken over an infinite interval and that, in order to calculate them, it is necessary to specify the rules for circumventing the singular points lying on the integration contours. The singular points are determined by those values of the variables of integration $\mathbf{p}$ and q that satisfy the dispersion relations for the corresponding types of waves occurring in the solar plasma:

$$\delta(q, \mathbf{p}) = q^2 - V_{A1}^2(\mathbf{s}_1\mathbf{p})^2 = 0,$$

$$\Delta(q, \mathbf{p}) = q^4 - q^2(V_{A1}^2 + V_{S1}^2)\mathbf{p}^2 + V_{S1}^2 N^2 \sin^2\theta_g \mathbf{p}^2$$
$$+ V_{A1}^2 V_{S1}^2(\mathbf{s}_1 \cdot \mathbf{p})^2 \mathbf{p}^2 = 0, \tag{3}$$

$$\tau(q, \mathbf{p}) = q^2 \pm 2(\mathbf{p} \cdot \Omega)^2/p = 0,$$

where Ω is the angular velocity and N is the Brent frequency. In particular, the dispersion relation $\delta(q, \mathbf{p}) = 0$ describes Alfvén waves, the dispersion relation $\Delta(q, \mathbf{p}) = 0$ describes MSG waves, and the dispersion relation $\tau(q, \mathbf{p}) = 0$ refers to inertial waves.

It should be noted that, in solving a boundary-value problem formulated in terms of differential equations, the local boundary conditions either can be satisfied by a single type of wave or it is necessary to invoke several types of waves in order to satisfy them. In the problem formulated in terms of integral equations, this complicated question is resolved automatically. This is provided by the extinction theorem, with which the physical meaning of the phenomenon becomes quite clear. According to this theorem, the mechanism for the onset of scattered waves in the internal medium is directly associated with the generation of the so-called secondary waves by the main wave. The main wave, which is characterized by the state vector $\mathbf{\Psi}_0$, acts as if it induces the sources emitting secondary waves. The interference between these waves produces the required oscillation modes. Mathematically, the secondary waves are described by the integral terms on the right-hand sides of Eq. (1). This naturally leads to the following algorithm for solving the boundary-value problem. In the first step, the field in the internal region $\{\mathbf{r}, t\} \in V(t)$ is determined by solving the integral equation and, in the second step, the field in the external region $\{\mathbf{r}, t\} \notin V(t)$ is determined from the already calculated internal field.

Let the *OX* and *OY* axes lie in an unperturbed scattering plane boundary between two media characterized by the parameters B_i, V_{Ai}, V_{Si}, and ρ_i ($i = 1, 2$), and let the *OZ* axis be perpendicular to this boundary and lie within the $i = 2$ medium. Let the perturbation of the boundary have the form

$$\xi(\mathbf{r}, t) = \mathbf{e}_z \xi_0 \sin(-\eta y + \Theta t), \qquad (4)$$

where $\xi(\mathbf{r}, t)$ is the displacement vector of the points of the boundary between two media under the action of an external force.

In order to outline the essence of the method proposed here, we set $\Omega = 0$ and $N = 0$ in Eq. (1); in other words, we assume that there are only Alfvén and magnetosonic waves, into which the MSG waves degenerate. Under this assumption, the integral equations for the velocity $\mathbf{u}(\mathbf{r}, t)$ and magnetic field $\mathbf{b}(\mathbf{r}, t)$ that are completely equivalent to the corresponding differential MHD equations and the conditions at the boundary between two media have the form

$$\mathbf{u}(\mathbf{r}, t) = \mathbf{u}_n(\mathbf{r}, t) + (V_{S1}^2 - V_{S2}^2)\hat{F}\nabla(\nabla \cdot \mathbf{\Pi_u}(\mathbf{r}, t))$$

$$+ \frac{\hat{F}}{B_1}(V_{A1}^2 \mathbf{s}_1 - \gamma V_{A2}^2 \mathbf{s}_2) \times (\nabla \times \frac{\partial}{\partial t}\mathbf{\Pi_b}(\mathbf{r}, t)) \qquad (5)$$

$$- V_{A1}^2 \hat{F}\mathbf{s}_1 \times (\nabla \times (\nabla \times ((\mathbf{s}_1 - \gamma^{-1}\mathbf{s}_2) \times \mathbf{\Pi_u}(\mathbf{r}, t))));$$

$$\gamma = B_1/B_2; \quad \mathbf{s}_i = \mathbf{B}_i/B_i; \quad i = 1, 2,$$

where $\mathbf{B}_i = \{0, B_{iy}, B_{iz}\}$ ($i = 1, 2$) and the operator

$$\hat{F} = \begin{pmatrix} 1 & 0 & 0 \\ 0 & \dfrac{\partial^2}{\partial t^2} - V_{A1}^2\Delta - V_{S1}^2\dfrac{\partial^2}{\partial x_3^2} & V_{S1}^2\dfrac{\partial^2}{\partial x_2 \partial x_3} \\ 0 & V_{S1}^2\dfrac{\partial^2}{\partial x_2 \partial x_3} & \dfrac{\partial^2}{\partial t^2} - V_{S1}^2\dfrac{\partial^2}{\partial x_2^2} \end{pmatrix} \qquad (6)$$

is written in terms of the orthogonal basis $\langle \mathbf{e}_x, \mathbf{e}_2, \mathbf{e}_3 \rangle$ such that $\mathbf{e}_2 = \mathbf{s}_1$ and the unit vectors $\mathbf{e}_2$ and $\mathbf{e}_3$ lie in the (y, z) plane.

The MHD potentials of the velocity and magnetic field, $\mathbf{\Pi_{u, b}}(\mathbf{r}, t)$, have the form

$$\begin{Bmatrix} \mathbf{\Pi_u} \\ \mathbf{\Pi_b} \end{Bmatrix} = \int\limits_{-\infty}^{\infty} dt' \int\limits_{V(t')} \begin{Bmatrix} \mathbf{u}(\mathbf{r}', t') \\ \mathbf{b}(\mathbf{r}', t') \end{Bmatrix} \mathbf{G}(\mathbf{r} - \mathbf{r}', t - t')d\mathbf{r}',$$

and the Green's function is

$$\mathbf{G} = \begin{pmatrix} G_a & 0 \\ 0 & G_m \end{pmatrix}.$$

The component G_a of the Green's function describes Alfvén waves, and the component G_m accounts for

magnetosonic waves,

$$G_a = -\frac{1}{V_{A1}s_{1z}}\delta(x - x')\delta\left(y - y' - \frac{s_{1y}|z - z'|}{s_{1z}}\right)$$

$$\times \theta\left(t - t' - \frac{|z - z'|}{V_{A1}s_{1z}}\right),$$

$$G_m = \frac{1}{(2\pi)^4}\int\limits_{-\infty + i\sigma_0}^{\infty + i\sigma_0} \exp[-iq(t - t')]dq \qquad (7)$$

$$\times \iiint\limits_{\infty} \frac{\exp[i\mathbf{p} \cdot (\mathbf{r} - \mathbf{r}')]}{\Delta(q, \mathbf{p})}d\mathbf{p},$$

where, by virtue of the chosen orientation of the magnetic field, the denominator in the integrand reduces to

$$\Delta(q, \mathbf{p}) = q^4 - q^2(V_{A1}^2 + V_{S1}^2)\mathbf{p}^2 + V_{A1}^2 V_{S1}^2(\mathbf{s}_1\mathbf{p})^2\mathbf{p}^2.$$

Recall that the denominator of the weighting Green's function contains the left-hand sides of Eqs. (3), which describe the dispersion relations for different types of waves. It can be seen from representation (2) that these waves are generally coupled to each other. However, in certain classes of problems, in particular, those dealing with plane-parallel structures, the components of weighting Green's function (7) and differential operator (6) can be separated into independent constituents, each describing the corresponding type of waves.

We consider a planar wave packet incident on a plane interface modulated by a running sinusoidal wave. We assume that the packet is a superposition of an Alfvén wave with the components u_x and b_x and a fast (+) and a slow (–) magnetosonic wave whose components u_j and b_j ($j = 2, 3$) have the form

$$u_{nx}(\mathbf{r}, t) = u_{0x}\exp[-i\mathbf{k}_{a0} \cdot \mathbf{r} + i\omega_0 t],$$

$$\mathbf{k}_{a0} = \omega_0\mathbf{n}_{a0}/V_{A1}(\mathbf{n}_{a0} \cdot \mathbf{s}_1); \qquad (8)$$

$$u_{nj}(\mathbf{r}, t) = u_{0j}^+\exp[-i\mathbf{k}_0^+ \cdot \mathbf{r} + i\omega_0 t]$$

$$+ u_{0j}^-\exp[-i\mathbf{k}_0^- \cdot \mathbf{r} + i\omega_0 t]; \quad j = 2, 3, \qquad (9)$$

where the wave vector $\mathbf{k}_0^\pm$ satisfies the dispersion relation

$$\omega_0^4 - \omega_0^2(V_{A1}^2 + V_{S1}^2)\mathbf{k}_0^2 + V_{A1}^2 V_{S1}^2(\mathbf{s}_1 \cdot \mathbf{k}_0)^2\mathbf{k}_0^2 = 0.$$

In order to determine the internal ($i = 2$) and the external ($i = 1$) field, we assume that the perturbation ξ is small in comparison to the spatial scale on which the scattering boundary of the inhomogeneity is modulated. This approximation allows us to take into account the motion of the inhomogeneity boundary. In this case,

the solution can be represented in the form

$$\mathbf{u} = \sum_k \mathbf{u}^{(k)}, \quad \mathbf{u}^{(k)} \sim |\xi|^k, \quad \mathbf{b} = \sum_k \mathbf{b}^{(k)}, \quad \mathbf{b}^{(k)} \sim |\xi|^k. \quad (10)$$

In the approximation in question, switching to the Lagrangian coordinates $\mathbf{r}' = \mathbf{r}_0 + \boldsymbol{\xi}(\mathbf{r}_0 t)$ (where $\mathbf{r}_0$ is the initial coordinate of a point at the inhomogeneity boundary) in the volume integral puts it into the form [4]

$$\int_{V(t')} f(\mathbf{r}', t')d\mathbf{r}' = \int_{V_0(t')} f(\mathbf{r}_0, t')d\mathbf{r}_0 + \oint_{S_0(t')} f(\mathbf{r}_0, t')(\boldsymbol{\xi} \cdot \mathbf{ds}). \quad (11)$$

We substitute series expansions (10) into the basic equation (5) and take into account relationship (11) to obtain the following equation for the nth term of the expansion:

$$\mathbf{u}^{(k)}(\mathbf{r}, t) = \mathbf{u}_k(\mathbf{r}, t) + (V_{S1}^2 - V_{S2}^2)\hat{F}\nabla(\nabla \cdot \boldsymbol{\Pi}_{\mathbf{u}}^{(k)}(\mathbf{r}, t))$$

$$+ \frac{\hat{F}}{B_1}(V_{A1}^2\mathbf{s}_1 - \gamma V_{A2}^2\mathbf{s}_2) \times \left(\nabla \times \frac{\partial}{\partial t}\boldsymbol{\Pi}_{\mathbf{b}}^{(k)}(\mathbf{r}, t)\right) \quad (12)$$

$$- V_{A1}^2\hat{F}\mathbf{s}_1 \times (\nabla \times (\nabla \times ((\mathbf{s}_1 - \gamma^{-1}\mathbf{s}_2) \times \boldsymbol{\Pi}_{\mathbf{u}}^{(k)}(\mathbf{r}, t)))),$$

$$\begin{Bmatrix} \boldsymbol{\Pi}_{\mathbf{u}}^{(k)} \\ \boldsymbol{\Pi}_{\mathbf{b}}^{(k)} \end{Bmatrix} = \int_{-\infty}^{\infty} dt' \int_{V(t')} \begin{Bmatrix} \mathbf{u}^{(k)}(\mathbf{r}', t') \\ \mathbf{b}^{(k)}(\mathbf{r}', t') \end{Bmatrix} G(\mathbf{r} - \mathbf{r}', t - t')d\mathbf{r}',$$

where the free term is determined by the relationships

$$\mathbf{u}_0(\mathbf{r}, t) = \mathbf{u}_n(\mathbf{r}, t),$$

$$\mathbf{u}_k(\mathbf{r}, t) = (V_{S1}^2 - V_{S2}^2)\hat{F}\nabla(\nabla \cdot \mathbf{H}_{\mathbf{u}}^{(k-1)}(\mathbf{r}, t))$$

$$+ \frac{\hat{F}}{B_1}(V_{A1}^2\mathbf{s}_1 - \gamma V_{S2}^2\mathbf{s}_2) \times (\nabla \times \frac{\partial}{\partial t}\mathbf{H}_{\mathbf{b}}^{(k-1)}(\mathbf{r}, t))$$

$$- V_{A1}^2\hat{F}\mathbf{s}_1 \times (\nabla \times (\nabla \times ((\mathbf{s}_1 - \gamma^{-1}\mathbf{s}_2) \times \boldsymbol{\Pi}_{\mathbf{u}}^{(k-1)}(\mathbf{r}, t)))),$$

$$\begin{Bmatrix} \boldsymbol{\Pi}_{\mathbf{u}}^{(k-1)} \\ \boldsymbol{\Pi}_{\mathbf{b}}^{(k-1)} \end{Bmatrix}(\mathbf{r}, t) = \int_{-\infty}^{\infty} dt' \oint_{S_0(t')} \begin{Bmatrix} \mathbf{u}^{(k-1)} \\ \mathbf{b}^{(k-1)} \end{Bmatrix} G(\boldsymbol{\xi}\mathbf{ds}).$$

Thus, the perturbation is accounted for by the free term in Eq. (12) and the problem formulated is solved by the following scheme. In the zeroth approximation, Eq. (12) is that of the problem of the refraction and reflection of an Alfvén and magnetosonic wave by a plane boundary between two media. The solution to this problem was obtained in [6, 7], where it was shown that, in the zeroth approximation, the solution to Eq. (12) is expressed in terms of the unperturbed incident field. Then, the integral that determines the free term is calculated in the next approximation and the field in the first approximation is calculated by the same scheme, and so forth.

According to [6, 7], the field of the transmitted wave in the zeroth approximation has the form

$$u_x^{(0)}(\mathbf{r}, t) = u_x^{(0)}\exp[-i\mathbf{k}_a^{(0)} \cdot \mathbf{r} + i\omega^{(0)}t], \quad (13)$$

$$u_j^{(0)}(\mathbf{r}, t) = u_j^{+(0)}\exp[-i\mathbf{k}^{+(0)} \cdot \mathbf{r} + i\omega^{(0)}t]$$
$$+ u_j^{-(0)}\exp[-i\mathbf{k}^{-(0)} \cdot \mathbf{r} + i\omega^{(0)}t]; \quad j = 2, 3. \quad (14)$$

The phase parameters of the internal field of an Alfvén wave are determined by the relationships

$$\omega^{(0)} = \omega_0, \quad \mathbf{k}_a^{(0)} = \omega_0\mathbf{n}_a^{(0)}/V_{A2}(\mathbf{n}_a^{(0)} \cdot \mathbf{s}_2);$$
$$\mathbf{n}_a^{(0)} = \{0, \cos\beta_a, \sin\beta_a\}, \quad (15)$$

where the angle of refraction β_a is related to the angle of incidence α_a by the expression

$$V_{A1}^2(s_{1y} + s_{1z}\cot\alpha_a) = V_{A2}^2(s_{2y} + s_{2z}\cot\beta_a). \quad (16)$$

For magnetosonic waves, the same phase parameters are

$$\omega^{(0)} = \omega_0, \quad \mathbf{k}^{\pm(0)} = k^\pm\mathbf{n}^\pm, \quad \mathbf{n}^\pm = \{0, \cos\beta^\pm, \sin\beta^\pm\},$$

where the wave vector $\mathbf{k}^\pm$ is determined by the relationship

$$\omega_0^4 - \omega_0^2(V_{A2}^2 + V_{S2}^2)(\mathbf{k}^\pm)^2 + V_{A2}^2 V_{S2}^2(\mathbf{s}_2 \cdot \mathbf{k}^\pm)^2(\mathbf{k}^\pm)^2 = 0 \quad (17)$$

and the angles of refraction $\beta^\pm$ are expressed in terms of the angles of incidence $\alpha^\pm$ as $k^\pm\sin\beta^\pm = k_0\sin\alpha^\pm$.

The external field, which is a superposition of the fields of the incident waves given by relationships (8) and (9) and the field of a reflected Alfvén wave, has the form

$$u_x^{(0)}(\mathbf{r}, t) = u_{refx}^{(0)}\exp[-ik_{a0y}y$$
$$+ i(k_0 + k_{a0y}s_{1y})(z/s_{1z}) + i\omega_0 t], \quad k_0 = \omega_0/V_{A1}. \quad (18)$$

For reflected magnetosonic waves, this field is

$$u_j^{(0)}(\mathbf{r}, t) = u_{refj}^{+(0)}\exp[-ik_{0y}^+y + ik_{0z}^+z + i\omega_0 t]$$
$$+ u_{refj}^{-(0)}\exp[-ik_{0y}^-y + ik_{0z}^-z + i\omega_0 t]; \quad j = 2, 3. \quad (19)$$

To save space, we do not write out the expressions for the field amplitudes.

The zero-order equation does not contain the perturbation. So, we consider the first approximation, in which the perturbation is taken into account in a linear fashion. To solve the equation, we calculate the free

term for an Alfvén wave,

$$u_{x1}(\mathbf{r}, t) = \frac{V_{A1}^2(\mathbf{s}_1 \cdot \mathbf{k}_{A1})^2 - V_{A2}^2(\mathbf{s}_2 \cdot \mathbf{k}_{A1})^2}{4V_{A1}s_{1z}(\omega_0 + \Theta)}$$

$$\times u_{0x}\exp[-i\mathbf{k}_{a1} \cdot \mathbf{r} + i\omega_1 t] \tag{20}$$

$$+ \frac{V_{A1}^2(\mathbf{s}_1 \cdot \mathbf{k}_{A2})^2 - V_{A2}^2(\mathbf{s}_2 \cdot \mathbf{k}_{A2})^2}{4V_{A1}s_{1z}(\omega_0 - \Theta)} u_{0x}\exp[-i\mathbf{k}_{a2} \cdot \mathbf{r} + i\omega_2 t],$$

where

$$\mathbf{k}_{a1} = \left\{0, k_{a0y} + \eta, \frac{\omega_1}{V_{A2}s_{1z}} - \frac{s_{1y}}{s_{1z}}(k_{a0y} + \eta)\right\};$$

$$\omega_1 = \omega_0 + \Theta,$$

$$\mathbf{k}_{a2} = \left\{0, k_{a0y} - \eta, \frac{\omega_1}{V_{A2}s_{1z}} - \frac{s_{1y}}{s_{1z}}(k_{a0y} - \eta)\right\};$$

$$\omega_1 = \omega_0 - \Theta,$$

$$\mathbf{k}_{a1} = \frac{(\omega_0 + \Theta)\mathbf{n}_1}{V_{A1}(\mathbf{n}_1 \cdot \mathbf{s}_1)}, \quad \mathbf{k}_{a2} = \frac{(\omega_0 - \Theta)\mathbf{n}_2}{V_{A1}(\mathbf{n}_2 \cdot \mathbf{s}_1)}.$$

For magnetosonic waves, we have

$$u_{j1}(\mathbf{r}, t) = \sum_{m=1}^{2} \{u_{j1m}^+ \exp[-i\mathbf{k}_m^+ \cdot \mathbf{r} + i\omega_1 t]$$

$$+ u_{j1m}^- \exp[-i\mathbf{k}_m^- \cdot \mathbf{r} + i\omega_2 t]\}; \quad j = 2, 3, \tag{21}$$

$$\omega_1 = \omega_0 + \Theta, \quad \mathbf{k}_1^\pm = \{0, k_{0y}^\pm + \eta, q_1^\pm\},$$

$$\omega_2 = \omega_0 - \Theta, \quad \mathbf{k}_2^\pm = \{0, k_{0y}^\pm - \eta, q_2^\pm\},$$

where the wave vectors $\mathbf{k}_m^\pm$ are solutions to the dispersion relation

$$(\omega_0 \pm \Theta)^4 - (\omega_0 \pm \Theta)^2(V_{A1}^2 + V_{S1}^2)(\mathbf{k}_m^\pm)^2$$

$$+ V_{A1}^2 V_{S1}^2(\mathbf{s}_1 \cdot \mathbf{k}_m^\pm)^2(\mathbf{k}_m^\pm)^2 = 0, \tag{22}$$

and the amplitudes $u_{j1m}^\pm$ are expressed in terms of $u_{0j}^\pm$ as

$$\begin{pmatrix} u_{21m}^\pm \\ u_{31m}^\pm \end{pmatrix} = \begin{pmatrix} V_{S1}^2(k_{m3}^\pm)^2 + V_{A1}^2(k_m^\pm)^2 - \omega_m^2 & -V_{S1}^2 k_{m2}^2 k_{m3}^2 \\ -V_{S1}^2 k_{m2}^2 k_{m3}^2 & V_{S1}^2(k_{m3}^\pm)^2 - \omega_m^2 \end{pmatrix}$$

$$\times \begin{pmatrix} (V_{S1}^2 - V_{S2}^2)(k_{m2}^\pm)^2 - V_{A2}^2 s_{23}^2(k_m^\pm)^2 & (V_{S1}^2 - V_{S2}^2)k_{m2}^\pm k_{m3}^\pm + V_{A2}^2 s_{22}s_{23}(k_m^\pm)^2 \\ (V_{S1}^2 - V_{S2}^2)k_{m2}^\pm k_{m3}^\pm + V_{A2}^2 s_{23}s_{22}(k_m^\pm)^2 & (V_{S1}^2 - V_{S2}^2)(k_{m3}^\pm)^2 - V_{A2}^2 s_{22}^2(k_m^\pm)^2 + V_{A1}^2(k_m^\pm)^2 \end{pmatrix} \begin{pmatrix} \dfrac{u_{20}^+}{\delta_1(q_m^\pm)} + \dfrac{u_{20}^-}{\delta_2(q_m^\pm)} \\ \dfrac{u_{30}^+}{\delta_1(q_m^\pm)} + \dfrac{u_{30}^-}{\delta_2(q_m^\pm)} \end{pmatrix},$$

$$\mathbf{k}_m^\pm = \{0, k_{m2}^\pm, k_{m3}^\pm\}, \quad k_{1y}^\pm = k_{0y}^\pm + \eta, \quad k_{2y}^\pm = k_{0y}^\pm - \eta,$$

$$\delta_i(q_m^\pm) = 2\{-\omega_i^2(V_{A1}^2 + V_{S1}^2)q_m^\pm$$

$$+ V_{A1}^2 V_{S1}^2[(s_{1y}k_{iy}^\pm + q_m^\pm s_{1z})k_{iy}^\pm$$

$$+ (s_{1y}k_{iy}^\pm + q_m^\pm s_{1z})^2 q_m^\pm]\}; \quad i = 1, 2,$$

with $q_m^\pm$ being the roots of the following equation for p_z:

$$(\omega_0 \pm \Theta)^4 - (\omega_0 \pm \Theta)^2(V_{A1}^2 + V_{S1}^2)[(k_{my}^\pm)^2 + p_z^2]$$

$$+ V_{A1}^2 V_{S1}^2(s_{1y}k_{my}^\pm + p_z s_{1z})^2[(k_{my}^\pm)^2 + p_z^2] = 0.$$

The transmitted field in the first approximation can be calculated by formally assuming that the components of the incident field, u_{x1} and u_{j1} ($j = 2, 3$), are given by relationships (20) and (21), which were calculated in the same approximation. Since the so-called incident field is now that of a packet of six waves (two Alfvén waves plus four magnetosonic waves), the transmitted field in the first approximation also refers to six planar waves. Thus, for two Alfvén waves, we have

$$u_x^{(1)}(\mathbf{r}, t) = \frac{2u_{x1}'\omega_1^{(1)}V_{A1}[\omega_1^{(1)}/V_{A1} - \mathbf{k}_{a1}^{(1)} \cdot \mathbf{s}_1]}{V_{A1}^2(\mathbf{k}_{a1}^{(1)}\mathbf{s}_1)^2 - V_{A2}^2(\mathbf{k}_{a1}^{(1)}\mathbf{s}_2)^2} u_{0x}$$

$$\times \exp[-i\mathbf{k}_{a1}^{(1)} \cdot \mathbf{r} + i\omega_1^{(1)}t]$$

$$+ \frac{2u_{x1}''\omega_2^{(1)}V_{A1}[\omega_2^{(1)}/V_{A1} - \mathbf{k}_{a2}^{(1)} \cdot \mathbf{s}_1]}{V_{A1}^2(\mathbf{k}_{a2}^{(1)} \cdot \mathbf{s}_1)^2 - V_{A2}^2(\mathbf{k}_{a2}^{(1)} \cdot \mathbf{s}_2)^2}u_{0x} \qquad (23)$$

$$\times \exp[-i\mathbf{k}_{a2}^{(1)} \cdot \mathbf{r} + i\omega_2^{(1)}t].$$

Here, u_x' and u_x'' are the wave amplitudes in relationship (20);

$$\omega_1^{(1)} = \omega_0 + \Theta, \quad \omega_2^{(1)} = \omega_0 - \Theta,$$

$$\mathbf{k}_{ai}^{(1)} = \omega_i^{(1)}\mathbf{n}_{ai}^{(1)}/V_{A2}(\mathbf{n}_{ai}^{(1)} \cdot \mathbf{s}_2), \qquad (24)$$

$$\mathbf{n}_{ai}^{(1)} = \{0, \cos\beta_{ai}^{(1)}, \sin\beta_{ai}^{(1)}\}; \quad i = 1, 2,$$

and the angles of refraction $\beta_{ai}^{(1)}$ in the first approximation are found from relationships analogous to relationship (16), the only difference being that the angles of incidence $\alpha_{ai}^{(1)}$ should be taken to be those obtained from the relationships

$$[\omega_0 + \eta V_{A1}(s_{1y} + s_{1z}\cot\alpha_a)](s_{1y} + s_{1z}\cot\alpha_{a1}^{(1)})$$
$$= (\omega_0 + \Theta)(s_{1y} + s_{1z}\cot\alpha_a),$$

$$[\omega_0 + \eta V_{A1}(s_{1y} + s_{1z}\cot\alpha_a)](s_{1y} + s_{1z}\cot\alpha_{a2}^{(1)})$$
$$= (\omega_0 - \Theta)(s_{1y} + s_{1z}\cot\alpha_a).$$

Similarly, for four magnetosonic waves, we have

$$u_j^{(1)}(\mathbf{r}, t) = \sum_{m=1}^{2} \{u_{jm}^{+(1)}\exp[-i\mathbf{k}_m^{+(1)} \cdot \mathbf{r} + i\omega_m^{(1)}t]$$

$$+ u_{jm}^{-(1)}\exp[-i\mathbf{k}_m^{-(1)} \cdot \mathbf{r} + i\omega_m^{(1)}t]\}; \quad j = 2, 3, \quad (25)$$

$$\omega_1^{(1)} = \omega_0 + \Theta, \quad \omega_2^{(1)} = \omega_0 - \Theta,$$

where the wave vectors $\mathbf{k}_m^{\pm(1)}$ satisfy the dispersion relation

$$(\omega_0 \pm \Theta)^4 - (\omega_0 \pm \Theta)^2(V_{A2}^2 + V_{S2}^2)(\mathbf{k}_m^{\pm(1)})^2$$
$$+ V_{A2}^2 V_{S2}^2(\mathbf{s}_2 \cdot \mathbf{k}_m^{\pm(1)})^2(\mathbf{k}_m^{\pm(1)})^2 = 0, \qquad (26)$$

the propagation directions of the waves are determined by the relationship $k_{0y}^{\pm} \pm \eta = k_m^{\pm(1)}\sin\beta_m^{\pm}$, $\beta_m^{\pm}$ are the angles of refraction for the magnetosonic waves, and the amplitudes $u_{jm}^{\pm(1)}$ are determined from relationships analogous to relationship (14) for the amplitudes in the zeroth approximation.

Thus, the transmitted field, as well as the reflected field, is that of a superposition of nine waves with different frequencies, wave vectors, and amplitudes up to the first order in ξ. These nine waves are as follows:

Transmitted field. The field component with the frequency $\omega = \omega_0$ refers to waves with amplitudes (13) and (14) and with the wave vectors $\mathbf{k}_a^{(0)}$ and $\mathbf{k}^{\pm(0)}$ determined, respectively, from relationships (15) and (17). The field components with the frequencies $\omega = \omega_0 \pm \Theta$ refer to waves with amplitudes (23) and (25) and with the wave vectors $\mathbf{k}_{ai}^{(1)}$ and $\mathbf{k}_m^{\pm(1)}$ determined, respectively, from relationships (24) and (26).

Reflected field. The field component with the frequency $\omega = \omega_0$ refers to waves with amplitudes (18) and (19) and with the wave vectors $\tilde{\mathbf{k}}_{a0}$ and $\tilde{\mathbf{k}}_0^{\pm}$ such that $\tilde{\mathbf{k}}_{a0}^{\pm} = \{0, -k_{a0y}, (k_0 + k_{a0}s_{1y})/s_{1z}\}$ and $\tilde{\mathbf{k}}_0^{\pm} = \{0, -k_{0y}^{\pm}, k_{0z}^{\pm}\}$. The field components with the frequencies $\omega = \omega_0 \pm \Theta$ refer to Alfvén waves given by $\exp[-i\tilde{\mathbf{k}}_{a1}^{(1)} \cdot \mathbf{r} + i(\omega_0 + \Theta)t]$ and $\exp[-i\tilde{\mathbf{k}}_{a2}^{(1)} \cdot \mathbf{r} + i(\omega_0 - \Theta)t]$, where $\tilde{\mathbf{k}}_{a1}^{(1)} = \{0, -(k_{a0y} + \eta), k_0 + (k_{a0} + \eta)s_{1y}/s_{1z}\}$ and $\tilde{\mathbf{k}}_{a2}^{(1)} = \{0, -(k_{a0y} - \eta), k_0 + (k_{a0y} - \eta)s_{1y}/s_{1z}\}$, and to magnetosonic waves given by $\exp[-i\tilde{\mathbf{k}}_1^{\pm(1)} \cdot \mathbf{r} + i(\omega_0 + \Theta)t]$ and $\exp[-i\tilde{\mathbf{k}}_2^{\pm(1)} \cdot \mathbf{r} + i(\omega_0 - \Theta)t]$, where the wave vectors $\tilde{\mathbf{k}}_m^{\pm(1)}$ satisfy dispersion relation (22) and have the form

$$\tilde{\mathbf{k}}_1^{\pm(1)} = \left\{0, -(k_{0y}^{\pm} + \eta), \sqrt{(k_1^{\pm(1)})^2 - (k_{0y}^{\pm} + \eta)^2}\right\},$$

$$\tilde{\mathbf{k}}_2^{\pm(1)} = \left\{0, -(k_{0y}^{\pm} - \eta), \sqrt{(k_1^{\pm(1)})^2 - (k_{0y}^{\pm} - \eta)^2}\right\}.$$

Hence, we see that the wave vectors of the transmitted and reflected waves with the frequencies $\omega_0 \pm \Theta$ (side satellites) lie in the plane of incidence on both sides of the wave vectors of the main waves with frequency ω_0. Even in the case of normal incidence (α_a, $\alpha^{\pm} = 0$), the satellites propagate at an angle to the scattering plane. Depending on the angle of incidence, as well as on the relationship between the phase parameters of the incident wave and of the sinusoidal wave that modulates the scattering plane, some satellites may disappear (i.e., they may be damped in space). Thus, in order for a satellite with the frequency $\omega_0 - \Theta$ to disappear in the field of a fast (+) or a slow (−) reflected magnetosonic wave, the phase velocity of the perturbation should satisfy the condition

$$U_f = \frac{\Theta}{\eta} \qquad (27)$$

$$> \frac{\sqrt{V_{A1}^2 + V_{S1}^2 \pm \sqrt{(V_{a1}^2 + V_{S1}^2)^2 - 4V_{A1}^2 V_{S1}^2(\mathbf{n}_0^{\pm} \cdot \mathbf{s}_1)^2}}}{\sqrt{2}(\omega_0/\Theta)[\sin\alpha^{\pm} - 1) + 1]}.$$

It can be seen that, in the case of normal incidence, condition (27) is governed by the Alfvén and sonic speeds in the corresponding medium and also by the relationship between the frequencies. When $\omega_0 \gg \Theta$, this condition is easily satisfied for low U_f values. As the frequency Θ increases, the range of the velocities U_f of the perturbation that gives rise to undamped satellites becomes wider and approaches a limiting value equal to the phase velocity of the magnetosonic waves,

$$(U_f)^2 = \frac{1}{2}\{V_{Ai}^2 + V_{Si}^2 \pm [(V_{Ai}^2 + V_{Si}^2)^2 - 4V_{Ai}^2 V_{Si}^2 (\mathbf{n}^{\pm} \cdot \mathbf{s}_i)^2]^{1/2}\};$$

$$i = 1, 2.$$

Of course, up to the next order in small parameter ξ, satellite harmonics with the frequencies $\omega_0 \pm n\Theta$ ($n > 1$) will play an important role in both transmitted and reflected fields. It should also be noted that, if the plane surface is modulated along the OY axis and if the wave vectors of the waves under consideration lie in the YOZ plane, then the periodicity of the boundary between two media does not lead to coupling between Alfvén and magnetosonic waves. In this case, however, the slow and fast magnetosonic waves are coupled to one another. For some other orientation of the wave vectors, Alfvén and magnetosonic waves are mutually coupled to each other even in the first-order approximation in ξ.

Recall that a wave packet in the solar atmosphere is a superposition of the four main types of waves. The particular results for Alfvén compression waves and for sonic waves can be immediately derived from the above analysis by setting $V_S = 0$ and $V_A \equiv 0$, respectively. More general cases (such as those of sonic–gravitational and magnetosonic–gravitational waves) can be studied by applying the algorithm developed here.

REFERENCES

1. E. R. Priest, *Solar Magnetohydrodynamics* (Reidel, Dordrecht, 1982; Mir, Moscow, 1985).
2. T. G. Cowling, *Magnetohydrodynamics* (New York, 1962; Mir, Moscow, 1964).
3. G. Nerukh and N. A. Khizhnyak, *Modern Problems of Nonstationary Macroscopic Electrodynamics* (Test-Radio, Kharkov, 1991) [in Russian].
4. A. A. Aleksandrova and N. A. Khizhnyak, *Boundary-Value Problems of Magnetohydrodynamics* (Test-Radio, Khar'kov, 1993) [in Russian].
5. A. A. Aleksandrova and Yu. N. Aleksandrov, Zh. Tekh. Fiz. **73** (10), 6 (2003) [Tech. Phys. **48**, 1226 (2003)].
6. A. A. Aleksandrova and N. A. Khizhnyak, Ukr. Fiz. Zh. **29**, 1497 (1984).
7. A. A. Aleksandrova and N. A. Khizhnyak, Ukr. Fiz. Zh. **31**, 1029 (1986).

Translated by O. Khadin

ATOMS, SPECTRA, RADIATION

Theoretical Study of Charge-Exchange and Excitation Processes in Collisions of He$^+$ Ions with C^{5+}, N^{6+}, and O^{7+} Hydrogen-Like Ions
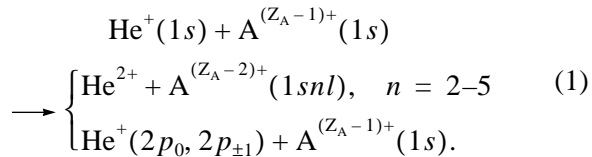
V. K. Nikulin and N. A. Guschina

Ioffe Physicotechnical Institute, Russian Academy of Sciences,
Politekhnicheskaya ul. 26, St. Petersburg, 194021 Russia
e-mail: nikulin@astro.ioffe.ru
Received December 23, 2003; in final form, April 27, 2004

Abstract—Data on the cross sections for single-electron charge exchange and excitation in collisions of He$^+$ ions with C^{5+}, N^{6+}, and O^{7+} ions in the He$^+$ ion energy range of 0.2–3.0 MeV are obtained for the first time. The cross sections for the single-electron charge transfer into the singlet and triplet $1snl$ states of C^{4+}, N^{5+}, and O^{6+} ions ($2 \leq n \leq 5$) and for the $1s \longrightarrow 2p_{0,\pm1}$ electronic excitation of He$^+(1s)$ ions are calculated. The calculations were performed by solving close-coupling equations on the basis of ten two-electron quasi-molecular states. © 2004 MAIK "Nauka/Interperiodica".

INTRODUCTION

In the central plasma region of controlled nuclear fusion devices, the following reactions occurring in collisions of He$^+$ ions with C^{5+}, N^{6+}, and O^{7+} (A$^{(Z_A-1)+}$) hydrogen-like impurity ions in the MeV collision energy range are of great importance [1]:

$$\text{He}^+(1s) + \text{A}^{(Z_A-1)+}(1s)$$

$$\longrightarrow \begin{cases} \text{He}^{2+} + \text{A}^{(Z_A-2)+}(1snl), & n = 2\text{–}5 \\ \text{He}^+(2p_0, 2p_{\pm1}) + \text{A}^{(Z_A-1)+}(1s). \end{cases} \quad (1)$$

Data on the cross sections for reactions (1) are needed both for simulating the behavior of α particles in plasma and for the spectroscopic diagnostics of high-temperature plasma. The emission from the excited impurity and helium ions produced in collisions is of great interest for the plasma core diagnostics. So far, reactions (1) have not been studied theoretically. On the other hand, it is rather difficult to perform direct experimental investigations of ion–ion collisions under conditions of strong Coulomb repulsion between the ions.

In this study, we calculate the cross sections for reactions (1) in the collision energy range of 0.2–3.0 MeV by solving close-coupling equations on the basis of the two-electron states of a (HeA)$^{Z_A+}$ quasi-molecule. The two-electron states are calculated using the single-configuration approach applied to diabatic one-electron screened diatomic molecular orbitals (SDMO) [2].

CALCULATION TECHNIQUE

The cross sections for single-electron charge exchange and excitation in reactions (1) are calculated by solving close-coupling equations in the impact-parameter approximation. Within this approach, the problem reduces to the determination of the electron wave function $\Psi(r_1, r_2, t)$ that satisfies the nonstationary Shrödinger equation

$$i\frac{\partial\Psi(r_1, r_2, t)}{\partial t} = H'(r_1, r_2, \text{R}(t))\Psi(r_1, r_2, t), \quad (2)$$

where H' is the total electron Hamiltonian, which depends parametrically on time through the internuclear distance R(t):

$$H' = \sum_{k=1,2}\left(-\frac{\nabla_k^2}{2} - \frac{Z_A}{r_{ak}} - \frac{Z_B}{r_{bk}}\right) + \frac{1}{r_{12}} + \frac{Z_A Z_B}{\text{R}}$$
$$\equiv H + \frac{Z_A Z_B}{\text{R}}. \quad (3)$$

In Eqs. (2) and (3), r_1 and r_2 are the electron coordinates; r_{ak} and r_{bk} are the distances between the kth electron and the nuclei with the charges Z_A and Z_B ($Z_B = Z_{\text{He}}$), respectively; and r_{12} is the distance between the electrons.

The wave function $\Psi(r_1, r_2, t)$ can be expanded into series on the basis set of two-electron single-configuration states

$$\phi_j(r_1, r_2; \text{R}) = \frac{1}{\sqrt{2(1+S_{0j}^2)}}(\psi_0(r_1; \text{R})\psi_j(r_2; \text{R})$$
$$\pm \psi_0(r_2; \text{R})\psi_j(r_1; \text{R})) \equiv [\psi_0, \psi_j], \quad (4)$$

constructed using the single-electron SDMO wave functions ψ_j (the plus and minus signs in Eq. (4) correspond to the singlet and triplet two-electron states of a quasi-molecule):

$$\Psi(r_1, r_2, t) = \sum_{j=1}^{n} a_j(t)\phi_j(r_1, r_2, R)$$

$$\times \exp\left(-i\int_0^t \left[E_j(R) + \frac{Z_A Z_B}{R}\right]dt'\right),$$

(5)

where

$$E_j(R) = \langle\phi_j(r_1, r_2; R)|H|\phi_j(r_1, r_2; R)\rangle. \quad (6)$$

The SDMO wave functions ψ_j [2] are the solutions to the stationary single-electron Shrödinger equation with the effective potential that optimally accounts for the screening of the nucleus charges by electrons and, moreover, enables the separation of the variables in the prolate spheroidal coordinate system

$$V_{eff}^j(r_k; R) = -\frac{Z_A}{r_{ak}} - \frac{Z_B}{r_{bk}} + \Delta V_{eff}^j(r_k; R),$$

$$\Delta V_{eff}^j = \frac{1}{2}\left[\frac{a_1^j - b_1^j}{r_{ak}} + \frac{a_1^j + b_1^j}{r_{bk}}\right.$$

(7)

$$\left.+ \frac{\tilde{a}_1^j + R a_0^j}{r_{ak}r_{bk}} + \frac{b_2^j(r_{ak} - r_{bk})^2)}{R r_{ak}r_{bk}}\right].$$

This allows one to obtain diabatic orbitals that conserve the orbital symmetry of the H_2^+ problem. In the limit of well separated nuclei ($R \longrightarrow \infty$), the SDMO function ψ_0 entering in formula (4) describes the $1s$ state of the electron coupled with a Z_A nucleus.

If initially (at $t \longrightarrow -\infty$ and $R \longrightarrow \infty$) the system was in the state $\phi_1(r_1, r_2) = \lim_{R \to \infty}\phi_1(r_1, r_2; R)$ with an energy $E_1(\infty)$, then we have

$$\Psi(r_1, r_2, t)|_{t \to -\infty} \longrightarrow \phi_1(r_1, r_2)\exp(-iE_1(\infty)t). \quad (8)$$

Substituting expression (5) into Eq. (2) with allowance for formula (8), we obtain a set of linear differential equations from which we can find the coefficients a_j. For an orthogonal set of the two-electron basis functions and a Coulomb trajectory of nuclei with charges Z_A and Z_B, the obtained set of linear differential equations can be rearranged to the form [3]

$$\frac{da_j(\tau)}{d\tau} = -\sum_{k \neq j} a_k(\tau)$$

$$\times \left\{\frac{\tau}{R - \gamma}R_{jk} + \frac{\rho}{R(R - \gamma)}L_{jk} + \frac{i}{v}\frac{R}{R - \gamma}H_{jk}\right\} \quad (9)$$

$$\times \exp\left(-\frac{i}{v}\int_0^\tau (E_k - E_j)\frac{R}{R - \gamma}d\tau\right)$$

$$(R(\tau) = (\tau^2 + \gamma^2 + \rho^2)^{1/2} + \gamma; \quad -\infty < \tau < \infty)$$

with initial conditions

$$a_j(-\infty) = \delta_{1j}\exp(-iv_1), \quad (10)$$

where

$$v_1 = \exp\left(\frac{1}{v}\int_0^\infty\left[E_1(R) - E_1(\infty) + \frac{Z_A Z_B}{R}\right]\frac{R}{R - \gamma}d\tau\right).$$

In Eq. (9), ρ is the impact parameter; v is the relative velocity of nuclei; and $\gamma = Z_A Z_B/\mu v^2$, with μ being the reduced mass. The matrix elements of the dynamic radial and rotational couplings ($R_{jk} = \langle\phi_j|d/dR|\phi_k\rangle$ and $L_{jk} = \langle\phi_j|iL_y|\phi_k\rangle$, respectively) and the potential coupling $H_{ik} = \langle\phi_i|H|\phi_k\rangle$ were calculated on two-electron states (4). In writing close-coupling equations (9), it was assumed that the y axis of the coordinate system is perpendicular to the collision plane (x, z) and the z axis is directed along the initial velocity of an He$^+$ ion.

In applying the quasi-molecular model to describing atomic collisions (i.e., in solving the close-coupling equations), the problem arises of electron momentum transfer in the course of charge exchange. Since pioneering study [4], this problem has not been rigorously solved even when considering single-electron quasi-molecular processes. It was shown in [4] that, because of ignoring the electron momentum translation in the course of nucleus motion, the basis functions (electron states) in an expansion of type (5) turn out to be coupled to each other for any nucleus positions. Hence, when the number n of the terms in the basis set is finite, the calculated results depend strongly on the set size. To eliminate nonphysical coupling between the states, it was proposed in [4] to use basis molecular functions (4) multiplied by the translation factors in the form of plane waves in expansion (5). To date, many different forms of the translation factors have been proposed for quasi-molecular and atomic bases, as well as for single-electron and two-electron colliding systems and for heteronuclear and homonuclear quasi-molecules.

In this study, an alternative approach proposed in [5] for single-electron quasi-molecules is used to take into account momentum transfer. In this approach, a special coordinate system for electrons is used to calculate the matrix elements of the dynamic coupling of the states. It was shown in [5] that, if the coordinate origin in a heteronuclear quasi-molecule He^{2+}–H($1s$) is set at the centroid of the charges on the internuclear axis (this is also the equipotential point—a natural boundary that separates the electrons belonging to one nucleus from the electrons belonging to the other), then the transition probabilities calculated as a function of the impact

parameter and total cross sections are close to those calculated with allowance for the translation factor in the form of a plane wave.

For the two-electron quasi-molecules considered in this study, this approach was verified in our recent paper [6] by calculating the processes reverse to reaction (1). It was shown that the results of our calculations were close to the results of quasi-molecular calculations performed in the low-energy range with allowance for the translation factor and in the high-energy range with the use an atomic basis. Moreover, it was shown that the approach used in [6] provides the best agreement with the available experimental data over a wide energy range.

For a given impact parameter ρ and given collision velocity v, the amplitude of the transition from the initial state $\phi_1(r_1, r_2)$ into the final state $\phi_j(r_1, r_2) = \lim_{R \to \infty} \phi_j(r_1, r_2; R)$ is

$$b_j(\rho, v) = \lim_{t \to \infty} \langle \phi_j(r_1, r_2) | \Psi(r_1, r_2, t) \rangle \exp(iE_j(\infty)t)$$
$$= a_j(\infty)\exp(-i\nu_j),$$
(11)

where

$$\nu_j = \frac{1}{v}\int_0^\infty \left[E_j(R) - E_j(\infty) + \frac{Z_A Z_B}{R} \right] \frac{R}{R-\gamma} d\tau. \quad (12)$$

In calculating reactions (1), the set of close-coupling equations (9) splits into two independent sets of equations for the singlet and triplet input channels because the matrix elements of the dynamic and potential couplings between the singlet and triplet states of a quasi-molecule are both equal to zero.

All the SDMOs, two-electron states, and matrix elements of the dynamic and potential interactions between these states were calculated using the software developed by us in [7].

Table 1. The energies E_{1s}^u and average effective potentials $\overline{V}_{eff}^0$ for the $1s\sigma$ and $1s\sigma'$ SDMOs in the limit of a united atom and the energies E_{1s}^s for the $1s\sigma$ or $1s\sigma'$ SDMOs in the limit of well-separated nuclei (all the quantities are given in atomic units)

	MO	E_{1s}^u	$\overline{V}_{eff}^0$	E_{1s}^s
(HeC)$^{6+}$	$1s\sigma$	29.66	61.747	18.00
	$1s\sigma'$	28.82	60.529	16.30
(HeN)$^{7+}$	$1s\sigma$	37.87	78.502	24.50
	$1s\sigma'$	40.91	78.930	22.46
(HeO)$^{8+}$	$1s\sigma$	47.51	97.764	32.00
	$1s\sigma'$	47.08	97.281	29.66

CALCULATION OF THE ENERGIES OF SINGLE-ELECTRON AND TWO-ELECTRON STATES OF (HeC)$^{6+}$, (HeN)$^{7+}$, AND (HeO)$^{8+}$ QUASI-MOLECULES

The energies $\varepsilon_j(R)$ and wave functions $\psi_j(r; R)$ of single-electron SDMOs were found by solving the single-electron Shrödinger equation with effective potential (7). The fact that SDMOs calculated for different effective potentials are nonorthogonal makes it rather difficult to solve the set of close-coupling equations. This is why, for all the orbitals under consideration, we use the same effective potential V_{eff}^1 that best describes the closest channel (with respect to the input one) for the single-electron charge transfer into the $3d$ state of an $A^{(Z_A-2)+}$ ($1snl$) ion, except for ψ_0, which, in the limit of well-separated nuclei, describes the very distant (in energy) $1s$ state of an electron coupled with the A nucleus. The method for determining the parameters of this potential is described in [8]. These parameters were found using the energies of the $3p$ and $3d$ levels of a united atom (in the limit R = 0), the $3d$ level of the $A^{(Z_A-2)+}$ ($1s3d$) ion [9], and the $1s$ level of He$^+$ ion. The parameters of the effective potentials (in atomic units) for calculating the ψ_j ($j \neq 0$) orbitals in a (HeA)$^{Z_A+}$ quasi-molecule are as follows:

$$(HeC)^{6+} - \tilde{a}_1^1 = -0.066, \quad a_1^1 = 1.023, \quad a_0^1 = -0.037,$$
$$b_1^1 = 0.997, \quad b_2^1 = 0.010;$$

$$(HeN)^{7+} - \tilde{a}_1^1 = -0.187, \quad a_1^1 = 1.096, \quad a_0^1 = -0.014,$$
$$b_1^1 = 0.997, \quad b_2^1 = -0.016;$$

$$(HeO)^{8+} - \tilde{a}_1^1 = -0.214, \quad a_1^1 = 1.124, \quad a_0^1 = -0.107,$$
$$b_1^1 = 0.996, \quad b_2^1 = -0.022.$$

Various effective potentials V_{eff}^0 were used to calculate the ψ_0 molecular orbital that describes the $1s$ electronic state of the $A^{(Z_A-1)+}$ ($1s$) ($\psi_0 = 1s\sigma$) and $A^{(Z_A-2)+}$ ($1snl$) ($\psi_0 = 1s\sigma'$) ions. The method for determining the parameters of these potentials is described in [10]. Table 1 presents the relevant energies of the $1s$ states of the united atoms and $A^{(Z_A-1)+}$ ($1s$) or $A^{(Z_A-2)+}$ ($1snl$) ions [9], as well as the average value of the effective potential V_{eff}^0 in the limit of a united atom,

$$\overline{V}_{eff}^0 = -\frac{Z^{*2}}{n^{*2}} + \frac{\tilde{a}_1 Z^{*2}}{2n^{*3}(s+1/2)}, \quad (13)$$

which were obtained by atomic calculations in [9].

In formula (13), $Z^* = Z_A + Z_B - a_1^0$; $n^* = n - (l + 1/2) + [(l + 1/2)^2 + \tilde{a}_1^0]^{1/2}$; n and l are the principal and orbital quantum numbers of the united atom, respectively; and s is the effective orbital moment related to l by $s(s + 1) = l(l + 1) + \tilde{a}_1^0$. The parameters of the effective potentials required for calculating the $1s\sigma$ and $1s\sigma'$ SDMOs are listed in Table 2 ($b_2^0 \equiv 0$).

The energies of the two-electron singlet and triplet states determined by formula (6) were calculated in the first order of the perturbation theory by using the residual interaction $W = 1/r_{12} - (V_{\mathrm{eff}}^0 + V_{\mathrm{eff}}^1)$:

$$E_j(R) = \varepsilon_0 + \varepsilon_j$$
$$+ \frac{1}{1 \pm S_{0j}^2}(J_j \pm Q_j \mp S_{0j}(V_{0j}^1 + V_{j0}^0) - (V^0 + V^1)), \quad (14)$$

where $S_{0j} = \langle\psi_0|\psi_j\rangle$; $J_j = \langle\psi_0(r_1)\psi_j(r_2)|1/r_{12}|\psi_0(r_1)\psi_j(r_2)\rangle$ and $Q_j = \langle\psi_0(r_1)\psi_j(r_2)|1/r_{12}|\psi_0(r_2)\psi_j(r_1)\rangle$ are the Coulomb and exchange integrals; and $V^l = \langle\psi_l|V_{\mathrm{eff}}^l|\psi_l\rangle$ ($l = 0, 1$) and $V_{lk}^k = \langle\psi_l|V_{\mathrm{eff}}^k|\psi_k\rangle$ are the diagonal and nondiagonal matrix elements of the effective potentials, respectively.

Among single-electron orbitals ψ_j ($j \neq 0$) used to calculate reactions (1), there were SDMOs describing the $1s$ and $2p_{0,\pm1}$ electronic states of a He^+ ion and the $2p_0$, $3d_{0,\pm1}$, $4f_{0,\pm1}$, and $5g_{0,\pm1}$ electronic states of an $A^{(Z_A - 2)+}$ ($1snl$) ion in the limit of well separated nuclei. The basis of the two-electron diabatic states $\phi_j(r_1, r_2; R) = [\psi_0, \psi_j]$ that are necessary to calculate reactions (1) is shown in Table 3 (the single-electron SDMOs are classified by the (nlm) spherical quantum numbers of a united atom's state). An analysis of the behavior of the SDMO wave functions showed that, after switching from $Z_A = 7$ to 8, the states describing the input channel in the limit of well-separated nuclei interchange with those describing the channel for the single-electron charge transfer into the $3d_0$ state of an $A^{(Z_A - 2)+}$ ion. After switching from $Z_A = 6$ to 7, the states describing the channels for $1s \longrightarrow 2p_{0,\pm1}$ excitation of a He^+ ion in the limit $R \longrightarrow \infty$ interchange with those describing the channels for the single-electron charge transfer into the $5g_{0,\pm1}$ state of an $A^{(Z_A - 2)+}$ ion. Table 3 presents the atomic limits of the two-electron states obtained taking into account that, for the collision energies under consideration, the distant quasi-intersection of the $[1s\sigma', 6h\sigma] - [1s\sigma', 7i\sigma]$ (at $R \sim 18$ au) and $[1s\sigma', 5g\pi] - [1s\sigma', 6h\pi]$ (at $R \sim 16$ a.u.) states of a $(NHe)^{7+}$ quasi-molecule are passed diabatically in the course of a collision event. Consequently, the $(NHe)^{7+}$ quasi-molecule has the same correlation diagram as the $(CHe)^{6+}$ quasi-molecule.

Table 2. Parameters of the effective potentials (in atomic units) for calculating the $1s\sigma$ and $1s\sigma'$ SDMOs of a $(HeA)^{Z_A+}$ quasi-molecule

|	MO	$\tilde{a}_1^0$	a_1^0	a_0^0	b_1^0
$(HeC)^{6+}$	$1s\sigma$	−0.036	0.585	1.045	−1.630
	$1s\sigma'$	−0.032	0.511	1.740	−1.627
$(HeN)^{7+}$	$1s\sigma$	−0.033	0.593	1.044	−1.637
	$1s\sigma'$	−0.030	0.515	−0.240	0.321
$(HeO)^{8+}$	$1s\sigma$	−0.026	0.519	1.172	−1.694
	$1s\sigma'$	−0.030	0.597	−0.368	0.366

Table 3. Basis of ten two-electron diabatic states $\phi_j(r_1, r_2, R)$ for calculating reactions (1)

He^+–C^{5+}, N^{6+}	He^+–O^{7+}	Atomic limits at $R \longrightarrow \infty$
$He^+(1s) + A^{(Z_A - 1)+}$ (1s) input channels		
$\phi_1 = [1s\sigma, 3d\sigma]$	$\phi_1 = [1s\sigma, 4f\sigma]$	
$He^{2+} + A^{(Z_A - 2)+}$ (1snl) charge-exchange channels		
		(nl)
$\phi_2 = [1s\sigma', 2p\sigma]$	$\phi_2 = [1s\sigma', 2p\sigma]$	$2p_0$
$\phi_3 = [1s\sigma', 4f\sigma]$	$\phi_3 = [1s\sigma', 3d\sigma]$	$3d_0$
$\phi_4 = [1s\sigma', 5g\sigma]$	$\phi_4 = [1s\sigma', 5g\sigma]$	$4f_0$
$\phi_6 = [1s\sigma', 7i\sigma]$	$\phi_5 = [1s\sigma', 6h\sigma]$	$5g_0$
$\phi_7 = [1s\sigma', 3d\pi]$	$\phi_7 = [1s\sigma', 3d\pi]$	$3d_{\pm1}$
$\phi_8 = [1s\sigma', 4f\pi]$	$\phi_8 = [1s\sigma', 4f\pi]$	$4f_{\pm1}$
$\phi_{10} = [1s\sigma', 6h\pi]$	$\phi_9 = [1s\sigma', 5g\pi]$	$5g_{\pm1}$
$He^+(2l) + A^{(Z_A - 1)+}$ (1s) excitation channels		
		($2l$)
$\phi_5 = [1s\sigma', 6h\sigma]$	$\phi_6 = [1s\sigma', 7i\sigma]$	$2p_0$
$\phi_9 = [1s\sigma', 5g\pi]$	$\phi_{10} = [1s\sigma', 6h\pi]$	$2p_{\pm1}$

Our calculations showed that, for all of the systems under study, the energies of the singlet (E_j^s) and triplet (E_j^{tr}) states differ slightly because the exchange interaction between the ground (ψ_0) and excited (ψ_j) electronic states is weak. The energies of the two-electron states of an $(OHe)^{8+}$ quasi-molecule are shown in Fig. 1 (the correlation diagrams for the $(CHe)^{6+}$ and $(NHe)^{7+}$ quasi-molecules are presented in [11]).

MATRIX ELEMENTS OF THE DYNAMIC AND POTENTIAL COUPLINGS

The matrix elements of the dynamic coupling between the singlet (d_{ij}^s) and triplet (d_{ij}^{tr}) two-electron
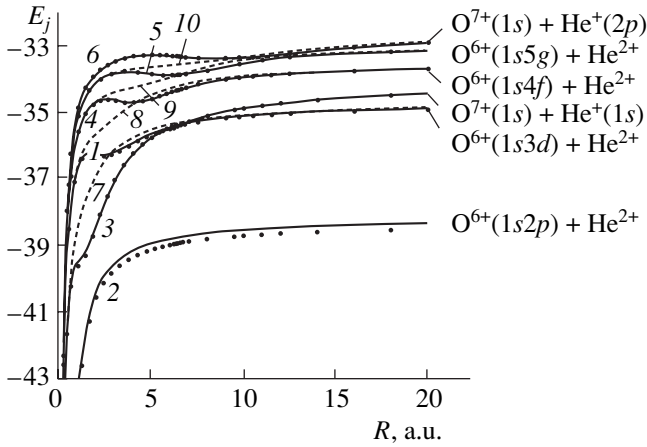
Fig. 1. Energies E_j of the singlet (the solid and dashed curves refer to the $^1\Sigma_j$ and $^1\Pi_j$ states, respectively) and triplet $^3\Sigma_j$ (closed circles) two-electron states ϕ_j of an $(OHe)^{8+}$ quasi-molecule. The entrance channel is $\phi_1 = [1s\sigma, 4f\sigma]$; the single-electron charge-exchange channels are $\phi_2 = [1s\sigma', 2p\sigma]$, $\phi_3 = [1s\sigma', 3d\sigma]$, $\phi_7 = [1s\sigma', 3d\pi]$, $\phi_4 = [1s\sigma', 5g\sigma]$, $\phi_8 = [1s\sigma', 4f\pi]$, $\phi_5 = [1s\sigma', 6h\sigma]$, and $\phi_9 = [1s\sigma', 5g\pi]$; and the excitation channels of He^+ are $\phi_6 = [1s\sigma', 7i\sigma]$ and $\phi_{10} = [1s\sigma', 6h\pi]$.

states (4) are the same and can be expressed via the matrix elements of the radial or rotational coupling between the single-electron ψ_i and ψ_j SDMOs:

$$d_{ij}^s = d_{ij}^{tr} \equiv d_{ij} = \begin{cases} R_{ij} = \langle \psi_i | d/dR | \psi_j \rangle, & \text{for } m_i - m_j = 0 \\ L_{ij} = \langle \psi_i | iL_y | \psi_j \rangle, & \text{for } |m_i - m_j| = 1, \end{cases} \tag{15}$$

where $i, j \neq 0$.

Expressions (15) were obtained without allowance for a minor nonorthogonality between the ground (ψ_0) and excited (ψ_i, ψ_j) states.

Based on the results of calculations, only the following most significant matrix elements of the dynamic coupling for He^+–C^{5+} and He^+–N^{6+} collision systems were retained in the close-coupling equations written on the basis of ten two-electron states listed in Table 3:

$$R_{12} = \langle 3d\sigma | d/dR | 2p\sigma \rangle, \quad R_{13} = \langle 3d\sigma | d/dR | 4f\sigma \rangle,$$

$$R_{14} = \langle 3d\sigma | d/dR | 5g\sigma \rangle, \quad R_{15} = \langle 3d\sigma | d/dR | 6h\sigma \rangle,$$

$$R_{34} = \langle 4f\sigma | d/dR | 5g\sigma \rangle, \quad R_{35} = \langle 4f\sigma | d/dR | 6h\sigma \rangle,$$

$$R_{36} = \langle 4f\sigma | d/dR | 7i\sigma \rangle, \quad R_{45} = \langle 5g\sigma | d/dR | 6h\sigma \rangle,$$

$$R_{46}^N = \langle 5g\sigma | d/dR | 7i\sigma \rangle, \quad R_{56} = \langle 6h\sigma | d/dR | 7i\sigma \rangle,$$

$$R_{89} = \langle 4f\pi | d/dR | 5g\pi \rangle, \quad R_{9,10} = \langle 5g\pi | d/dR | 6h\pi \rangle$$

and

$$L_{17} = \langle 3d\sigma | iL_y | 3d\pi \rangle, \quad L_{38} = \langle 4f\sigma | iL_y | 4f\pi \rangle,$$

$$L_{48} = \langle 5g\sigma | iL_y | 4f\pi \rangle, \quad L_{49} = \langle 5g\sigma | iL_y | 5g\pi \rangle,$$

$$L_{5,10} = \langle 6h\sigma | iL_y | 6h\pi \rangle, \quad L_{6,10} = \langle 7i\sigma | iL_y | 6h\pi \rangle.$$

For He^+–O^{7+} collision system, the following matrix elements were retained:

$$R_{13} = -\langle 3d\sigma | d/dR | 4f\sigma \rangle, \quad R_{14} = \langle 4f\sigma | d/dR | 5g\sigma \rangle,$$

$$R_{15} = \langle 4f\sigma | d/dR | 6h\sigma \rangle, \quad R_{16} = \langle 4f\sigma | d/dR | 7i\sigma \rangle,$$

$$R_{23} = -\langle 3d\sigma | d/dR | 2p\sigma \rangle, \quad R_{34} = \langle 3d\sigma | d/dR | 5g\sigma \rangle,$$

$$R_{35} = \langle 3d\sigma | d/dR | 6h\sigma \rangle, \quad R_{45} = \langle 5g\sigma | d/dR | 6h\sigma \rangle,$$

$$R_{46} = \langle 5g\sigma | d/dR | 7i\sigma \rangle, \quad R_{56} = \langle 6h\sigma | d/dR | 7i\sigma \rangle,$$

$$R_{89} = \langle 4f\pi | d/dR | 5g\pi \rangle, \quad R_{9,10} = \langle 5g\pi | d/dR | 6h\pi \rangle$$

and

$$L_{37} = \langle 3d\sigma | iL_y | 3d\pi \rangle, \quad L_{18} = \langle 4f\sigma | iL_y | 4f\pi \rangle,$$

$$L_{48} = \langle 5g\sigma | iL_y | 4f\pi \rangle, \quad L_{49} = \langle 5g\sigma | iL_y | 5g\pi \rangle,$$

$$L_{59} = \langle 6h\sigma | iL_y | 5g\pi \rangle, \quad L_{5,10} = \langle 6h\sigma | iL_y | 6h\pi \rangle,$$

$$L_{6,10} = \langle 7i\sigma | iL_y | 6h\pi \rangle.$$

In calculating the matrix elements of dynamic coupling, the origin of the electron coordinate system was set in the centroid of the nuclear charges of a quasi-molecule.

The matrix elements of the potential coupling $H_{ij} = \langle \phi_i | H | \phi_j \rangle$ ($i < j$) between the two-electron states of a quasi-molecule are

$$H_{ij} = \frac{1}{[(1 \pm S_{0i}^2)(1 \pm S_{0j}^2)]^{1/2}}$$

$$\times [(\varepsilon_0 + \varepsilon_j)(S_{ij} \pm S_{0j} S_{i0}) + (I_{0j0i} \pm I_{j00i} \tag{16}$$

$$- V_{ij}^1 - S_{ij} V^0 \mp S_{i0} V_{0j}^1 \pm S_{0j} V_{i0}^0)] \delta(m_i - m_j),$$

where $I_{klmn} = \langle \psi_k(r_1) \psi_l(r_2) | 1/r_{12} | \psi_m(r_1) \psi_n(r_2) \rangle$ are the integrals of interelectron interaction.

More detailed information on the matrix elements of dynamic and potential couplings for $(CHe)^{6+}$ and $(NHe)^{7+}$ quasi-molecules is presented in [11]. A specific feature of $(OHe)^{8+}$ quasi-molecules is a sharp change in the d_{ij} and H_{ij} matrix elements (that contain $3d\sigma$ and $4f\sigma$ SDMOs) in the vicinity of the quasi-intersection between these orbitals at an internuclear distance of $R \simeq 6.4$ a.u.

CALCULATION OF THE CROSS SECTIONS
FOR SINGLE-ELECTRON CHARGE EXCHANGE
AND EXCITATION IN COLLISIONS OF He^+ IONS
WITH C^{5+}, N^{6+}, AND O^{7+} HYDROGEN-LIKE IONS

The cross sections for single-electron charge exchange and excitation in collisions of He^+ ions with

C^{5+}, N^{6+}, and O^{7+} ions were calculated by solving close-coupling equations in the energy range of incident He^+ ions from 0.2 to 3.0 MeV.

For a given collision velocity v, the partial cross sections for populating two-electron singlet and triplet states $\phi_j(r_1, r_2) = \lim_{R \to \infty} \phi_j(r_1, r_2; R)$ were calculated by the formula

$$\sigma_j(v) = 2\pi \int_0^\infty d\rho |b_j(\rho, v)|^2, \qquad (17)$$

where $b_j(\rho, v)$ are the amplitudes of transition (11) from the initial state $\phi_1(r_1, r_2)$ into the final state $\phi_j(r_1, r_2)$ calculated for singlet and triplet input channels (when solving the close-coupling equations, the minor nonorthogonality of the basis of two-electron states, $\langle \phi_i | \phi_j \rangle < 10^{-3}$, was not taken into account).

The amplitudes $b_j(\rho, v)$ were calculated using the TANGO code [12] kindly put at our disposal by A. Salin.

In the close-coupling equations, the radial couplings between the input channel (ϕ_1) and the channel for the excitation (ϕ_j) into the $2p_0$ state of a He^+ ion that did not vanish at $R \longrightarrow \infty$ were artificially cut off using an exponentially decaying function:

$$R_{1j}(R) = \begin{cases} R_{1j}(R) & \text{for} \quad R \le R_c \\ R_{1j}(R_c)\exp[-\beta(R - R_c)] & \text{for} \quad R > R_c, \end{cases}$$

where $j = 5$ for He^+–C^{5+} and He^+–N^{6+} collisions and $j = 6$ for He^+–O^{7+} collisions. For all of the systems under study, the constant R_c and β were set to be about 7.0 and 0.3 au, respectively (in the range of large R, the above couplings describe the same radial coupling between the $1s$ and $2p_0$ states of a He^+ ion in all of the three systems).

1. Cross Sections for Single-Electron Charge Exchange and Excitation in $He^+(1s)$–$C^{5+}(1s)$ Collisions

In the case of a He^+–C^{5+} quasi-molecule, the close-coupling equations were solved for the singlet and triplet input channels. The total cross section σ_{sec} and the partial cross section $\sigma_{sec}(n)$ for the single-electron charge transfer into the $1snl$ state of a C^{4+} ion for $n = 2$–5 were calculated by the formulas

$$\sigma_{sec} = \sum_{n=2-5} \sigma_{sec}(n), \qquad (18)$$

where

$$\sigma_{sec}(2) = \sigma_2(2p_0), \quad \sigma_{sec}(3) = \sigma_3(3d_0) + \sigma_7(3d_{\pm1}),$$

$$\sigma_{sec}(4) = \sigma_4(4f_0) + \sigma_8(4f_{\pm1}),$$

$$\sigma_{sec}(5) = \sigma_6(5g_0) + \sigma_{10}(5g_{\pm1}).$$

The total cross section σ_{exc} and the partial cross section $\sigma_{exc}(2p_{0, \pm1})$ for the excitation of a He^+ ion were calculated by the formulas

$$\sigma_{exc} = \sigma_{exc}(2p_0) + \sigma_{exc}(2p_{\pm1}), \qquad (19)$$

where

$$\sigma_{exc}(2p_0) = \sigma_5(2p_0), \quad \sigma_{exc}(2p_{\pm1}) = \sigma_9(2p_{\pm1}).$$

It was found that the partial cross sections for the single-electron charge exchange and excitation calculated on the basis of the singlet states of a $(HeC)^{6+}$ quasi-molecule differed only slightly from those calculated on the basis of the triplet states (for the sake of comparison, Fig. 2 shows the total cross sections for the charge-exchange and excitation processes calculated on the basis of singlet and triplet states without allowance for the single-electron charge transfer into the $1s5g$ state of a C^{4+} ion). This is because the energies of the singlet and triplet states are close to one another since the exchange interaction is weak and the matrix elements of the dynamic interaction (which makes the main contribution to the cross sections of the processes under study) between the singlet (d_{ij}^s) states completely coincide with those for the triplet (d_{ij}^{tr}) states. Hence, to a good accuracy, the total cross sections for the single-electron charge exchange (Σ_{sec}) and excitation (Σ_{exc}) in $He^+(1s)$–$C^{5+}(1s)$ collisions are

$$\Sigma_{sec} = 0.25\sigma_{sec}^s + 0.75\sigma_{sec}^{tr}$$

and

$$\Sigma_{exc}(2p_l) = 0.25\sigma_{exc}^s + 0.75\sigma_{exc}^{tr},$$

where σ_{sec}^s, σ_{exc}^s, σ_{sec}^{tr}, and σ_{exc}^{tr} are the total cross sections for charge exchange and excitation calculated on the basis of singlet and triplet two-electron quasi-molecular states.

The calculated total cross sections for charge exchange and excitation are shown in Fig. 2. At low collision energies ($E_c < 0.9$ MeV), the main process is single-electron charge exchange. The total cross section for single-electron charge exchange increases from 7.9×10^{-16} to 27.98×10^{-16} cm^2 with increasing E_c throughout the entire collision energy range under study, though at $E_c > 1.6$ MeV the energy dependence is weak. At collision energies of $E_c < 0.65$ MeV, the electron is mainly transferred into the $3l$ states of a $C^{4+}(1snl)$ ion; at $0.65 < E_c < 1.0$ MeV, it is mainly transferred into the $5l$ states of a C^{4+} ion; and at $E_c > 1.0$ MeV, it is mainly transferred into the $4l$ states. The total excitation cross section has a feebly marked maximum (39.53×10^{-16} cm^2) at $E_c = 2.33$ MeV. The partial cross section $\sigma_{exc}(2p_0)$ increases with collision energy throughout the entire collision energy range under study, whereas the partial cross section $\sigma_{exc}(2p_{\pm1})$ has a
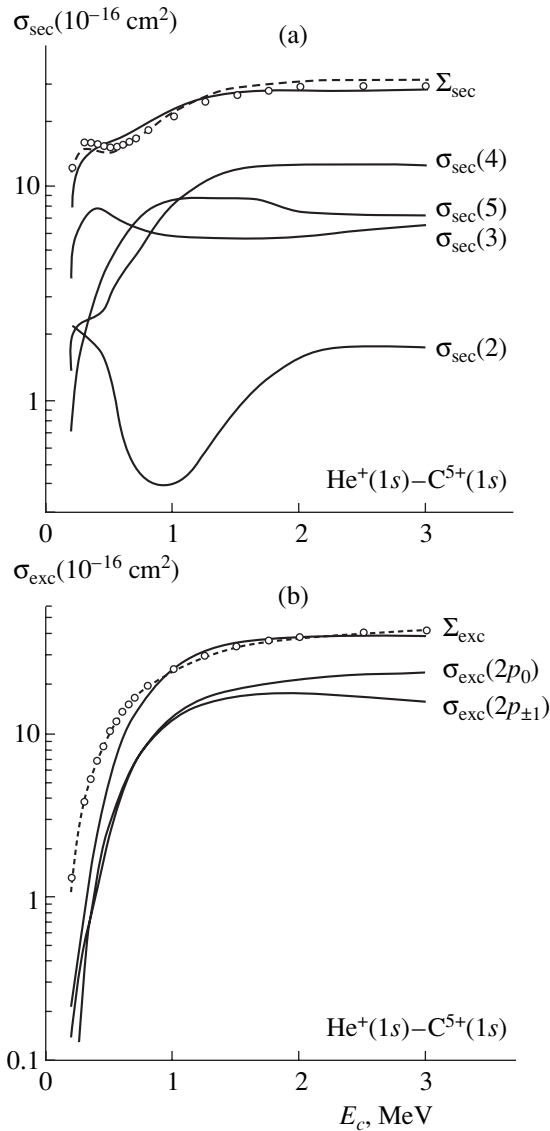
Fig. 2. Cross sections for single-electron charge exchange and excitation in He$^+$–C^{5+} collisions (the dashed curves and circles show the total cross sections for single-electron charge exchange and excitation calculated on the basis of singlet and triplet quasi-molecular states without allowance for the charge transfer into $1s5g$ state of a C^{4+} ion). (a) The total (Σ_{sec}) and partial ($\sigma_{sec}(n)$) cross sections for the single-electron charge transfer into the $1snl$ state of a C^{4+} ion: $\Sigma_{sec} = \sum_{n=2-5}\sigma_{sec}(n)$, $\sigma_{sec}(2) = \sigma_2(2p_0)$, $\sigma_{sec}(3) = \sigma_3(3d_0) + \sigma_7(3d_{\pm1})$, $\sigma_{sec}(4) = \sigma_4(4f_0) + \sigma_8(4f_{\pm1})$, and $\sigma_{sec}(5) = \sigma_6(5g_0) + \sigma_{10}(5g_{\pm1})$. (b) The total ($\Sigma_{exc}$) and partial ($\sigma_{exc}(2p_l)$) cross sections for the $1s \longrightarrow 2p_l$ electronic excitation of a He$^+$ ion: $\Sigma_{exc} = \sigma_{exc}(2p_0) + \sigma_{exc}(2p_{\pm1})$; $\sigma_{exc}(2p_0) = \sigma_5(2p_0)$, and $\sigma_{exc}(2p_{\pm1}) = \sigma_9(2p_{\pm1})$.

maximum (17.5×10^{-16} cm^2) at $E_c = 2.0$ MeV. In the range $0.5 < E_c < 1.3$ MeV, these partial cross sections nearly coincide; at higher E_c, they begin to diverge, and at $E_c = 3.0$ MeV, $\sigma_{exc}(2p_0)$ exceeds $\sigma_{exc}(2p_{\pm1})$ by approx-

imately 1.5 times ($\sigma_{exc}(2p_0) = 23.52 \times 10^{-16}$ cm^2 against $\sigma_{exc}(2p_{\pm1}) = 15.62 \times 10^{-16}$ cm^2).

2. Cross Sections for Single-Electron Charge Exchange and Excitation in Collisions of He$^+$($1s$) Ions with N^{6+}($1s$) and O^{7+}($1s$) Ions

Taking into account the results of the study of He$^+$–C^{5+} collisions, the cross sections for single-electron charge exchange and excitation in collisions of He$^+$ ions with N^{6+} and O^{7+} ions were calculated only on the basis of singlet two-electron states. It was also assumed that the cross sections calculated in this way agree well with the statistically weighted total cross sections for the charge-exchange and excitation processes in He$^+$–N^{6+} and He$^+$–O^{7+} collisions.

The total and partial cross sections for single-electron charge exchange and excitation in collisions of He$^+$ ions with N^{6+} ions were calculated by formulas (18) and (19). The calculated results are shown in Fig. 3. The total cross section for single-electron charge exchange, Σ_{sec}^N, is maximum (27.3×10^{-16} cm^2), at a collision energy E_c of about 1 MeV. At low collision energies ($E_c < 0.4$ MeV), the electron is mainly transferred into the N^{5+}($1snl$) state with $n = 3$; at $0.4 < E_c < 1.1$ MeV, it is mainly transferred into states of an N^{5+} ion with $n = 4$; and, at $E_c > 1.1$ MeV, into states with $n = 5$. Throughout the entire collision energy range under study, the cross section for the excitation of a He$^+$($1s$) ion into the $2p_{0,\pm1}$ state in collisions with a N^{6+}($1s$) ion remains smaller than the cross section for single-electron charge exchange (the maximum value of Σ_{exc}^N is 14.5×10^{-16} cm^2 at $E_c \simeq 1.0$ MeV). The main contribution into the excitation cross section comes from the excitation into the $2p_0$ state of a He$^+$ ion; however, in contrast to the case of He$^+$+C^{5+} collisions, this contribution is now less significant. The $\sigma_{exc}^N(2p_0)$ and $\sigma_{exc}^N(2p_{\pm1})$ excitation cross sections have clearly pronounced maxima at collision energies of 1.0 and 1.2 MeV, respectively. The maximum values of the cross sections are $\sigma_{sec}^N(2p_0)|_{E_c = 1.0 \text{ MeV}} = 10.92 \times 10^{-16}$ cm^2 and $\sigma_{exc}^N(2p_{\pm1})|_{E_c = 1.2 \text{ MeV}} = 3.60 \times 10^{-16}$ cm^2.
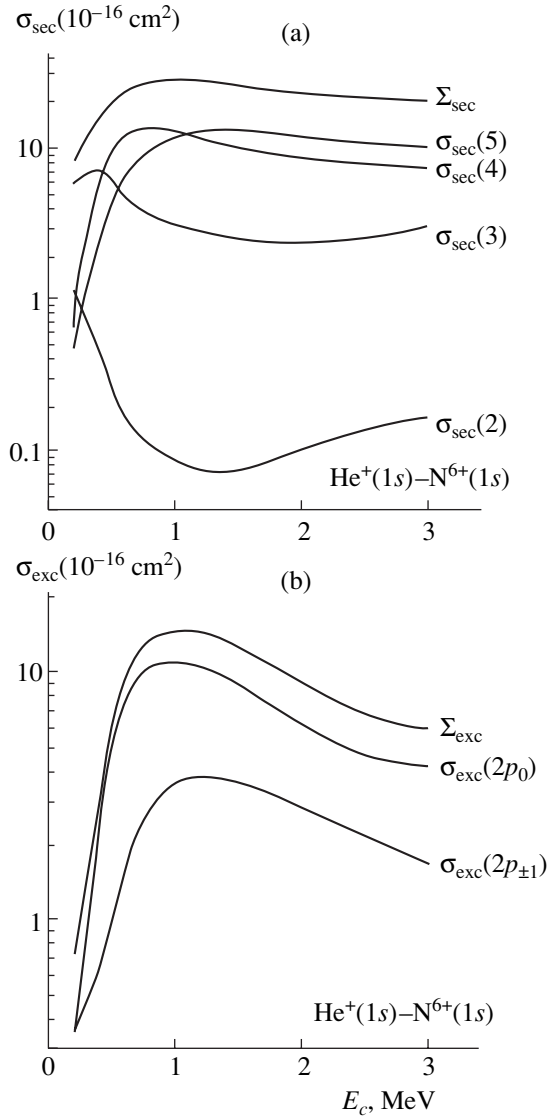
In calculating the cross sections for the single-electron charge exchange and excitation in collisions between He$^+$ and O^{7+} ions, the expressions for $\sigma_{sec}(5)$ and $\sigma_{exc}(2p)$ in formulas (18) and (19) were replaced with the following ones:

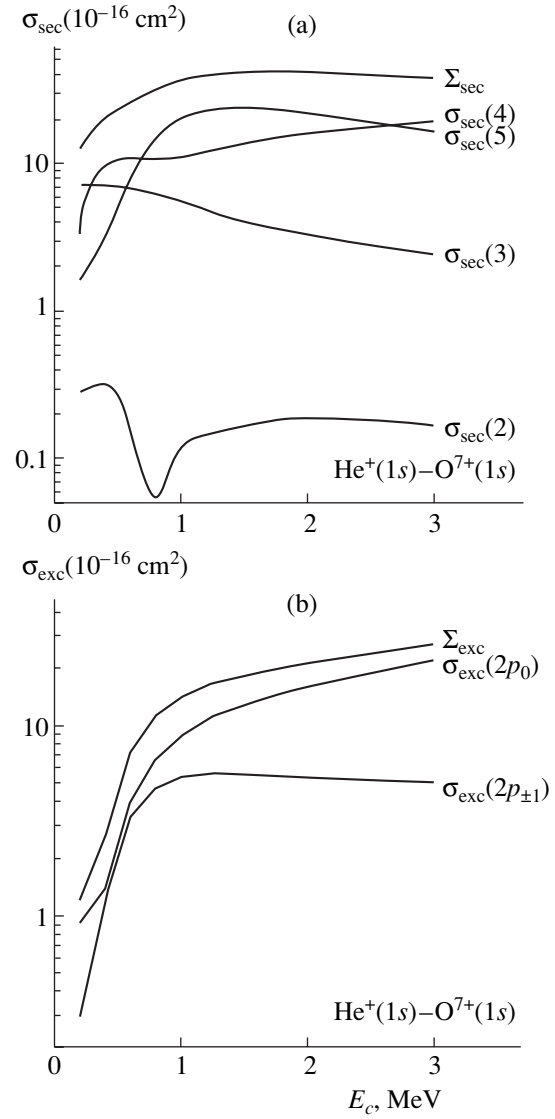$$\sigma_{sec}(5) = \sigma_5(5g_0) + \sigma_9(5g_{\pm1})$$

and

$$\sigma_{exc}(2p_0) = \sigma_6(2p_0), \quad \sigma_{exc}(2p_{\pm1}) = \sigma_{10}(2p_{\pm1}).$$

Fig. 3. Cross sections for the single-electron charge exchange and excitation in He^+–N^{6+} collisions. (a) The total (Σ_{sec}) and partial ($\sigma_{sec}(n)$) cross sections for the single-electron charge transfer into the $1snl$ state of an N^{5+} ion: $\Sigma_{sec} = \sum_{n=2-5} \sigma_{sec}(n)$, $\sigma_{sec}(2) = \sigma_2(2p_0)$, $\sigma_{sec}(3) = \sigma_3(3d_0) + \sigma_7(3d_{\pm1})$, $\sigma_{sec}(4) = \sigma_4(4f_0) + \sigma_8(4f_{\pm1})$, and $\sigma_{sec}(5) = \sigma_6(5g_0) + \sigma_{10}(5g_{\pm1})$. (b) The total ($\Sigma_{exc}$) and partial ($\sigma_{exc}(2p_l)$) cross sections for the $1s \longrightarrow 2p_l$ electronic excitation of a He^+ ion: $\Sigma_{exc} = \sigma_{exc}(2p_0) + \sigma_{exc}(2p_{\pm1})$, $\sigma_{exc}(2p_0) = \sigma_5(2p_0)$, and $\sigma_{exc}(2p_{\pm1}) = \sigma_9(2p_{\pm1})$.

Fig. 4. Cross sections for the single-electron charge exchange and excitation in He^+–O^{7+} collisions. (a) The total (Σ_{sec}) and partial ($\sigma_{sec}(n)$) cross sections for the single-electron charge transfer into the $1snl$ state of an O^{6+} ion: $\Sigma_{sec} = \sum_{n=2-5} \sigma_{sec}(n)$, $\sigma_{sec}(2) = \sigma_2(2p_0)$, $\sigma_{sec}(3) = \sigma_3(3d_0) + \sigma_7(3d_{\pm1})$, $\sigma_{sec}(4) = \sigma_4(4f_0) + \sigma_8(4f_{\pm1})$, and $\sigma_{sec}(5) = \sigma_5(5g_0) + \sigma_9(5g_{\pm1})$. (b) The total ($\Sigma_{exc}$) and partial ($\sigma_{exc}(2p_l)$) cross sections for the $1s \longrightarrow 2p_l$ electronic excitation of a He^+ ion: $\Sigma_{exc} = \sigma_{exc}(2p_0) + \sigma_{exc}(2p_{\pm1})$, $\sigma_{exc}(2p_0) = \sigma_6(2p_0)$, and $\sigma_{exc}(2p_{\pm1}) = \sigma_{10}(2p_{\pm1})$.

The calculated results are shown in Fig. 4. The total cross section for single-electron charge exchange, Σ_{sec}^O, has a maximum (40.95×10^{-16} cm^2) at a collision energy of $E_c \simeq 1.75$ MeV. At low collision energies ($E_c \le 0.4$ MeV), the electron is mainly transferred into the ground state $n = 3$ of the $O^{6+}(1snl)$ ion. In the energy ranges $0.4 < E_c < 0.7$ MeV and $0.7 < E_c < 2.6$ MeV, it is

mainly transferred into the states with $n = 4$ and 5, respectively. At $E_c > 2.6$ MeV, the electron is again mainly transferred into the $O^{6+}(1snl)$ ion states with $n = 4$. The total excitation cross section Σ_{exc}^O increases with E_c throughout the entire collision energy range under study but is always smaller than the total cross section for single-electron charge exchange. At $E_c > 1.0$ MeV,

the He$^+$ ion is mainly excited into the $2p_0$ state. At $E_c = 3.0$ MeV, $\sigma_{exc}^O(2p_0)$ is approximately four times larger than $\sigma_{exc}^O(2p_{\pm 1})$ (21.84×10^{-16} versus 5.05×10^{-16} cm^2, respectively).

CONCLUSIONS

New data are obtained on the total and partial cross sections for the single-electron charge exchange and excitation in collisions of He$^+$ ions with C^{5+}, N^{6+}, and O^{7+} hydrogen-like ions in the collision energy range of 0.2–3.0 MeV.

The total cross section for single-electron charge exchange (40.95×10^{-16} cm^2) is maximum for He$^+$–O^{7+} collisions at $E_c = 1.75$ MeV. The total cross section (39.53×10^{-16} cm^2) for the excitation of a He$^+$ ion is maximum for He$^+$–C^{5+} collisions at $E_c = 2.33$ MeV. For He$^+$–N^{6+} and He$^+$–O^{7+} collisions, the cross section for single-electron charge exchange is larger than the excitation cross section throughout the entire collision energy range under study, whereas for He$^+$–C^{5+} collisions, this is the case only for $E_c < 0.9$ MeV.

At low collision energies, the electron is mainly transferred into the $1s3l$ states of an A$^{(Z_A - 2)+}$ ion for all of the systems under study. As E_c increases, the following charge-exchange channels become dominant: In the case of He$^+$–C^{5+} collisions, this is the single-electron charge transfer into the $1s5l$ state and then into $1s4l$ state of a C^{4+} ion; for He$^+$–N^{6+} collisions, this is the single-electron charge transfer into the $1s4l$ state and then into the $1s5l$ state of an N^{5+} ion; and, for He$^+$–O^{7+} collisions, this is the single-electron charge transfer into the $1s4l$ state, then into the $1s5l$ state, and then again into the $1s4l$ state of an O^{6+} ion. The ranges of collision energies (in MeV) within which the electron is mainly transferred into the nth states of an A$^{(Z_A - 2)+}$ ($1snl$) ion are listed below for all the systems under consideration (the numbers in parentheses are the maximum values of the cross sections $\sigma_{sec}(n)$ in units of 10^{-16} cm^2 for each of the energy ranges):

$$n = 3 \qquad n = 4$$

C$^{4+}(1snl)$: $E_c < 0.7(7.79)$; $E_c > 1.0(12.58)$;

N$^{5+}(1snl)$: $E_c < 0.4(7.02)$; $0.4 < E_c < 1.1(13.25)$;

O$^{6+}(1snl)$: $E_c < 0.4(7.05)$; $0.4 < E_c < 0.71(10.69)$;

$$E_c > 2.6(20.30)$$

$$n = 5$$

C$^{4+}(1snl)$: $0.7 < E_c < 1.0(8.72)$;

N$^{5+}(1snl)$: $E_c > 1.1(12.63)$;

O$^{6+}(1snl)$: $0.7 < E_c < 2.6(23.28)$.

For all of the systems under study, the partial cross sections for the single-electron charge transfer into the $1s2p$ state of an A$^{(Z_A - 2)+}$ ion are small: $\sigma_{sec}^C(2) < 2.0 \times 10^{-16}$ cm^2, $\sigma_{sec}^N(2) < 1.0 \times 10^{-16}$ cm^2, and $\sigma_{sec}^O(2) < 0.3 \times 10^{-16}$ cm^2.

In all of the systems, the He$^+$ ion is mainly excited into the $2p_0$ state.

ACKNOWLEDGMENTS

REFERENCES

1. H. Tawara, *Roles of Atomic and Molecular Processes in Fusion Plasma Researches: NIFS-DATA-25, Nagoya, 1995.*

2. V. K. Nikulin and N. A. Guschina, J. Phys. B **11**, 3553 (1978).

3. N. A. Guschina and V. K. Nikulin, Opt. Spektrosk. **73**, 458 (1992) [Opt. Spectrosc. **73**, 268 (1992)].

4. D. R. Bates and R. McCarroll, Proc. R. Soc. London, Ser. A **245**, 175 (1958).

5. G. J. Hatton, N. F. Lane, and T. G. Winter, J. Phys. B **12**, L571 (1979).

6. V. K. Nikulin and N. A. Guschina, Atomic Plasma and Material Interaction Data for Fusion **10**, 95 (2002).

7. N. A. Guschina and V. K. Nikulin, Preprint No. 1717, FTI im. A. F. Ioffe (Ioffe Physicotechnical Institute, Russian Academy of Sciences, St. Petersburg, 1998).

8. V. K. Nikulin and N. A. Guschina, Zh. Tekh. Fiz. **69** (1), 15 (1999) [Tech. Phys. **44**, 12 (1999)].

9. I. M. Band, M. B. Trzhaskovskaya, and V. I. Fomichev, Preprint No. 299, LIYaF im. B. P. Konstantinova AN SSSR (Konstantinov Institute of Nuclear Physics, Academy of Sciences of USSR, Leningrad, 1977).

10. N. A. Guschina, V. K. Nikulin, A. V. Samoĭlov, *et al.*, Preprint No. 811, FTI im. A. F. Ioffe (Ioffe Physicotechnical Institute, Academy of Sciences of USSR, Leningrad, 1983).

11. V. K. Nikulin and N. A. Guschina, Preprint No. 1764, FTI im. A. F. Ioffe (Ioffe Physicotechnical Institute, Russian Academy of Sciences, St. Petersburg, 2003).

12. R. D. Piacentini and A. Salin, Comput. Phys. Commun. **12**, 199 (1976).

Translated by N. Ustinovskiĭ

GASES
AND LIQUIDS

On the Existence of One-Dimensional Periodic Structures of Polarons in Metal–Ammonia Systems

V. K. Mukhomorov

Agrophysical Research Institute, St. Petersburg, 195220 Russia

e-mail: vmukhomorov@agrophys.ru

Received November 4, 2003

Abstract—The possibility of existence of a periodic one-dimensional structure of small-amplitude polarons that is imposed on the polaron uniform distribution in metal–ammonia structures is estimated in terms of temperature and concentration criteria. A dispersion relation between the probability of existence of the one-dimensional polaron structure and the translational velocity of the polarons is found. The upper limit of the translational velocity when the periodic contribution to the distribution vanishes is determined. It is shown that this specific polaron–polaron interaction leads to results that are basically different from those observed for Coulomb polaron interaction. © *2004 MAIK "Nauka/Interperiodica"*.

INTRODUCTION

One-dimensional and quasi-one-dimensional electron structures are of applied interest. For example, in quasi-one-dimensional (capillary) electroneutral metal–ammonia systems, exotic electron properties are observed, such as a drastic (by several orders of magnitude) drop of the electrical conductivity with decreasing temperature, which resembles the superconducting transition.

In this work, the author studies the possibility of existence of one-dimensional filamentary polaron structures in insulating media, specifically in metal–ammonia systems. Earlier, it was established [1–4] that the interpolaron potential for adiabatically and strongly coupled polarons offers attraction properties. Under certain conditions imposed on the dielectric parameters of the medium and the electron–phonon coupling constant, coupled two-particle objects of bipolaron character arise. At the same time, it is known [5] that attraction between the particles may alter the collective properties of a many-particle system. Namely, the initially uniform distribution of the particles becomes unstable and may change to the nonuniform structured state under specific conditions imposed on the temperature of the medium, particle concentration, and parameters of the pair interpolaron potential.

BASIC EQUATIONS

To study the collective properties of an equilibrium polaron structure in one-dimensional filamentary systems, we will use an infinite set of coupled steady-state integro-differential Bogoliubov equations [6] for simple $F_1(z)$, binary $F_2(z_1, z_2)$, and other spatial distribution functions,

$$\frac{\partial F_1(z_1)}{\partial z_1} + \frac{N}{\vartheta L} \int_{(L)} \frac{\partial \Phi(|z_1 - z_2|)}{\partial z_1} F_2(z_1, z_2) dz_2 = 0,$$

$$\frac{\partial F_2(z_1, z_2)}{\partial z_1} + \frac{1}{\vartheta} \frac{\partial \Phi(|z_1 - z_2|)}{\partial z_1} F_2(z_1, z_2) \qquad (1)$$

$$+ \frac{N}{\vartheta L} \int_{(L)} \frac{\partial \Phi(|z_1 - z_2|)}{\partial z_1} F_3(z_1, z_2, z_3) dz_3 = 0,$$

subject to the normalization conditions

$$\lim_{L \to \infty} \frac{1}{L} \int_{(L)} F_1(z) dz = 1,$$

$$\lim_{L \to \infty} \frac{1}{L} \int_{(L)} F_s(z_1, z_2, ..., z_s) dz_s = F_{s-1}(z_1, z_2, ..., z_{s-1}),$$

$$\qquad (2)$$

$$\lim_{L \to \infty} \frac{1}{L^s} \int_{(L)} ... \int_{(L)} F_s(z_1, z_2, ..., z_s) dz_1, dz_2, ..., dz_3 = 1,$$

$$\vartheta = k_B T.$$

Here, L is the macroscopic length of the one-dimensional structure along the z axis, $N_0 = N^3$ is the mean volumetric density of polarons, and $\Phi(z)$ is the one-dimensional potential function of (central) pair polaron–polaron interaction.

We assume that the equilibrium polaron system is stable because of the presence of neutralizing positive charges. As was shown [7], the state of polarons is unre-

Fig. 1. Pair three-dimensional interpolaron potential for polarons in ammonia.

Fig. 2. Pair one-dimensional interpolaron potential $\Phi(z)$ in ammonia.

lated to the valence of alkali metals dissolved. From set (1), it follows that the distribution functions depend on a set of parameters of a pair potential, temperature (T), and particle concentration.

It was shown [8] that the three-dimensional pair interpolaron potential as a function of the distance between the centers of gravity of polarons (Fig. 1) can be fairly accurately approximated by the analytical formula

$$\Phi(r) = 2\alpha^2\hbar\omega_0\{[d + cr^2 + (a + b(r - r_0)^2)$$
$$\times (1 - \exp(-\gamma r))] \qquad (3)$$
$$\times \exp(-\delta r) + \varepsilon^*(1 - \exp(-\delta r))\exp(-\kappa r)/\varepsilon_\infty r\}.$$

The author determined the interpolaron potential by the direct variational method in the framework of the adiabatic translation-invariant theory of bipolaron [1–3]. In the works cited, quantum exchange effects and interelectron correlations were included with the proviso that an additional restricting condition, the validity of the virial theorem, is met. Ignoring this necessary condition (see, e.g., [9]) overestimates the contribution of the correlation effects to the binding energy of polarons. In this case, the results obtained involve nonoptimal wave functions and, hence, make no physical sense. In (3), the energy is measured from the total energy of two polarons infinitely far away from each other ($\Phi(\infty) \longrightarrow 0$); r is the distance between the centers of gravity of the polarons; $\alpha = (1/2\varepsilon^*)(e^2/\hbar\omega_0)(2m^*\omega_0/\hbar)^{1/2}$ is the dimensionless constant of electron–phonon coupling; $\kappa = (4\pi e^2 N_0/\varepsilon_s\vartheta)^{1/2}$ is the reciprocal Debye screening length for long-range Coulomb interactions; $\varepsilon^{*-1} = \varepsilon_\infty^{-1} - \varepsilon_s^{-1}$ is the effective permittivity of the medium; and ε_s and ε_∞ are the static and high-frequency permittivities, respectively.

In the specific case of polarons in metal–ammonia systems, the parameters of pair potential (3) are as follows: $a = -5.175 \times 10^{-7}$, $b = 6.885 \times 10^{-3} a_0^{*-2}$ ($a_0^* = \hbar^2\varepsilon^*/e^2 m^*$ is the effective Bohr radius), $c = 6.857 \times$

$10^{-3} a_0^{*-2}$, $d = 0.001$, $r_0 = 8.67 \times 10^{-3} a_0^*$, $\delta = 0.2 a_0^{*-1}$, $\gamma = 0.245 a_0^{*-1}$, $\varepsilon_s = 22.7$, $\varepsilon_\infty = 1.756$, and $\alpha = 13.4$. Effective isotropic electron mass $m^* = 1.73m$ was determined by comparing the predicted and experimentally found absorption band maxima for a polaron in metal–ammonia systems [8].

One-dimensional interpolaron pair potential $\Phi(z)$ (Fig. 2) was found from the three-dimensional potential:

$$\Phi(z) = \int_{(L)} dx \int_{(L)} dy \Phi(x, y, z) F_1(x) F_1(y)$$
$$= \frac{N^2}{L^2} \int_0^{2\pi} d\varphi \int_0^\infty \Phi(\rho, z)\rho \, d\rho, \quad \rho = (x^2 + y^2)^{1/2}. \qquad (4)$$

To decouple the equations in infinite set (1), we will use the multiplicative approximation

$$F_2(z_1, z_2) = Q(|z_1 - z_2|) F_1(z_1) F_1(z_2) \qquad (5)$$

for the binary equilibrium distribution function. In (5), factor $Q(|z_1 - z_2|)$ takes into account the correlated arrangement of interacting polarons and, thus, allows for multipolaron effects. The absolute values of $Q(|z_1 - z_2|)$ may serve as a measure of order or structuring in the spatial polaron distribution. The analytical form of correlation function $Q(|z_1 - z_2|)$ will be looked for near the uniform particle distribution under the assumption that $F_1(z) = f_0 = $ const in the zero approximation. Seeing that the correlation loosens with increasing quasi-particle spacing, we impose a natural additional condition on the correlation function: $Q(|z_1 - z_2|) \longrightarrow 1$ at $|z_1 - z_2| \longrightarrow \infty$. Substituting approximation (5) into the second equation of set (1) and omitting the integral terms

yields an equation for the approximate analytical form of function $Q(|z_1 - z_2|)$:

$$\frac{\partial Q(|z_1 - z_2|)}{\partial z_1} F_1(z_1)F_1(z_2)$$

$$+ \frac{1}{\vartheta}\frac{\partial \Phi(|z_1 - z_2|)}{\partial z_1} Q(|z_1 - z_2|)F_1(z_1)F_1(z_2) = 0. \tag{6}$$

From (6), we can find the correlation function in the form

$$Q(|z_1 - z_2|) = C\exp(-\Phi(|z_1 - z_2|)/\vartheta). \tag{7}$$

Since the correlation loosens at large distances, we can put $C = 1$. Thus, the binary distribution function for the polarons whose spatial distribution is nearly uniform may be written as

$$F_2(z_1, z_2) = F_1(z_1)F_1(z_2)\exp(-\Phi(|z_1 - z_2|)/\vartheta). \tag{8}$$

Representation (8) of the binary function makes it possible to decouple infinite set (1). Substituting (8) into the first equation of (1) and integrating over z_1, we arrive at a nonlinear integral equation for the simple distribution function:

$$\ln(\mu F_1(z_1)) + \frac{N}{L}\int\limits_{(L)} K(|z_1 - z_2|)F_1(z_2)dz_2 = 0, \tag{9}$$

where $K(|z_1 - z_2|) = 1 - \exp(-\Phi(|z_1 - z_2|)/\vartheta)$.

Undetermined factor μ is coordinate-independent and is found from the normalizing condition for the simple distribution function.

Nonlinear integral equation (9) is a Hammerstein nonlinear integral equation. A trivial solution to (9) is function $F_1(z) = $ const, which corresponds to the uniform spatial distribution of polarons and meets the normalizing condition. In the absence of external fields and away from surfaces, function $F_1(z)$ specifies the equiprobable arrangement of the particles and corresponds to their uniform distribution.

It is known, however, that Hammerstein nonlinear integral equations have many solutions. For certain values of the parameters involved in (9), there appear bifurcational solutions of a qualitatively different character, which are not spatially uniform functions. To find the bifurcational nontrivial solutions to Eq. (9), we apply the method of successive approximations. Let us expand F_1, μ, and ϑ in small parameter $(\vartheta - \vartheta_0)^{1/2}$:

$$F_1(z) = f_0 + (\theta_0 - \theta)^{1/2}\varphi_1(z) + (\theta_0 - \theta)\varphi_2(z) + \ldots,$$

$$\mu = \mu_0 + (\theta_0 - \theta)^{1/2}\mu_1 + (\theta_0 - \theta)\mu_2 + \ldots, \tag{10}$$

$$\frac{1}{\vartheta} = \frac{1}{\vartheta_0} + \frac{\theta_0 - \theta}{\vartheta^2} + \ldots,$$

subject to

$$\lim_{L\to\infty}\frac{1}{L}\int\limits_{(L)} f_0 dz = 1, \lim_{L\to\infty}\frac{1}{L}\int\limits_{(L)} \varphi_1(z)dz = 0, \ \varphi_1 \ll f_0 = 1.$$

For a given polaron concentration, temperature $\vartheta \leq \vartheta_0$ meets the existence conditions for the bifurcational solutions to initial nonlinear integral equation (9), which differ from the spatially uniform distribution and reflect the irregular (spatial) arrangement of the particles.

Substituting expansion (10) into Eq. (9) and collecting the terms with equal powers of $(\theta_0 - \theta)^{1/2}$, we obtain a set of integral equations. The first equation from this set (the zero approximation) has the form

$$\ln\mu_0 + \frac{N}{L}\int\limits_{(L)} K_0(|z_1 - z_2|)dz_2 = 0. \tag{11}$$

In the first approximation, we have

$$\varphi_1(z_1) + \frac{N}{L}\int\limits_{(L)} K_0(|z_1 - z_2|)\varphi_1(z_2)dz_2 = -\frac{\mu_1}{\mu_0}. \tag{12}$$

Here, $K_0(|z_1 - z_2|) = 1 - \exp(-\Phi(|z_1 - z_2|)/\vartheta_0)$. From (11), we obtain the requirement imposed on the effective potential:

$$\int\limits_{(L)} K_0(|z_1 - z_2|)dz < \infty.$$

Critical temperature ϑ_0 is defined as the principal eigenvalue of homogeneous integral equation (12) when the deviations from the spatially uniform distribution are small:

$$\varphi_1(z_1)$$

$$+ \frac{N}{L}\int\limits_{(L)} (1 - \exp(-\Phi(|z_1 - z_2|)/\vartheta_0))\varphi_1(z_2)dz_2 = 0. \tag{13}$$

Since integral equations of type (13) have many solutions [9], we introduce an additional condition on solutions to Eq. (13); namely, we require that these solutions be periodic. In other words, the additional contribution to the initial distribution function will have the form

$$\varphi_1(z) = C\exp(-ik_z z), \tag{14}$$

where k_z is the wavenumber.

Substituting Eq. (14) into integral equation (13) and integrating yields a relationship from which one can determine critical temperature ϑ_0. Below this temperature, the homogeneous system of polarons becomes unstable against an additional periodic one-dimen-
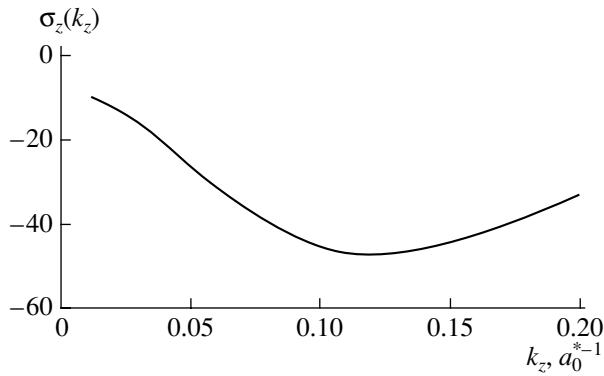
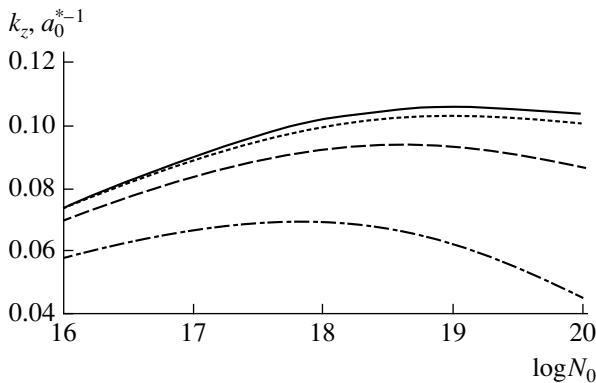**Fig. 3.** Fourier transform $\sigma_z(k_z)$ of the pair one-dimensional interpolaron potential $\Phi(z)$.

sional structured component in the distribution. This relationship appears as

$$\frac{N}{L}\sigma_z(k_z) = -1, \qquad (15)$$

where

$$\sigma_z(k_z) = \int\limits_{(L)} K_0(z)\exp(-ik_z z)dz, \quad L \longrightarrow \infty.$$

Obviously, criterion (15) applies to equilibrium systems only if $\sigma_z < 0$. Figure 3 plots the Fourier transform of σ_z against wavenumber k_z. The periodic contribution to the polaron distribution appears as soon as the parameters in relationship (15) reach strictly defined values. The period of structured contribution $\varphi_1(z)$ to the spatial distribution is found from the relationship $d_z = 2\pi/k_z$, k_z being determined from the minimum condition for $\sigma_z(k_z)$ (Fig. 4). The critical temperature $T_{cr} = \vartheta_0/k_B$ specifies the upper temperature limit of existence

of the periodic component in distribution function $F_1(z)$ and rises with increasing concentration (Fig. 5).

The distance between one-dimensional filamentary polaron structures is found from the minimum condition for the two-dimensional potential:

$$\Phi(\rho) = \frac{N^2}{L^2}\int\limits_{(L)}\int\Phi(|\mathbf{r}-\mathbf{r'}|)F_2(z,z')dzdz'. \qquad (16)$$

Figure 6 plots two-dimensional potential $\Phi(\rho)$ against distance. Optimal distance ρ_0 between the one-dimensional structures is found from the minimum condition for potential $\Phi(\rho)$ and depends on both the parameters and concentration. The distance between the one-dimensional periodic polaron structures decreases monotonically with increasing particle concentration (Fig. 7).

Using the binary distribution function, one can calculate the internal energy of the one-dimensional periodic contribution:

$$E = \frac{N\vartheta}{2} + \frac{N^2}{L^2}\int\limits_{(L)}\int\Phi(|z-z'|)F_2(z,z')dzdz'.$$

This energy must be compared with the internal energy of the polaron uniform distribution. Analysis shows that, for the one-dimensional structure, the energy of the periodic contribution to the distribution is lower than for the uniform one-dimensional distribution throughout the temperature and concentration ranges. This indicates the instability of the initial state with a uniform polaron density.

EFFECT OF POLARON TRANSLATIONAL MOTION ON THE PERIODIC CONTRIBUTION TO THE DISTRIBUTION AND DISCUSSION OF RESULTS

Consider now the conditions favoring the occurrence of the periodic one-dimensional structures when

Fig. 4. Wavenumber vs. polaron concentration for $\Omega = 0$ (continuous curve), 0.5 (dotted curve), 1.0 (dashed curve), and 1.5 (dash-and-dot curve).
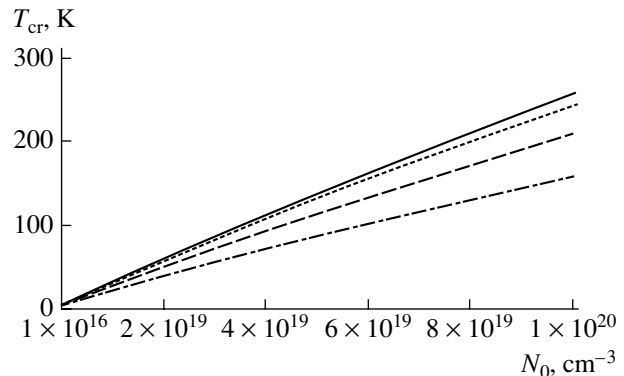
Fig. 5. Critical temperatures below which the periodic structures may exist. $\Omega = 0$ (continuous curve), 0.5 (dotted curve), 1.0 (dashed curve), and 1.5 (dash-and-dot curve).
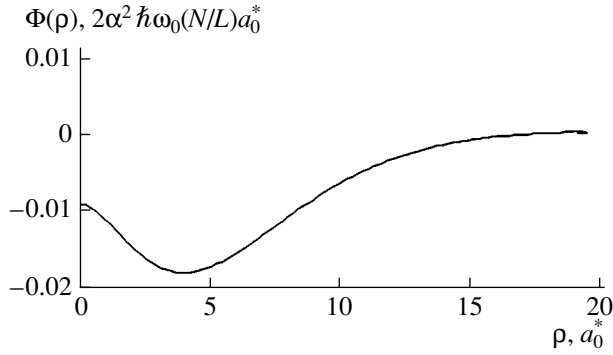
$\Phi(\rho),\, 2\alpha^2\,\hbar\omega_0(N/L)a_0^*$

Fig. 6. Two-dimensional interpolaron potential $\Phi(\rho)$.
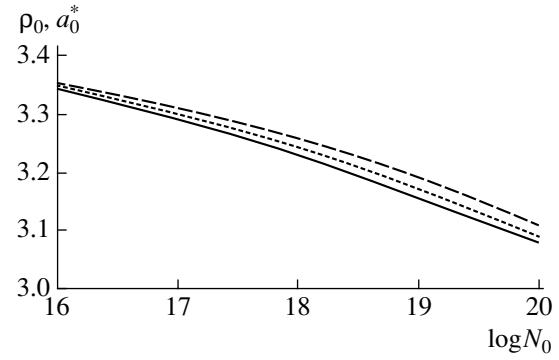
$\rho_0,\, a_0^*$

Fig. 7. Concentration dependence of the distance between the one-dimensional periodic polaron structures. $\Omega = 0$ (continuous curve), 1.0 (dotted curve), and 1.5 (dashed curve).

polarons execute translational motion along the filamentary structure with a mean velocity v_z. To this end, we will use the nonstationary kinetic equation for one-dimensional distribution function $F_1(t, z, v_z)$ [5],

$$\frac{\partial F_1(t, z, v_z)}{dt} + v_z\frac{\partial F_1(t, z, v_z)}{dz}$$

$$-\frac{\vartheta}{M}\nabla_{v_z}F_1\nabla_z\left(\int_{(L)} K|(z - z')|F_1(t, z, v_{z'})dv_{z'}dz'\right) = 0,\qquad(17)$$

where $M = 0.023\alpha^4 m^* \gg m^*$ is the translational mass of a polaron.

It is known [5] that Eq. (17) has an exact solution, $F_1 = F_1(v_z)$, that depends only on the translational velocity of the particle and corresponds to the spatially uniform particle distribution.

We will linearize Eq. (17) to investigate the solutions other than spatially uniform functions. When the space charge is neutralized, on average, by the positive ion background, Eq. (17) can be linearized to the form

$$\frac{\partial\varphi(t, z, v_z)}{dt} + v_z\frac{\partial\varphi(t, z, v_z)}{dz}$$

$$-\frac{\vartheta}{M}\nabla_{v_z}f_0(v_z)\nabla_z\left(\int K(|z - z'|)\varphi(t, v_{z'}, z')dv_{z'}dz'\right)\quad(18)$$

$$-\frac{\vartheta}{M}\nabla_{v_z}\varphi(t, v_z, z)\nabla_z\left(\int K(|z - z'|)f_0(v_z')dv_{z'}dz'\right) = 0.$$

It is assumed here that $F_1(t, z, v_z) = f_0(v_z) + \varphi(t, z, v_z)$ subject to $\varphi \ll f_0$. Such an approximation is consistent with that used to derive Eq. (10) for the stationary case. Linearized integro-differential equation (18) can be replaced by the equivalent integral equation (pro-

vided that the zero time is uncertain)

$$\varphi(t, z, v_z) = \frac{1}{2}\int_{-\infty}^{t}\Phi(\tau, z - v_z(t - \tau), v_z)d\tau$$

$$+\frac{1}{2}\int_{\infty}^{t}\Phi(\tau, z - v_z(t - \tau), v_z)d\tau,\qquad(19)$$

where

$$\Phi(t, z, v_z) = \frac{\vartheta}{M}\nabla_{v_z}f_0\nabla_z$$

$$\times\left(\int K(|z - z'|)\varphi(t, z', v_{z'})dv_{z'}dz'\right).$$

Let us introduce the spatial density function by integrating disturbance ρ of equilibrium function $\varphi(t, z, v_z)$ over velocity:

$$\rho(t, z) = \int\varphi(t, z, v_z)dv_z.$$

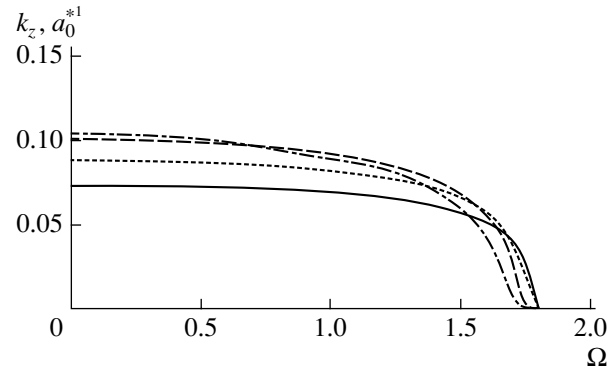As for the case of integral equation (13), periodic solutions for the excess macroscopic spatial density

$k_z,\, a_0^{*1}$

Fig. 8. Wavenumber vs. the drift velocity of polarons in the z direction. $N_0 = 10^{16}$ (continuous curve), 10^{17} (dotted curve), 10^{18} (dashed curve), and 10^{19} cm^{-3} (dash-and-dot curve).

will be sought by putting $\rho(t, z) = \rho_k(t)\exp(ik_z z)$. Substituting this equation into integral equation (19) gives an equation for $\rho_k(t)$:

$$\rho_k(t) = \frac{1}{2}\int_{-\infty}^{t} G_k(t-\tau)\rho_k(\tau)d\tau$$

$$+ \frac{1}{2}\int_{t}^{\infty} G_k(t-\tau)\rho_k(\tau)d\tau, \tag{20}$$

where the kernel of the integral equation is

$$G_{k_z}(t-\tau) = \frac{\sigma_z(k_z)\vartheta}{M}\int_{-\infty}^{\infty} e^{-ik_z v_z(t-\tau)}(ik_z\nabla_{v_z}f_0)dv_z,$$

$$\sigma(k_z) = 2\int_{0}^{\infty} K(z)\cos(k_z z)dz.$$

Here, it is assumed that the coordinates and momenta of the particles are statistically independent in equilibrium. Then, for Eq. (20) to be solvable, it is necessary that the equation

$$\int_{0}^{\infty} G_{k_z}(t)\cos(k_z v_z)dt = 1 \tag{21}$$

be met.

When deriving relationship (21), we introduced the velocity of translational motion along the z axis, $v' = v - v_z$, into velocity distribution function $f_0(v'^2)$. Using Maxwell velocity distribution function $f_0[(v - v_z)^2]$, one can write criterion (21) for the occurrence of the periodic component in a system of moving polarons in the form

$$\frac{2N\sigma_z(k_z)}{L}J(\Omega) = -1,$$

$$J(\Omega) = \int_{0}^{\infty} x\exp(-x^2)\cos(\Omega x)dx, \tag{22}$$

where dimensionless parameter $\Omega = v_z(2M/\vartheta)^{1/2}$ includes the translational velocity of polarons.

For quiescent polarons ($v_z = 0$), criterion (22) obviously coincides with criterion (15). As the translational velocity along the z axis increases, the temperature range where the periodic contribution to the polaron distribution exists shrinks (Fig. 5) and spontaneously disappears when critical velocity $v_z^{cr} = 1.307(\vartheta_0/M)^{1/2}$ ($\Omega_{cr} = 1.848$) is reached. The distance between the periodic structures increases with increasing velocity and decreases with increasing concentration (Fig. 7).

The variation of the optimal wavenumber (and, hence, the polaron structure period) with translational

velocity is shown in Figs. 4 and 8. For a given polaron concentration, wavenumber k_z slowly decreases with increasing polaron translational velocity and the periodic contribution disappears virtually stepwise as the velocity approaches its critical value Ω_{cr} (integral $J(\Omega)$ changes sign at $\Omega = \Omega_{cr}$ and then becomes negative).

In a set of classical charges interacting by the Coulomb law ($\Phi(r) = e^2/r$), the periodic structure arises in quite a different manner. To simplify calculations and make them clearer, we will invoke the self-consistency method [5]. Such an approach does not change the results qualitatively. The criterion of occurrence of the periodic structure then takes the form

$$-\frac{N}{L^3}\frac{8\pi e^2}{k_z^2\vartheta_0}J(\Omega) = 1. \tag{23}$$

This criterion applies only if Ω reaches critical value Ω_{cr} (i.e., at $v_z^{cr} = \Omega_{cr}(\vartheta_0/2M)^{1/2}$, above which integral $J(\Omega) < 0$. Clearly, if the translational velocity of the particles is less than critical, $v_z < v_z^{cr}$ (in this case, $J(\Omega) > 0$), criterion (23) fails and the structured periodic contribution to the distribution of like-charged particles may apparently appear only if the critical velocity is exceeded. That is, the situation here is opposite to that arising in the polaron system, which features specific interaction (3).

Consider now pair screened Coulomb interaction between particles, $\Phi(r) = e^2\exp(-\kappa r)/r$. In this case, the criterion of periodic structure occurrence may be written as follows:

$$-\frac{2N\sigma(k_z)}{L^3\vartheta_0}J(\Omega) = 1, \tag{24}$$

where

$$\sigma(k_z) = 2\int_{0}^{\infty} \Phi(z)\cos(k_z z)dz = \frac{4\pi e^2}{\kappa^2 + k_z^2},$$

$$\Phi(z) = 2\pi\int_{0}^{\infty} \frac{\exp(-\kappa w(\rho, z))}{w(\rho, z)}d\rho,$$

$$w(\rho, z) = (\rho^2 + z^2)^{1/2}.$$

From (24), we obtain the criterion of periodic structure occurrence for classical like-charged particles:

$$-\frac{8N\pi e^2}{L^3(\kappa^2 + k_z^2)\vartheta_0}J(\Omega) = 1. \tag{25}$$

Taking into account the definition of Debye screening length κ, criterion (25) may be recast as

$$k_z^2 = -\frac{4\pi e^2 N}{L^3\vartheta_0}\left(\frac{1}{\varepsilon_s} + 2J(\Omega)\right). \tag{26}$$

For negative $J(\Omega)$, this criterion will obviously have the form $|2J(\Omega)| > 1/\varepsilon_s$.

REFERENCES

1. V. K. Mukhomorov, Opt. Spektrosk. **55**, 246 (1983) [Opt. Spectrosc. **55**, 145 (1983)]; Opt. Spektrosk. **74**, 1083 (1993) [Opt. Spectrosc. **74**, 644 (1993)].

2. V. K. Mukhomorov, Khim. Fiz. **2**, 642 (1983).

3. V. K. Mukhomorov, Phys. Status Solidi B **231**, 462 (2002).

4. V. K. Mukhomorov, J. Phys. C **13**, 3633 (2001); Fiz. Tverd. Tela (St. Petersburg) **44**, 232 (2002) [Phys. Solid State **44**, 241 (2002)].

5. A. A. Vlasov, *Theory of Many Particles* (GITTL, Moscow, 1950) [in Russian].

6. N. N. Bogoliubov, *Problems of Dynamic Theory: Selected Works on Statistical Physics* (Izd. Mosk. Gos. Univ., Moscow, 1979) [in Russian].

7. N. F. Mott, *Metal–Insulator Transitions* (Taylor & Fransis, London, 1974; Nauka, Moscow, 1979).

8. V. K. Mukhomorov, Zh. Tekh. Fiz. **67** (8), 1 (1997) [Tech. Phys. **42**, 855 (1997)]; Phys. Status Solidi B **219**, 71 (2000).

9. N. I. Kashirina, V. D. Lakhno, and V. V. Sychev, Fiz. Tverd. Tela (St. Petersburg) **45**, 163 (2003) [Phys. Solid State **45**, 171 (2003)].

10. N. Nazarov, *Hammerstein Nonlinear Integral Equations* (Uzgosizdat, Tashkent, 1941), Ser. V-a: Mathematics, No. 33.

Translated by V. Isaakyan

Influence of Weak Electrostatic Perturbations on the Trajectories of Circulating Particles in a Tokamak Magnetic Field

A. Yu. Chirkov

Bauman Moscow State Technical University, Vtoraya Baumanskaya ul. 5, Moscow, 105005 Russia
e-mail: chirkov@power.bmstu.ru
Received March 23, 2004

Abstract—The influence of weak electrostatic perturbations on the trajectories of circulating particles in a tokamak magnetic field is analyzed. The parameters of the trajectories calculated in the drift approximation allow one to determine the spatial scale of diffusion. The resonant interaction between particles and waves is considered. The possibility of the emergence of collisionless diffusion in the strong turbulence regime is analyzed. © 2004 MAIK "Nauka/Interperiodica".

INTRODUCTION

The shape and parameters of the trajectories of plasma particles are among the basic factors determining the rate of transport processes in the complicated magnetic field of a tokamak. According to the neoclassical transport theory, the main contribution to these processes comes, depending on the collision frequency (plasma density), either from trapped or circulating particles. At a low turbulence level in the *H*-mode, the ion losses in tokamaks correspond to the neoclassic diffusion coefficients [1]. Therefore, it is of interest to study how the shape and parameters of the particle trajectories in a tokamak magnetic field vary under the action of the factors affecting these trajectories. For example, a toroidal electric field causes a significant distortion of the particle trajectories [2].

In the present paper, we examine how weak electrostatic perturbations distort the trajectories of circulating particles in a tokamak magnetic field and, consequently, increase the spatial scale of diffusion. Previous calculations performed for simple magnetic configurations showed that, at sufficiently large perturbation amplitudes and a large number of perturbation modes, anomalous collisionless diffusion may arise [3–5]. The objective of the present paper is to analyze the trajectories of circulating particles in a tokamak under the action of sufficiently weak perturbations, i.e., such that do not necessarily cause collisionless transport. We consider low-frequency long-wavelength electrostatic perturbations with frequencies much lower than the ion cyclotron frequency and wavelengths appreciably longer than the Larmor radius of an ion. The trajectories are calculated in the drift approximation. For definiteness, we consider ions. The results obtained can be, in principle, extended to electrons; however, in this case, it is necessary to take into account that the electro-static interaction between light electrons and heavy ions limits the escape of electrons from the confinement system. Conditions are determined under which the spatial scale of diffusion increases appreciably compared to that in the case of unperturbed trajectories.

THEORETICAL MODEL

In the equations of motion of a particle guiding center, along with the basic factors causing particle drift in the tokamak magnetic field, we also took into account the influence of the finite plasma pressure (this effect may be important for low-aspect-ratio tokamaks [6]) and the radial electric field. A configuration with circular magnetic surfaces was considered in toroidal coordinates, with r being the radius, θ being the poloidal angle, and φ being the toroidal angle. In these coordinates, the toroidal magnetic field is

$$B_\varphi = \chi \frac{B_0 R}{R + r\cos\theta}, \qquad (1)$$

where B_0 is the vacuum magnetic field at the axis; R is the major tokamak radius; and χ is the diamagnetic susceptibility, which describes a decrease in the magnetic field due to the finite plasma pressure.

The poloidal component B_θ of the magnetic field was specified by the safety factor

$$q(r) = \frac{B_\varphi r}{B_\theta R}, \qquad (2)$$

which was assumed to be a parabolic function monotonically increasing from 1.2 to 3.5.

In a tokamak, the particles drift along the normal to the equatorial plane with the velocity

$$V_y = \frac{m v_\parallel^2 + \mu B}{\chi^2 Z e B_0 R},\qquad(3)$$

where e is the electron charge, Z is the particle charge number, m is the particle mass, $v_\parallel$ is the velocity component parallel to the magnetic field, μ is the magnetic moment of a particle, and $B = \sqrt{B_\varphi^2 + B_\theta^2}$.

The poloidal rotation velocity due to diamagnetism is

$$V_d = \frac{\partial \chi}{\partial r} \frac{R + r\cos\theta}{\chi} V_y.\qquad(4)$$

The wave potential was given in the form

$$\tilde{\Phi} = \Phi_0 g(r)\cos(-\omega t + n_\theta\theta + n_\varphi\varphi + \psi),\qquad(5)$$

where Φ_0 is the wave amplitude; $g(r)$ is the radial wave profile; ω is the frequency; n_θ and n_φ are the poloidal and toroidal wave numbers, respectively; and ψ is the initial phase.

The components of the electric field of the wave are

$$\tilde{E_\theta} = -\frac{1}{r}\frac{\partial \tilde{\Phi}}{\partial \theta},\quad \tilde{E_\varphi} = -\frac{1}{R + r\cos\theta}\frac{\partial \tilde{\Phi}}{\partial \varphi},$$

$$\tilde{E_r} = -\frac{\partial \tilde{\Phi}}{\partial r}.$$

Note that the radial wave profile stems from a nonlocal approach to the analysis of instabilities [7–10]. In our calculations, the characteristic width of the radial profile was taken to be several times larger than the radial displacement of a particle.

In our case, the drift equations describing the motion of the particle guiding center have the form

$$\frac{dr}{dt} = V_y\sin\theta + \frac{\tilde{E_\varphi}B_\theta - \tilde{E_\theta}B_\varphi}{B^2},\qquad(6)$$

$$r\frac{d\theta}{dt} = V_y\cos\theta - V_d + v_\parallel\frac{B_\theta}{B} + \frac{E_r B_\varphi}{B^2} + \frac{\tilde{E_r}B_\varphi}{B^2},\qquad(7)$$

$$(R + r\cos\theta)\frac{d\varphi}{dt} = V_d\frac{B_\theta}{B_\varphi} + v_\parallel\frac{B_\varphi}{B} - \frac{E_r B_\theta}{B^2} - \frac{\tilde{E_r}B_\theta}{B^2},\qquad(8)$$

$$\frac{dv_\parallel}{dt} = -\frac{1}{m}\frac{\mu B\sin\theta}{R + r\cos\theta}\frac{B_\theta}{B_\varphi} + \frac{Ze}{m}\frac{\tilde{E_\theta}B_\theta + \tilde{E_\varphi}B_\varphi}{B},\qquad(9)$$

where E_r is the static radial electric field.

ANALYSIS OF THE TRAJECTORIES AND CALCULATED RESULTS

Since the longitudinal velocity $v_\parallel$ of the circulating particles varies slightly, we can assume for the unperturbed particle trajectories that

$$\dot\theta \equiv \frac{d\theta}{dt} \approx \Omega_E + \frac{v_\parallel B_\theta}{rB} \approx \Omega_E + \frac{v_\parallel}{qR},\qquad(10)$$

$$\dot\varphi \equiv \frac{d\varphi}{dt} \approx \frac{v_\parallel B_\varphi}{(R + r\cos\theta)B} \approx \frac{v_\parallel}{(R + r\cos\theta)},\qquad(11)$$

where

$$\Omega_E = \frac{E_r B_\varphi}{rB^2} - \frac{V_d}{r}.$$

The calculations showed that the wave field of form (5) most strongly distorts the particle trajectories that satisfy the resonance condition

$$\omega - n_\theta\dot\theta - n_\varphi\dot\varphi = 0.\qquad(12)$$

Since $v_\parallel$, $\dot\theta$, and $\dot\varphi$ are not constant along the particle trajectory, condition (12) may be satisfied only at definite points on this trajectory. Consequently, in order for the entire trajectory may be regarded as resonant, it is necessary to consider not only an infinitely narrow resonance defined by condition (12) but also a certain vicinity of this resonance. The width of such a resonance region can be defined by the requirement that the maximum change in the wave phase along the particle trajectory should not exceed $\pi/2$.

At $n_\theta = 0$, the entire particle trajectory lies within the resonance region defined in such a way if the following condition is satisfied:

$$\left|\frac{n_\varphi\Delta\dot\varphi}{\dot\varphi}\right| < \frac{1}{4},\qquad(13)$$
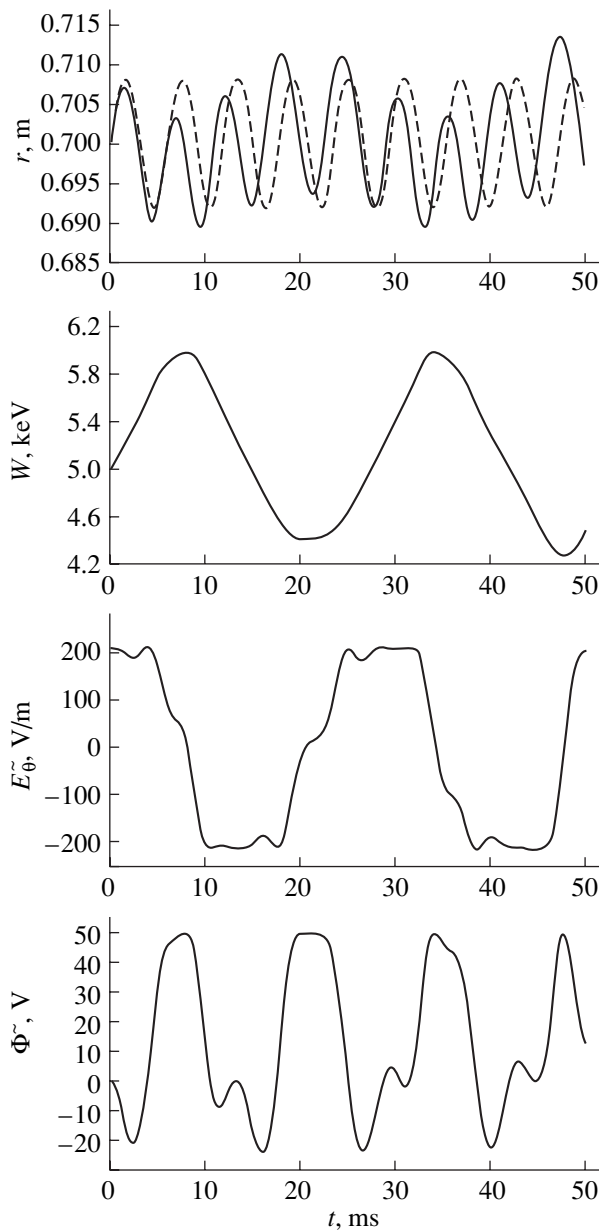
where

$$\Delta\dot\varphi \approx \frac{2v_\parallel r}{R^2 - r^2}\qquad(14)$$

is the variation in the angular velocity of toroidal rotation for an unperturbed trajectory.

Condition (13) of the resonant interaction is satisfied at

$$|n_\varphi| < \frac{R^2 - r^2}{8Rr}.\qquad(15)$$

This inequality, in turn, may be met only in regions close to the magnetic axis of the system. Hence, from the standpoint of resonant interaction, perturbations

Fig. 1. Results of calculations of an ion (proton) trajectory in a tokamak magnetic field under the action of a wave field with $n_\theta = 3$ and $\omega = 3.24 \times 10^5$ rad/s for $W_{\|0}/W_0 = 0.6$. The other parameters are as follows: $W_0 = 5$ keV, $\Phi_0 = 50$ V, $B_0 = 3$ T, $R = 3$ m, the small radius of the plasma column is $a = 1$ m, $r_0 = 0.7$ m, and $q(r_0) = 3$.

with $n_\varphi = 0$ are of the greatest interest. At $n_\varphi = 0$, the resonant interaction condition is

$$\left| \frac{n_\theta \Delta \dot{\theta}}{\dot{\theta}} \right| < \frac{1}{4}, \qquad (16)$$

where the relative change in the angular velocity of the

poloidal rotation of a particle is equal to

$$\frac{\Delta \dot{\theta}}{\dot{\theta}} \approx \frac{\Delta v_\|}{v_\|}\left(1 + \frac{qR\Omega_E}{v_\|} \right)^{-1}$$

$$= \frac{1}{2}\frac{Rr}{R^2 - r^2}\left(\frac{v_\perp}{v_\|} \right)^2\left(1 + \frac{qR\Omega_E}{v_\|} \right)^{-1}. \qquad (17)$$

Here, $\Delta v_\|$ is the amplitude of variations in the longitudinal velocity along the trajectory and $v_\perp$ is the particle velocity component transverse to the magnetic field (the Larmor rotation velocity).

Condition (16) is satisfied at

$$|n_\theta| < \frac{R^2 - r^2}{2Rr}\left(\frac{v_\|}{v_\perp} \right)^2\left| 1 + \frac{qR\Omega_E}{v_\|} \right|. \qquad (18)$$

It follows from this that, at a sufficiently large ratio between the longitudinal and transverse velocities, the poloidal wave number of a resonant mode may be fairly large.

Figures 1–3 present the results of calculations performed for different magnitudes of the poloidal wave number n_θ and different ratios of the longitudinal kinetic energy $W_{\|0}$ at the start point to the total kinetic energy W_0 at the same point. The figures demonstrate time variations in the radial coordinate r (for perturbed and unperturbed trajectories), the particle kinetic energy W, the poloidal component $E_{\tilde{\theta}}$ of the wave field, and the wave potential $\Phi^\sim$ at the trajectory. The trajectories were calculated for the particle start radius $r_0 = 0.7$ m and the poloidal start angle $\theta_0 = \pi/2$. The calculations were performed for a conventional tokamak with an aspect ratio of $A = 3$. The plasma pressure was assumed to be sufficiently low that the diamagnetic effect could be ignored ($\chi = 1$).

The calculations showed that the particle does not remain in the resonance for an infinitely long time. This is apparently related to variations in the particle energy under the action of the wave field. Note that variations in the longitudinal velocity were determined from dynamic equation (9). Therefore, the particle energy does not remain constant. A considerable change in the particle energy is related to the longitudinal acceleration (or deceleration) caused by the longitudinal (with respect to the magnetic field) component of the electric field

$$E_\|^\sim \approx \frac{r}{qR}E_{\tilde{\theta}}. \qquad (19)$$

As long as the particle remains in the resonance region, it continuously accelerates (or decelerates) along the magnetic field. Therefore, the particle energy may substantially change even at very small amplitudes of the wave potential. For example, for the cases represented in Figs. 1–3, the ratio $Ze\Phi_0/W_0$ is as low as 1%, while the particle energy varies by approximately 20%.
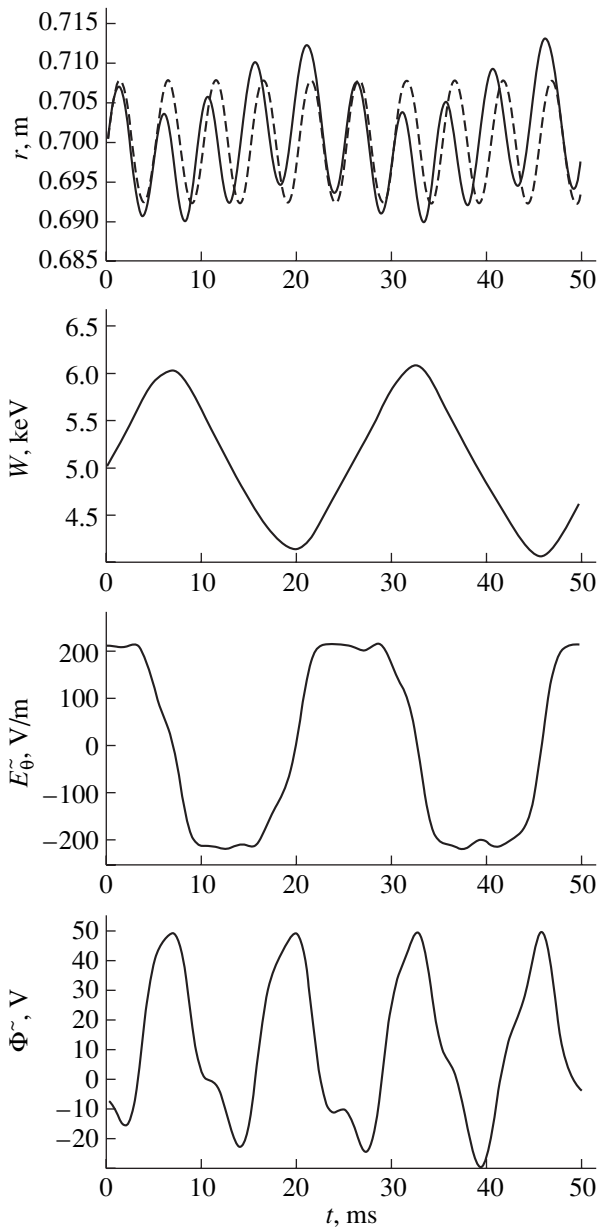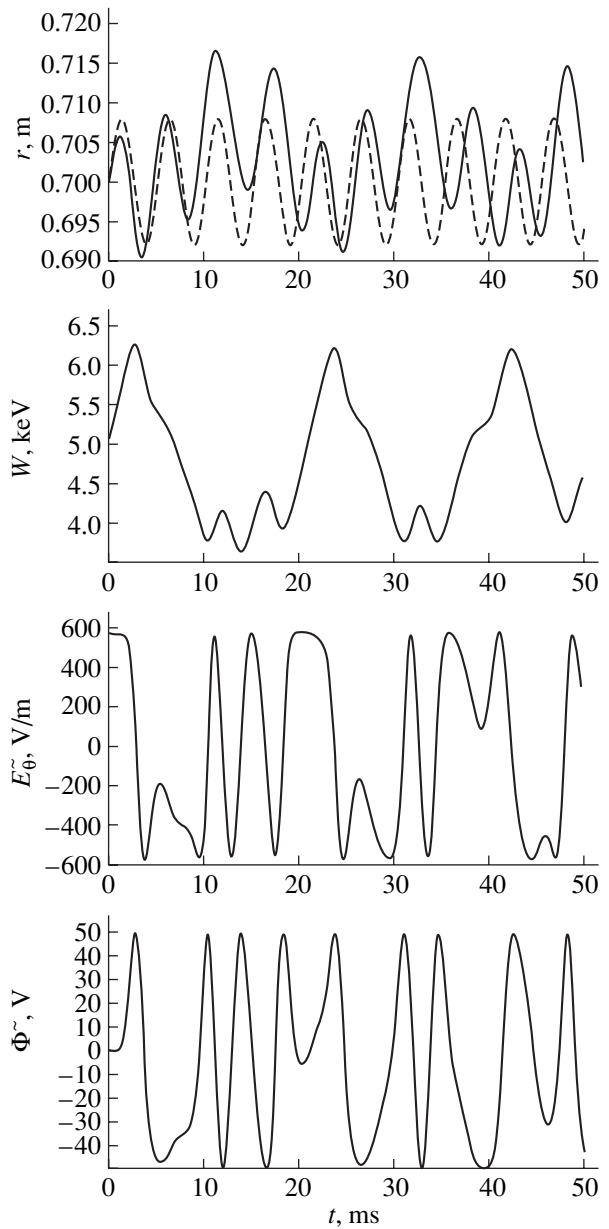
Fig. 2. Results of calculations of an ion (proton) trajectory in a tokamak magnetic field under the action of a wave field with $n_\theta = 3$ and $\omega = 3.74 \times 10^5$ rad/s for $W_{\parallel 0}/W_0 = 0.8$. The parameters W_0, Φ_0, B_0, R, a, r_0, and $q(r_0)$ are the same as in Fig. 1.

Fig. 3. Results of calculations of an ion (proton) trajectory in a tokamak magnetic field under the action of a wave field with $n_\theta = 8$ and $\omega = 9.98 \times 10^5$ rad/s for $W_{\parallel 0}/W_0 = 0.8$. The parameters W_0, Φ_0, B_0, R, a, r_0, and $q(r_0)$ are the same as in Fig. 1.

At the resonant interaction, the radial drift velocity is

$$V_r \approx \frac{n_\theta \Phi_0}{rB}, \quad (20)$$

and the duration of the resonant interaction can be determined by calculations.

Condition (16) allows one to estimate the width of the resonance:

$$\delta v_\parallel = \left| \frac{v_\parallel}{4n_\theta}\left(1 + \frac{qR\Omega_E}{v_\parallel}\right) \right|, \quad (21)$$

where the resonant value of the longitudinal velocity is

$$v_\parallel = \frac{qR(\omega - n_\theta \Omega_E)}{n_\theta}. \quad (22)$$

At $\omega \ll \omega_{ci}$ (where ω_{ci} is the ion cyclotron frequency), the resonant velocity may be on the order of the ion thermal velocity. This means that the resonant

interaction of the wave field with ions plays an important role in both the damping (or excitation) of the wave and the processes of particle transport across the magnetic field.

When the particle trajectory is affected by wave field (5), the particle remains in the resonance region if the condition

$$|\Delta v_\parallel| + \sqrt{\frac{Ze\Phi_0}{m}} \leq \delta v_\parallel \qquad (23)$$

is satisfied.

This condition is similar to that for particle trapping by a wave in the case of a nonlinear Landau damping [11]. Condition (23) allows one to estimate the maximum perturbation amplitude at which resonant interaction is possible. For example, at $v_\perp \ll v_\parallel$ and $qR\Omega_E \ll v_\parallel$, the relative amplitude is

$$\frac{Ze\Phi_0}{k_B T} < \frac{1}{8n_\theta^2}\left(\frac{v_\parallel}{v_T}\right)^2 = \frac{q^2 R^2 (\omega - n_\theta \Omega_E)^2}{8n_\theta^4 v_T^2} \ll 1, \quad (24)$$

where k_B is the Boltzmann constant and T and v_T are the temperature and thermal velocity of the particles under consideration, respectively.

At $qR\Omega_E \gg v_\parallel$, we have

$$\frac{Ze\Phi_0}{k_B T} < \frac{1}{8n_\theta^2}\left(\frac{qR\Omega_E}{v_T}\right)^2 \ll 1. \qquad (25)$$

When deriving relationships (24) and (25), it was assumed that the condition of the smallness of the perturbation amplitude defined by these expressions is satisfied at $v_\parallel \lesssim v_T$ and $qR\Omega_E \ll v_T$.

CONCLUSIONS

The effect of the above weak perturbations is appreciable only at electron–ion collisions frequencies that are not too high as compared to the perturbation frequency. Such perturbations may significantly influence diffusion if the deviation of a particle from an unperturbed trajectory is comparable to or larger than the spatial scale of neoclassic diffusion. In a collisional regime and under conditions of weak turbulence (assuming that the growth rate is $\gamma \ll \omega$ and the electron–ion collision frequency is $\nu_{ei} \lesssim \omega$), the diffusion coefficient of the resonant particles is

$$D_{col} \sim V_r^2 \nu_{ei}^{-1}. \qquad (26)$$

If there are many overlapped modes in the plasma, then collisionless diffusion may arise [12]. Under conditions of strong turbulence ($\gamma \sim \omega$), the coefficient of anomalous collisionless diffusion is

$$D_{anom} \sim V_r^2 \omega^{-1}. \qquad (27)$$

For drift waves, we have $\omega \propto k_B T_e (eB)^{-1} L^{-1} r^{-1}$, where L is the characteristic scalelength on which the density or temperature vary. This scalelength may be different for different types of drift waves [7–9]. In view of this fact, we have

$$D_{anom} \propto \left(\frac{e\Phi_0}{k_B T_e}\right)^2 \frac{k_B T_e}{eB}\frac{L}{r}. \qquad (28)$$

We note that the above model possesses a number of specific features that should be taken into account when considering the particle behavior at the plasma periphery. First, while in the plasma core, the perturbation amplitudes $e\Phi_0$ are small in comparison to the thermal energy $k_B T$ of the particles (as in the examples presented in Figs. 1–3), these amplitudes may become comparable to $k_B T$ as the perturbations propagate toward the plasma periphery, because the temperature decreases substantially from the central region to the periphery. In this case, the resonant particles may be subject to so-called ballistic transport [13]. Second, due to considerable variations in the particle energy under the action of perturbations, even a relatively small flux of the resonant particles leaving the confinement system can result in a considerable heat flux.

The results obtained in this study allows one to estimate the resonant particle flux arising under the action of weak perturbations. This, in turn, may be useful when self-consistently analyzing particle transport and the onset of instabilities in plasma.

REFERENCES

1. K. H. Burrel, Phys. Plasmas **4**, 1499 (1997).
2. M. G. Haines and P. Martin, Phys. Plasmas **3**, 4536 (1996).
3. V. I. Khvesyuk and A. Yu. Chirkov, Fusion Technol. **39**, 398 (2001).
4. V. I. Khvesyuk, A. Yu. Chirkov, and A. V. Kovalev, Fiz. Plazmy **28**, 854 (2002) [Plasma Phys. Rep. **28**, 787 (2002)].
5. V. I. Khvesyuk and A. Yu. Chirkov, Zh. Tekh. Fiz. **74** (4), 18 (2004) [Tech. Phys. **49**, 396 (2004)].
6. A. Sykes, Zh. Tekh. Fiz. **69** (9), 50 (1999) [Tech. Phys. **44**, 1047 (1999)].
7. J. D. Huba, J. F. Drake, and N. T. Gladd, Phys. Fluids **23**, 552 (1980).
8. R. D. Ferrato, H. Sanuki, R. G. Littlejohn, and B. D. Fried, Phys. Fluids **28**, 2181 (1985).
9. M. Artun and W. M. Tang, Phys. Fluids B **4**, 1102 (1992).
10. Y. Idomura, S. Tokuda, and M. Wakatani, Phys. Plasmas **6**, 4658 (1999).
11. A. S. Kingsep, *Introduction to Nonlinear Plasma Physics* (MFTI, Moscow, 1996), Chap. 3 [in Russian].
12. W. Horton, H.-B. Park, J.-M. Kwon, *et al.*, Phys. Plasmas **5**, 3910 (1998).
13. B. P. van Milligen, E. de la Luna, F. L. Tabares, *et al.*, Nucl. Fusion **42**, 787 (2002).

Translated by N. Mende

$=$ **SOLIDS** $=$

Peculiarities of the Mechanoelectrical Response in Dielectric Materials in the Region of Structural Phase Transformations

T. V. Fursa, E. P. Naĭden, K. Yu. Osipov, and R. U. Usmanov

Tomsk Polytechnical University, Tomsk, 634034 Russia

e-mail: osipov@tpu.ru

Received April 5, 2004

Abstract—The influence of thermally induced structural phase transformations on the electromagnetic response of gypsum upon impact excitation is investigated. It is found that the electromagnetic response upon impact excitation is the structure-sensitive characteristics of dielectric materials. Data on the character of phase transformations in gypsum heated above 150°C are obtained using X-ray diffraction techniques. © *2004 MAIK "Nauka/Interperiodica".*

Dielectric materials are frequently exposed to temperature fields, and, in some instances, they may undergo phase transformations, which adversely affect their technical characteristics. Therefore, there is a problem of determining structural transformations taking place in such materials. This problem can be solved using the phenomenon of mechanoelectrical response in dielectric materials [1, 2]. Previous studies showed that the mechanical characteristics and the defectness of solids determine the parameters of their electromagnetic response to impact excitation [3]. This study is concerned with the investigation of the influence of structural changes in dielectric materials on the characteristics of their electromagnetic response to impact excitation.

The study was carried out using gypsum ($CaSO_4 \cdot 2H_2O$). The structural changes in gypsum were performed by heating from room temperature to 220°C. Gypsum was selected because of its low thermal stability. It is known that the crystallization water is removed from gypsum even on heating to a temperature of about 150°C, which initiates the process of structural transformation [4]. The samples for studying the parameters of electromagnetic response to impact excitation had the form of parallelepipeds with dimensions $10 \times 5 \times 5$ cm.

The structural transformations taking place in gypsum on heating were detected by X-ray diffraction. The phase composition of the initial samples, as well as of the samples subjected to thermal treatment, was determined using a computerized X-ray diffractometer based on a commercial DRON-4M instrument using a $Fe_{K\alpha}$ source. An analysis of the X-ray diffractograms of the samples subjected to various thermal treatments (Fig. 1) showed that heating gypsum is accompanied by substantial changes in the diffraction pattern, which are indicative of structural transformations in the temperature range under consideration. A virtually complete coincidence of the experimental data obtained from the X-ray diffraction measurements of our samples before thermal treatment with the values available from JCPDS Database [5] for $CaSO_4 \cdot 2H_2O$ (see table) was evidence of a small amount of foreign impurities in gypsum used in this study.

After heating gypsum to 150°C, the intensity of reflections of the initial phase decrease and new reflections appear that are characteristic of the calcium sulfite hydrate phase $CaSO_4 \cdot 0.15H_2O$ [6]. As can be seen from the table, the diffractogram of gypsum heated to 150°C contains virtually all peaks corresponding to both $CaSO_4 \cdot 2H_2O$ and $CaSO_4 \cdot 0.15H_2O$ phases. The
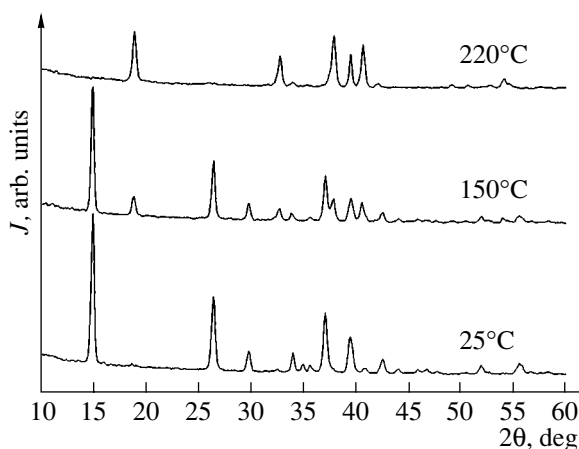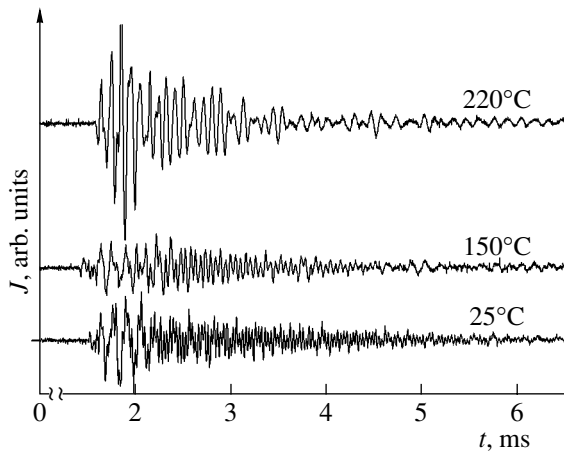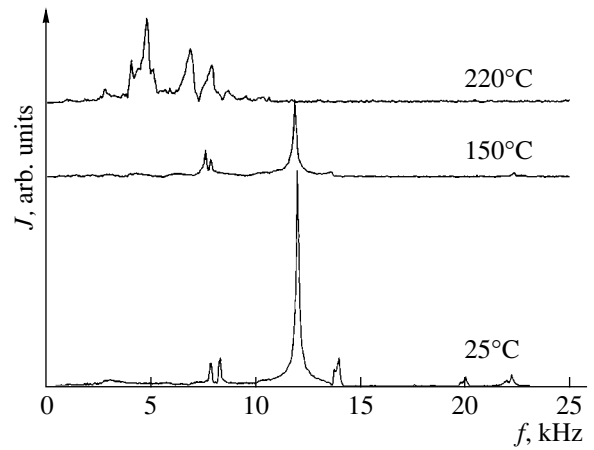

Fig. 1. X-ray diffraction patterns of gypsum at various temperatures.

Fig. 2. Electromagnetic responses registered upon impact excitation of gypsum samples subjected to different thermal treatments.

Fig. 3. Spectral characteristics of the electromagnetic responses from gypsum samples annealed at various temperatures.

intensity of reflections corresponding to the $CaSO_4 \cdot 0.15H_2O$ phase is still rather small, and the intensity of the reflections corresponding to the original gypsum phase is reduced insignificantly.

These results show that heating gypsum to 150°C induces only the initial stage of the structural phase transformations. On further heating up to 220°C, the diffraction peaks corresponding to the $CaSO_4 \cdot 2H_2O$

Comparison of experimental values of the diffraction peak intensities for gypsum samples subjected to various thermal treatments with analogous values from JCPDS Database for $CaSO_4 \cdot 2H_2O$ and $CaSO_4 \cdot 0.15H_2O$

JCPDS data				Experimental data (annealing temperature)		
$CaSO_4 \cdot 2H_2O$		$CaSO_4 \cdot 0.15H_2O$		25°C	150°C	220°C
2θ, deg	I, a.u.	2θ, deg	I, a.u.	I, a.u.	I, a.u.	I, a.u.
14.66	77			100	100	
		18.42	100		<1	97
26.15	100			46	57	
29.56	26			54	11	
		32.2	40		9	58
37.01	55			38	33	
		37.42	85		13	100
39.35	42			24	14	62
40.62	8	40.5	20		14	81
		41.68	5			7
42.3	31			8	4	

phase disappear almost completely. Thus, we have observed the thermally induced structural transformation from gypsum to the $CaSO_4 \cdot 0.15H_2O$ phase.

In order to study the mechanoelectric response in gypsum, we used the impact excitation by means of a steel ball, which was dropped from a fixed height so as to strike the middle of the sample. Using this procedure, it is possible to produce pulsed excitation with an energy on the order of 0.001 J and a duration of about 20 μs. Registration of the electric component of the electromagnetic response was performed by a capacitive sensor fixed on a side surface of the sample. The high-frequency electric signal from the sensor was monitored by a PC-Scope PSC-500 oscilloscope linked to a computer.

As gypsum samples were heated from room temperature to 220°C, the characteristics of the electromagnetic response exhibited a change. Figure 2 shows typical electromagnetic responses from the gypsum samples subjected to various thermal treatments, while Fig. 3 shows the spectral characteristics of these signals. It is clear from these figures that the thermal treatment of gypsum results in variations of the amplitude of the electromagnetic response, as well as in substantial modification of its spectral characteristics.

In our opinion, the electromagnetic response from dielectric materials upon impact excitation is due to a change of the dipole moments of the double electrical layers at the boundaries of inhomogeneities [2]. Transformation of the material structure causes a change in the state of these double electrical layers. Moreover, the structural transformations result in a change in the characteristics of the acoustic waves generated in the material upon impact excitation. Changes in the electromagnetic response parameters are probably caused by these two processes.

In order to evaluate the contribution from each of the above-mentioned processes, we performed the mea-
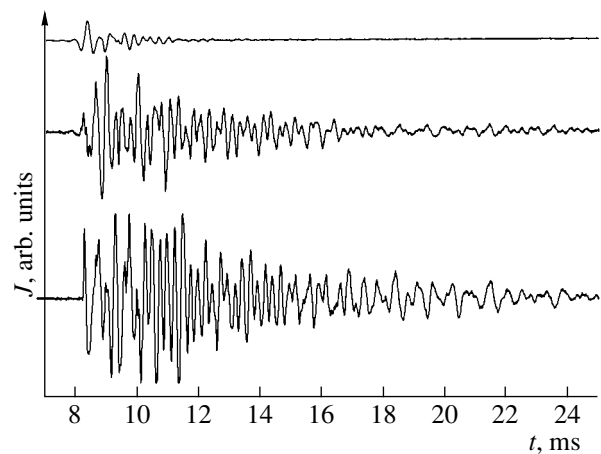
surements of the acoustic emission signals simultaneously with the measurements of the electromagnetic response (Fig. 4). It is seen from this figure that the thermal treatment of gypsum samples causes a successive decrease in the amplitude of acoustic signals. In this case, the amplitude changes by a factor of 1.5 on heating to 150°C, whereas further heating to 220°C reduces the amplitude approximately by a factor of three. Such a considerable decrease in the acoustic signal amplitude is a consequence of an increase in the porosity of gypsum after thermal treatment, The increase in porosity is confirmed by a decrease in the density of gypsum from 1260 to 1210 kg/m³ at 150°C and to 1100 kg/m³ at 220°C.

In contrast, the amplitude of the electromagnetic response remains virtually unchanged when gypsum is heated from 25 to 150°C and increases by a factor of two after further heating to 220°C. This circumstance may be the result of variation of the parameters of double electrical layers at the boundaries of inhomogeneities related to the formation of a new phase. In addition, the electromagnetic response can be related to the acousticwave-induced static charge related to the curvature of the pore surfaces [7]. Therefore, an increase in the response amplitude must be observed together with an increase in the porosity of gypsum upon heat treatment, which is indicated by a decrease in the density of samples. Thus, the observed increase in the amplitude of the electromagnetic response upon annealing is most likely caused by the total effect of variation of the double electrical layer characteristics and the porosity of gypsum.

The study of mechanical characteristics showed a considerable change in the mechanical compressive strength of gypsum (from 9 to 1.7 MPa) upon heating from room temperature to 220°C, which was also indicative of the heating-induced structural transformations in this material. It is known that, on heating to a temperature above 270°C, gypsum loses virtually all crystallization water and transforms into the so-called calcined gypsum or alabaster [4]. Apparently, the considerable reduction of the mechanical compressive strength is also related to structural changes and the loss of water observed on heating the samples to 220°C.

In the course of heat treatment of the gypsum samples, the main spectral maxima of the electromagnetic responses not only changed in intensity, but also shifted toward lower frequencies (Fig. 3). The shift in the frequency of the main spectral peaks can be related to a change in the velocity of sound in gypsum upon heating. The velocity of the longitudinal acoustic waves in the samples was measured using a pulsed ultrasonic technique. According to this, a single electric pulse with abrupt leading edge was supplied from a generator to a piezotransducer. The transducer converts this pulse into an elastic wave, which enters through the acoustic contact into gypsum and propagates from one sample end to another. On the opposite end of the sample, a

Fig. 4. Typical acoustic emission signals emerging upon impact excitation of gypsum samples subjected to various thermal treatments.

piezoelectric sensor receives the elastic wave via the acoustical contact and converts it to the output electric signal. The velocity of the ultrasonic wave propagation is determined using the known sample length and the measured delay time between the sync pulse arriving simultaneously with the voltage supplied to the piezotransducer and the pulse registered by the piezoelectric sensor. The delay time was measured using a dual-trace oscilloscope (PC-Scope PSC-500).

Heating a gypsum sample from 25 to 150°C results in reduction of the sound velocity from 2.4×10^3 to 2.3×10^3 m/s, and, after subsequent heating to 220°C, the sound velocity becomes equal to 1.5×10^3 m/s. Figure 3 shows a very small displacement of the main maximum of the spectral characteristic of the electromagnetic response in a sample heated to 150°C. In the sample annealed at 220°C, the response signal with a much lower frequency is observed, in accordance with a considerably (almost twofold) lower velocity of sound in these samples as compared to the initial gypsum sample. Moreover, it should be noted that the spectrum of the electromagnetic signal from the samples annealed at 220°C has virtually no signal components in common with the spectrum of the initial sample.

The extent of variation of the electromagnetic response characteristics in thermally treated gypsum was evaluated using correlation analysis. It is found that the coefficient of mutual correlation of the electromagnetic responses of the initial gypsum and the sample annealed at 150°C is 0.67, while, for the sample heated to 220°C, this coefficient decreases to 0.1.

The results of our study showed that the presence of structural phase transformations in gypsum subjected to various thermal treatment can be monitored by measuring the parameters of the electromagnetic response upon impact excitation of a sample. The proposed

approach can be used for determining the extent of structural transformations in various materials.

REFERENCES

1. V. L. Chakhlov, Yu. P. Malyshkov, V. F. Gordeev, *et al.*, Izv. Vyssh. Uchebn. Zaved., Stroit., No. 5–6, 54 (1995).

2. T. V. Fursa, N. N. Khorsov, and E. A. Baturin, Zh. Tekh. Fiz. **69** (10), 51 (1999) [Tech. Phys. **44**, 1175 (1999)].

3. T. V. Fursa and N. N. Khorsov, Defektoskopiya, No. 2, 68 (2000).

4. N. L. Glinka, *General Chemistry* (Khimiya, Leningrad, 1985).

5. D. K. Smith, International Center for Diffraction Data (ICDD) Grant-in-Aid (Department of Geosciences, Penn. State Univ., University Park, 1985).

6. N. Bushuev and N. Dorisov, Russ. J. Inorg. Chem., No. 27, 341 (1982).

7. I. M. Lifshits, Ya. B. Geguzin, and A. M. Kosevich, *Physics of Real Crystals and Disordered Systems: Collection of Selected Works* (Nauka, Moscow, 1987) [in Russian].

Translated by M. Lebedev

<div align="center">

OPTICS,
QUANTUM ELECTRONICS

</div>

Optical Filter with Controlled Transfer Function on the Basis of Dynamic Volume Holograms in Barium Titanate

V. M. Petrov*, S. Lichtenberg**, and A. Chamrai*

* Ioffe Physicotechnical Institute, Russian Academy of Sciences,
Politekhnicheskaya ul. 26, St. Petersburg, 194021 Russia

** Institute of Applied Physics, Darmstadt University of Technology,
Hochschulstrasse 6, Darmstadt, 64293 Germany

e-mail: achamrai@mail.ioffe.ru
Received March 11, 2003

Abstract—The feasibility of optical control over the spectral characteristics of an optical filter based on 3D holographic grating recorded in a photorefractive crystal is considered. It is shown experimentally that the transfer function can be configured in real time by introducing phase shifts between the hologram sections. © 2004 MAIK "Nauka/Interperiodica".

Controllable (tunable) optical filters are the key elements of modern optical systems. The most promising application fields include high-speed telecommunication lines based on the wavelength division multiplexing (WDM) principle, tunable lasers, and optical sensor systems [1, 2].

In view of the high spectral selectivity of 3D holographic gratings in reflection geometry [3, 4], they can be used as optical filters. Of special interest are the 3D reflection holographic gratings recorded in photorefractive crystals, since such crystals possess some physical properties (electrooptical and piezoelectric effects, reversible holographic recording) that make it possible to control the characteristics of gratings. In this context, an important point is the development of new methods of control over the spectral transfer function of such filters.

The transfer function (TF) of a reflective holographic grating is described by the well-known Kogelnik formula [3]. Conventionally, the spectral characteristic is defined by the spatial distribution of the grating amplitude, which is recorded in crystal as described, for example, in [5, 6]. It was demonstrated [7] that the presence of the electrooptical effect enables one to shift the TF, that is, to change the selected wavelength, by applying an external electric field. Recently, we have developed and experimentally demonstrated a new technique making use of the electrooptical effect in a nonuniform electric field, which provides control not only over the spectral position of the grating TF but also over its shape [8]. However, the latter possibility is limited by the comparatively low electrooptical coefficients of materials available nowadays.

The holographic gratings recorded in photorefractive crystals with short Maxwell relaxation time (for example, in barium titanate doped with cobalt,

BaTiO$_3$:Co, this time ranges from 0.1 to 0.3 s) admit rapid rerecording and make possible operative optical control over the TF. Such holographic gratings are called dynamic because their maintenance requires continuous exposure of the crystal to the interference pattern.

It is known that the shape of the TF of a holographic grating significantly depends on the phase ratios in the grating profile. For example, the TF shape can be transformed from a stop- (reflection) to a pass-band (transmission) mode by introducing a phase discontinuity of π in the middle of the grating. In the case of BaTiO$_3$:Co, such a transformation of the TF occurs within the time of recording a new hologram [9]. It was shown [10] that the filter TF can be effectively modified by creating phase shifts in the dynamic holographic grating profile.

This paper presents the results of theoretical and experimental investigation of an optical method providing for real-time flexible control of the TF shape by introducing a number of controllable phase shifts into the dynamic holographic grating.

THEORETICAL BACKGROUND

In the case of low diffraction efficiency, the TF shape of a reflection holographic grating comprised of sections with various phase shifts can be found via the Fourier transform of the phase profile of the grating [9]. The amplitude transfer function $D(\lambda)$ of a reflection hologram is defined as

$$D(\lambda) = \frac{A_{out}}{A_{in}}, \tag{1}$$

where A_{in}, A_{out} are the complex amplitudes of the input (incident) and the output (diffracted) light, respectively.
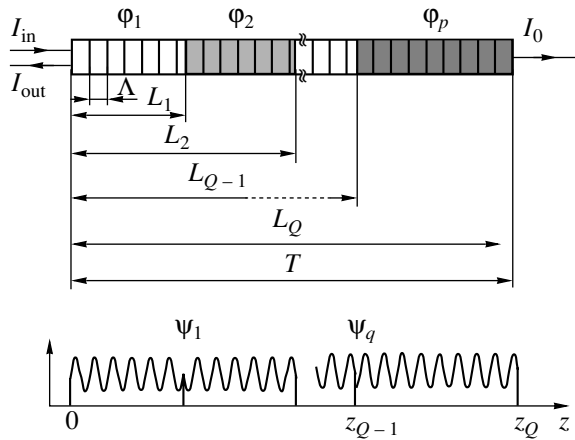
Fig. 1. The reflective hologram of the length T consisting of Q sections with equal grating period Λ: ψ_q is the phase discontinuity at the boundary between sections; I_{in}, I_{out}, and I_0 are the incident (readout), the output (diffracted), and the transmitted (zero diffraction order) light beam intensities, respectively.

In the case of low diffraction efficiency, the transfer function $D(\lambda)$ of a reflection holographic grating relates to the refractive index $n(z)$ via the Fourier transform:

$$D(\lambda) \sim \begin{cases} -iF[n(z)] \\ \lambda = \dfrac{4\pi}{K}n_0. \end{cases} \qquad (2)$$

Here, $F[n(z)]$ denotes the Fourier transform and the spectrum of the grating wavevectors K is set as a parametric function of the readout light wavelength λ. For a hologram with the length T comprised of Q phase-shifted sections (Fig. 1), we have

$$n(z) = n_0 + \Delta n \sum_{p=1}^{Q} \cos\left(\frac{2\pi}{\lambda}z_p + \varphi_p\right), \qquad (3)$$

where

$$\varphi_p = \sum_{q=1}^{p} \psi_q, \qquad (4)$$

$$L_{p-1} < z_p \le L_p. \qquad (5)$$

Here, L_p is the grating length between $z = 0$ and the end of the pth section (i.e., $L_0 = 0$, $L_Q = T$); ψ is the phase jump at the boundary between two neighboring sections; n_0 is the mean refractive index of the crystal; and Δn is the amplitude of the refractive index grating. The summation by index q means the summation with respect to all preceding sections.

Figure 2 presents examples of holograms consisting of five sections with equal lengths: their phase profiles (first column), the numerically calculated power TFs

$|D(\lambda)|^2$ (second column), and the experimental results (third column). It is seen from Fig. 2 that a change in the phase relations between particular sections of the grating has a strong influence on the TF shape.

EXPERIMENTAL SETUP AND RESULTS

Figure 3 shows the geometry of recording the dynamic holographic grating. The hologram is recorded in the symmetric transmission geometry using the write light wavelength λ_w and is read out in the reflection geometry at the wavelength λ_r. In order to meet the Bragg condition required for readout in the reflection mode, the recoded hologram period must satisfy the condition

$$\Lambda = \frac{\lambda_w}{2\sin\theta} = \frac{\lambda_r}{2n_0}, \qquad (6)$$

where n_0 is the refractive index of the crystal and θ is the angle of incidence of the recording beam.

The experimental setup realizing the optical filter with controlled spectral TF is presented in Fig. 4. The hologram is continuously recorded by the second harmonic of cw Nd–YAG laser (*1*), $\lambda_w = 532$ nm. A plane wave is formed with the help of a spatial filter consisting of collimator and point diaphragm (*2*). The BaTiO$_3$:Co crystal is illuminated by two beams coming out of the beam-splitting cube. The crystal has a size of $3 \times 3 \times 10$ mm; its optical axis C and the wavevector of the recorded hologram are parallel to its long side. The Co dopant concentration is 0.05 wt %. The input beam I_{in} of tunable laser (*6*) covering the range from 1456 to 1583 nm is used for readout in the reflection mode. For the readout beam to meet the Bragg condition in the range from 1550 to 1570 nm, the angle of incidence θ of the recording beams, calculated by formula (6), ranges between 49° and 51°. The diffracted output beam I_{out} enters IR detector (*11*).

Phase jumps between the adjacent sections of grating were produced by means of liquid-crystal (LC) phase modulator (*12*) consisting of five independently controlled cells, which was introduced into the cross section of one of the recording beams. All five cells (*13*) have equal length, which provides for obtaining a hologram with five sections of equal length.

We measured the diffraction efficiency of the hologram, that is, the quantity $|D(\lambda)|^2$, as a function of the readout wavelength at various phase shifts between sections. Both the angle between the recording beams and their intensity remained constant.

The first column in Fig. 2 depicts grating sections with the phase ratios used in the experiment. These phase ratios were selected by computer simulation so as to obtain most practically interesting TF shapes. For each of the phase distributions considered, we present the spectra of $|D(\lambda)|^2$ resulting from numerical calcula-
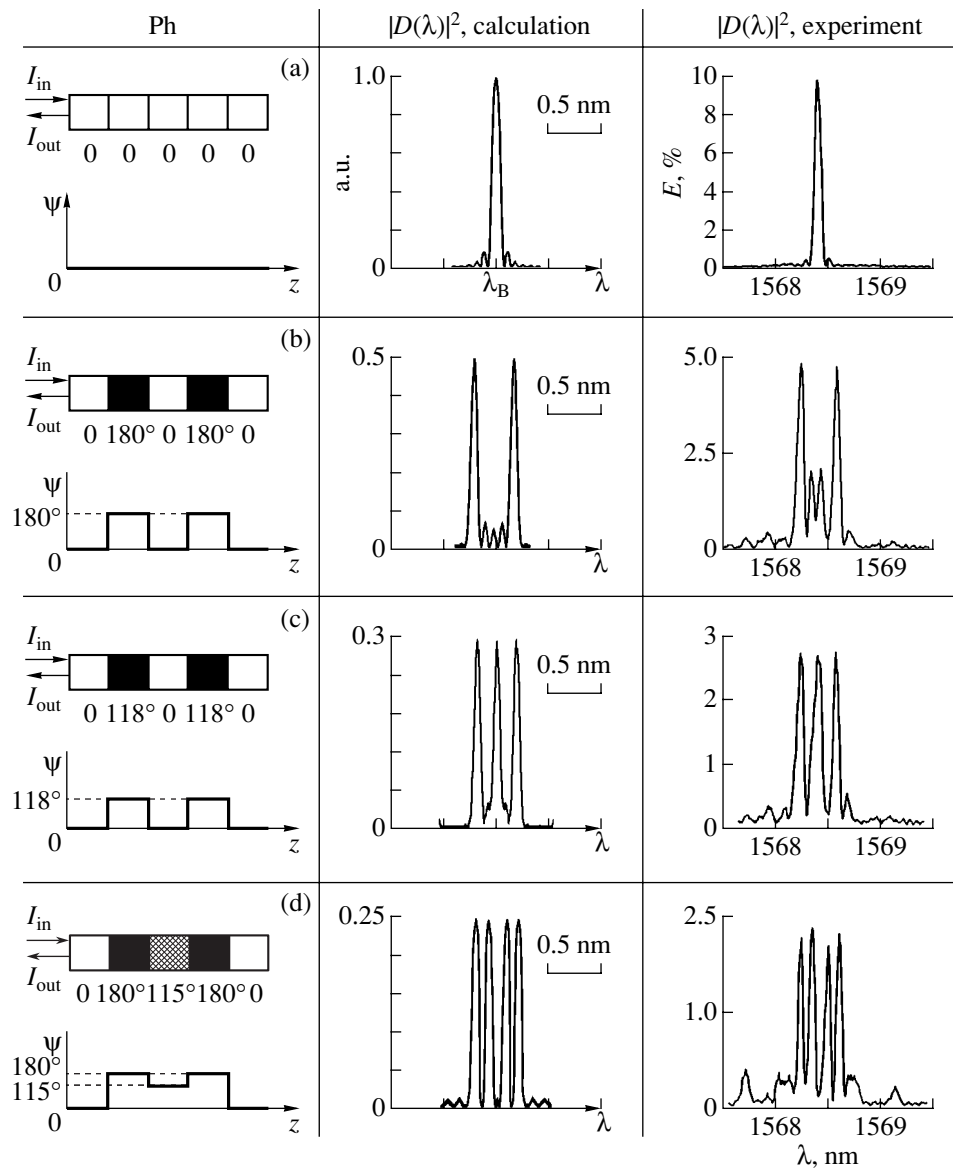
Fig. 2. Examples of phase-shift TF control showing (first column) the phase distribution Ph over the hologram sections, (second column) numerical calculation of $|D(\lambda)|^2$, and (third column) experimental results: (a) a simple (without phase shifts) reflective hologram; (b, c) reflection holograms with the phase shifts in the second and fourth sections $\psi_2 = \psi_4 = 180°$ and $118°$, respectively; (d) reflection hologram with the phase shifts in the second and fourth sections $\psi_2 = \psi_4 = 180°$ and in the third section $\psi_3 = -65°$. I_{in} and I_{out} are the input (readout) and the output (diffracted) beams, respectively; E is the diffraction efficiency.

tion and from the experimental data (the second and the third columns, respectively).

In the first case (Fig. 2a), all five cells of the LC modulator are in phase and no phase shift is introduced between sections, $\varphi = 0$. The resulting TF corresponds to that of a simple 3D holographic grating (without phase shifts) and has a single peak. The readout light wavelength at which the diffraction efficiency reaches maximum is determined by the Bragg conditions ($\lambda_r \approx$ 1568.442 nm). In our case, the diffraction efficiency reached 10% and the spectral selectivity was $\delta\lambda \approx$ 53 pm (by spectral selectivity, we mean the deviation of

the readout light wavelength from Bragg conditions (6), which yields the first minimum of the diffraction efficiency).

In the second case (Fig. 2b), we consider a hologram with phase shifts $\varphi = 180°$ in the second and fourth sections. The corresponding TF has two peaks, which are positioned symmetrically relative to the central wavelength λ_r. The diffraction efficiency of each peak is approximately 4.8%. The peaks are spaced by about 0.47 nm, which is in good agreement with the numerical results. The sidelobes observed between the main peaks are higher than predicted by the theory. In addi-
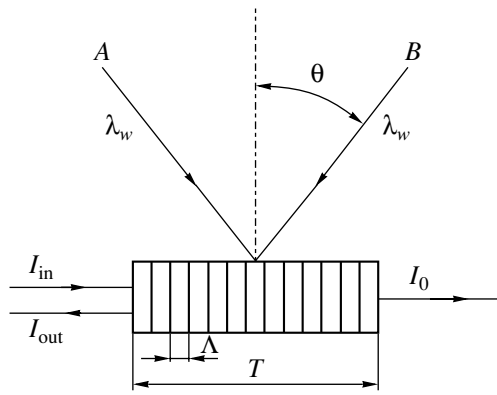
Fig. 3. The geometry of hologram recording: *A* and *B* are the recording beams; $\lambda_w = 532$ nm; I_{in} and I_{out} are the intensities of the input (readout) and the output (diffracted) beams, respectively; I_0 is the intensity of the zero-order diffraction; *T* and Λ are the length and the period of the holographic grating.
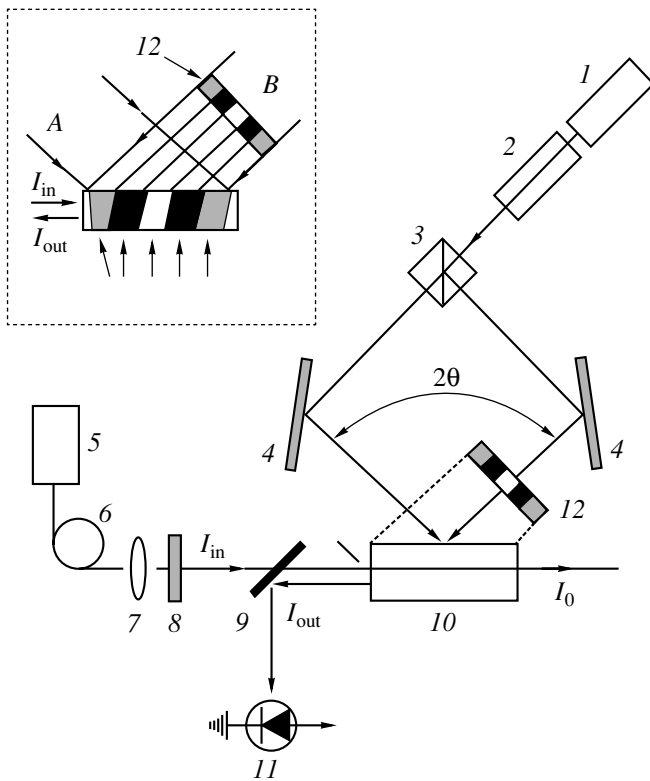
Fig. 4. Experimental setup: (*1*) Nd–YAG laser with $\lambda_w = 532$ nm; (*2*) beam-forming system (microlens, point diaphragm, collimating lens); (*3*) beamsplitter; (*4*) mirrors; (*5*) tunable readout laser (1456–1583 nm); (*6*) single-mode optical fiber; (*7*) collimating IR lens; (*8*) IR polarizer; (*9*) IR beamsplitter; (*10*) BaTiO$_3$:Co crystal; (*11*) IR photodetector; (*12*) LC phase modulator consisting of five independently controlled cells. The inset shows the formation of phase-shifted sections in the hologram. Arrows point to five sections with different phase shifts.

tional experiments, we showed that this discrepancy is caused by low optical quality of the LC modulator, which itself introduces a parasitic phase modulation into the phase distribution of the hologram.

In the third case (Fig. 2c), the phase shifts in the second and fourth section are $\varphi = 118°$. In this case, the TF has three peaks. The position of the central peak coincides with that of the single peak in the case of a simple grating (Fig. 2a). The diffraction efficiency of each peak is approximately 2.7%.

In the fourth case (Fig. 2d), we introduce the phase shift $\varphi = 180°$ in the second and fourth sections and $\varphi = 115°$ in the third section of the grating. The corresponding TF displays four symmetric peaks with a diffraction efficiency of about 2.3% each.

Note that, in any case (Figs. 2a–2d), the spectral selectivity of each peak was almost the same ($\delta\lambda \approx 52$ pm), which is typical of the low diffraction efficiency approximation.

DISCUSSION

Both the experimental data and the results of numerical calculations presented above suggest that the transfer function of an optical filter can be controlled by introducing certain phase shifts into the holographic grating.

For the first time, the real-time control of the TF shape is realized on the basis of a dynamic grating with five controlled-phase-shift sections. In particular, the transfer functions with two, three, and four transmission bands are obtained in real time.

It is important to note that each new pass-band resulting from the TF transformation of this type has the same width because, in the case of low diffraction efficiency, the repeated reflection from each section is negligible and the peak width is defined as the interval at which the phase of light reflected from a full-length grating shifts totally by π.

This study was carried out under conditions of low-amplitude grating; that is, we disregarded the effects related to repeated reflections and the diffraction loss of the readout signal amplitude inside the grating. Such a condition was imposed exclusively with the aim of making possible the use of the Fourier transform method for the TF shape calculations. This approach holds much promise, since it allows one to solve also the inverse problem, that is, to find the appropriate phase profile for a given spectral TF shape and, thus, to synthesize a filter with the desired spectral characteristics.

Additional experiments showed that the method proposed for the TF shape control also works well in the case of gratings with high amplitudes; however, determining the TF shape with high accuracy in this case requires using other, more complicated calculation techniques instead of the Fourier transform.

Another advantageous feature of the proposed method is that it may potentially incorporate fast variation of the wavelength λ_r by changing the refractive index of the crystal under the action of an external electric field [4].

CONCLUSIONS

It is shown that the shape of the transfer function of an optical filter based on a dynamic holographic grating can be controlled in real time by introducing phase discontinuities into the profile of grating (phase-shift keying). For the first time, the transfer functions of a filter with two, three, and four transmission bands are configured in the real-time regime. In our experiments, the TF transformation time ranged from 0.1 to 0.3 s and depended on the properties of the crystal. Such filters hold much promise for switching between spectral channels in the optical telecommunication systems incorporating the WDM principle.

REFERENCES

1. Y. P. Li and C. H. Henry, in *Handbook of Optical Fiber Telecommunications (Optical Fiber Telecommunications III)*, Ed. by I. P. Kaminow (Academic, 1997).

2. C. K. Madsen and J. H. Zhao, *Optical Filter Design and Analysis: A Signal Processing Approach* (Wiley, New York, 1999).

3. R. J. Collier, C. B. Burckhardt, and L. H. Lin, *Optical Holography* (Academic, New York, 1971; Mir, Moscow, 1973).

4. V. M. Petrov, S. Lichtenberg, J. Petter, *et al.*, J. Opt. A **5**, 471 (2003).

5. A. K. Zajtsev, S. H. Lin, and K. Y. Hsu, Opt. Commun. **190**, 103 (2001).

6. S. Breer, H. Vogt, I. Nee, and K. Buse, Electron. Lett. **34**, 2419 (1998).

7. V. M. Petrov, S. Lichtenberg, J. Petter, *et al.*, OSA Trends Opt. Photonics Ser. **87**, 582 (2003).

8. M. P. Petrov, A. V. Chamrai, A. S. Kozlov, and I. V. Il'ichev, Pis'ma Zh. Tekh. Fiz. **30**, 75 (2004) [Tech. Phys. Lett. **30**, 120 (2004)].

9. V. M. Petrov, S. Lichtenberg, J. Petter, *et al.*, OSA Trends Opt. Photonics Ser. **87**, 564 (2003).

10. V. M. Petrov, S. Lichtenberg, J. Petter, and T. Tschudi, Opt. Commun. **229**, 131 (2004).

Translated by A. Sidorova

OPTICS,
QUANTUM ELECTRONICS

Interaction of Molecular Hydrogen with the Doped Silica Core of an Optical Fiber at Elevated Temperatures

A. V. Lanin, K. M. Golant, and I. V. Nikolin

Fiber Optics Research Center, Prokhorov General Physics Institute, Russian Academy of Sciences,
ul. Vavilova 38, Moscow, 119991 Russia
e-mail: lanin@fo.gpi.ru
Received December 30, 2003; in final form, May 13, 2004

Abstract—Optical fibers with cores made of germanosilicate, phosphosilicate, and nitrosilicate glasses are loaded by molecular hydrogen at a pressure of 10 MPa and room temperature. Then, preloaded fibers are kept in a hydrogen atmosphere at the same pressure and various fixed temperatures up to 700°C and the transmission spectra of the fibers are measured *in situ* at a constant temperature with equal time intervals. The kinetics of the chemical interaction between hydrogen and the silica is determined by analyzing an increase in the optical absorption at the overtones of OH and NH groups. © *2004 MAIK "Nauka/Interperiodica".*

INTRODUCTION

The interaction of hydrogen with optical fibers is of interest mainly due to the experimental data on the effect of hydrogen on the practically important properties of optical fibers, such as the optical loss increase spectrum, radiation-induced losses, and photosensitivity.

It is well known that glasses are permeable to gases, especially to hydrogen and helium [1]. Hydrogen dissolved in a glass "heals" radiation-induced color centers—point defects induced in the glass by ionizing radiation—and, thus, decreases additional optical losses [2].

Saturation of the optical fibers with molecular hydrogen is used in the technology of in-fiber Bragg gratings [3]. An increase in the photosensitivity of a fiber upon saturation with molecular hydrogen is a key factor, for example, in fabricating fiber lasers and amplifiers based on the effect of stimulated Raman scattering in phosphosilicate optical fibers [4, 5]. Hydrogen saturation increases the photosensitivity of phosphosilicate fibers to a level sufficient for writing the Bragg gratings using 193-nm radiation of an ArF excimer laser [6].

At the same time, the hydrogen molecules present in silica cause additional resonance light absorption with a complex spectrum [7]. At elevated temperatures, hydrogen interacts with the oxygen atoms of the glass network and is incorporated into this structure in the form of hydroxyl groups. The overtone of the optical resonance absorption of OH groups at a wavelength of 1.38 µm falls within a spectral range that is important for telecommunication applications; therefore, an increase in the concentration of these groups deteriorates the properties of communication lines.

Previously [8, 9], it was demonstrated that, at temperatures below 500°C, molecular hydrogen diffuses into fused silica via interstices without significant chemical interaction with the glass network. However, the problem of determining the effect of temperature on the chemical interaction of hydrogen with fiber cores doped to different levels with various impurities is still a challenge. Solving this problem would allow one to determine the optimum temperatures for the saturation of optical fibers with molecular hydrogen to a level not involving noticeable chemical interaction. Such data would make it possible to optimize the process of saturation, since an increase in the temperature substantially decreases the time required for the complete saturation of materials with a gas. For example, at temperatures below 100°C, it takes about 20 h to reach the maximum hydrogen concentration (in equilibrium with the ambient gas atmosphere) in a standard optical fiber. An increase in the temperature to 300°C shortens this time to a few hours, and, at 500°C, this process takes only a few minutes.

EXPERIMENTAL

To date, most experiments devoted to the saturation of optical fibers with molecular hydrogen were performed without controlling the dynamics of gas penetration into a glass network. As a rule, fiber samples were placed in a hermetically sealed vessel filled with gas at a certain pressure and kept there at a preset temperature for a certain time. Then, the samples were extracted from the vessel for optical measurements. This technique cannot provide monitoring of the optical properties of a sample and, hence, the hydrogenation dynamics *in situ* during hydrogen saturation.

A key point in our experiments is the design and use of a special chamber for the saturation of optical fibers with molecular hydrogen. With this chamber, we can monitor the dynamics of hydrogen penetration and interaction with glass atoms at room and elevated temperatures using optical spectroscopy. Monitoring of the intensities of absorption peaks characteristic of the molecules dissolved in the glass and the atomic groups formed as a result of reactions at elevated temperatures makes it possible to analyze the dynamics of changes in the concentrations of these species.

The setup created for the saturation of optical fibers with molecular hydrogen consists of a high-pressure vessel in the form of a reactor tube connected with two stainless steel buffer tanks (Fig. 1). Loops of the optical fiber to be studied are placed in the reactor, and its ends are led out through seals in the flanges. The ends can be connected to outside spectrometric equipment. The total length of the optical fiber accommodated in the vessel is 10 m. The reactor is equipped with an external heater, which allows the dynamics of changes in the optical spectra to be traced at a reactor temperature of up to 700°C. The setup design provides local heating of the fiber virtually without increasing pressure in the vessel over the whole working temperature range.

Each fiber sample was studied in two stages. In the first stage, a sample was hydrogen-saturated at room temperature. The saturation degree was estimated from the time dynamics of the absorption peak at 1.24 μm, which corresponds to the first vibrational overtone of a hydrogen molecule [7].

In the second stage, optical fibers saturated with dissolved molecular hydrogen were held at various temperatures above room temperature. During heating, the fibers were in a hydrogen atmosphere at a nearly constant pressure. In this stage, we paid particular attention to the absorption band near 1.4 μm, which is associated with a combination of the bands of Si–OH (at 1.385 μm) [7, 10, 11], Ge–OH (1.41 μm) [10, 11], and H_2O (1.42 μm) [11], and to the band of Si–NH (1.505 μm), which is manifested in optical fibers with a core made of nitrogen-doped silica [12].

The optical absorption spectra were recorded on an automated computer-assisted setup (Fig. 2). The light of a halogen lamp is filtered, diaphragmed, and focused by a silica lens through a chopper on the entrance slit of a monochromator. The image of the exit slit is focused by a lens on the edge face of a fiber that is placed in the vessel to be saturated by molecular hydrogen (Fig. 1). The intensity of the light passed through the system is measured in the lock-in mode with a GaAs-based photodiode; the output signal from this photodiode is fed to the input of a lock-in amplifier. A computer adjusts the monochromator to the required wavelength and periodically reads information from the lock-in amplifier and accumulates it in a data file. The dynamic range of the apparatus is ≈20 dB. The available spectral range is
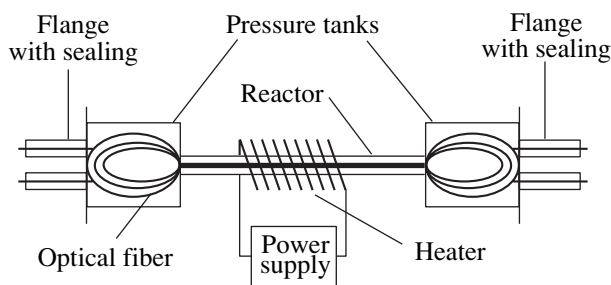
Fig. 1. Schematic diagram of the experimental setup for saturating optical fibers with molecular hydrogen and monitoring the optical transmission spectra.
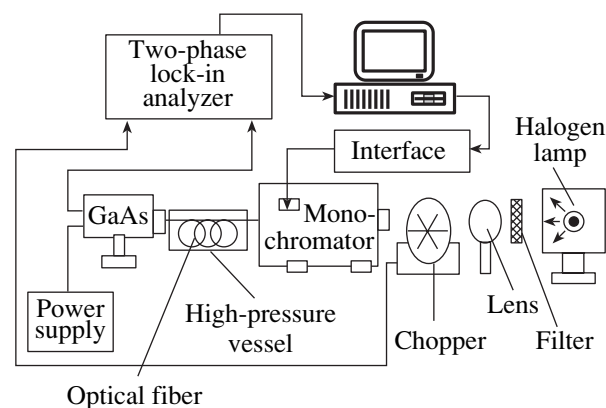
Fig. 2. Schematic diagram of the automated experimental setup for recording the optical absorption spectra of hydrogenated fibers.

190–1700 nm. In this study, we recorded the absorption spectra of optical fibers in the range 1000–1600 nm.

The main parameters of the fibers under study are given in Table 1. Sample 1 is a standard SMF-28 optical fiber (Corning) with the core of germanosilicate glass. Sample 2 is an MCVD-produced germanosilicate optical fiber containing about 26 mol % GeO_2 in the core. Sample 3 is an MCVD-produced optical fiber with a core made of phosphorus-doped silica. Sample 4 is an optical fiber with a core made of nitrogen-doped silica, which was fabricated by reduced-pressure plasma-chemical vapor deposition [12].

RESULTS AND DISCUSSION

As a result of saturation of the optical fibers with molecular hydrogen, the optical absorption in the near infrared (NIR) region increases (Fig. 3). The total optical losses also increase, and well-resolved absorption bands corresponding to various H_2 vibrational states appear. According to [13], the absorption of 3.4 dB/km at a wavelength of 1.24 μm corresponds to a molecular hydrogen concentration of 10^{18} cm^{-3} in the glass network. Thus, the molecular hydrogen concentrations in samples 1–4 saturated at room temperature can be esti-
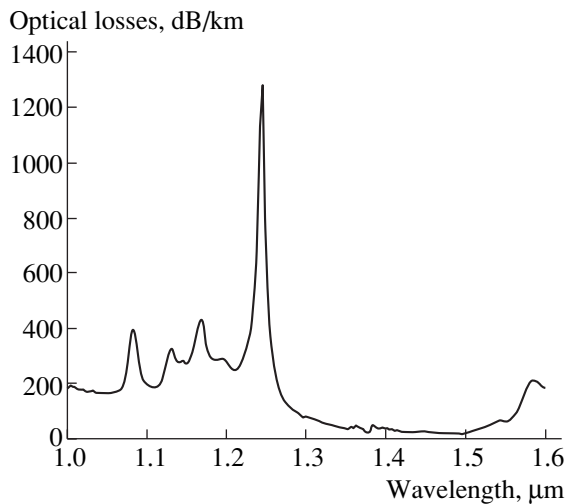
Table 1. Parameters of optical fibers

Sample no.	Core material/diameter	Cladding material/diameter	Type	Difference between core and cladding indices of refraction
1	Ge : SiO_2/8.5 μm	SiO_2/125 μm	Single-mode	0.0055
2	Ge : SiO_2/19.2 μm	SiO_2/125 μm	Multimode	0.035
3	P : SiO_2/19.5 μm	SiO_2/125 μm	Multimode	0.01
4	N : SiO_2/10 μm	SiO_2/125 μm	Multimode	0.042

mated as 3.78×10^{20}, 4.29×10^{20}, 2.64×10^{20}, and 1.7×10^{20} cm^{-3}, respectively.

Note that, in this stage, the samples do not exhibit an increase in the optical absorption by hydroxy groups, since molecular hydrogen does not interact with the glass network at room temperature. However, the absorption related to molecular hydrogen dissolved in the glass increases. This means that the diffusion rate of H_2 at about 20°C significantly exceeds the rate of formation of hydroxy groups due to chemical interaction. Thus, before annealing, the H_2–SiO_2 system is in thermodynamic equilibrium; that is, the fibers are saturated with molecular hydrogen. The measurements show that, upon subsequent heating, the molecular hydrogen concentration in the glass network remains the same to an accuracy of 2%.

Active hydrogen incorporation into the glass with the formation of hydroxyl and NH groups becomes significant when the samples are heated to various temperatures above room temperature. The temperatures of the onset of the chemical interaction are found to be 300°C for sample 1, 200°C for sample 2, and 400°C for samples 3 and 4.
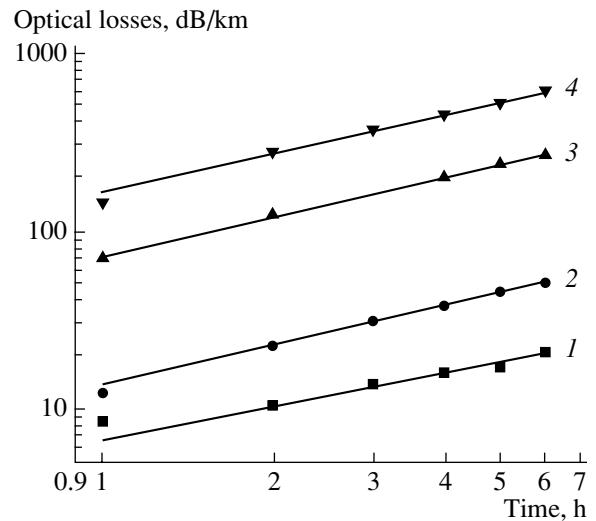
The induced absorption spectra were resolved into bands corresponding to various hydroxyl and HN groups by means of the ORIGIN software package. Thus, we determined the contribution of each band to the induced absorption and followed the band dynamics.

Figure 4 shows the experimental time variation of the absorption band intensities for hydrogen-saturated fiber 4 heated to various temperatures. The other fibers exhibit analogous dynamics of increase in the optical losses. The solid lines show the absorption by the hydrogen bound to the silica network, according to the approximation of the chemical reaction rate [14]

$$\Delta\alpha = k(T, p)t^x,$$

where $\Delta\alpha$ is the increase in the optical losses, dB/km; $k(T, p)$ is the proportionality constant (which is a function of the absolute temperature T and the molecular hydrogen partial pressure p); t is the annealing time, h; and x is a constant that depends on the type of the optical fiber and can be determined from the approximation in Figs. 4–7.

The values of x for optical fibers 1–4 are given in Table 2.

Optical losses, dB/km

Fig. 3. Optical absorption spectrum of sample 1 saturated by molecular hydrogen at room temperature. The absorption lines of H_2 dissolved in silica (1.24, 1.59, 1.54, 1.197, 1.168, 1.146, 1.132, and 1.083 μm) are characteristic of samples of all types.

Optical losses, dB/km

Fig. 4. Dynamics of an increase in the optical losses of fiber 4 related to the absorption by NH groups (at 1.505 μm) at different temperatures: (*1*) 400, (*2*) 500, (*3*) 600, and (*4*) 650°C.

The factor $k(T, p)$ can be considered as the rate constant of chemical bond formation as a result of the chemical interaction of glass with hydrogen. At a constant hydrogen pressure, the temperature dependence of $k(T, p)$ can be described by the Arrhenius equation [14]

$$k = Ae^{-\frac{E}{RT}},$$

where A is a constant depending on the glass composition, dB/km h^x; E is the reaction activation energy, kJ/mol; T is the absolute temperature, K; and $R = 8.31$ J/(mol K) is the universal gas constant.

The values of the Arrhenius parameters obtained from the experimental data for various optical fibers are listed in Table 3. When heated to 400°C, fiber 1 does not exhibit a significant increase in losses in the short-wavelength region. Additional optical losses did not exceed 30 dB/km at each temperature. There were no loss increments in the long-wavelength region as well. Nor did we not detect the Ge–OH band at 1.41 μm.

The main loss increment in fiber 2 was related to the absorption by Si–OH (at 1.385 μm) and Ge–OH (at 1.41 μm) hydroxy groups. The short-wavelength losses strongly increased (the losses increased to 320 dB/km at a wavelength of 1 μm within 6 h at 250°C), but we detected no increase in the long-wavelength region. The absorption intensity at the Ge–OH (1.41 μm) overtone was significantly higher than at the Si–OH (1.39 μm) overtone, which was related to a high germanium concentration in the fiber core (about 26 mol %).

Fiber 3 features a sharp increase in the absorption in the long-wavelength region, because of which we could not continue the experiment after 6-h heating at 400°C. However, at 300°C, we detected no increase in the optical absorption. The intensity of absorption by molecular water (at 1.42 μm) was found to be higher than the intensity of absorption by the hydroxy groups (at 1.39 μm). The character of the absorption increment upon heating of this sample is much like that observed for the ultraviolet radiation-induced increase in the losses of phosphosilicate optical fibers saturated by molecular hydrogen (when absorption at wavelengths above 1.6 μm also increases and gives an intense wing in the range 1.2–1.6 μm) [11].

It should be noted that, when nitrogen-doped hydrogen-saturated molecular optical fibers are heated, the rate of increase in the absorption by the OH groups is less intense as compared to that by the NH groups by a factor of 1.5–4, depending on the temperature. Fiber 4 exhibits an increase in the optical losses in the short-wavelength spectral region.

Figure 5 shows the resulting spectra of the induced optical losses in the optical fibers under study after all annealing cycles in a hydrogen atmosphere. The decrease in the absorption in the range 1.08–1.24 μm upon heating of the molecular-hydrogen–saturated
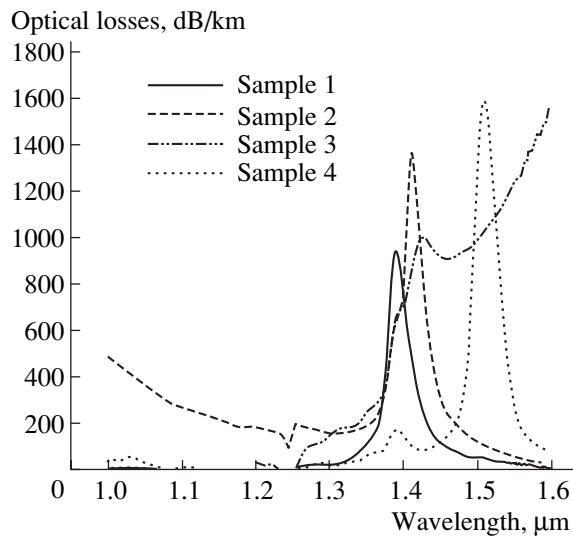

Fig. 5. Induced optical losses in various samples: Si–OH groups absorb at 1.385 μm; Ge–OH, at 1.41 μm; H$_2$O, at 1.42 μm; and Si–NH, at 1.505 μm.

optical fibers is related to a decrease in the molecular hydrogen solubility in silica with increasing temperature, along with simultaneous chemical reactions in the glass network with the formation of OH and NH

Table 2. Values of x for various samples of optical fibers

Sample no.	Si–OH groups (1.39 μm)	Ge–OH groups (1.41 μm)	Molecular water (1.42 μm)	Si–NH groups (1.505 μm)
1	0.79 ± 0.02	–	–	–
2	0.85 ± 0.04	0.93 ± 0.04	–	–
3	0.92 ± 0.05	–	0.76 ± 0.02	–
4	–	–	–	0.71 ± 0.02

Table 3. Arrhenius parameters for various samples of optical fibers

Sample no.	k, dB/km h^x		
	at 1.39 μm	at 1.41 μm	at 1.505 μm
1	$3.89 \times 10^7 e^{-\frac{72.43}{RT}}$	–	–
2	$1.61 \times 10^{10} e^{-\frac{83.82}{RT}}$	$8.8 \times 10^{12} e^{-\frac{108.19}{RT}}$	–
3	The experimental data obtained are insufficient to calculate the preexponential factor and activation energy		
4	–	–	$3.51 \times 10^7 e^{-\frac{95.04}{RT}}$

groups. Therefore, the corresponding absorption band intensities also decrease.

CONCLUSIONS

The rates of increase in the optical losses of molecular-hydrogen-saturated optical fibers upon heating depend on the fiber-core composition. The threshold temperatures of the onset of interaction between molecular hydrogen and various silicate matrices are also different. For each type of optical fiber, we propose temperature conditions for their fastest saturation by H_2 without chemical interaction between molecular hydrogen and the glass.

The threshold temperatures depend strongly on the concentration of dopants in the fiber core. For example, in standard low-doped germanosilicate sample 1, Si–OH groups begin to form only at 300°C, whereas in high-doped sample 2, this phenomenon starts at 200°C. The intensity of absorption by the Si–OH groups at 1.39 μm reaches 200 dB/km in sample 2 at 250°C before leveling off, whereas in low-doped sample 1 the absorption does not reach this value even at 350°C.

Heavily doped sample 2 features a rapid increase in absorption by Ge–OH groups, which is more intense than the absorption by Si–OH groups. In sample 1 with low germanium content, the band at 1.41 μm was not detected at all.

The nitrosilicate matrix of the fiber 4 core is less sensitive to chemical interaction with molecular hydrogen, although it has a high (more than 4 at. %) nitrogen concentration. Even after annealing at $T = 650$°C, the band at 1.39 μm is an order of magnitude smaller than that in the germanosilicate samples held at 250–350°C. Apart from the band at 1.39 μm, the spectrum of fiber 4 contains a more intense band at 1.505 μm, which is associated with absorption due to the Si–NH bond vibrations. However, this band increases at relatively high (above 400°C) temperatures.

Optical fiber 3 contains a low phosphorus concentration; the threshold of interaction with molecular hydrogen in this fiber is higher than that in germanosilicate samples and is lower than in the nitrogen-doped optical fiber.

Apart from the increase in the optical absorption by hydroxy groups, we would like to note a strong increase in losses in the long-wavelength range for fiber 3 and in the short-wavelength range for fiber 2.

Thus, the kinetics of interaction between glasses and molecular hydrogen depends substantially on their compositions.

ACKNOWLEDGMENTS

REFERENCES

1. W. Espe, *Werkstoffkunde der Hochvakuumtechnik* (Deutscher Verlag der Wissenschaften, Berlin, 1959; Gosénergoizdat, Moscow, 1962), Vol. 2.
2. A. L. Tomashuk, K. M. Golant, E. M. Dianov, *et al.*, in *Proceedings of the 5th European Conference on Radiation and Its Effects on Components and Systems RADECS-99, Fontevraud, France, 1999*, pp. 471–476.
3. P. J. Lemaire, R. M. Atkins, V. Mizrahi, *et al.*, Electron. Lett. **29**, 1191 (1993).
4. E. M. Dianov, M. V. Grekov, I. A. Bufetov, *et al.*, Electron. Lett. **33**, 1542 (1997).
5. I. A. Bufetov, M. M. Bubniv, Y. V. Larionov, *et al.*, Laser Phys. **13**, 234 (2003).
6. B. Malo, J. Albert, F. Bilodeau, *et al.*, Appl. Phys. Lett. **65**, 394 (1994).
7. J. Stone, J. Lightwave Technol. **LT-5**, 712 (1987).
8. R. W. Lee, R. C. Frank, and D. E. Swets, J. Chem. Phys. **36**, 1062 (1962).
9. J. E. Shelby, J. Appl. Phys. **48**, 3387 (1977).
10. N. Uchida and N. Uesugi, J. Lightwave Technol. **LT-4**, 1132 (1986).
11. S. L. Semjonov, A. A. Rybaltovsky, Y. J. Larionov, *et al.*, in *Proceedings of Bragg Gratings, Photosensitivity, and Poling in Glass Waveguides, OSA Trends in Optics and Photonics Series BGPP-2000-TOPS, 2000*, Vol. 33, pp. 267–271.
12. E. M. Dianov, K. M. Golant, R. R. Khrabba, *et al.*, J. Lightwave Technol. **13**, 1471 (1995).
13. N. Shibata, K. Noguchi, N. Uesugi, *et al.*, Jpn. J. Appl. Phys. **24**, 196 (1985).
14. K. Noguchi, N. Shibata, N. Uesugi, *et al.*, J. Lightwave Technol. **LT-3**, 236 (1985).

Translated by K. Shakhlevich

====================== **RADIOPHYSICS** ======================

On the Magnetic Dipole Absorption of Electromagnetic Radiation by a Fine Conducting Particle

S. V. Berezkina, I. A. Kuznetsova, and A. A. Yushkanov

Demidov State University, Sovetskaya ul. 14, Yaroslavl, 150000 Russia
Received November 23, 2003

Abstract—The cross section of absorption of electromagnetic radiation by a fine spherical conducting particle is estimated in terms of the classical kinetic theory of electrical conduction. The mixed diffuse–specular mechanism of charge carrier reflection from the sample boundary is considered. A correlation between the coefficient of specular reflection and the absorption cross section at different temperatures is analyzed. © *2004 MAIK "Nauka/Interperiodica".*

The electromagnetic properties of fine conducting particles may differ substantially from those of bulk samples [1–4]. From the classical point of view, this difference is due to the fact that the electron free path λ in the particles and their size a are of the same order of magnitude. In this case, nonlocal effects resulting from the interaction of charge carriers with the sample boundary considerably influence the optical properties of the particle (specifically, the absorption cross section) [2–4].

It should be noted that the equations of macroscopic electrodynamics are valid only for bulk samples ($a \gg \lambda$). Therefore, the classical theory of interaction between electromagnetic radiation and spherical conducting particles (the Mie theory [5]) is inapplicable for describing the above size effects and the problem should be tackled in terms of the kinetic approach.

The magnetic dipole absorption of radiation by a fine spherical metal particle at zero temperature was considered in [2, 6]. The authors of [7] took into account the temperature dependence of the absorption cross section for a conducting semiconductor or semimetal particle. However, their analysis is restricted to perfectly diffuse reflection of carriers from the sample boundary.

In this work, we estimate the absorption cross section of a conducting particle in the case of the mixed diffuse–specular mechanism of carrier reflection from the boundary at nonzero temperatures. The absorption due to the variable magnetic field of an electromagnetic wave is calculated. This type of absorption prevails for highly conducting particles about 10 nm across [2].

The radius a of the particle is assumed to be smaller than the skin depth δ; therefore, the skin effect is ignored.

PROBLEM DEFINITION

Let us consider the behavior of a fine particle of a metal, semimetal, or heavily doped $n(p)$-semiconductor in a time-periodic magnetic field

$$\mathbf{H} = \mathbf{H}_0 \exp(-i\omega t). \tag{1}$$

This field induces a vortex electric field, which, according to the Maxwell equation of induction, has the form

$$\mathbf{E} = \frac{1}{2c}\left[\mathbf{r} \times \frac{\partial \mathbf{H}}{\partial t}\right] = \frac{\omega}{2ic}[\mathbf{r} \times \mathbf{H}_0]\exp(-i\omega t), \tag{2}$$

where ω is the angular frequency of the wave, c is the velocity of light, $\mathbf{H}_0$ is the amplitude of the magnetic field of the wave, and $\mathbf{r}$ is the radius vector (the origin is at the center of the particle).

Field (2) generates eddy currents, which are responsible for the magnetic dipole absorption of radiation by the particle. The mean power dissipated in the volume of the particle per unit time is given by [8]

$$Q = \int \overline{(\mathrm{Re}\mathbf{E}) \cdot (\mathrm{Re}\mathbf{j})}d^3r = 1/2\mathrm{Re}\int \mathbf{j} \cdot \mathbf{E}^* d^3r, \tag{3}$$

where $\mathbf{j}$ is the eddy current density. The bar and asterisk mean time averaging and complex conjugation, respectively.

If $a \gg \lambda$, current density $\mathbf{j}$ can be found from the differential Ohm's law

$$\begin{aligned}\mathbf{j} &= \Sigma(\omega)\mathbf{E}, \\ \Sigma(\omega) &= \Sigma(0)/(1 - i\tau\omega),\end{aligned} \tag{4}$$

where $\Sigma(\omega)$ is the Drude conductivity.

Dividing (3) by the mean energy flux $cH_0^2/8\pi$ in the wave, we get a classical formula for the cross section

σ_{cl} of magnetic absorption by a particle [8]:

$$\sigma_{cl} = \frac{8\pi\Sigma(0)\omega^2\alpha^2}{15c^3(1+\omega^2\tau^2)}, \tag{5}$$

where $\Sigma(0) = e^2 n\tau/m$ is the static conductivity; e is the electron charge; n and m are, respectively, the equilibrium concentration and effective mass of an electron (hole); and τ is the relaxation time.

If the radius a of the particle is comparable to electron (hole) free path λ, macroscopic electrodynamics is inapplicable, since the relationship between $\mathbf{E}$ and $\mathbf{j}$ is of local character. The electric field acts on carriers in the particle, as a result of which their distribution function f deviates from Fermi equilibrium function f_0 by f_1:

$$f(\mathbf{r},\mathbf{v}) = f_0(\varepsilon) + f_1(\mathbf{r},\mathbf{v}), \tag{6}$$

$$f_0 = \frac{1}{\exp((\varepsilon-\mu)/k_0 T)+1}. \tag{7}$$

Here, $\varepsilon = mv^2/2$ is the kinetic energy of an electron (hole) in a spherically symmetric energy band, μ is the chemical potential, T is the temperature of the particle, and k_0 is the Boltzmann constant. The field generates the eddy current

$$\mathbf{j} = e\int\mathbf{v}f2\frac{d^3(m\mathbf{v})}{h^3} = 2\left(\frac{m}{h}\right)^3 e\int\mathbf{v}f_1 d^3 v. \tag{8}$$

Thus, the problem reduced to finding the deviation f_1 of the distribution function from Fermi equilibrium function f_0, where f_1 arises under the action of vortex field (2). In an approximation linear in external field, function f_1 satisfies the Boltzmann kinetic equation [9, 10]

$$-i\omega f_1 + \mathbf{v}\cdot(\partial f_1/\partial\mathbf{r}) + e\mathbf{v}\cdot\mathbf{E}(\partial f_0/\partial\varepsilon) = -f_1/\tau. \tag{9}$$

Here, it is assumed that f_1 is a stationary function of time ($f_1 \sim e^{-i\omega t}$) and the collision integral is taken in the relaxation time approximation:

$$(df_1/dt)_s = -f_1/\tau. \tag{10}$$

Thus, solving Eq. (9), we can find f_1 and then current $\mathbf{j}$ from (8) and mean dissipated power Q from (3). The equation can be uniquely solved only if a boundary condition for unknown function f_1 is set on the surface of the particle. Physically, this means that, if $a \le \lambda$, the absorption cross section considerably depends on the type of carrier–boundary interaction. In [7], this problem was solved for the diffuse reflection of charge carriers. In this case, the distribution function becomes equilibrium immediately after the reflection:

$$f_1(\mathbf{r},\mathbf{v}) = 0 \quad\text{at}\quad \begin{cases}|\mathbf{r}| = a \\ \mathbf{r}\cdot\mathbf{v} < 0.\end{cases} \tag{11}$$

In this work, we consider general boundary conditions, which allow the simulation of the mixed diffuse–specular reflection of carriers from the sample boundary:

$$f_1(\mathbf{r},\mathbf{v}) = qf_1(\mathbf{r},\mathbf{v}') \quad\text{at}\quad \begin{cases}|\mathbf{r}| = a \\ \mathbf{r}\cdot\mathbf{v} < 0.\end{cases} \tag{12}$$

Here, $\mathbf{v}' = \mathbf{v} - 2\mathbf{r}(\mathbf{r}\cdot\mathbf{v})/a^2$ is the velocity vector for specular reflection from the inner surface of the sphere, which turns to vector $\mathbf{v}$ at point $\mathbf{r}(|\mathbf{r}| = a)$, and q is the coefficient (probability) of specular reflection [6]:

$$0 \le q \le 1. \tag{13}$$

Obviously, at $q = 0$, condition (12) coincides with (11) and, at $q = 1$, the reflection becomes perfectly specular. Thus, varying q in limits (13), one can analyze different types of carrier reflection from the sample boundary. Our aim is to study the dependence of the absorption cross section of a conducting particle on specular reflection coefficient q at different temperatures.

MATHEMATICAL MODEL AND CALCULATION

Kinetic equation (9) is solved by the method of characteristics [11]. Along the particle trajectory

$$d\mathbf{r} = \mathbf{v}dt \tag{14}$$

the variation of f_1 is given by

$$df_1 = -\left(\nu f_1 + e(\mathbf{E}\cdot\mathbf{v})\frac{\partial f_0}{\partial\varepsilon}\right)dt, \tag{15}$$

where

$$\nu = \tau^{-1} - i\omega \tag{16}$$

is the complex frequency of scattering.

Boundary condition (12) makes it possible to trace the variation of f_1 along a specularly reflecting trajectory. At the point of reflection, $t = t_n$, function $f_1(t)$ experiences a jump:

$$f_1(t_n+0) = qf_1(t_n-0), \tag{17}$$

where n is the integer subscript that enumerates points of reflection in the order of their appearance along the trajectory of a "specularly reflecting" electron (hole) and t_n is the value of the parameter of an nth reflection. For specular reflection, the angular momentum is kept constant: $[\mathbf{r}\times\mathbf{v}] = [\mathbf{r}\times\mathbf{v}']$; hence, for the trajectory being considered,

$$[\mathbf{r}\times\mathbf{v}] = \text{const}, \tag{18}$$

and the difference $t_n - t_{n-1}$ does not depend on the number n of the point of reflection:

$$t_n = nT + \text{const}, \quad n\in Z. \tag{19}$$

Here, T is the time the particle with velocity $\mathbf{v}$ takes to cover the distance from point $\mathbf{r}_{n-1}$ to point $\mathbf{r}_n$:

$$T = -2(\mathbf{v}_n \cdot \mathbf{r}_n)/v^2. \qquad (20)$$

The value of $\mathbf{E} \cdot \mathbf{v}$ is also constant on the trajectory (see formula (2)):

$$\mathbf{E} \cdot \mathbf{v} = \frac{\omega}{2ic}[\mathbf{r} \times \mathbf{H}] \cdot \mathbf{v} = \frac{i\omega}{2c}[\mathbf{r} \times \mathbf{v}] \cdot \mathbf{H} = \text{const.} \quad (21)$$

Solving Eq. (15) in the interval (t_{n-1}, t_n) and applying condition (17), we find a relationship between the initial values of f_1 on two adjacent segments of the trajectory:

$$f_1(t_n + 0) = q\left\{-\frac{e(\mathbf{E} \cdot \mathbf{v})}{\nu} \cdot \left(\frac{\partial f_0}{\partial \varepsilon}\right)(1 - \exp(-\nu T))\right.$$

$$\left. + f_1(t_{n-1} + 0)\exp(-\nu T)\right\}. \qquad (22)$$

Then, using this recursive relation, we express $f_1(t_{n-1} + 0)$ through $f_1(t_{n-2} + 0)$, etc., and eventually obtain a formula where $f_1(t_{n-1} + 0)$ is expressed via the sum of the geometrical progression with ratio $q\exp(-\nu T)$:

$$f_1(t_n + 0) = -q$$
$$\times \left[\frac{e(\mathbf{E} \cdot \mathbf{v})}{\nu}\left(\frac{\partial f_0}{\partial \varepsilon}\right)(1 - \exp(-\nu T))\right]/(1 - \exp(-\nu T)). \qquad (23)$$

Integrating Eq. (15) with initial condition (23) yields

$$f_1(t) = \frac{e(\mathbf{E} \cdot \mathbf{v})}{\nu}\left(\frac{\partial f_0}{\partial \varepsilon}\right)\left[\frac{(1-q)\exp(-\nu t)}{1 - q\exp(-\nu T)} - 1\right]. \quad (24)$$

Parameters t and T can be related to the coordinates of point $(\mathbf{r}, \mathbf{v})$ in the phase space with conditions [2]

$$\mathbf{r} = \mathbf{r}_0 + \mathbf{v}t; \quad \mathbf{v} \cdot \mathbf{r}_0 < 0; \quad \mathbf{r}_0^2 = a^2;$$
$$T = -2(\mathbf{v} \cdot \mathbf{r}_0)/a^2. \qquad (25)$$

Here, parameter t is the time an electron (hole) moving along the trajectory with velocity $\mathbf{v}$ takes to cover the distance from the boundary to point $\mathbf{r}$. Eliminating $\mathbf{r}_0$ from (25), we get

$$t = [(\mathbf{r} \cdot \mathbf{v}) + ((\mathbf{r} \cdot \mathbf{v})^2 + v^2(a^2 - r^2))^{1/2}]/v^2, \quad (26)$$

$$T = 2((\mathbf{r} \cdot \mathbf{v})^2 + v^2(a^2 - r^2))^{1/2}/v^2. \qquad (27)$$

Relationships (25)–(27) completely specify function $f_1(\mathbf{r}, \mathbf{v})$. Using the distribution function found, one

can calculate the current by (8):

$$j = \frac{Ee^2na}{8v_1z}\left[\int_{-1}^{1}\int_{0}^{\infty}\left(1 - \frac{(1-q)\exp(-z\eta)}{1 - q\exp(-z\eta_0)}\right)\right.$$

$$\left. \times \frac{u^{3/2}\exp(u - u_\mu)}{(\exp(u - u_\mu) + 1)^2}(1 - \beta^2)du d\beta\right]A, \qquad (28)$$

$$A = \left[\int_{0}^{\infty}\frac{u^{1/2}du}{\exp(u - u_\mu) + 1}\right]^{-1},$$

where

$$z = va/v_1 = x - iy, \quad x = a/(v_1\tau), \quad y = a\omega/v_1, \quad (29)$$

$$\eta = v_1 t/a = (v_1/v)[\xi\beta + (\xi^2\beta^2 + 1 - \xi^2)^{1/2}], \quad (30)$$

$$\eta_0 = 2(v_1/v)(\xi^2\beta^2 + 1 - \xi^2)^{1/2}, \qquad (31)$$

$$\xi = r/a, \quad \beta = \cos(\widehat{\mathbf{v}; \mathbf{r}}) = (\mathbf{v} \cdot \mathbf{r})/(vr), \quad (32)$$

$$u = mv^2/(2k_0 T), \quad u_\mu = \mu/(k_0 T). \qquad (33)$$

Here, dimensional variables x, y, and z are normalized to the characteristic charge carrier velocity v_1, which is defined as follows:

$$nv_1 = \frac{5}{3}\int v^2 f_0 \frac{2d^3(mv)}{h^3}. \qquad (34)$$

For the case of degenerate Fermi gas $(T \longrightarrow 0)$, $v_1 \longrightarrow v_0$, where v_0 is the Fermi velocity, which is defined by expression (34) for Fermi function f_0 $(T \longrightarrow 0)$. In the other limit $T \longrightarrow \infty$, v_1 tends to $\sqrt{5kT/m}$, i.e., is comparable to the mean thermal velocity of charge carriers in order of magnitude.

The absorption cross section is found by substituting formula (28) into integral (3) and dividing Q by the mean energy flux in the plane electromagnetic wave:
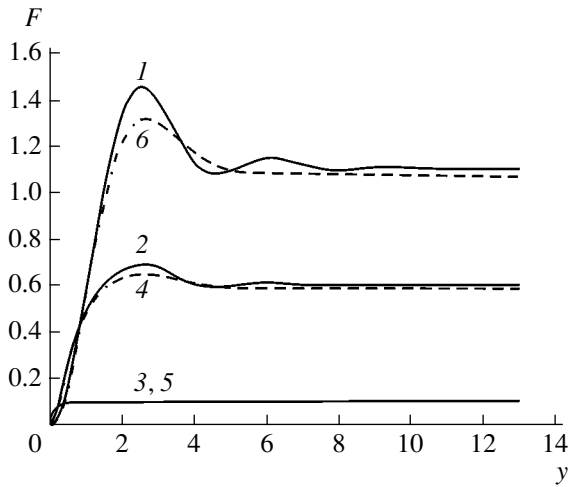
$$\sigma = (4\pi/cH_0^2)\text{Re}\int \mathbf{j} \cdot \mathbf{E}^* d^3r = \sigma_0 F(x, y, q, u_\mu), \quad (35)$$
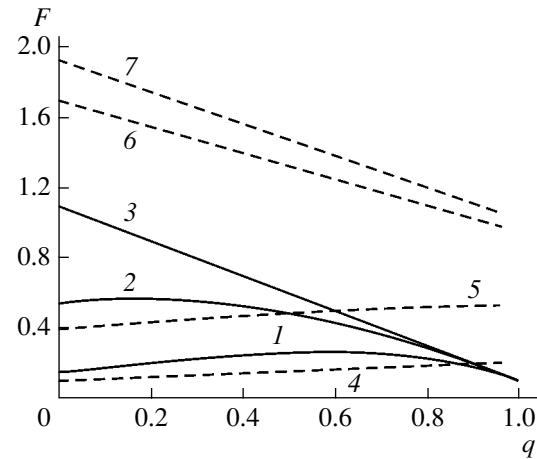
$$\sigma_0 = \pi^2 e^2 a^4 v_1 n/(2c^3 m), \qquad (36)$$

$$F(x, y, q, u_\mu) = \frac{8y^2}{3z}\left[\text{Re}\int_{0}^{1}\int_{-1}^{1}\int_{0}^{\infty}\xi^4(1 - \beta^2)\right.$$
$$\times \frac{u^{3/2}\exp(u - u_\mu)}{(\exp(u - u_\mu) + 1)^2}\left(1 - \frac{(1-q)\exp(-z\eta)}{1 - q\exp(-z\eta_0)}\right)du d\beta d\xi\right]A. \qquad (37)$$

The triple integral is reduced to the double integral if we change the variables: $(\xi; \beta) \longrightarrow (k; s)$, where

$$k = (\xi^2\beta^2 + 1 - \xi^2)^{1/2}, \quad s = \xi\beta, \qquad (38)$$

Fig. 1. Dimensionless cross section F vs. dimensionless frequency y for $u_\mu = 10$ (continuous curves) and 0.5 (dashed curves); $x = 0.1$; and $q = $ (*1, 6*) 0, (*2, 4*) 0.5, and (*3, 5*) 1.

Fig. 2. Dimensionless cross section F vs. specular reflection coefficient q for $u_\mu = 10$; $x = 0.1$ (continuous curves) and 1 (dashed curves); and $y = $ (*1, 4*) 0.5, (*2, 5*) 1, (*3, 7*) 5, and (*6*) 3.

and integrate over s from $-k$ to k:

$$F(x, y, q, u_\mu) = \frac{8}{3} y^2 A \mathrm{Re}$$

$$\times \int\limits_0^1 \int\limits_0^\infty (1 - k^2) k \left[\frac{2k}{z} - \frac{\sqrt{u}(1-q)(\exp(-2zk\tilde{v}_1/\sqrt{u}))}{\tilde{v}_1 z^2 (1 - q\exp(-2zk\tilde{v}_1/\sqrt{u}))} \right] \quad (39)$$

$$\times \frac{u^{3/2}\exp(u - u_\mu)}{(\exp(u - u_\mu) + 1)^2} du dk.$$

Here, $\tilde{v}_1 = v_1/\sqrt{2k_0 T/m}$ is the dimensional velocity. The results of numerical calculation of absorption coefficient (39) for different values of parameters q, u_μ, x, and y are shown in Figs. 1–4.

DISCUSSION

Consider several limiting cases.

(1) If the reflection is perfectly diffuse ($q = 0$), absorption coefficient (39) at low temperatures ($u_\mu \gg 1$) is calculated analytically and is given by the expression derived in [2]. For arbitrary temperatures, the integral in (39) cannot be taken analytically (the related results are given in [7]).

(2) For purely specular reflection ($q \longrightarrow 1$), the low-temperature absorption coefficient is given by

$$F \longrightarrow F_{\mathrm{cl}} = 4y^2 \mathrm{Re} \frac{4}{15z} = \frac{16xy^2}{15(x^2 + y^2)}. \quad (40)$$

This expression is consistent with classical result (5) and indicates that the boundary does not affect distribution function f_1.

(3) Consider the low-frequency approximation ($y \ll 1$) for the case $q \neq 0$. In the limit $x \longrightarrow 0$ (large free paths), the integral in (39) at nonzero temperatures simplifies significantly, taking the form

$$F(x = 0; y \ll 1, q \neq 0, u_\mu) = \frac{4}{9} \sqrt{\frac{5}{3} \frac{(1+q)}{(1-q)}}$$

$$\times \ln[1 + \exp(u_\mu)] \left[\int\limits_0^\infty \frac{u^{3/2} du}{\exp(u - u_\mu) + 1} \right]^{\frac{1}{2}} \quad (41)$$

$$\times \left[\int\limits_0^\infty \frac{u^{1/2} du}{\exp(u - u_\mu) + 1} \right]^{-\frac{3}{2}} y^2.$$

For a generate electron plasma ($u_\mu \longrightarrow +\infty$) in the low-frequency range, expression (41) reduces to the form

$$F(u_\mu \longrightarrow +\infty; x = 0; y \ll 1; q \neq 0) = \frac{2(1+q)}{3(1-q)} y^2, \quad (42)$$

which agrees with the result of [6].

(4) Consider another limiting case for classical gas: $u_\mu \longrightarrow -\infty$. In expression (39), we can neglect unity (which is much smaller than the exponential), which greatly simplifies this integral. Expanding in powers of y simplifies (39) still further and allows us to obtain the result in analytical form:
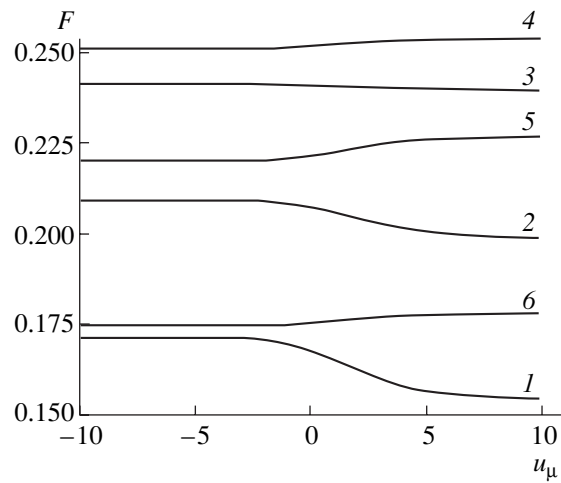
$$F(u_\mu \longrightarrow -\infty; x = 0; y \ll 1; q \neq 0)$$

$$= \frac{4}{9} \sqrt{\frac{10}{\pi}} \frac{(1+q)}{(1-q)} y^2. \quad (43)$$

(5) Figure 1 shows the dependence of dimensionless absorption cross section F on dimensionless frequency
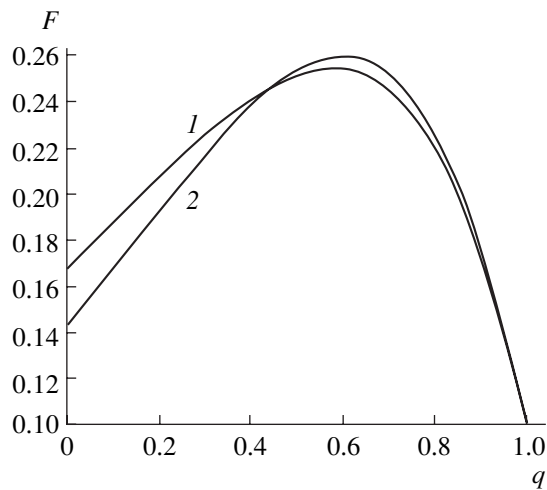
Fig. 3. Dimensionless cross section F vs. specular reflection coefficient q for $x = 0.1$, $y = 0.5$, and different temperatures $u_\mu = (1)$ 0.1 and (2) 10.

Fig. 4. Dimensionless cross section F vs. u_μ ($u_\mu = \mu/(k_0 T)$) for $x = 0.1$, $y = 0.5$, and different specular reflection coefficient q (curves 1–6).

y for dimensionless reciprocal free path $x = 0.1$, $u_\mu = 0.5$ and 10 ($u_\mu = u/(k_0 T)$), and different values of the coefficient q of specular reflection. It is seen that, as q grows, spectral dependence $F(y)$ becomes more monotonic and tends to saturation with increasing y more rapidly at any temperature. This is because the effect of the boundary on distribution function f_1 weakens with increasing q at any temperature; therefore, the differential Ohm's law for the eddy current remains valid for any x at $q \longrightarrow 1$.

From Fig. 1, it also follows that the cross section oscillations smooth out with increasing temperature; that is, the contribution of nonlocal surface effects to the cross section decreases.

Figure 2 plots $F(q)$ for $u_\mu = 10$ and different x and y. At small x (large charge-carrier free paths) and $q \longrightarrow 1$, curves $F(q)$ tend to coincide irrespective of frequency y. This is consistent with classical result (40). It should be noted that, as x and y increase ($x \geq 1$ and $y > 1$), dependence $F(q)$ approaches a linear decreasing function with increasing q at any temperature.

Figure 3 plots curves $F(q)$ for different temperatures ($u_\mu = 0.1$ and 10) at $x = 0.1$ and $y = 0.5$. Here, the curves diverge most considerably in the case of perfectly diffuse reflection ($q = 0$) throughout the temperature range.

In Fig. 4, F is plotted against $u_\mu = u/(k_0 T)$ for different q and given x and y. At small and large u_μ, curves $F(u_\mu)$ are seen to have different asymptotics. The form of curve $F(u_\mu)$ varies with the specular reflection coefficient. For the given x and y, the difference between the asymptotics is maximal (11%) at $q = 0$.

REFERENCES

1. I. D. Morokhov, V. I. Petinov, L. I. Trusov, and V. F. Petrunin, Usp. Fiz. Nauk **133**, 653 (1981) [Sov. Phys. Usp. **24**, 295 (1981)].

2. A. G. Lesskis, V. E. Pasternak, and A. A. Yushkanov, Zh. Éksp. Teor. Fiz. **83** (1), 310 (1982) [Sov. Phys. JETP **56**, 170 (1982)].

3. P. M. Tomchuk and B. P. Tomchuk, Zh. Éksp. Teor. Fiz. **112** (2), 661 (1997) [JETP **85**, 360 (1997)].

4. É. V. Zavitaev, A. A. Yushkanov, and Yu. I. Yalamov, Zh. Tekh. Fiz. **71** (11), 114 (2001) [Tech. Phys. **46**, 1460 (2001)].

5. M. Born and E. Wolf, *Principles of Optics*, 4th ed. (Pergamon, Oxford, 1969; Nauka, Moscow, 1973).

6. A. G. Lesskis, A. A. Yushkanov, and Yu. I. Yalamov, Poverkhnost, No. 11, 115 (1987).

7. I. A. Kuznetsova and A. A. Yushkanov, Opt. Spektrosk. **94**, 669 (2003) [Opt. Spectrosc. **94**, 613 (2003)].

8. L. D. Landau and E. M. Lifshitz, *Course of Theoretical Physics*, Vol. 8: *Electrodynamics of Continuous Media* (Nauka, Moscow, 1982; Pergamon, New York, 1984).

9. J. M. Ziman, *Electrons and Phonons* (Clarendon, Oxford, 1960; Inostrannaya Literatura, Moscow, 1962).

10. W. A. Harrison, *Solid State Theory* (McGraw-Hill, New York, 1970; Mir, Moscow, 1972).

11. R. Courant and D. Hilbert, *Methods of Mathematical Physics*, Vol. 2: *Partial Differential Equations* (Interscience, New York, 1962; Mir, Moscow, 1964).

Translated by V. Isaakyan

SURFACES,
ELECTRON AND ION EMISSION

Effect of the Space Charge of Emitted Electrons on Field Electron Emission

V. G. Pavlov

Ioffe Physicotechnical Institute, Russian Academy of Sciences,
Politekhnicheskaya ul. 26, St. Petersburg, 194021 Russia
e-mail: vpavlov@ms.ioffe.rssi.ru
Received March 24, 2004

Abstract—It is shown that the conventional technique of substituting the field strength at the space charge–emitter interface that is calculated with the Poisson equation into the Fowler–Nordheim formula considerably overestimates the effect of space charge on field electron emission. In this work, the space-charge-induced field attenuation as a function of the emission current density and radius of curvature of the emitter surface is derived using the model of a planar space-charge layer. It is argued that field electron emission cannot be studied in terms of the spherical diode model, since it assumes the presence of a space charge on the back (nonemitting) emitter surface, which is in fact absent. It is stated that one should consider the discrete character of the charges when investigating the space charge in field electron emission, because the mean spacing between the electrons emitted far exceeds the emission barrier width. © *2004 MAIK "Nauka/Interperiodica"*.

INTRODUCTION

Recently, research on and applications of field electron emitters have attracted considerable interest. These emitters eject electrons from nanometer conducting inclusions embedded in an insulating or semiconductor matrix [1], from carbon nanotubes [2], or from nanometer protrusions including those made in artificial vacuum microcavities (Spindt cathodes) [3]. Because of a small emitting surface area, the emission current density reaches the point where the space charge (SC) of the electrons emitted is viewed as a decisive factor controlling the emissivity of the cathodes [4–9]. It is therefore instructive to study the SC effect especially as applied to emission from small objects or from objects with a small (1–10 nm) radius of curvature of the emitting surface. Such objects are of special theoretical interest, because their sizes and radii of curvature are comparable to the width of the field electron emission (FEE) potential barrier [4, 10–14], so that it is necessary to separate the size and SC effects.

Today, it is generally accepted that the SC of the electrons emitted limits the emission current density at the level $j \approx 5 \times 10^6$ A/cm^2 [4–9, 15]. This fact is recognized as both theoretically and experimentally established and also serves as an explanation for the deviation of the *I–V* characteristic in the Fowler–Nordheim coordinates from a straight line toward lower currents. At the same time, experiments where the FEE current density was as high as 10^{10} A/cm^2 (i.e., three to four orders of magnitude higher than the above limit) were reported [16, 17].

Field electron emission differs from other types of emission in that the electric field (including that produced by the SC) not only influences the passage of the vacuum gap by the electrons but also affects the electron escape from the emitter. The conventional approach to studying the SC effect on FEE is based, by analogy with thermionic emission, on calculating the electric field strength at the SC boundary near the emitter surface with the Poisson equation for a planar [4, 6, 8, 18–21] or spherical [4, 8, 22–25] diode, as well as for a diode with a more intricate shape of the electrodes [4, 5, 7, 15]. In this work, we show that such an approach in the case of FEE overestimates the amount of this effect, thereby leading to incorrect results.

PLANAR DIODE

Consideration of the SC effect on FEE was first carried out in [18], and the quantitative solution of this problem and comparison with experimental data were first undertaken in [20]. In the works cited, the model of planar diode with infinite electrodes was used. The problem was solved by analogy with the problem of SC effect on current passage in a planar vacuum diode by using the Poisson equation [26–28]

$$\Delta U = -4\pi\rho \qquad (1)$$

(or

$$d^2 U/dx^2 = -4\pi\rho(x) \qquad (2)$$

for a one-dimensional planar diode), the continuity equation

$$j = \rho v \qquad (3)$$

and the energy conservation law

$$1/2 m v^2 = Ue. \qquad (4)$$

Here, Δ is the Laplacian, U is the electric potential, ρ is the charge density, x is the distance to the cathode, j is the current density, v is the electron velocity, m is the electron mass, and e is the electron charge.

If we take $v(0) = 0$ (the initial electron velocity is much lower than that gained upon passing the diode), the diode current limitation condition takes the form

$$dU/dx(0) = 0. \qquad (5)$$

The solution of set (2)–(5) yields the Child's law: the current density through the diode is proportional to the potential difference V between the electrodes in the three-seconds power:

$$j = AV^{3/2}/d^2, \qquad (6)$$

where A is a constant and d is the electrode spacing.

For the case of FEE, this set of equations was modified as follows [18–20]: condition (5) was disregarded, and the Fowler–Nordheim formula, which relates current density to the field near the emitter surface [4] was added:

$$j = e^3/8\pi h t^2(y)F^2/\varphi$$
$$\times \exp[-8\pi\theta(y)(2m)^{1/2}/3he\varphi^{3/2}/F], \qquad (7)$$

where F is the field at the cathode surface, h is the Planck constant, $t(y)$ and $\theta(y)$ are the tabulated Nordheim functions of $y = (e^3F)^{1/2}/\varphi$, and φ is the work function for the emitter surface.

From set (2)–(4) and Eq. (7), a relationship between the field at the cathode surface and the potential difference between the electrodes of a planar diode in the presence of the SC was derived. The current density versus potential difference was examined to study the SC effect on FEE. The current density was determined by substituting the found value of F into (7).

It should be noted that expression (7) was derived under the assumption that the potential barrier for the electrons on the emitter surface is the sum of the image force potential and the potential of a uniform external field [4]. In the presence of the SC, another relationship between the field at the surface and the shape and width of the potential barrier (hence, the current density) is expected. Figure 1 plots the potential energy of an electron against the distance to the emitter surface for the case where the electrons leave the emitter with a zero initial velocity (the planar diode model considered in [20]). The current density at which the SC decreases the surface field by half is taken as an example. The substitution of the surface field strength obtained by solving the problem (the slope of the tangent to potential curve 2) into the Fowler–Nordheim formula implies that the potential barrier for the electrons has the form of curve 3, i.e., is much higher than the actual barrier in the given model (curve 2). Thus, the calculation of the
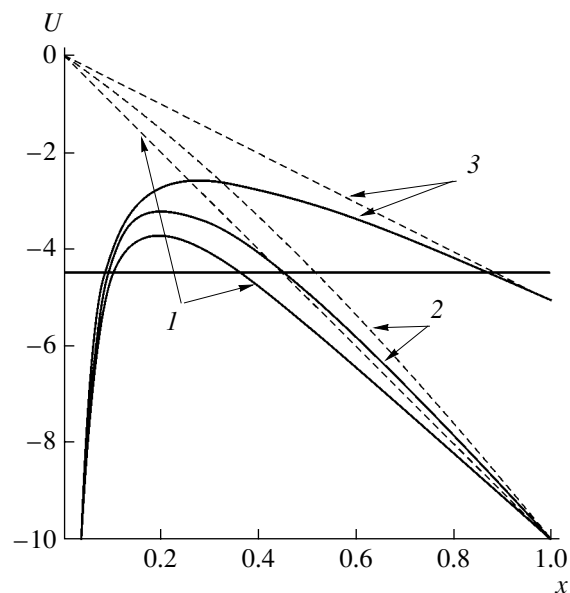

Fig. 1. Electric potential (dashed lines) and potential energy (continuous lines) of an electron vs. the distance to the metal surface in the planar diode model. Lower curves *1* are drawn without considering the SC, middle curves *2* take into account the SC, and upper curves *3* are obtained when the field at the SC–emitter interface is substituted into the Fowler–Nordheim formula (the tangent to the middle dashed curve at point $x = 0$).

field at the SC boundary near the emitter surface—the basic way of estimating the SC effect on FEE in the published works—significantly overestimates this effect. This is related to the fundamental curvature of the electric field potential in the SC region. In addition, this curvature (field nonuniformity) grows as the emitter surface is approached and also when the current density increases. Therein lies the basic difference between the SC-related field nonuniformity and the field nonuniformity associated with the electrode geometry.

This disadvantage of the above method could be eliminated if, when calculating the current density, one used the Fowler–Nordheim barrier, which is equivalent to the SC-modified barrier (Fig. 1, curve 2). Alternatively, one could directly calculate the transparency of the barrier. However, the model considered involves other inconsistencies with the case of FEE.

This model assumes that the electrons escaping from the emitter into a vacuum have the zero initial velocity. Such a situation corresponds to overbarrier (e.g., thermionic) emission. In the case of FEE, the electrons have a zero velocity within a distance to the surface equal to the barrier width and then move following the same laws as in the model considered if the emission surface is taken to be the plane of electron escape from under the barrier (in other words, if the SC region is offset by the barrier width from the emitter surface) (Fig. 2a). If, in the negative electron kinetic
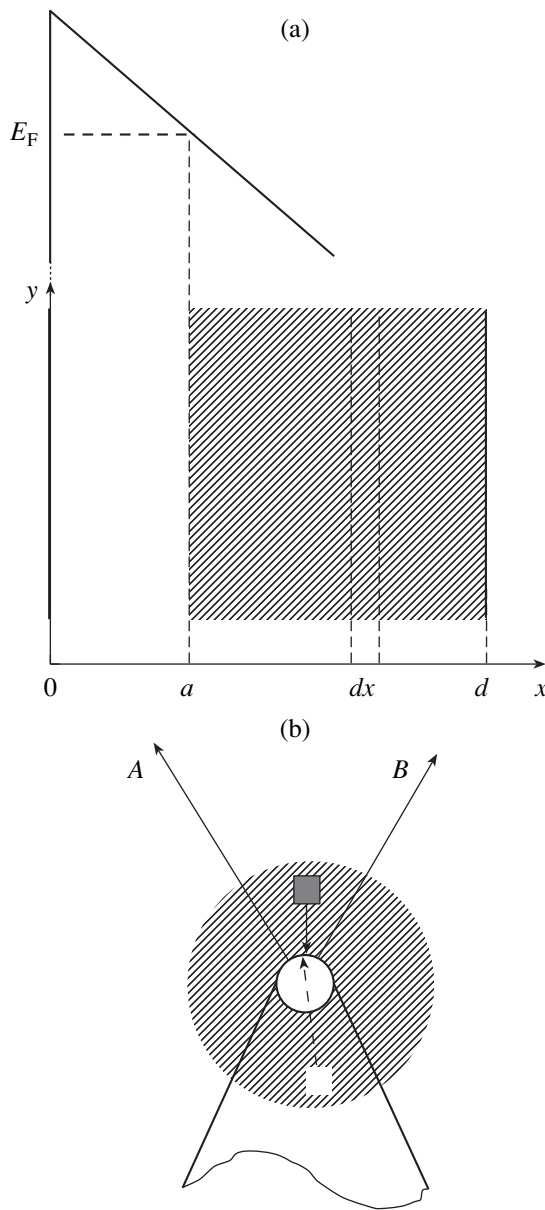
Fig. 2. Models used in considering the problem of SC effect on FEE: (a) planar diode and (b) spherical diode. The SC regions presumed are hatched. The hatched square, real charge; empty square, charge nonexistent in the case of emission from the tip.

energy range (under the barrier), electric charges are assumed to be absent (or, more specifically, if the electron emission does not produce an excess surface charge) and if the presence of surface charges that screen the SC field in the metal is taken into account, the geometry of the problem reduces to a plane capacitor formed by the emitter surface and the plane of electron escape from under the barrier (the beginning of the SC region). For fixed charges, the field in a plane capacitor does not depend on the plate spacing and the problem is reduced to calculating the instantaneous net

charge of the electrons emitted. Extra SC field F_q is produced by the SC and the equivalent positive charge that is induced on the metal surface.

Such an approach applies if the anode of the model plane capacitor is a virtual electrode that only fixes the potential. If the anode is conducting, the charge induced on it will be the same as on the cathode and completely compensate for the field produced by the screening charge on the cathode. Then, the SC field (the field of a plane charged layer) will be half as high as the field in the capacitor:

$$F_q = 2\pi\sigma,$$

where $\sigma = \int_a^d \rho(x)dx$ is the reduced surface charge density in the plane SC layer.

This field is subtracted from the external field due to the potential difference applied. Based on the principle of superposition, one can calculate the field of the plane layer separately. It should be only taken into account that the SC density depends on the electron velocity, so that it is necessary to consider the motion of the electrons in the real field (which is the resultant of the external field, SC field, and image force field) in calculating the total SC.

The solution simplifies, owing to the fact that the field of an infinite layer (and the field in a plane capacitor) is uniform; hence, the barrier on the emitter surface is totally equivalent to the barrier in the Fowler–Nordheim theory. Let us assume that all the electrons emitted are of the same energy (i.e., they tunnel from the Fermi level). Then, the statement of the problem includes Eq. (7) and the set of equations

$$F = F_g - 2\pi\sigma = F_g - 2\pi\int_a^d \rho(x)dx, \qquad (8)$$

$$\rho(x) = j/v(x) = j\{2m/e[U(x) - U(a)]\}^{1/2}, \quad (9)$$

$$U(0) = 0; \; U(a) = Fa; U(d) = V; \; F_g = V/d, \;\; (10)$$

$$a = (\varphi^2 - e^3F)^{1/2}/eF. \qquad (11)$$

Here, F is the electric field strength at the emitter surface with regard to the SC of the electrons emitted, V is the potential difference, d is the emitter–anode distance in the model plane diode, a is the distance between the cathode surface and the site where the electrons escape from under the barrier (the barrier width), and F_g is the field at the cathode for given potential difference V in the absence of the SC (geometric field).

It seems that an exact analytical solution to this problem cannot be obtained, so that numerical methods should be applied. One can estimate the SC effect on FEE, somewhat simplifying the statement of the problem. To this end, it is necessary to calculate the integral in (8). This can be done by taking a certain value of the current density and a certain distribution of the electric

potential in the SC region. The calculation of the integral in (8) yields the following values of the field at the emitter:

$$F = F_g - 2\pi\sigma = F_g - 4\pi(m/2e)sjdV^{-1/2}$$
$$= F_g - 1.9 \times 10^5 sjd^{1/2}F_g^{-1/2}, \tag{12}$$

where s is a coefficient that is equal to 1 for curve 1 and 1.5 for curve 3 in Fig. 2. In (12), j is given in A/cm^2; d, in centimeters; V, in volts; and F and F_g, in V/cm.

Formula (12) gives the absolute value of the field attenuation due to the SC of the electrons emitted. Coefficient s appearing in the formula ($1 < s < 1.5$) characterizes the distortion of the charge density distribution that stems from the fact that the electron motion is not uniformly accelerated motion. It grows with j. The case $s = 1$ means that the SC does not affect the electron motion, while $s = 1.5$ means that the barrier produced by the SC in the electrode gap carries the diode to the off state. This barrier, which adds up with the existing barrier on the emitter surface, is much larger than the latter and may be considered as nontransparent. For these two extremes, the charge density distribution in the electrode gap is known [26, 28] and the ratio of the integrals in (8) equals 1.5. If we take $s = 1.3$, which is a reasonable value for high current densities, we arrive at a formula that is convenient for further analysis:

$$F = F_g - 2.5 \times 10^5 jd^{1/2}F_g^{-1/2}. \tag{13}$$

Introducing the coefficient k of SC-related field attenuation,

$$k = F/F_g,$$

and substituting $F_g = F/k$ into (13) yields the expression

$$2.5 \times 10^5 jd^{1/2}F^{-3/2}k^{3/2} + k - 1 = 0. \tag{14}$$

Substituting a certain value of F and its associated value of j found from Fowler–Nordheim formula (7) into (14), we come to an equation for k. It has a single real root. The results of calculation for two values of the work function (4.5 and 2.0 eV) and several values of d from the interval 10^{-7}–10^{-4} cm are shown in Fig. 3.

DISCUSSION OF THE MODEL

The features of the SC effect on FEE in the plane diode model suggest that it is strongly dependent on the electrode gap value. In FEE experiments and applications, the emitters are made in the form of a tip. These metal tips, smoothed out (blunted) by high-temperature annealing, have the radius of curvature of the top in the range 10^{-5}–10^{-4} cm. Natural and artificial microprotrusions on the surface, the corners of the tip reconstructed, unheated (weakly heated) tips, Spindt cathodes, filamentary crystals, carbon nanotubes, etc., may have radii of curvature on the order of 10^{-7}–10^{-6} cm.

$$k = F/F_g$$
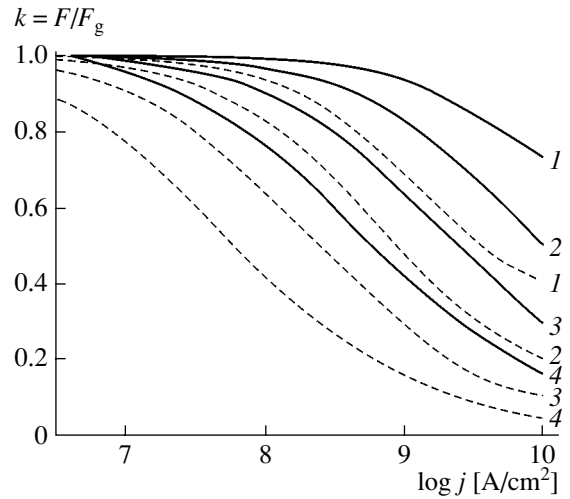
Fig. 3. Field attenuation coefficient k in the planar diode model vs. emission current density j for different electrode spacings d in the model diode. $d = (1)\ 10^{-7}$, $(2)\ 10^{-6}$, $(3)\ 10^{-5}$, and $(4)\ 10^{-4}$ cm. Work function φ equals 4.5 (continuous curves) and 2.0 eV (dashed curves).

The applicability of the plane diode model to the analysis of the SC effect on FEE [19, 20] can be justified as follows. The charge density emitted from the tip rapidly drops with distance to the surface because of the radial divergence of the trajectories and increase in the electron velocity; therefore, the charge at a distance larger than some distance d may be neglected. At the same time, when the spherical geometry of radially divergent trajectories is replaced by parallel trajectories (as in the plane diode model), the charge density increases $[(R + x)/R]^2$ times (R is the tip radius and x is the distance to the tip surface). This offsets the neglect of the charge that is away from the surface. At a some distance d, the offset will be complete and the SC effect on FEE in the plane diode model will be equivalent to the real SC effect at the top of the tip. The equivalent plane diode must have the electrode gap in the interval

$$0.1R < d < R, \tag{15}$$

since, at $d = R$, the charge density on the anode of the model plane diode is four times higher than the actual value (because of the trajectory divergence alone). In [19, 20], d was taken to be equal to 20 nm at $R = 200$ nm; that is, $d = 0.1R$.

One may try to estimate more accurately the thickness of an infinite planar SC layer that produces the same field at the top of the tip as the cone of the electrons emitted by the tip. The SC field strength at the top can be expressed as

$$F = 2\pi j_0 \int_0^\infty dx \int_0^{(x+R)\tan\alpha} x^{3/2}y$$
$$\times [(x+R)^2 + y^2]^{-1}(x^2 + y^2)^{-2}v^{-1}(x, y)dy, \tag{16}$$

where j_0 is the emission current density, R is the radius of the tip, x is the distance to the top along the emission cone axis, α is the apex half-angle, and $v(x, y)$ is the velocity of the electrons at point (x, y).

Numerical estimate (16), which is made under the assumption of uniformly accelerated motion of the electrons, shows that, for $15° < \alpha < 85°$, the thickness of an infinite planar SC layer that is equivalent to an infinite emission cone lies in the interval $0.25R < d < 0.6R$; that is, it is confirmed that condition (15) is valid. For the real geometry of the electrodes, the electron trajectories are not necessarily radially divergent: they may both converge (tip cathodes) and diverge (Spindt cathodes with an extending emitter). One may assume, however, that this factor will hardly violate inequality (15).

When deriving the dependences depicted in Fig. 3, we ignored the effect of the SC-induced screening charges at the emitter surface on the emission. Such a situation is similar to the case where the charge induced on the anode of the model planar diode completely neutralizes the field produced by the screening charge on the cathode. For other electrode configurations, such as the tip emitter–planar anode geometry or Spindt cathodes [3, 29], this neutralization may be incomplete and the SC effect will be akin to the case of a plane capacitor. This reasoning might be taken into account by introducing a coefficient into (12)–(14) that varies between 1 and 2. This coefficient would appear in the term involving j, $d^{1/2}$, and s, which allows for the deviation of the electron motion from uniformly accelerated motion. The allowable variations of these two coefficients are equivalent to a variation of d by less than one order of magnitude.

In view of the aforesaid, one may conclude that the data spread including all the simplifications and assumptions, as well as the difference in electrode configuration, does not exceed the separation between the curves in Fig. 3. It would be incorrect to say that the SC effect shows up at a certain current density. A very strong dependence of this effect on the radius of curvature of the emitter is observed.

The given approach shows in which cases the SC effect on FEE may be disregarded, as well as allows one to estimate the order of the current density at which the SC affects the emission slightly or significantly. From Fig. 3 and condition (15), it follows that, for typical (blunted by high-temperature heating) tips ($R = 10^{-5}$–10^{-4} cm and $\varphi = 4.5$ eV), the effect becomes appreciable (F changes by 1–10%) at $j = 5 \times 10^7$–1×10^8 A/cm^2 and significant (this change attains 50%) at $j \geq 10^9$ A/cm^2 (to obtain such j, the voltage must be increased twice or more compared with the theoretical value). For objects with $R = 10^{-7}$–10^{-6} cm (such as field thermal microprotrusions [16] and carbon nanotubes [30]), the effect is noticeable at $j \sim 10^9$ A/cm^2 and significant at $j \geq 10^{10}$ A/cm^2.

Comparing these values of the current density with those measured in the experiments shows that the values at which the SC effect of the emission becomes tangible are never reached. This is also true for the case where deviation from the Fowler–Nordheim dependence is observed. It seems likely that this deviation is associated not with the presence of the SC but, e.g., with a barrier shape other than that adopted in the Fowler–Nordheim model (this difference may arise at high field strengths [31]).

The SC effect may be expected in going from field electron emission to explosive electron emission [4]. Were the SC effect significant, which the earlier study [8] insists on, one could assume that the SC slows down the transition of FEE to explosive emission and a much higher voltage must be applied to stimulate this transition. However, this is not so in the experiments; it appears, therefore, that the SC does not suppress the emission (electron escape from the emitter surface) in this case too. The SC influences only electron transfer through the vacuum diode that is formed by the expanding plasma surface and anode.

SPHERICAL DIODE

The emitter in FEE applications is usually a tip, and the electrons are emitted from its near-semispherical top. Therefore, the use of the spherical diode model and the adoption of the spherical geometry seem to be logical in considering FEE-related problems. However, as regards the SC effect, such an approach falls far short of being adequate to the reality. The emission is actually localized within a rather narrow solid angle, and the SC is located on one side of the emitting surface. Consequently, all SC regions make a like contribution to the electric field variation at the emitter surface. In the case of the spherical geometry, the SC is located on both sides of a certain emitting area (Fig. 2b). The action of the (actually absent) SC from the "back" side of the emitter-simulating sphere is subtracted from the action of the really existing SC. In this case, net action of the SC arises because the spacings between the SCs on the front and back sides differ, this difference being dependent on the radius of the emitting sphere. In the statement of the problem according to the spherical diode model, this circumstance was disregarded and omitted from the boundary conditions and solution [4, 8, 22–25]. If the SC region had been restricted by the emission cone, the spherical geometry (symmetry) would have lost their advantages and the parameters would have been dependent not only on the radius.

Thus, the spherical diode model is inappropriate for studying the SC effect on FEE. Moreover, the solutions obtained in terms of the spherical diode model suffer the same disadvantages as those derived using the planar diode model: (i) the shape of the SC barrier differs from that of the Fowler–Nordheim barrier and (ii) the

surface of the initial zero electron velocities coincides with the emitter surface.

CHARGE DISCRETENESS

The problem of SC effect on electron emission was first solved for thermionic emission in a planar diode [26] by using Poisson equation (1). The boundary conditions were the zero field at the cathode and a constant potential difference between the electrodes. The same approach was applied to solving the problem for FEE [18–20]. It is assumed by default that the charge density varies insignificantly (and continuously) in space and is time-independent. Otherwise, the differential equations cannot be used. Let us take up the situation for FEE. To this end, we will estimate the mean distance between the emitted electrons near the emitter surface.

The mean time between electron escapes from surface area s at current density j is $t = e/js$. In this time, the electron moving in uniform accelerating field F travels distance $x = eFt^2/2m = e^3F/2j^2s^2m$. Putting $s = x^2$, we arrive at an estimator of the mean distance between the electrons at the emitter surface:

$$x^5 = e^3F/2j^2m. \quad (17)$$

The table lists the mean interelectron distance obtained by (17) and the barrier width at the Fermi level for a work function of 4.5 eV. The interelectron distance is seen to far exceed the barrier width. Consequently, the applicability condition for the differential Poisson equation (the distance between point charges is much less than the characteristic size of a system, $x \ll a$) fails. This conclusion is irrelevant to thermionic emission or current passage through a vacuum diode, where the SC produces a barrier of macroscopic size. Thus, as applied to FEE, the concept of continuous spatial charge distribution may lead to incorrect results and conceal some effects. To estimate the SC effect on FEE, it is necessary to consider the charge distribution as discrete.

The averaging of the effect of individual (point) charges by smearing the total charge over the space may yield results other than those obtained by statistically averaging the effect of the emitted electron charge on the barrier transparency. Furthermore, with the charge discreteness taken into account, the emission current becomes a function of time (frequency). An electron emitted attenuates the field and increases the barrier near the emission site, as though locally suppressing the emission. As the electron moves away, the emission probability rises. This effect is bound to smooth out the emission nonuniformity both over the emitting surface and in time, which is expected to reflect on the noise characteristics of the emission current. The effect of an individual point charge changes not only the width but also the spatial configuration of the barrier, making it locally "convex." A "corrugated"

Calculated barrier width a and mean distance x between electrons emitted vs. field F and emission current density j. The calculation was made in terms of the Fowler–Nordheim model for a work function of 4.5 eV

F, V/nm	$\log j$ [A/cm^2]	x, nm	a, nm
5	5.59	5885	0.72
6	6.62	2383	0.57
7	7.36	1245	0.46
8	7.94	751	0.34
9	8.39	508	0.27
10	8.76	369	0.25
12	9.32	288	0.23
14	9.94	134	0.22

time-variable barrier arises. This may also influence the angular distributions of the electrons emitted.

The effect of an individual electron emitted cannot be considered in terms of the one-dimensional planar model. Moreover, the calculated value of the field produced by the electron at the surface cannot be used as a correction to the applied field in the Fowler–Nordheim formula. To find the shape and transparency of the barrier, it is necessary to consider the potential energy of the metal–emitted electrons–virtual electron (i.e., the electron that is trying to be emitted) system as a function of the virtual (probing) electron coordinate. It is also desirable to consider the interaction of the virtual electron with other electrodes. Let the emitter surface be assumed to be planar and the interaction with one electron emitted be considered (Fig. 4). Then, the part of the potential energy of the system that depends on probing (virtual) electron coordinate x is the sum of the energy of the virtual electron in the external field $-eFx$, the energy of interaction between the electron and metal (mirror image) $-e^2/4x$, the energy of interaction between the electrons $e^2/[(h - x)^2 + y^2]^{1/2}$, and the energy of interaction between the charges induced by both electrons on the metal surface (mirror images) $-e^2/[(h + x)^2 + y^2]^{1/2}$. Here, h is the distance from the emitted electron to the surface and y is the distance between the normal projections of the electrons onto the emitter plane. The first two terms specify the barrier in the Fowler–Nordheim model, and the others describe
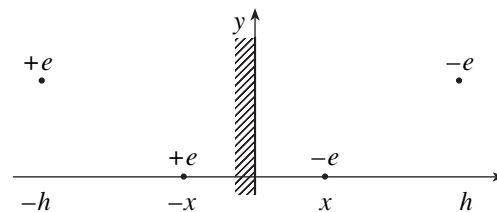

Fig. 4. Schematic representation of interaction between the emitted and virtual (probing) electrons.

the SC effect as such. The energy versus x dependence rapidly decreases with increasing h and y. Therefore, the interaction with the electron nearest to the emission site presumed is a factor controlling the variation of the barrier. If it is assumed that the electrons are emitted at regular intervals and $y = 0$, the energy of interaction with the nearest electron exceeds the energy of interaction with other electrons (from the second one on). The energy of interaction and the transparency of the barrier strongly depend on h and, hence, on the time elapsed from the electron escape.

Thus, if the SC of the electrons emitted is viewed as distributed, its effect on the emission may be weak. Conversely, the consideration of the point charge motion shows that the electrons emitted may change both the total emission current (because the surface is partially "cut off") and the electron distribution.

CONCLUSIONS

(1) If the problem of the space charge effect on field electron emission is tackled by solving the Poisson equation and calculating the field at the SC–emitter interface, this effect turns out to be overestimated. Depending on the radius of curvature of the emitter surface and the electrode configuration, the current density at which this effect shows up may differ by several orders of magnitude. None of the works yet published have reported the current density values at which the SC effect on FEE is significant. It can be therefore argued that the observed deviations from the Fowler–Nordheim dependence are associated with other reasons.

(2) As applied to the SC effect on FEE, the spherical diode model fails, since it erroneously assumes the presence of the SC on the back side of the emitting surface.

(3) Considering the discrete nature of the charges shows that the emitted electron charge may locally affect the emission even if it does not macroscopically limit the current. These local effects may influence not only the emission current but also the noise characteristics of the emission, the emission uniformity over the emitting surface and in time, and the energy and angular distributions of the electrons emitted.

REFERENCES

1. R. G. Forbes, Solid-State Electron. **45**, 779 (2001).
2. M. A. Guillorn, X. Yang, A. V. Melechko, *et al.*, J. Vac. Sci. Technol. B **22**, 35 (2004).
3. C. A. Spindt, J. Appl. Phys. **39**, 3504 (1968).
4. *Nonincandescent Cathodes*, Ed. by M. I. Elinson (Sov. Radio, Moscow, 1974) [in Russian].
5. W. A. Anderson, J. Vac. Sci. Technol. B **11**, 383 (1993).
6. Y. Y. Lau, Y. Liu, and R. K. Parker, Phys. Plasmas **1**, 2082 (1994).
7. G. N. A. Van Veen, J. Vac. Sci. Technol. B **12**, 655 (1994).
8. A. V. Batrakov, I. V. Pegel', and D. I. Proskurovskiĭ, Pis'ma Zh. Tekh. Fiz. **25** (11), 78 (1999) [Tech. Phys. Lett. **25**, 454 (1999)].
9. D. Morris, B. Gilchrist, and A. Gallimore, AIP Conf. Proc. **552**, 467 (2001).
10. A. Rabinovich, Surf. Sci. **70**, 181 (1978).
11. R. G. Forbes, in *Proceedings of the 9th International Vacuum Microelectronics Conference, St. Petersburg, 1996*, pp. 58–64.
12. G. N. Fursey and D. V. Glazanov, J. Vac. Sci. Technol. B **16**, 910 (1998).
13. A. Modinos, Solid-State Electron. **45**, 809 (2001).
14. K. Yuasa, A. Shimoi, I. Ohba, and Ch. Oshima, Surf. Sci. **520**, 18 (2002).
15. K. L. Jensen, E. G. Zaidman, and M. A. Kodis, AIP Conf. Proc. **391**, 95 (1997).
16. V. G. Pavlov, A. A. Rabinovich, and V. N. Shrednik, Zh. Tekh. Fiz. **45**, 2126 (1975) [Sov. Phys. Tech. Phys. **20**, 1337 (1975)].
17. G. N. Fursey, L. M. Baskin, D. V. Glasanov, *et al.*, J. Vac. Sci. Technol. B **16**, 232 (1998).
18. T. E. Stern, B. S. Gossling, and R. H. Fowler, Proc. R. Soc. London, Ser. A **124**, 699 (1929).
19. W. P. Dyke and J. K. Trolan, Phys. Rev. **89**, 799 (1953).
20. J. P. Barbour, W. W. Dolan, J. K. Trolan, *et al.*, Phys. Rev. **92**, 45 (1953).
21. S. Liu and R. A. Dougal, J. Appl. Phys. **78**, 5919 (1995).
22. N. B. Aĭzenberg, Zh. Tekh. Fiz. **24**, 2079 (1954).
23. A. S. Kompaneets, Dokl. Akad. Nauk SSSR **128**, 1160 (1959) [Sov. Phys. Dokl. **4**, 1077 (1959)].
24. V. A. Gor'kov, M. I. Elinson, and V. B. Sandomirskiĭ, Radiotekh. Élektron. (Moscow), No. 7, 1495 (1962).
25. N. B. Aĭzenberg, Radiotekh. Élektron. (Moscow), No. 12, 2147 (1964).
26. C. D. Child, Phys. Rev. **31**, 492 (1911).
27. I. Langmuir, Phys. Rev. **2**, 450 (1913).
28. L. N. Dobretsov and M. V. Gomoyunova, *Emission Electronics* (Nauka, Moscow, 1966) [in Russian].
29. W. Jarupoonphol, K. Murakami, K. Sakata, *et al.*, J. Vac. Sci. Technol. B **21**, 1598 (2003).
30. K. Nagaoka, H. Fujii, K. Matsuda, *et al.*, Appl. Surf. Sci. **182**, 12 (2001).
31. C. D. Lewis, Phys. Rev. **101**, 1694 (1956).

Translated by V. Isaakyan

SURFACES,
ELECTRON AND ION EMISSION

Adsorption and Electron Properties of Thin Nickel Films on W(110) Surface

T. T. Magkoev[1], M. Song[2], T. Magome[2], and Y. Murata[2]

[1] *North Ossetian State University, Vladikavkaz, North Ossetia (Alania), 362020 Russia*
[2] *Institute for Solid State Physics, University of Tokyo, Tokyo 106, Japan*
e-mail: magkoev@osetia.ru
Received March 23, 2004

Abstract—The evolution of the properties of ordered nickel films with thicknesses increasing from one to three atomic monolayers (ML) adsorbed on the W(110) single crystal surface is studied under ultrahigh vacuum conditions by the methods of reflection–absorption infrared spectroscopy (RAIRS) and ultraviolet photoelectron spectroscopy (UPS). The film structure corresponds to that of the Ni(111) single crystal face. The RAIRS technique is used to study the vibrational properties of the probing NO molecules adsorbed on the nickel films studied. In the course of the nickel film growth, whereby its thickness increases from 1 to 3 ML, both the vibrational and photoelectron spectra exhibit significant variation, which is indicative of a change in the adsorption and electron properties of the film. Stabilization of the IR and photoelectron spectra at a film thickness of 3 ML indicates that this thickness corresponds to the formation of the main adsorption and electron properties of the deposit. At the same time, the vibrational spectra of NO molecules adsorbed on a monoatomic nickel film exhibit features typical of adsorption on the W[110] surface of a massive tungsten crystal. © *2004 MAIK "Nauka/Interperiodica".*

The adsorption of metals and the formation of metal films on solid surfaces have been extensively studied for many years because these processes are of considerable interest from the standpoints of both basic science and applications [1]. Despite this research activity, many questions still remain unanswered [1]. One of these questions concerns the thickness of a metal film at which its properties are close to those of the bulk material. According to one point of view, even a monoatomic metal film on the surface of a metal substrate possesses all the main adsorption and electron properties inherent in the bulk metal; a more commonly accepted notion is that this requires at least a few tens of monolayers [1–3].

This paper presents the results of our investigation into the laws of evolution of the electron properties of thin nickel films in the course of their growth on the (110)-oriented tungsten crystal surface. The samples were studied by the methods of IR and ultraviolet photoelectron spectroscopy (UPS). This film–substrate system was selected because of the possibility of obtaining a sharp Ni/W(110) interface with continuous well-ordered nickel films forming beginning with submonolayer coverages [4–6].

EXPERIMENTAL

The experiments were performed under ultrahigh vacuum (UHV) ($P = 10^{-10}$ Torr) conditions. The sample surface was studied by reflection-absorption IR spectroscopy (RAIRS) and by UPS with a synchrotron radiation source.

RAIRS is advantageous for investigation of the electron and adsorption properties of metal films on metal substrates because the properties of some molecules (e.g., NO and CO) adsorbed on the surface of such films are determined by the electron properties of substrates 7, 8. One such parameter, which is most sensitive to the state of the substrate, is the frequency of intramolecular vibrations. This vibrational frequency is determined by redistribution of the electron density between molecular orbitals of the adsorbate and the electron states of the substrate in the course of chemisorption [8]. In this study, the role of such a probing adsorbate, the properties of which provide information on the state of a Ni film deposited on the W(110) surface, was performed by nitric oxide (NO). The results of some previous investigations showed that NO molecules are extremely sensitive to the state of the metal substrate on which the adsorption takes place [9]. The RAIRS measurements were performed with a Nicolet Nexus 870 IR spectrometer. The monochromator and detector parts of the instrument were arranged relative to the sample so as to ensure glancing incidence (~85°) of the probing IR beam on the sample surface. In this geometry, RAIRS is most effective for the study of molecules adsorbed on the surface of metal substrates [10].

The UPS measurements were performed in the Synchrotron Laboratory at the Institute for Solid State Physics (University of Tokyo). The photoelectron energies were analyzed with a double-focusing cylindrical

mirror analyzer. The angles of the primary radiation beam relative to the sample surface normal and the energy analyzer axis were 50° and 90°, respectively. The UHV system allowed the sample surface to be additionally characterized by the methods of low energy electron diffraction (LEED) and Auger electron spectroscopy (AES).

The W(110) crystal surface was preliminarily cleaned using the standard procedures of annealing in oxygen followed by high-temperature flashing. Nickel films on the W(110) substrate were formed by means of thermal evaporation in vacuum. In order to compare the properties of Ni films to those of the massive metal, a reference Ni(111) crystal was mounted in the same spectrometer chamber. The adsorption of NO molecules on the surface of samples was performed at a substrate temperature of 110 K. The methods of investigation and the formation of nickel films are described in more detail elsewhere [11–13].
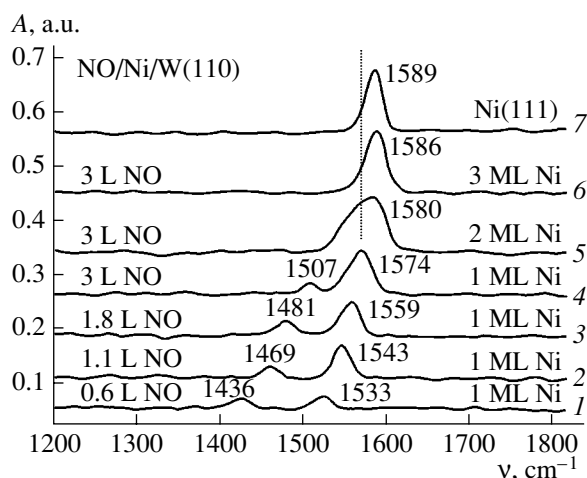
RESULTS AND DISCUSSION

The structure of nickel films deposited in vacuum on the W(110) crystal surface has been studied in sufficient detail [4–6]. Continuous films possess a hexagonal symmetry characteristic of the Ni(111) crystal face. At a monolayer coverage ($\theta_{Ni} = 1$ ML), the film structure is distorted because of a certain misfit between crystal lattices of the deposit and substrate. As the coverage increases to 5 ML, the film acquires a nondistorted structure corresponding to the Ni(111) crystal surface. In this context, it was of interest to compare the behavior of NO molecules adsorbed on the surface of a

Fig. 1. IR absorption spectra $A(\nu)$ of NO molecules adsorbed on the surface of Ni/W(110) films with thicknesses of (*1–4*) 1, (*5*) 2, and (*6*) 3 ML and (*7*) on a bulk Ni(111) crystal. The substrate temperature during adsorption was 110 K. Curves (*1–4*) correspond to the adsorption of NO at various exposures on a 1-ML-thick Ni film. The NO exposure corresponding to saturation is 3 L.

thin Ni film and on a bulk nickel crystal of the same orientation.

Figure 1 shows the IR absorption spectra of the system NO/Ni/W(110) for (111)Ni films with thicknesses corresponding to 1, 2 and 3 ML. Here, spectra *1–4* correspond to NO adsorption on a 1-ML-thick Ni film under conditions of increasing NO exposure. For an exposure of 0.6 L (1 L = 10^{-6} Torr s), the spectrum displays two absorption bands peaked at the wavenumbers $\nu = 1436$ and 1533 cm^{-1}. As the NO exposure increases, these absorption bands shift toward higher wavenumbers and become closer to each other. At a saturation exposure (3 L), the spectrum consists of two absorption bands of different intensities with maxima at 1507 and 1574 cm^{-1}. As the exposure increases further, the spectrum exhibits no significant changes. The absence of an absorption band at 1880 cm^{-1} (this band is usually related to dissociation of NO molecules [14]) suggests that the monolayer nickel coverage suppresses the ability of the W(110) surface to induce the decomposition of NO molecules.

The IR spectrum of NO adsorbed on a monoatomic film differs from the spectra observed upon NO adsorption on the surface of a bulk Ni(111) crystal. In the latter case, the spectrum contains a single absorption band, which shifts with increasing NO exposure toward higher wavenumbers until reaching a value of 1587 cm^{-1} for the saturation exposure. It is believed that this band is due to the intramolecular vibrations of NO adsorbed in the twofold bridge site configuration, and the increase in the peak wavenumber with the exposure is explained by a change in the geometry of this configuration from sloped (at small coverages) to perpendicular at saturation [15]. Figure 1 presents the spectrum of NO adsorbed on the Ni(111) crystal at a saturation exposure (curve *7*), showing an absorption band peaked at $\nu = 1589$ cm^{-1}. With a comparison of this spectrum to that of NO adsorbed on a monoatomic film, we may conclude that the film (in contrast to the crystal) features two types (rather than one) of adsorbed NO molecules with different intramolecular vibration frequencies (1507 and 1574 cm^{-1}). The proximity of the latter value to the ν(NO) for the bulk crystal (1589 cm^{-1}) suggests that the surface of the monoatomic Ni film contains adsorption centers that are close with respect to geometry and electron structure to those existing on the bulk Ni(111) crystal. At the same time, a certain difference in frequencies of these NO vibrations ($\Delta\nu = 15$ cm^{-1}) and especially the presence of the additional band at $\nu = 1507$ cm^{-1} (see spectrum *4*) indicate that the properties of the monoatomic Ni film with a (111) structure formed on the W(110) substrate are not perfectly identical to those of the bulk Ni(111) crystal.

When NO molecules are adsorbed on a nickel film with a thickness of 2 ML, the less intense low-frequency band is not observed in the IR spectrum, while the more intense band shifts from 1574 to 1580 cm^{-1}

and exhibits broadening (Fig. 1, curve *5*). Apparently, we may assume that the separation of bands initially located at 1507 and 1574 cm^{-1} (curve *4*) further decreases for NO adsorbed on the 2-ML-thick film, and it is the superposition of two bands that accounts for the observed broadening (curve *5*). As the nickel film thickness increases to 3 ML, the absorption band exhibits narrowing and shifts to 1586 cm^{-1} (Fig. 1, curve *6*). The good coincidence of the shape and position of this band with those observed for NO adsorption on the bulk crystal surface (cf. curves *6* and *7*) allows us to suggest that the adsorption properties of the (111)-oriented nickel film with a thickness of 3 ML are virtually identical to those of the bulk Ni(111) crystal.

The observed evolution of the IR absorption spectra (curves *4–6*) with increasing thickness of the nickel film can be explained by changes in the degree of influence of the W(110) substrate on the intramolecular NO bond characteristics and in the structure of Ni deposit with increasing thickness. Although the 1-, 2-, and 3-ML-thick films exhibit LEED patterns corresponding to that from the Ni(111) crystal face, the aforementioned misfit between crystallographic directions and crystal lattice parameters of W(110) and Ni(111) results in a small (~7%) distortion of the (111) structure as compared to that of the Ni(111) surface [4–6]. Such a distortion in the adsorbate superstructure for a monolayer coverage is related to the possibility of Ni(111) domain formation as a result of adsorption of Ni atoms at the threefold hole adsorption centers. The structure of such a film can be represented as a superposition of the (111) structures of two types formed as a result of occupation of the tetrahedral and octahedral voids. The region of contact of the superstructures of two types features a distortion of the orientation characteristic of Ni(111). As the subsequent atomic layers are deposited, these distortions tend to decrease.

In this context, we may suggest that the low-energy (low-frequency) band (1507 cm^{-1}) in the absorption spectrum of NO adsorbed on a monoatomic Ni film is related to NO molecules adsorbed at the domain boundaries. As the nickel film thickness increases, the intensity of this absorption band decreases because the film structure approaches that typical of the nondistorted Ni(111) surface. This explanation is consistent with the recently observed decrease in mechanical stresses in a Ni film on a W(110) surface at a nickel coverage exceeding 1 ML [16]. In addition, the almost complete relaxation of stresses at a film thickness corresponding to θ_{Ni} = 3 ML [16] is in good agreement with the fact of stabilization of the vibrational properties of NO molecules adsorbed on such films. Another, still less evident distinction between the IR spectra of NO adsorbed on 1- and 3-ML-thick Ni films is that the wavenumber of the dominating absorption band in the former case is smaller by 12 cm^{-1}. This difference is indicative of a somewhat different electron state of the adsorbed molecules in the two cases. Apparently, this difference is

related, in turn, to a difference between the electron states of Ni films with different thicknesses.

In order to trace the variation of the electron state depending on the film thickness, we have measured the UPS spectra of the Ni/W(110) system. These spectra are presented in Fig. 2a. As can be seen, the presence of even submonolayer nickel coverage (θ_{Ni} = 0.5 ML) leads to a dramatic change in the energy distribution of photoelectrons emitted from W(110). The main peculiarity is the appearance of a rather intense peak at 0.7 eV. This peak is related to a localized *d*-state of Ni [17]. In addition, there is a shift in the energy of the photoemission peak of W at 1.8 eV (by 0.2 eV toward lower binding energies). This behavior is evidence of a significant redistribution of the electron density as a result of the formation of the Ni–W(110) chemisorption bond. Additional evidence is provided by the appearance of a new peak near the Fermi level (at 0.15 eV), which acquires the maximum intensity at a coverage of 1 ML, significantly decreases at θ_{Ni} = 2 ML, and almost completely disappears at 3 ML. The
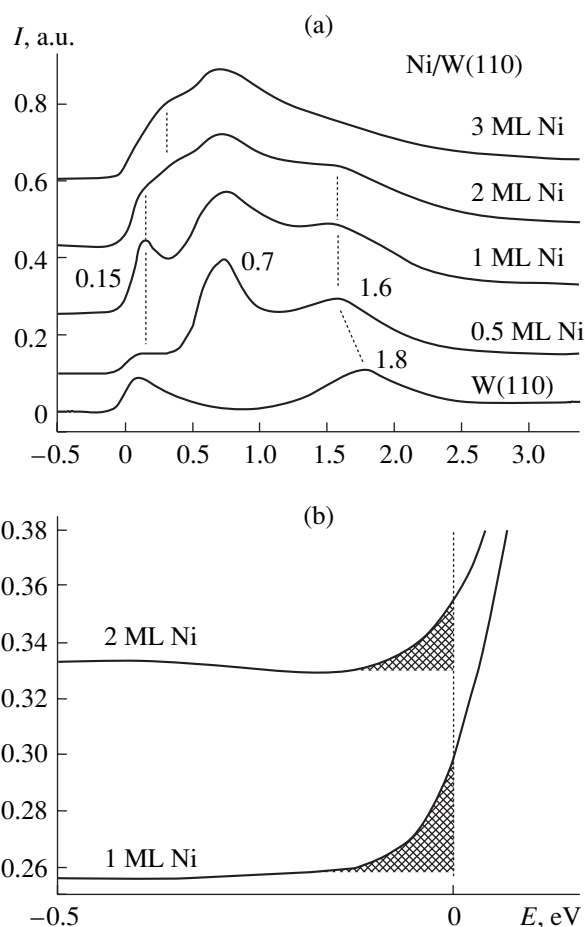
Fig. 2. UPS spectra of the Ni/W(110) system: (a) the spectra for various Ni coverages measured for the photoelectrons emitted along the normal to the sample surface; (b) comparison of the spectra near the Fermi level for the 1- and 2-ML-thick Ni films.
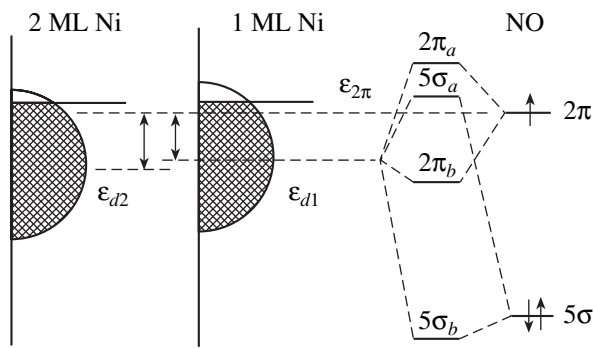
Fig. 3. Schematic diagram illustrating the influence of occupation of the valence band of Ni on the efficiency of interaction in the NO adsorbate–substrate system.

fact that the maximum intensity of this peak is observed at $\theta_{Ni} = 1$ ML indicates that this feature is related to the properties of the Ni/W(110) interface. This interpretation is consistent with the behavior of the peak at 1.6 eV related to the formation of the adsorption bond, the intensity of which also decreases when the nickel coverage increases above 1 ML. A sharp drop in intensity of the peak near the Fermi level, which is observed when the Ni film thickness increases from 1 to 2 ML, indicates that the properties of the interface are subject to significant changes upon this transition. Apparently, the film growth leads to a difference in the electron properties of Ni atoms occurring in the first and second atomic layers, which is manifested by a difference of the UPS spectra observed for the 1- and 2-ML-thick films. A more thorough analysis of these spectra in the region of the Fermi level (Fig. 2b) reveals that the density of states at $E = E_f$ in the latter case ($\theta_{Ni} = 2$ ML) is somewhat reduced as compared to that for the 1-ML coverage. This behavior indicates that the center of the valence band of Ni is shifted toward higher binding energies on the passage from 1- to 2-ML-thick film.

This situation is schematically depicted in Fig. 3. The results of calculations of the properties of systems formed as a result of the adsorption of NO molecules on the surface of some transition metals showed that the efficiency of interaction between molecular orbitals (MOs) and, hence, of the electron exchange with the substrate is determined by the proximity of the energy of the corresponding MO to the center of the valence band of the given metal [8]. In particular, the energy of interaction between the antibonding 2π MO and the substrate ($E_{d-\pi}$) is described by the relation [8]

$$ E_{d-\pi} \approx -4 f \frac{V_\pi^2}{\varepsilon_{2\pi} - \varepsilon_d}, $$

where f is the d-band occupancy, V is the matrix element of the interaction, and $\varepsilon_{2\pi}$ and ε_d are the energy positions of the 2π orbital and the d-band center, respectively.

This analysis shows that the efficiency of interaction between the MOs of the adsorbate and the valence band of the metal increases when the corresponding energies approach each other. Figure 3 shows, in addition to the scheme of the valence band filling accompanied by the shift of the band center ($\varepsilon_{d2}\varepsilon_{d1}$), the MOs of the free and adsorbed NO molecules. The latter are constructed based on the results of measurements performed for the NO/Ni(111) system by direct (for the occupied bands) [18] and reverse (for the free bands) [19] UPS techniques. As can be seen, the $\varepsilon_{2\pi} - \varepsilon_d$ difference for the monoatomic film is smaller than that for the 2-ML-thick film. With allowance for the above relation, this implies that the efficiency of interaction between the antibonding 2π MO of NO and the (1 ML)Ni/W(110) system in the former case is higher. This results in a lower strength of the intramolecular NO bond on the surface of the monoatomic film as compared to the case of a 2-ML or thicker film. This weakening of the bond, in turn, must lead to a decrease in the frequency of intramolecular vibrations—in agreement with what is revealed by the comparison of the corresponding IR absorption spectra (Fig. 1).

Thus, differences between the properties of a monoatomic Ni film and those of thicker (2- and 3-ML-thick) films manifested in the vibrational spectra of adsorbed NO molecules can be subdivided into two types: structural and electron. A difference in the geometric structure leads to the appearance of an additional absorption band at 1507 cm⁻¹ in the IR spectrum of NO adsorbed on a 1-ML-thick Ni film on W(110). A difference in the electron properties is manifested by a 12 cm⁻¹ shift between the frequencies of intramolecular vibrations corresponding to the main absorption bands. Of course, this separation of the two effects is rather conditional because the geometric structure and the electron state of the adsorption system are mutually interrelated. As the deposit thickness increases, the properties of the film exhibit stabilization and, at $\theta_{Ni} = 3$ ML (Fig. 3), correspond to the properties observed for a bulk crystal. This statement is confirmed by the results of measurements of mechanical stresses in a Ni film on a W(110) surface, which also reached a stationary level for a nickel coverage close to 3 ML [16].

The notion of the system properties being stabilized at $\theta_{Ni} = 3$ ML somewhat contradicts the fact of stabilization of the work function φ observed at a significantly lower coverage (~1 ML) [4]. However, the work function was measured by the retarded electron beam technique (Anderson's method), whereby the obtained φ values possess an average character and are insensitive to structural features (such as defects, islands, and domain walls) on the sample surface, the effective dimensions of which are smaller than the coherence length (~300–400 Å) of electrons with the energies employed. Moreover, the work function is also weakly sensitive with respect to details of the surface electron structure and is determined predominantly by the

mutual arrangement of the Fermi level and the vacuum level. Nevertheless, the fact of stabilization of the φ value at a monoatomic coverage is a good qualitative test for the formation of the main properties of a film on the whole, followed by the final formation of some details of the electron structure [1].

These considerations are consistent with the behavior of the IR spectra of NO adsorbed on the surface of nickel films of various thicknesses. Despite the fact that the spectra corresponding to the nickel coverages of 1, 2, and 3 ML differ from each other, these spectra exhibit an important common feature. Indeed, the dominating absorption band in all these spectra is that with a maximum at 1580–1590 cm^{-1}. At θ_{Ni} = 1 ML, the spectrum displays a band at 1574 cm^{-1}, which rather insignificantly (by ~12 cm^{-1}) changes its position when the film thickness increases further. This variation of ν(NO) can be considered insignificant in comparison with a change accompanying the growth of the surface concentration of NO on the surface of the same substrate: in particular, for a Ni(111) surface, this change reaches ~140 cm^{-1} [14, 15]. By the same token, a difference in the ν values for the molecules adsorbed on samples of the same material (Ni) with different surface structures may also reach a considerable level (up to 60 cm^{-1} [9]). Taking these facts into account, we may believe that the proximity of the ν(NO) wavenumbers for θ_{Ni} = 1 ML (1574 cm^{-1}) and 2–3 ML (1586 cm^{-1}) indicates that the electron properties of a monoatomic metal film are quite close to those of thicker films. Since the frequency of the intramolecular vibrations is highly sensitive to the electron state of a molecule and this state, in turn, is determined by the electron state of the substrate [7, 8], we may ascertain that the properties of a film are formed predominantly during filling of the first atomic monolayer. However, according to the data presented in Figs. 1 and 2, the final formation of some details of the electron structure require the presence of at least three atomic layers with a structure corresponding to that of the given bulk crystal face.

It should be noted that, for the adsorption of most metals on metal substrates, stabilization of the concentration dependence of the work function is observed upon the formation of a continuous monoatomic layer [1, 20]. In addition, in some cases, the low-energy electron loss spectra also show the appearance of the lines due to plasmon losses typical of thick adsorbate layers [21, 22]. This behavior suggests that the formation of the main features of the electron properties of adsorbed films on reaching a thickness of 1 ML is in common for adsorbates possessing metallic properties. For the formation of the electron properties inherent in bulk metals, it is necessary that discrete valence atomic levels broaden so as to form the corresponding electron bands. On the surface of a substrate, this process is possible by virtue of at least two factors: (i) "smearing" of a discrete level of a singe adatom into a band in accordance with the Gurney model [20] and (ii) further

broadening of the level and the resulting band formation due to lateral interaction between adatoms increasing with the coverage. Apparently, the extent of collectivization of electrons reaches a level at which a band is formed with a width comparable with that of the valence band of a bulk metal. This suggestion is confirmed, in particular, by the formation of collective properties (plasmons) of such itinerant electrons in a film observed already for a monolayer coverage [21, 22]. Additional evidence is provided by the fact that a maximum in the density of the d states of Ni at an energy of 0.7 eV below the Fermi level is already formed at a film thickness of 1 ML (Fig. 2a). As the film thickness grows further, this maximum exhibits no significant changes. Another piece of evidence is the appearance of a dominating vibrational frequency manifested in the IR spectrum of a monoatomic film at a wavenumber (1574 cm^{-1}) close to the value characteristic of a bulk crystal (1589 cm^{-1}) (see Fig. 1, curves *4* and *7*).

Thus, we may conclude that the adsorption and electron properties of continuous ordered nickel films with a structure corresponding to that of the Ni(111) face, grown on a W(110) substrate surface, consistently evolve as the film thickness increases from 1 to 3 ML. This is evidenced, on the one hand, by variation of the vibrational spectra of the probing NO molecules adsorbed on the surface of nickel and, on the other hand, by variation of the photoelectron spectra of the valence band of the Ni/W(110) system with increasing Ni film thickness. Stabilization of both the IR and UPS spectra observed for a deposit thickness corresponding to 3 ML suggests that the formation of the main adsorption and electron properties of the Ni film is accomplished at this very film thickness. At the same time, even a monoatomic film exhibits features characteristic of a bulk metal crystal.

REFERENCES

1. *Handbook of Surface Science: Electronic Structure*, Ed. by K. Horn and M. Scheffler (Elsevier, Amsterdam, 2000).
2. *Growth and Properties of Ultrathin Epitaxial Layers*, Ed. by D. A. King and D. P. Woodruff (Elsevier, Amsterdam, 1997).
3. R. D. Diehl and R. McGrath, J. Phys.: Condens. Matter **9**, 951 (1997).
4. J. Kolaczkiewicz and E. Bauer, Surf. Sci. **144**, 495 (1984).
5. C. Schmidthals, D. Sander, A. Enders, *et al.*, Surf. Sci. **417**, 361 (1998).
6. J. H. van der Merwe, E. Bauer, D. L. Toensing, *et al.*, Phys. Rev. B **49**, 2127 (1994).
7. G. Blyholder, J. Phys. Chem. **68**, 2772 (1964).
8. Y. Morikawa, J. J. Mortensen, B. Hammer, *et al.*, Surf. Sci. **386**, 67 (1997).
9. W. A. Brown and D. A. King, J. Phys. Chem. B **104**, 2578 (2000).

10. R. G. Greenler, J. Vac. Sci. Technol. **12**, 1410 (1975).

11. T. T. Magkoev and M. Song, Poverkhnost, No. 11, 45 (1999).

12. T. T. Magkoev, K. Fukutani, M. B. Song, *et al.*, Surf. Sci. **363**, 281 (1996).

13. K. Fukutani, T. T. Magkoev, Y. Murata, *et al.*, J. Electron Spectrosc. Relat. Phenom. **88–91**, 597 (1998).

14. J. G. Chen, W. Erley, and H. Ibach, Surf. Sci. **227**, 79 (1990).

15. J. L. Gland and B. Sexton, Surf. Sci. **94**, 355 (1980).

16. D. Sander, C. Schmidthals, A. Enders, *et al.*, Phys. Rev. B **57**, 1406 (1998).

17. H. Tsunematsu, M. Aita, A. Tanaka, *et al.*, J. Electron Spectrosc. Relat. Phenom. **101–103**, 281 (1999).

18. H. P. Bonzel and G. Pirug, Surf. Sci. **62**, 45 (1977).

19. G. Rangelov, N. Memmel, E. Bertel, *et al.*, Surf. Sci. **251–252**, 965 (1991).

20. L. A. Bol'shov, A. Napartovich, A. G. Naumovets, and A. G. Fedorus, Usp. Fiz. Nauk **122**, 125 (1977) [Sov. Phys. Usp. **20**, 432 (1977)].

21. A. G. Eguiluz and D. A. Campbell, Phys. Rev. B **31**, 7572 (1985).

22. A. Liebsch, *Electronic Excitations at Metal Surfaces* (Plenum, New York, 1997).

Translated by P. Pozdeev

BRIEF
COMMUNICATIONS

Effect of Nitrogen Concentration on the Magnetic Properties of Fe–Ta–N Thin Films

A. S. Kamzin[1], S. Yu. Mal'tsev[1], S. A. Kamzin[1], Fulin Wei[2], and Zheng Yang[2]

[1] *Ioffe Physicotechnical Institute, Russian Academy of Sciences, St. Petersburg, 194021 Russia*
[2] *Scientific Research Institute of Magnetic Materials, Lanzhou University 730000 Lanzhou, China*
e-mail: Kamzin@pop.ioffe.rssi.ru
Received April 2, 2004

Abstract—Soft magnetic nanocrystalline thin films with a high content of Ta (10 wt %) are synthesized by the method of reactive RF magnetron sputtering with subsequent annealing. It is established that the microstructure and magnetic properties of the films depend on the nitrogen partial pressure during sputtering and on the annealing temperature. Annealing of the amorphous films leads to the formation of α-Fe nanocrystallites whose properties and interactions determine the film parameters. A decrease in the α-Fe grain size to a level below the length of ferromagnetic exchange interaction sharply increases the magnetic softness. The role of nitrogen ions in the formation of a α-Fe nanocrystallite structure and uniaxial magnetic anisotropy of Fe–Ta–N films is established. The optimum technological regimes of deposition and annealing of the Fe–Ta–N films are determined, which ensure the synthesis of Fe–Ta–N nanocrystalline thin films with a high magnetic softness ($B_s = 1.6$ T, $H_c = 0.2$ Oe, and $\mu_1(1$ MHz$) = 3400$). © 2004 MAIK "Nauka/Interperiodica".

The need to increase data recording density stimulates the search for new magnetic carriers and the development of write–read devices based on soft magnetic films with high saturation magnetization M_s and high magnetic permeability [1]. The intricate temperature regimes of operation for such devices pose additional requirements for the thermal stability of the material parameters. Fe–M–N films, where M is a doping element (including Ta, Nb, Zr, Hf or Al [2–4]) introduced to increase their thermal stability, meet such requirements [5–9]. However, ions of various types introduced as the third element have different effects on the magnetic properties of the material.

It was shown [5] that Fe–M–N thin films with a small content of dopant M immediately after deposition are characterized by a nanocrystalline structure and possess soft magnetic properties, while as-deposited films with a high dopant content are amorphous [5, 10]. It was suggested [5,10] that introducing Ta substantially improves the magnetic softness of Fe–N films due to a relatively strong interaction between Ta and nitrogen ions [11], which increases the solubility of N atoms in the Fe–Ta–N system and decreases the α-Fe grain size [12]. The most effective method of obtaining magnetically soft materials consists in annealing amorphous Fe–M–N compositions. The properties of the magnetic materials synthesized using this method depend both on the deposition regime and on the regime of thermal treatment of the deposited compounds. In this connection, investigations of the influence of the regime of synthesis on the microstructure and magnetic properties of Fe–Ta–N films with high

content of Ta ions, aimed at obtaining materials with the required properties, are of great interest.

Thin Fe–Ta–N films were deposited on glass substrates by reactive RF magnetron sputtering of a target in a gaseous mixture of Ar and N_2. The target was a plate of pure iron, with a 20% fraction of the area covered by a Ta foil. The experiments showed that RF sputtering of such a composite target leads to the deposition of Fe–Ta–N films with 10% of Fe ions replaced by Ta ions. The content of N ions depends on the partial pressure of nitrogen in the Ar–N_2 gas mixture in the chamber during the film deposition. The Fe–Ta–N films were deposited under the following conditions: residual pressure in the chamber, 5×10^{-7} Torr; gas pressure during the deposition, 2×10^{-3} Torr; partial pressure of nitrogen, 0–10%, RF bias voltage, 2.8 kV; substrate temperature, 20°C; film thickness, 400 nm; deposition rate, 20–28 nm/min. After deposition, the films were annealed in a vacuum furnace at a residual pressure of ~10^{-5} Torr.

The film structure was studied by X-ray diffraction (XRD). The phase analysis was carried out by XRD and Mössbauer spectroscopy. The film morphology was studied by transmission electron microscopy and atomic force microscopy. The saturation magnetization M_s of the films was measured using a highly sensitive vibrating-sample magnetometer. The energy of anisotropy was calculated from B–H hysteresis loops as described in [13].

Figure 1 shows the X-ray diffraction patterns of samples deposited at various partial pressures $P(N_2)$ of nitrogen and measured (Fig. 1a) immediately after dep-
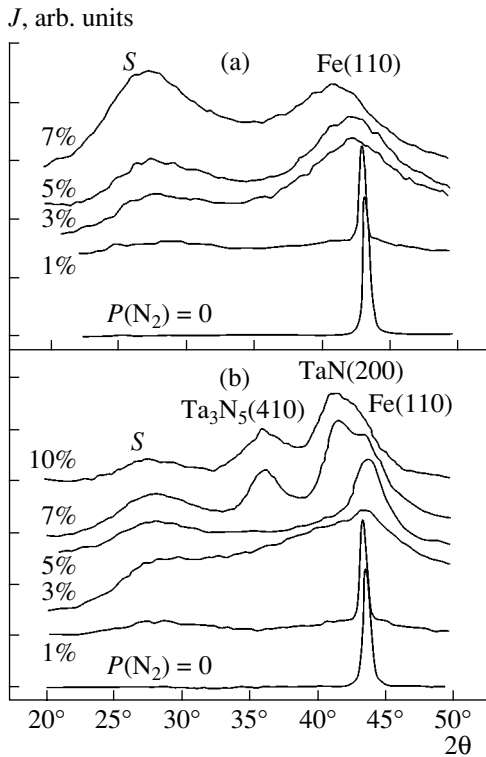
Fig. 1. X-ray diffraction patterns of (a) as-deposited and (b) annealed (450°C) Fe–Ta–N films deposited at various partial pressures $P(N_2)$ of nitrogen in the sputtering chamber (*S* is the curve of a clean substrate).
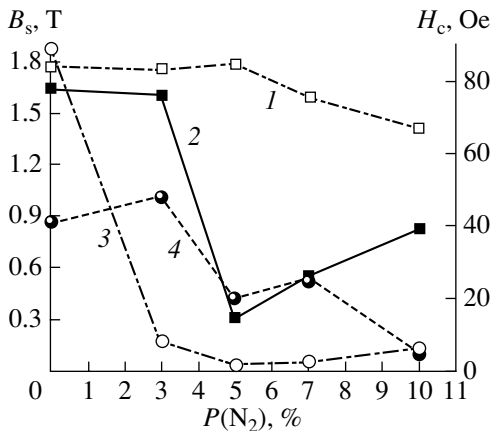
Fig. 2. Plots of the (*1*, *2*) saturation induction B_s and (*3*, *4*) coercive force H_c vs. the nitrogen partial pressure $P(N_2)$ for (*2*, *4*) as-deposited and (*1*, *3*) annealed (450°C) Fe–Ta–N films.

osition and (Fig. 1b) upon annealing at 450°C. The analysis of the spectra in Fig. 1a showed that nitrogen-free films consist of α-Fe grains in which the interplanar spacing $d(110) = 2.073$ Å is higher than that in pure α-Fe (2.026 Å). This fact allows us to suggest that Ta ions replace Fe ions in the α-Fe lattice, forming the substitutional solid solution α-Fe(Ta). As partial pres-

sure $P(N_2)$ increases, the (110) diffraction line corresponding to the α-Fe state broadens and shifts toward lower angles. These changes can be explained assuming that nitrogen atoms incorporated in the α-Fe lattice occupy interstitial positions and expand the lattice. The films deposited at $P(N_2) \geq 3\%$ are almost completely amorphous. The values of the saturation induction B_s and coercive force H_c of the as-deposited films are shown in Fig. 2 as functions of the partial pressure of nitrogen. As can be seen, none of these films has the required magnetic properties.

Low or very low anisotropy of the material (in units of J/m^3) is the main condition for obtaining high magnetic softness [14]. For an α-Fe grain size of about ~10 nm, the anisotropy is several J/m^3 due to the exchange interaction between α-Fe nanoparticles. The experiments showed that nitrogen-free films are polycrystalline and the α-Fe grain size is greater than the length of the ferromagnetic interaction. In this case, the magnetization process depends on the magnetocrystalline anisotropy of the grains and proceeds by a mechanism analogous to that observed in bulk iron. The nitrogen-containing films behave as amorphous materials, which follows from the results of measurements showing a monotonic increase both in the saturation magnetization and H_c on decreasing the temperature to -173°C. In contrast, H_c in the crystalline films depends on the exchange interactions between grains and should be inversely proportional to the magnetization M_s [14].

The most effective method for the synthesis of nanostructured alloys is the crystallization of amorphous material governed by thermal treatment. Investigations of the saturation induction B_s and the coercive force H_c of the films as functions of the annealing temperature T_{an} showed a drastic change in B_s and H_c upon annealing in the interval $350 \leq T_{an} \leq 400$°C. This fact indicates that the crystallization of α-Fe nanoparticles is completed. On reaching $T_{an} = 500$°C, H_c approaches the minimum value (0.2 Oe), while B_s stays constant (~1.8 T). Hence, 450°C is the optimum annealing temperature of the films.

Figure 1b shows the X-ray diffraction patterns of the films annealed at 450°C. A comparison to Fig. 1a shows that the curves deposited in the range $P(N_2) < 3\%$ have the same shape before and after annealing. The synthesis in the range of nitrogen pressures $P(N_2) \geq 3\%$ leads to the formation of nanocrystalline particles appearing as if incorporated into the surrounding amorphous matrix.

Figure 2 shows the dependences of the magnetic characteristics on the partial pressure of nitrogen for both as-deposited films and the films annealed at 450°C. As can be seen from these data, the H_c value of the annealed films sharply decreases with increasing nitrogen pressure. As the nitrogen pressure grows from $P(N_2) = 0$ to $P(N_2) = 5\%$, the coercive force drops to a minimum. Further increase in the pressure $P(N_2)$ leads

to a small smooth increase in H_c. These changes are due to the film components exhibiting crystallization in the course of annealing. The annealing results in an increase in the saturation induction B_s, but the growth of B_s is most pronounced in the films deposited at high $P(N_2)$. After annealing, the value of B_s remains almost unchanged in the films deposited in the range $P(N_2) <$ 5% and monotonically decreases as $P(N_2)$ increases above 5%. The increase in B_s in the films obtained for $P(N_2) \leq 5\%$ is related to the fact that α-Fe nanoparticles are predominantly crystallized at low partial pressures of nitrogen, while, in the range of $P(N_2) > 5\%$, both α-Fe nanoparticles and the TaN compound are simultaneously crystallized in the deposit. It has been suggested [15] that TaN is incorporated into facets of α-Fe grains. Nonmagnetic TaN particles either reduce the saturation induction B_s in the films or block the exchange interaction of α-Fe particles. Since the size of a Ta atom (1.46 Å) is comparable with that of an Fe atom (1.28 Å), the cubic symmetry of α-Fe particles is not broken and the magnetocrystalline anisotropy is retained [16]. All this leads to a decrease of the magnetic softness of the films.

In Fe–Ta–N films, nitrogen ions occupy interstices in α-Fe and expand the bcc crystal lattice, so that the cubic symmetry of α-Fe is broken and a uniaxial anisotropy is induced. Due to their small size, nitrogen atoms usually occupy the octahedral positions in (110) planes of the α-Fe lattice and bind to Ta atoms, substituting for iron [17]. The axis of the Ta–N bond determines the direction of the induced uniaxial anisotropy. If only α-Fe nanoparticles are crystallized in the films, the films have excellent soft magnetic properties because the effective anisotropy in such films is substantially suppressed due to the exchange interaction between α-Fe nanoparticles [11]. It should be noted (Fig. 1b) that annealing of the films obtained at $P(N_2) =$ 5% leads predominantly to the formation of α-Fe nanoparticles crystallized in the amorphous matrix, and the (110) plane of these α-Fe grains is predominantly oriented parallel to the film surface.

Figure 3 presents the typical Mössbauer spectrum of the annealed Fe–Ta–N film deposited at $P(N_2) =$ 5%. The spectrum was recorded with detection of the conversion and Auger electrons in backscattering geometry. An analysis showed that the spectrum represents a Zeeman sextet with a line width of 0.30 ± 0.003 mm/s and an effective magnetic field on the nuclei of iron ions of 333.8 ± 0.4 kOe. The relative areas of lines in the Zeeman sextet are 3 : 4 : 1 : 1 : 4 : 3. This means that the magnetic moments of iron ions in the films are oriented perpendicularly to the propagation vector of gamma radiation (directed perpendicularly to the film surface). Hence, the magnetic moments of iron ions occur in the film plane. The lines observed in the region of "zero" Doppler velocity of the Mössbauer source indicate that the films contain a small amount of a compound in which iron is in the paramagnetic state. The
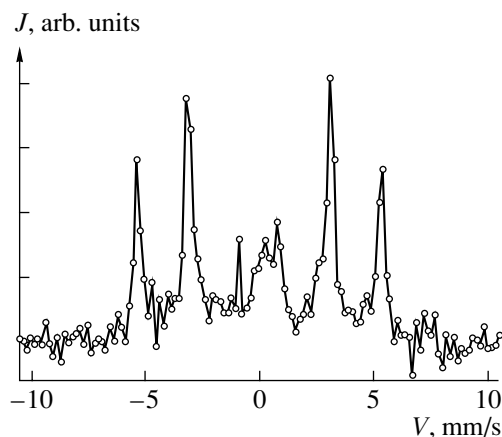
Fig. 3. The typical Mössbauer spectrum of the annealed Fe–Ta–N film deposited at $P(N_2) = 5\%$, recorded for conversion and Auger electrons in backscattering geometry.

parabolic shape of the background line points to the presence of a small amount of iron in the amorphous state. According to data of electron force microscopy, the films obtained at $P(N_2) = 5\%$ consist of α-Fe grains with dimensions within ~5–10 nm, which is smaller than the length of the ferromagnetic exchange interaction. These films contain the maximum volume fraction of nanocrystallites and (due to a strong ferromagnetic exchange interaction) exhibit the maximum magnetic softness in comparison to the films deposited under other partial pressures of nitrogen.

Thus, as a result of this investigation, we established the optimum regimes of synthesis of soft magnetic nanocrystalline Fe–Ta–N films with a high content of Ta (10 wt%). The synthesis used the method of reactive RF sputtering in an Ar–N_2 gas mixture, followed by the thermal-treatment-governed crystallization of the deposited amorphous films. The dependences of the microstructure and magnetic properties of the films on the nitrogen partial pressure $P(N_2)$ during sputtering are determined. In the films deposited at $P(N_2) = 0$, Ta ions substitute for Fe ions in an α-Fe lattice, and a readily crystallizable α-Fe-based substitutional solid solution is formed. Further increase in $P(N_2)$ results in that more and more nitrogen atoms are incorporated into the interstitial sites of α-Fe and modify its lattice. During annealing, α-Fe nanoparticles crystallize from the amorphous state. The crystallization process starts at 350°C and is accomplished at 450°C. The size of the particles formed in this range of temperature is below 10 nm. The films deposited at $P(N_2) = 5\%$ have excellent soft magnetic properties, namely, a low coercivity ($H_c < 0.3$ Oe) at a high saturation induction ($B_s = 15$ kG) and magnetic permeability (above 3000). The thermal stability of the magnetic parameters of the synthesized Fe–Ta–N films is much higher than that of the FeN films. Thus, we have obtained materials, which are, as confirmed by the experimental results, highly promising for use in high-density data write/read devices.

REFERENCES

1. O. Kohomoto, IEEE Trans. Magn. **27**, 3640 (1996).

2. S. Wang and M. H. Kryder, J. Appl. Phys. **69**, 5625 (1991).

3. S. Wang and M. H. Kryder, J. Appl. Phys. **67**, 5134 (1990).

4. R. E. Jonen and J. Williams, Jr., J. Appl. Phys. **67**, 5134 (1990).

5. B. Viala, M. K. Minor, and J. A. Barnard, J. Appl. Phys. **80**, 3941 (1996).

6. N. Terada, Y. Hoshi, M. Naoe, and S. Yamanaka, IEEE Trans. Magn. **20**, 1451 (1984).

7. Y. Watanabe, H. Oura, and N. Onazato, IEEE Trans. Magn. **26**, 1170 (1990).

8. C. Gao and W. D. Doyle, J. Appl. Phys. **73**, 6579 (1993).

9. M. Takahashi, H. Shoji, T. Shimatsu, *et al.*, IEEE Trans. Magn. **26**, 6547 (1993).

10. B. Viala, M. K. Minor, and J. A. Barnard, IEEE Trans. Magn. **32**, 3506 (1996).

11. R. D. Pehlke and F. Elliott, AIME Trans. **218**, 1088 (1960).

12. K. Nakauishi, O. Shimiz, and S. Yoshida, IEEE Trans. Magn. **28**, 7128 (1992).

13. K. H. J. Buschow, *Handbook of Magnetic Materials* (Elsevier Science, Amsterdam, 1997), Vol. 10, p. 433.

14. G. Herzer, IEEE Trans. Magn. **26**, 1937 (1990).

15. N. Hasegawa and M. Saito, IEEE Trans. Magn. **6**, 91 (1991).

16. B. D. Cullity, *Introduction to Magnetic Materials* (Addison-Wesley, Reading, 1973).

17. E. Van de Riet, W. Klaassens, and F. Roozeboom, J. Appl. Phys. **81**, 806 (1997).

Translated by M. Astrov

BRIEF
COMMUNICATIONS

Fine Structure of Optical Vortices in a Crystal: A Monochromatic Singular Beam

A. V. Volyar, Yu. A. Egorov, A. F. Rybas', and T. A. Fadeeva

Vernadsky National University, Simferopol, 95007 Ukraine
e-mail: volyar@ccssu.crimea.ua
Received April 2, 2004

Abstract—The fine structure of optical vortices in a perturbed singular beam past the uniaxial crystal–polarization filter system is considered. The method of determination of the relative weight of the partial vortices contained in the perturbed vortex is discussed. The dependence of the relative weight of the partial vortices on the displacement of the perturbed vortex from the beam axis is presented. © 2004 MAIK "Nauka/Interperiodica".

The considerable attention devoted in recent years to singular beams in crystals is due to the prospects of obtaining beams with preset compositions of optical vortices, whose spatial position can be controlled with relative ease [1–3]. Furthermore, in uniaxial crystals, singular beams acquire a number of special properties not inherent in such beams in any other optical system. For example, an astigmatic converter [4], optical wedge [5], and optical fiber [6] provide for the algebraic summation and subtraction of optical vortices, while a uniaxial crystal performs the operations of multiplication and division [1] manifested by a change in the topological charge of a vortex by two units. Moreover, a uniaxial crystal is capable of generating polychromatic ("white") vortices [1] (another method of white vortex generation is presented in [7]). At the same time, the optical vortices in crystals also admit mathematical summation as a result of a change in their fine structure.

In this paper, we present the results of experimental investigations of the fine structure of the topological charge of an optical vortex in a singular beam subjected to polarization perturbation.

Let a monochromatic circularly polarized beam propagate through a uniaxial crystal along its optical axis and then cross two successive $\lambda/4$ plates and a polarizer. As is known [8], the polarization perturbation of the beam in the first $\lambda/4$ plate splits the degenerate axial vortex and causes the radial displacement of two newly formed vortices in opposite directions. Along with this process, optical vortices also appear at the beam periphery and move radially toward the beam axis under the action of the perturbation. The interaction between the vortices of two types at some distance from the axis results in the formation of ring dislocations. Does the topological charge of each vortex change upon the radial motion or not? In order to answer this question, let us analyze the expression for the beam field (see [8, Eq. (1)]):

$$E_x = \{\cos\delta/2[\cos\Delta/2 + i\sin\Delta/2\exp(i2Q)]$$

$$+ i\sin\delta/2\exp(i2\varphi)[\cos\Delta/2 + i\sin\Delta/2\exp(-i2Q)]\}G_0,$$

$$E_y = i\{\cos\delta/2[\cos\Delta/2 - i\sin\Delta/2\exp(i2Q)]$$

$$- i\sin\delta/2\exp(i2\varphi)[\cos\Delta/2 - i\sin\Delta/2\exp(-i2Q)]\}G_0, \quad (1)$$

where $\delta \approx ar^2$, a is the crystal constant, Δ is the phase difference induced by the polarization perturbation, $G_0 = \exp\{-ikr^2/2Z\}/Z$ is the wave function of the fundamental Gaussian beam, $Z = z + iz_0$, $z_0 = k\rho^2/2$, and ρ is the beam waist radius at $z = 0$.

We assume that the initial beam has a right-hand circular polarization and the e axis of the $\lambda/4$ plate forms angle Q with the abscissa axis of the laboratory system of coordinates. Let the $\lambda/4$ plate be oriented so that $Q = \pi/4$ and let this plate introduce a small additional polarization perturbation μ, so that $\Delta = \pi/2 + \mu$. Then, expression (1) transforms to
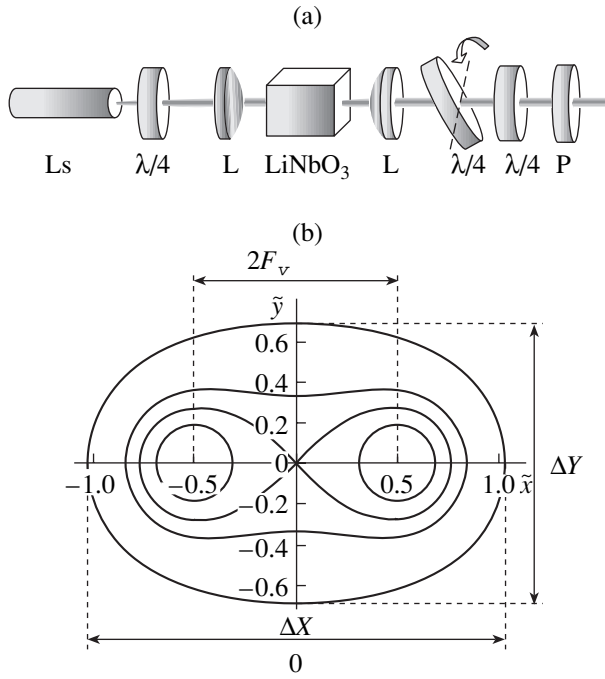
$$E_x = \{-\sin\mu/2\cos\delta/2$$
$$+ i\cos\mu/2\sin\delta/2\exp(i2\varphi)\}G_0, \quad (2)$$

$$E_y = i\{\cos\mu/2\cos\delta/2$$
$$+ i\sin\mu/2\sin\delta/2\exp(i2\varphi)\}G_0. \quad (3)$$

Note that, in the absence of perturbation, the E_x component contains an optical vortex at the axis with a double topological charge:

$$E_x = i\sin\delta/2\exp(i2\varphi)G_0, \quad E_y = i\cos\delta/2G_0. \quad (4)$$

The position of the perturbed vortices of the E_x component that are nearest to the axis is defined by the conditions [7] $\text{Re}(E_x) = 0$ and $\text{Im}(E_x) = 0$: $r_0 = \sqrt{\mu/a}$, $\varphi_0 =$

Fig. 1. (a) Optical scheme of the experimental setup: (Ls) He–Ne laser; ($\lambda/4$) quarter-wave plate; (L) lens; (P) polarizer. (b) Cassinian ovals in the vicinity of perturbed vortices.

$-\pi/4$, $3\pi/4$. In the vicinity of these points, the E_x component in Eq. (2) can be expressed as

$$E'_x \approx (Ax' + iBy')G_0(x', y'), \qquad (5)$$

where $A = \sqrt{a\mu}$, $B = \sqrt{a}\sin\mu/\sqrt{\mu}$.

It is not difficult to represent Eq. (5) as a sum of two singular beams bearing optical vortices with opposite topological charges:

$$E'_x \approx \{(A + B)(x' + iy') + (A - B)(x' - iy')\}G_0/2, \quad (6)$$

where

$$w^+ = (A + B)/2, \quad w^- = (A - B)/2 \qquad (7)$$

are the weight coefficients of the vortices forming the fine structure of the perturbed vortex.

It also follows from Eq. (7) that small variations of the polarization perturbation induced by the tilt of the $\lambda/4$ plate are analogous to the algebraic summation of vortices. In order to determine the weight of each vortex, we use the method developed in [5]. Indeed, using expression (5), we can write the equation of equal-intensity lines in the vicinity of the perturbed vortex:

$$(x'/A)^2 + (y'/B)^2 = C, \qquad (8)$$

where $C = $ const.

These lines appear as a family of ellipses with semiaxes A and B, so that the ellipticity of the level line is

$$Q = B/A = \sin\mu/\mu. \qquad (9)$$

Once the ellipticity Q is known, we can always find the ratio between the weight coefficients

$$w = w^-/w^+ = (Q - 1)/(Q + 1). \qquad (10)$$

However, one should bear in mind that, at a small perturbation μ, the vortices almost merge so that their positions can hardly be distinguished in experiment. Therefore, it is necessary to analyze the level line shape for $\mu \ll 1$.

Based on Eq. (2), we can express the intensity near the axis as

$$
\begin{aligned}
I_x &\propto E_x E_x^* \approx \sin^2\mu/2 \\
&+ (a/2)^2\cos^2\mu/2(x^2 + y^2)^2 + (a/2)\sin\mu xy,
\end{aligned}
\qquad (11)
$$

where $\sin\delta/2 \approx ar^2/2$ and $\cos\delta/2 \approx 1$.

Introducing a new system of coordinates $x = \tilde{x}\cos\alpha + \tilde{y}\sin\alpha$, $y = -\tilde{x}\sin\alpha + \tilde{y}\cos\alpha$, we rewrite Eq. (11) for $\alpha = \pi/4$ as

$$(\tilde{x}^2 + \tilde{y}^2)^2 - 2(\mu/a)(\tilde{x}^2 - \tilde{y}^2) + (\mu/a)^2 = C(2/a)^2. \quad (12)$$

Under the condition that $a > 0$, $\mu > 0$, and $C > 0$, Eq. (12) presents the family of Cassinian ovals (Fig. 1b), whose shape depends on the value of perturbation μ. The perturbed optical vortices are located in two focuses: $\tilde{y}_0 = 0$, $\tilde{x}_0 = \pm\sqrt{\mu/a}$. The two edge points of the level line along the $0\tilde{x}$ and $0\tilde{y}$ axes are spaced by $\Delta X = 2\sqrt{\tilde{A}^2 + \tilde{B}^2}$ and $\Delta Y = 2\sqrt{\tilde{A}^2 - \tilde{B}^2}$, respectively, where $\tilde{A}^2 = C(2/a)^2$ and $\tilde{B} = \mu/a$. These values can be measured experimentally. The coordinates of vortices can be expressed via the measurable quantities in the following way:

$$\tilde{y}_0 = 0, \quad \tilde{x}_0 = \pm F_v = \pm\sqrt{(\Delta X^2 - \Delta Y^2)/8}. \quad (13)$$

Equation (13) suggests that, in the vicinity of the points $(\tilde{x}_0, \tilde{y}_0)$, the level lines have a circular shape and, under the condition of small polarization perturbation ($\mu \ll 1$), the perturbed vortex contains a charge of only one sign. A more detailed pattern can be obtained from experiment.

Our experimental arrangement is schematically depicted in Fig. 1. In this scheme, a circulary polarized fundamental Gaussian beam of He–Ne laser ($\lambda = 0.6328$ μm) propagates along the optical axis of a LiNbO$_3$ crystal and passes through two quarter-wave plates and a polarizer. The orientation of the $\lambda/4$ plate closest to the crystal could be smoothly varied, which allowed a controlled polarization perturbation to be introduced into the singular beam. The second $\lambda/4$ plate and the polarizer form a polarization filter used to separate a combined singular beam containing optical vortices with given characteristics out of the inhomogeneously broadened wave. The distribution of the beam intensity over the surface of the working element of a
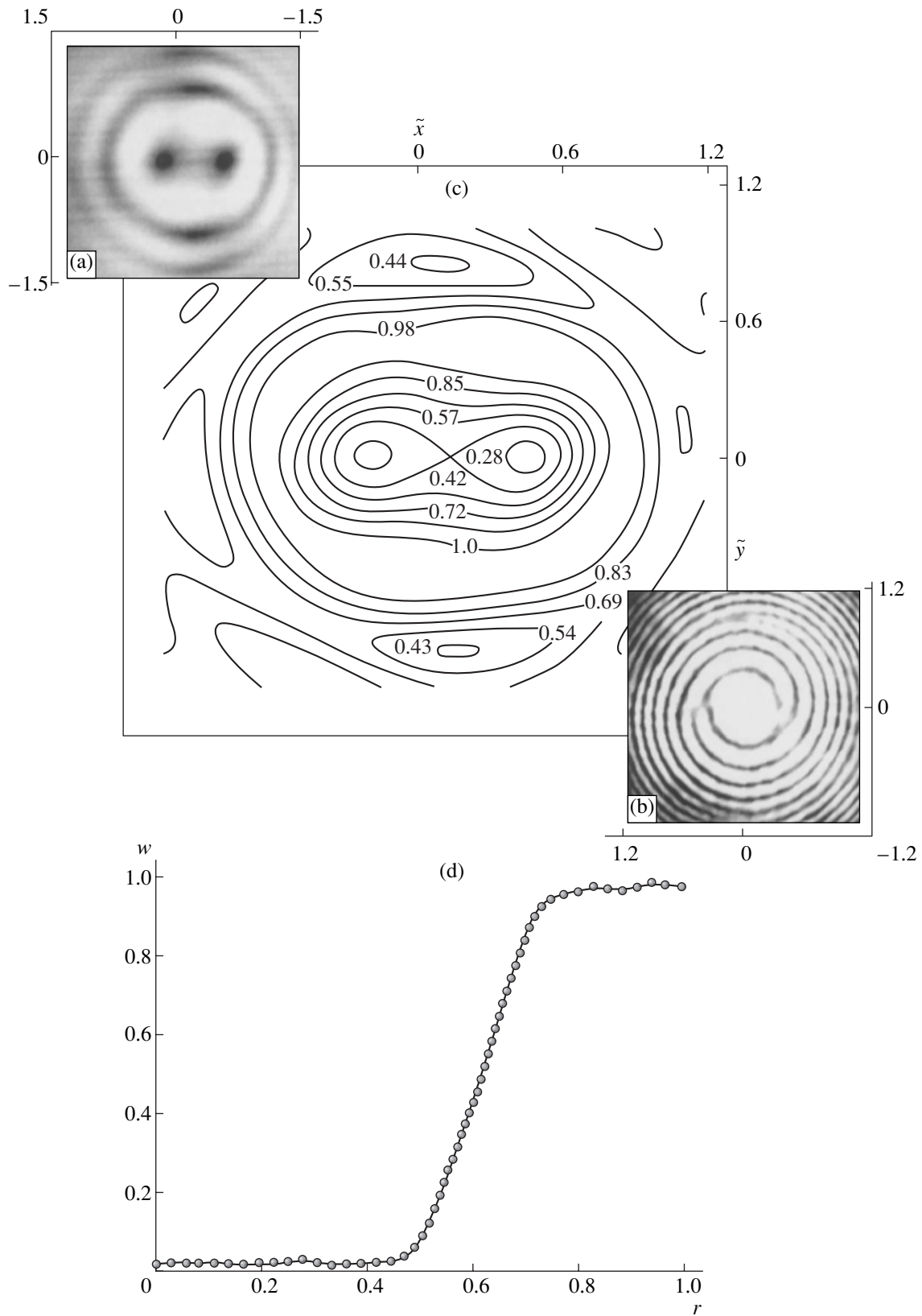
Fig. 2. A singular beam with perturbed vortices: (a) intensity distribution; (b) interference pattern; (c) level lines in the vicinity of the perturbed vortices; (d) the relative weight of the partial vortices vs. the off-center displacement of the combined vortex. Figures 2a–2c are plotted in $(\tilde{x}, \tilde{y})$ coordinates.

CCD camera was processed by a computer. An attenuator reduces the beam intensity so that the CCD camera gives a linear response to a change in the signal intensity in the vicinity of the vortex core.

Prior to measuring the weight coefficients of the perturbed optical vortices, we studied the amplitude (Fig. 2a) and the phase (Fig. 2b) structures of the beam. Figure 2b shows two branches of a double spiral, which form in the vicinity of intensity minima and correspond to two optical vortices with similar unit topological charges.

As the first step to determine the relative weight of the vortices w, we carried out Gaussian averaging of the intensity distribution, since the fine-grained structure of the image obtained in coherent light introduced a considerable error into the results of measurements. A typical appearance of the equal-intensity lines is shown in Fig. 2c, where the numbers by the curves correspond to the relative intensity of light in the given region of the beam. A small tilt of the axis connecting centers of the vortices is caused by imperfect adjustment of the optical scheme in the experimental setup.

To determine the position of the vortex core, we measured the segments ΔX and ΔY (major and minor semiaxes of the oval in Fig. 1b) at a small relative distance between vortices $r = F_v/R \leq 0.3$ (R is the radius of the first ring dislocation in the absence of perturbation $\mu = 0$) and used formula (13). Practically, this value corresponds to the minimal distance between vortices, which can still be resolved by the experimental setup to within a relative error of 0.1. The point of intersection of the segments ΔX and ΔY yields the coordinates of the beam axis. At large distances R, the level lines near the vortex center were almost elliptical. The major and minor axes of the ellipse were measured at $r > 0.3$; their intersection indicated the position of the vortex center and their ratio yielded the ellipticity Q of the vortex.

Figure 2d presents the relative weight of vortices w calculated using formula (10). When the axial displacement r of the perturbed vortex is small, the contribution of the partial vortex with the opposite topological charge is negligible and $w \approx 0$. In the region of $r \approx 0.45$, the vortex core is noticeably deformed, which leads to a drastic increase in the contribution of the partial vortex with the opposite topological sign. When $r > 0.75$, the weights of the oppositely charged vortices become almost equal, so that, at $r = 1$, the vortices collapse into a ring dislocation.

Thus, based on the experimental data, we demonstrated the presence of a fine structure in the perturbed optical vortices transported by a singular beam. Each vortex represents a sum of two oppositely charged partial vortices. The relative weight of these vortices can be smoothly varied by means of an external polarization perturbation.

REFERENCES

1. A. V. Volyar and T. A. Fadeeva, Opt. Spektrosk. **94**, 264 (2003) [Opt. Spectrosc. **94**, 235 (2003)].
2. A. Ciattoni, G. Cincotti, D. Provenziani, and C. Palma, Phys. Rev. E **66**, 036614 (2002).
3. N. S. Kasak, N. A. Khio, and A. A. Ryzhevich, Kvantovaya Élektron. (Moscow) **29**, 1020 (1999).
4. L. Allen, M. J. Padjett, and M. Babiker, Prog. Opt. **39**, 291 (1999).
5. A. V. Volyar, T. A. Fadeeva, and V. G. Shvedov, Opt. Spektrosk. **93**, 285 (2002) [Opt. Spectrosc. **93**, 267 (2002)].
6. K. N. Alekseev, A. V. Volyar, and T. A. Fadeeva, Opt. Spektrosk. **93**, 639 (2002) [Opt. Spectrosc. **93**, 588 (2002)].
7. J. Leach and M. J. Padgett, New J. Phys. **5**, 154 (2003).
8. A. V. Volyar and T. A. Fadeeva, Opt. Spektrosk. **95**, 846 (2003) [Opt. Spectrosc. **95**, 792 (2003)].

Translated by A. Sidorova

Roentgenoluminescence from Silicon Carbide

G. I. Babayants, K. G. Babayants, and V. A. Popenko

Federal Unitary State Enterprise, Research Institute at NPO Luch,
Podol'sk, Moscow Oblast, 142116 Russia
e-mail: Lutch@Lotsia.com
Received April 2, 2004

Abstract—It is found that single crystals of silicon carbide exposed to soft X rays exhibit luminescence in the visible spectral range. The luminescence intensity from the single crystals produced by different methods differs by three- to fivefold. Also, the emission intensity is nonuniformly distributed over the single crystal surface, which may be related to the nonuniform distribution of impurities (activators). © 2004 MAIK "Nauka/Interperiodica".

A variety of inorganic materials that luminesce under the action of X rays are known. They are finding wide application as scintillators and screens. Basically, these are alkali halides and zinc sulfide–based compounds activated by rare-earth elements [1]. Silicon carbide offers a high sublimating temperature and is chemically passive in both alkaline and acidic media. To date, SiC roentgenoluminescence has not been reported. We managed to detect luminescence from α-SiC 6H single crystals under the action of soft X rays. The single crystals were produced by the Lely method (Podol'sk Chemicometallurgical Plant) and the modified Lely method (Research Institute at the NPO Luch). Depending on the production conditions, the crystals had a black, green, or yellow color and also different degrees of purity and structural perfection.

X rays were generated by a URS-2.0 X-ray source (nickel anode, voltage across the tube 25 kV, and current 30 mA). Luminescence from the crystals could be observed visually in the absence of natural lighting. The most intense glow was observed from black α-SiC 6H crystals. The glow intensity from the green and yellow single crystals was three to five times lower than that from the black samples. After the high voltage across the tube had been switched off, afterglow of the single crystals was observed for about 0.4 s.

The emission of the single crystals was photographed in full darkness with a color photographic film of 400-ISO sensitivity. The exposure time was 6–12 h. Figure 1 shows the growth-defect-containing (0001) surface of an α-SiC 6H single crystal (Research Institute at the NPO Luch) under natural lighting and its roentgenoluminescent image. It turned out that the main colors of the glow are red and yellow (the gray and bright areas, respectively, on the photograph). The photograph also shows that the surface has regions where the glow is absent (the black areas on the photograph). Starting from the physics of luminescence, one may assume that such a luminescence nonuniformity is

associated with the nonuniform impurity concentration in the bulk of the single crystal. Comparing the photographs, one can notice that the luminescent and nonlu-
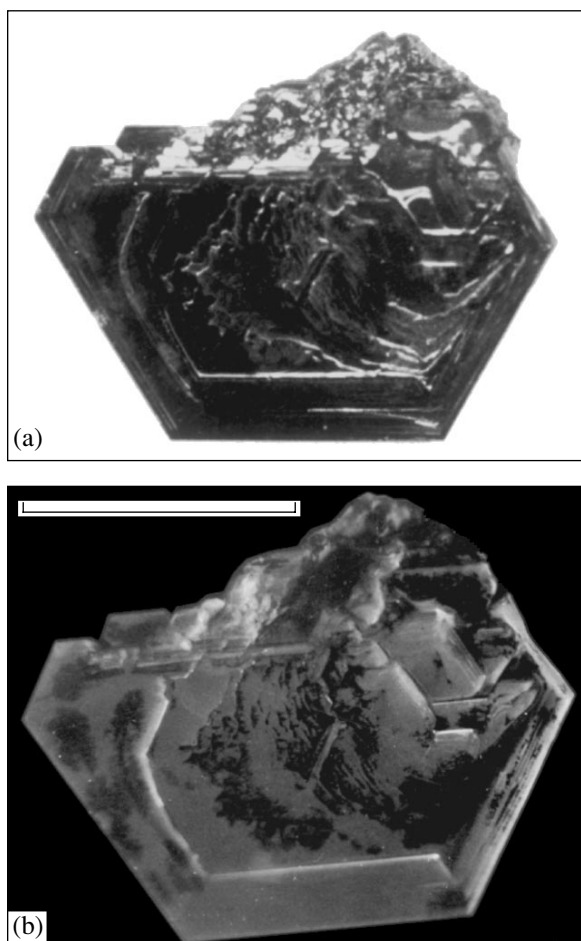
Fig. 1. (a) Growth surface of the single crystal upon natural lighting and (b) the roentgenoluminescence image of the crystal. The scale strip is 5 mm in size.

minescent regions of the crystal differ in color. Qualitative spectral analysis showed that the dominant impurity in the single crystals is iron. Other elements, such as Co, Ni, and Cr, are present in smaller amounts.

In view of the high stability of silicon carbide against intense neutron fluxes and ionizing radiation, the effect observed can be used, for example, in radiometric sensors. It is also of interest to study roentgenoluminescence from silicon carbide doped by various elements. The results of such studies may be of practical importance, for example, in microelectronics. The effect of nonuniform glow, which is associated with the nonuniform concentration of impurities, can be used to in doping quality control.

REFERENCES

1. V. V. Antonov-Romanovskiĭ, *The Kinetics of Photoluminescence in Crystal Phosphors* (Nauka, Moscow, 1966) [in Russian].

Translated by Yu. Vishnyakov

BRIEF
COMMUNICATIONS

Effect of Self-Conjugate Perforation in Amorphous Silicon Carbide Layers

V. A. Karachinov, S. B. Toritsyn, and D. V. Karachinov

Novgorod State University, ul. Sankt-Peterburgskaya 41, Novgorod, 173003 Russia
e-mail: deptptr@novsu.ac.ru
Received April 2, 2004

Abstract—SiC films on glass substrates are found to have an amorphous structure, high insulating properties, and good mechanical strength. The integrated transmission coefficient of the SiC films in the spectral range $\lambda = 0.4$–0.7 μm depends on their thickness. The SiC films subjected to etching in hydrofluoric acid exhibit self-conjugate perforation. © 2004 MAIK "Nauka/Interperiodica".

(1) For a number of applications, thin silicon carbide plates and membranes, which serve as pressure transducers, optically transparent protective layers, masks, and so on [1–8], are necessary. Thin-film SiC structures of a certain configuration are usually prepared by photolithography and chemical etching. The application of intermediate ("sacrificial") layers significantly extends the potentialities of these methods [9]. For example, because of the difference between the chemical activities of the substrate and a SiC layer, one can fabricate self-supporting membranes and active elements for 3D micromechanics [6, 7, 9]. However, the local removal of the sacrificial layer may result in relaxation processes, which may deform or even break down the SiC layer [9, 10].

In this work, we present the results of experimentally studying the morphology, as well as the electrophysical and protective properties, of silicon carbon coatings applied on glass.

(2) SiC films ~0.7–5.0 μm thick were applied on $48 \times 48 \times 2.5$-mm glass substrates using electron-beam evaporation in a vacuum. A polycrystalline cake was used as the source of SiC vapor. The optical properties and morphology of the SiC films were investigated by metallographic and photometric methods (using a metallographic television microscope with computer-assisted image processing, a photometer configured with a Yu116 luxmeter, and an MII-4 interferometer), as well as by the methods of scanning electron microscopy (a BS-340 scanning electron microscope operating in the secondary-electron and electron diffraction modes) and X-ray diffraction.[1] The electrophysical properties of the SiC films were studied on test resistive structures.

The chemical resistance and mechanical properties of the SiC layers were also examined.

According to the X-ray diffraction data, the SiC films are homogeneous and do not have grains typical of polycrystals. Additional electron diffraction studies indicated that the films are amorphous [11]. They offer high insulating properties: the surface resistivity of the films was much higher than 10 kΩ/□.

The optical measurements revealed the strong dependence of integrated transmission coefficient τ on film thickness d in the visual range ($\lambda = 0.4$–0.7 μm). As follows from Fig. 1, the experimental dependence $\tau(d)$ is a rapidly decreasing function. For example, the transmission coefficient of the 3- to 5-μm-thick SiC films is less than 15%. Such a variation of τ may be due to a nonstoichiometric composition of the SiC layers [12].

(3) Coatings made of single- and polycrystalline SiC are known to be highly resistant to acids, alkaline solutions, and molten metals, as well as to the action of abrasive particles [13]. Mechanical tests showed that the SiC amorphous films deposited on glass belong to the group of highest strength (zero group) according to State Standard 3-1901-85. The SiC layers withstood a

---

[1] X-ray diffraction measurements were performed in the AO Akron analytical center.
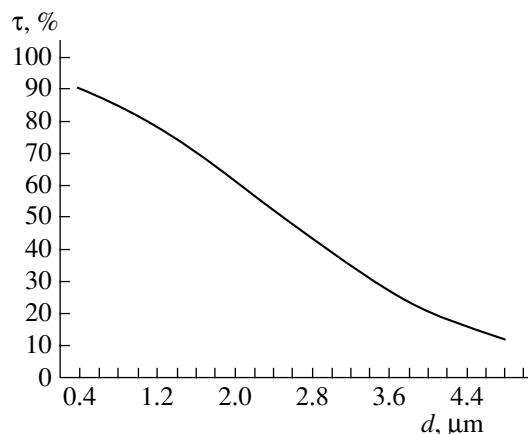
Fig. 1. Experimental dependence of the integrated transmission coefficient of the SiC film on its thickness.
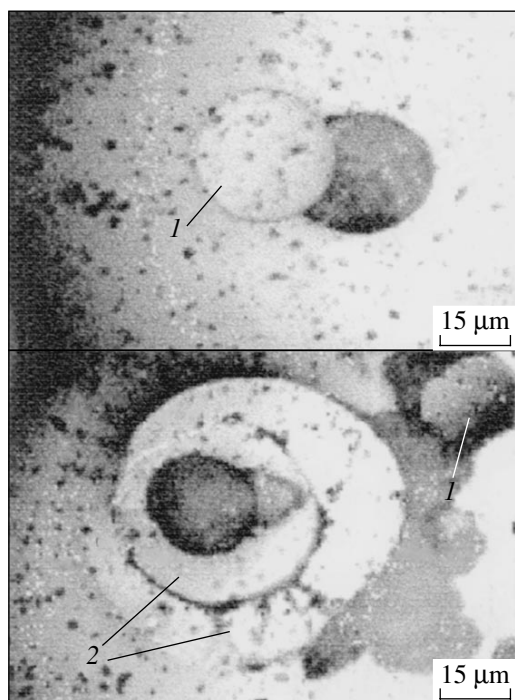
Fig. 2. Self-conjugate perforation of the SiC film subjected to etching in hydrofluoric acid: (*1*) disk and (*2*) ring.

wear load of 3500 revolutions from a lawn-wrapped rubber tip pressed against the sample by a compressive force of 220 g (the acceptable (normal) result is 3000 revolutions). Only a wire netting made of stainless steel begins to scratch the coating after 150 revolutions of the abrasive.

Our experiments also showed that the SiC films offer a good chemical resistance to nitric acid, hydrochloric acid, the mixture of these acids, and an aqueous-alkaline solution (KOH). However, when subjected to hydrofluoric acid, the SiC layer is detached purely mechanically via swelling (i.e., without dissolution). Swelling occurs when hydrofluoric acid reacts with the glass through pores in the SiC film. Locally forming salt columns (H_2SiF_6 [14]) and other products of the chemical reaction produced the effects of perforation of the SiC film (Fig. 2). Self-conjugate regular figures are

cut out in this process: disks early in etching and a disk–ring–ring at the final stage.

It should be noted that the regions perforated and the pores through which the etchant penetrated were clearly visible in polarized light.

REFERENCES

1. Y. Tawada, K. Tsuge, and M. Kondo, Appl. Phys. **53**, 5273 (1982).
2. V. I. Vaganov, *Integrated Strain Gages* (Énergoatomizdat, Moscow, 1983) [in Russian].
3. Yonezawa Toshio, Ajima Takashi, and Uchida Masato, US Patent No. 4,224,636 (1980).
4. N. I. Dolotov, V. A. Karachinov, Yu. M. Tairov, *et al.*, Kristallografiya **32**, 526 (1987) [Sov. Phys. Crystallogr. **32**, 308 (1987)].
5. P. A. Ivanov and V. E. Chelnokov, Fiz. Tekh. Poluprovodn. (St. Petersburg) **29**, 1921 (1995) [Semiconductors **29**, 1003 (1995)].
6. A. N. Komov, V. I. Chepurnov, and T. P. Fridman, in *Proceedings of the 3rd International Workshop "Silicon Carbide and Related Materials", Novgorod, 2000* (Novg. Gos. Univ., Novgorod, 2000), pp. 108–109.
7. A. V. Korlyakov, V. V. Luchinin, and N. V. Nikitin, in *Proceedings of the 3rd International Workshop "Silicon Carbide and Related Materials," Novgorod, 2000* (Novg. Gos. Univ., Novgorod, 2000), pp. 111–112.
8. A. V. Korlyakov, S. V. Kostromin, M. M. Kosyreva, *et al.*, Opt. Zh. **68** (12), 109 (2001).
9. A. V. Korlyakov, V. V. Luchinin, and P. P. Mal'tsev, Mikroelektronika, No. 3, 201 (1999).
10. Yu. A. Tkhorik and L. S. Khazan, *Plastic Strain and Misfit Dislocations in Heteroepitaxial Systems* (Naukova Dumka, Kiev, 1983) [in Russian].
11. E. E. Violin, K. D. Demakov, A. A. Kal'nin, *et al.*, Fiz. Tverd. Tela (Leningrad) **26**, 1575 (1984) [Sov. Phys. Solid State **26**, 960 (1984)].
12. R. S. Sussman and R. Ogden, Philos. Mag. B **44**, 137 (1981).
13. G. V. Samsonov and I. M. Vinitskiĭ, *Refractory Compounds* (Metallurgiya, Moscow, 1976) [in Russian].
14. B. D. Luft, *Physicochemical Treatment of Semiconductors Surfaces* (Radio i Svyaz', Moscow, 1982) [in Russian].

Translated by K. Shakhlevich

<div align="center">

BRIEF
COMMUNICATIONS

</div>

Potential of Planar Channeling in the Surface Layer of a LiH Crystal

N. A. Korkhmazyan, N. N. Korkhmazyan, and N. É. Babadzhanyan

Abovyan Pedagogical University, Yerevan, 375010 Armenia

Received September 1, 2003

Abstract—It is shown that the potential in the surface layer of a LiH crystal somewhat differs from the bulk value. The difference is extremely small (about 3%). It is also demonstrated that the thickness of the layer where the potential changes is negligible compared with the dechanneling length. © *2004 MAIK "Nauka/Interperiodica".*

1. PROBLEM DEFINITION

The effective potential of planar channeling along the charged (111) and $(1\bar{1}1)$ planes in light LiH and LiD ionic crystals was studied in [1]. In this work, we show, in particular, that the dechanneling length in these crystals is more than one order of magnitude larger than in other crystals, which makes them much more promising for applications. It seems that this circumstance has stimulated the extensive experimental research undertaken in [2], where the radiation of electrons and positrons as a result of channeling along different crystallographic planes in LiH and LiD crystals was studied and, specifically, the radiation due to the tunnel transition between energy levels of two neighboring potential wells was first discovered.

In [1], the effective channeling potential was found for an infinite crystal. In our previous work [3], we, however, showed that the notion of an "infinite crystal" appears to be ambiguous as applied to the problem considered. The fact is that the final result considerably depends on in which order the longitudinal and transverse (relative to the channel) dimensions of the crystal tend to infinity. This is a rare case in physics when this order is a controlling consideration. In [3], this problem was solved for a finite LiH crystal. Specifically, we estimated the thickness of the surface layer where the formulas for the effective potential [1] cannot be applied without refinement.

In this work, we study the behavior of the potential in the surface layer of a LiH crystal with the aim of completing the theory elaborated.

2. BASIC FORMULAS

The effective potential is given by [3]

$$\langle \varphi_{tot} \rangle = \frac{2\pi e}{d_0}(f^- + f^+) + I_{av},$$

$$f^- = \frac{1}{\lambda^- d_0}\Big[(\lambda^-|z| + 3)e^{-\lambda^-|z|}$$

$$- (\lambda^-\sqrt{R_0^2 + z^2} + 3)e^{-\lambda^-\sqrt{R_0^2 + z^2}}\Big],$$

$$\lambda = \frac{2z^*}{a_0}, \quad z^* = z - 5/16, \quad z^-(\text{H}) = 1, \quad z^+(\text{Li}) = 3, \tag{1}$$

$$I_{av} = I^-(a) + I^+(b)$$

$$= \frac{e}{d_0}\sum_n\left[\sum_l\int_{-1/2}^{1/2}\ln\frac{(l-x)^2 + a^2}{(l-x)^2 + b_2}dx\right],$$

$$a^2 = p^2(n-z)^2, \quad b^2 = p^2\left(n + \frac{1}{2} - z\right)^2,$$

$$p = \frac{d_z}{d_0} = 0.8774.$$

Here, $a_0 = 0.528$ Å is the Bohr radius, $d_0 = 3^{1/4}d/2 = 2.687$ Å is the side of the equivalent quadratic cell of averaging, $d = 4.084$ Å is the lattice constant, $\pi R_0^2 = d_0 \times d_0$, $d_z = d/\sqrt{3} = 2.358$ Å is the spacing between like-charged planes, e is the electron charge, and I_{av} is the averaged potential of the point crystal lattice.

The crystal-related coordinate system is shown in Fig. 1a. It is assumed that the crystal is infinite along the y axis, plane (x, y) is the channeling plane, and a particle moves along the x axis. Figure 1b shows the cell of potential averaging. The coordinates of the negative sublattice sites are $\bar{L} = (ld_0, md_0, nd_z)$, where $l, m, n = 0, \pm 1, \pm 2, \ldots$. The positive sublattice is displaced relative to the negative one by vector $(0, 0, d_z/2)$. In (1), function f^+ is derived from f^- by substituting λ^+ for λ^-
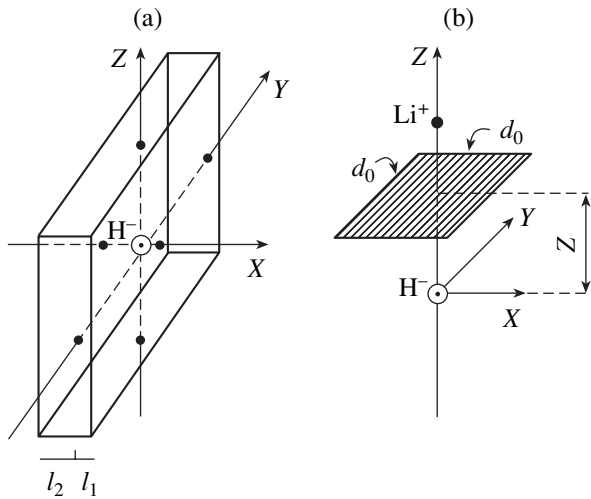
Fig. 1. (a) Coordinate system and (b) the location of the cell of averaging.
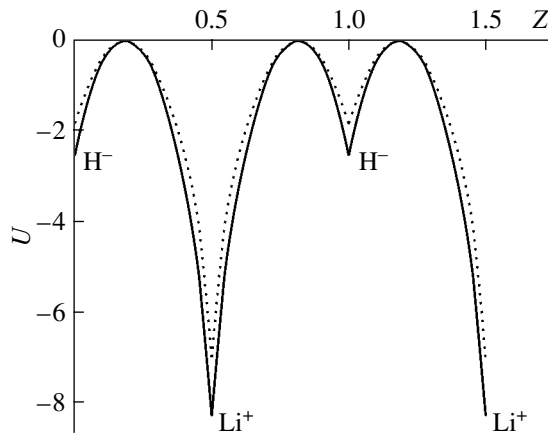
Fig. 2. Comparison between the potentials obtained in this work (continuous curve) and in [1] (dotted curve) for the planes $(1\bar{1}1)$. U and z are measured in electronvolts and in units of d_z.

and $-(1/2 - z)$ for z. In the expressions for f^- and f^+, the segments are taken in units of d_z.

Let the center of the cell of averaging (a point in the z axis) be l_1 (in units of d_0) distant from the center of the extreme right cell (Fig. 1a) and l_2 distant from the center of the extreme left cell. Since $(l_1 + l_2)$ is large ($\geq 10^6$) in all feasible cases, we may assume that $l_2 \gg 1$ and $l_2 \geq l_1$. The positive integer l_1 may vary in the interval $0 \leq l_1 \leq l_2$. As for the number n of charged planes located along the z axis, it is natural to assume that $-N \leq n \leq N$ and $N \gg l_2$.

3. POTENTIAL IN THE SURFACE LAYER OF THE CRYSTAL

To calculate the effective potential in the surface layer, summation in (1) is carried out over l from $-l_2$

to l_1:

$$I_{\mathrm{av}} = I(l_1) + I(l_2)$$

$$= \frac{e}{d_0}\sum_n\left[\int_0^{l_1+1/2}\ln\frac{x^2+a^2}{x^2+b^2}dx + \int_0^{l_2+1/2}\ln\frac{x^2+a^2}{x^2+b^2}dx\right]. \quad (2)$$

Integrating this expression and putting $(l_{1,2} + 1/2)/p = A_{1,2}$ yields

$$I(l_1) = \frac{e}{d_0}p\sum_{n=-N}^{N\gg l_1}\{A_1\ln[A_1^2+(n-z)^2]$$

$$- A_1\ln[A_1^2+(n+1/2-z)^2]+2(n-z)\arctan A_1/(n-z)$$
$$- 2(n+1/2-z)\arctan A_1/(n+1/2-z)\}, \quad (3)$$

and $I(l_2)$ is obtained by substituting A_2 for A_1.

Since $A_2 \gg 1$ in our case, we have, according to [3],

$$I(l_2) = \frac{\pi e}{d_0}p(z-1/4). \quad (4)$$

Consider expression (3). In the case under consideration, l_1 does not necessarily satisfy the condition $l_1 \gg 1$. Therefore, expression (3) must be calculated numerically. Then, for the potential energy of an electron, we get

$$U = -\frac{2\pi e^2}{d_0}\left\{f^- + f^+ + \frac{p}{2}(z-1/4)\right.$$

$$+ p\sum_{n=-N}^{N\gg l_1}\left[\frac{A_1}{2\pi}\ln\frac{A_1^2+(n-z)^2}{A_1^2+(n+1/2-z)^2}+\frac{n-z}{\pi}\arctan\frac{A_1}{n-z}\right.$$

$$\left.\left. - \frac{n+1/2-z}{\pi}\arctan\frac{A_1}{n+1/2-z}\right]\right\}. \quad (5)$$

For $l_1 \gg 1$, the sum in (5) gives $(z - 1/4)/2$ and we arrive at formula (35) in [3]:

$$U = -\frac{2\pi e^2}{d_0}[f^- + f^+ + p(z-1/4)]. \quad (6)$$

This function describes the behavior of the potential in the bulk of the crystal and is represented by the continuous curve in Fig. 2. This curve follows both from formula (5) for $l_1 = 100$ ($N = 10^4$) and from formula (6). Formula (5) was also used to construct potentials $U(z)$ in the surface layer of the crystal for $l_1 = 0$, 10, and 20 in units of d_0. The plots of these potentials are nearly coincident with the continuous curve in Fig. 2. The variation of the potential across the depth is illustrated in the table. The first row lists the values of z in terms of d_z; the second, the values of z in angstroms. The potential energies are given with opposite sign. As fol-

Table

l_1	Z										
	0.00	0.05	0.10	0.15	0.20	0.25	0.30	0.35	0.40	0.45	0.50
	0.00	0.12	0.23	0.35	0.47	0.59	0.70	0.82	0.94	1.06	1.18
0	2.53	1.28	0.46	0.05	0.00	0.25	0.80	1.64	2.90	4.85	8.09
10 (27 Å)	2.47	1.22	0.42	0.03	0.00	0.28	0.86	1.73	3.00	4.97	8.22
20 (54 Å)	2.46	1.21	0.41	0.03	0.00	0.28	0.86	1.73	3.00	4.98	8.22
100 (270 Å)	2.45	1.21	0.41	0.02	0.00	0.28	0.86	1.73	3.01	4.98	8.23

lows from the table, the difference between the potentials at the surface ($l_1 = 0$) and in the bulk amounts to 1.7–3.2%, decreasing to 0.4% at a depth of 50 Å. Thus, at depths close to 50 Å (measured along the particle trajectory), the potential can be calculated by formula (6) accurate to 0.4%. At a depth of about 100 Å, the inaccuracy is as small as 0.05%.

The dotted line in Fig. 2 is the plot of the same function according to [1]. The continuous and dotted curves diverge most considerably on the LiH and LiD planes (by 18 and 35%, respectively). This discrepancy stems from the fact that the expressions for f^- and f^+ derived in [1] lack the terms involving R_0.

The result obtained shows that the potentials in the surface layer and in the bulk of the crystal differ insig-nificantly; hence, formula (6) may be applied to the entire crystal with a high accuracy.

REFERENCES

1. V. I. Vysotskiĭ, R. N. Kuz'min, and N. V. Moksyuta, Zh. Éksp. Teor. Fiz. **93**, 2015 (1987) [Sov. Phys. JETP **66**, 1150 (1987)].

2. B. L. Berman *et al.*, Nucl. Instrum. Methods Phys. Res. B **1119**, 71 (1996).

3. N. A. Korkhmazyan, N. N. Korkhmazyan, and N. E. Babadjanyan, Zh. Tekh. Fiz. **73** (8), 16 (2003) [Tech. Phys. **48**, 939 (2003)].

Translated by V. Isaakyan

BRIEF COMMUNICATIONS

Heterogeneous Charge Transfer Due to Resonance Contact Photoionization

B. P. Kashnikov*, V. V. Makarov**, E. V. Makarov**, and G. I. Smirnov**

* Institute of Semiconductor Physics, Siberian Division, Russian Academy of Sciences,
pr. Akademika Lavrent'eva 13, Novosibirsk, 630090 Russia

** International Institute of Nonlinear Investigations, Siberian Division, Russian Academy of Sciences,
Novosibirsk, 630090 Russia

e-mail: smirnov.g.i@iae.nsk.su

Received February 26, 2004

Abstract—A qualitative model of heterogeneous charge transfer between atoms in polycrystalline films or semiconductor–insulator structures resonantly interacting with radiation and the metallic surface of the contact is suggested. The probability of resonance contact photoionization in heterogeneous solid-state nanostructures is determined, which makes it possible to use this process for data transfer and measuring the amount of information in nanotechnology. © 2004 MAIK "Nauka/Interperiodica".

INTRODUCTION

Interest in heterogeneous charge transfer in the field of resonance radiation is being stimulated by recently discovered possibilities of using this process in nanotechnology, nonlinear information systems, charge-coupled device technology, laser ion-drag accelerators, and optoelectronics [1–4]. A subject of heated discussion is also surface effects in the photoabsorption/photodesorption spectra of particles interacting with a surface (see, e.g., [5–7]). An intriguing example of these effects is the vibrational spectrum asymmetry due to energy exchange between a molecule and a surface by the mechanism of electron–hole pairs [5]. The effect of resonance surface photoionization was first reported in [8, 9]. A wealth of information about electron–atom interaction (a topical issue in solid-state physics, optoelectronics, and nuclear physics) may also be gained by studying the contact photoionization of atoms in polycrystalline films or solid-state heterostructures. In this work, we construct a qualitative model of charge exchange between atoms in semiconductor grains or heterogeneous semiconductor–insulator structures resonantly interacting with radiation and the metallic surface of the contact. The probability of the contact laser photoionization of the atoms localized in the polycrystalline films and in semiconductor–insulator nanostructures near the metal surface is found.

MODEL

We assume that the grains of a light-sensitive film have the n type of conductivity and are surrounded by tunnel-transparent insulating oxide layers (spacers). If the excited state of an atom in an n-semiconductor corresponds to the allowed band of a metal above the

Fermi level, activation-free charge exchange between the atom and metal is the basic mechanism of photoionization. In [10], the probability of activation-free charge exchange between a surface atom and a metal was determined by solving the problem of atom ionization in an external electric field [11]. Using the model of contact photoionization adopted in this work, we show that, when an atom in a grain that is near the metal surface is excited by a photon of energy roughly equal to half the energy gap, the state of the atom is similar to the self-ionization level against the continuum formed by the quasi-continuous electron spectrum of normal metals [12]. Note that resonance contact photoionization in heterogeneous semiconductor–insulator nanostructures that are in contact with a metal surface proceeds in the same way.

In this situation, the spectra of resonance photoabsorption and surface photoionization are determined by the nonlinear interference interaction between this continuum and the energy states of the grains that correspond to the valence band top and conduction band bottom. In doped semiconductors, impurity (donor) centers in the energy gap may be viewed as the ground or excited states.

Next, we analyze the dependence of nonlinear interference effects associated with resonance near-surface photoionization on the distance between a semiconductor atom and the metal surface. Similar interference effects are observed during the resonance scattering of laser radiation [13].

To be definite, we assume that the temperature of the polycrystalline film is sufficiently low, so that the energy states at the conduction band bottom and at the valence band top can be approximately considered as discrete. When an atom absorbs radiation and passes

from ground state n to excited state m that lies, unlike the former, above the Fermi level of the metal, the quantum-mechanical description of the contact photo-ionization process involves the complete Hamiltonian

$$H = H_a + H_M + \hbar(U + V), \qquad (1)$$

where the sum of three terms, H_a, H_M, and $\hbar U$, is represented by Anderson's model Hamiltonian [14, 15]. Anderson's Hamiltonian describes the electron states of a system comprising a metal and a two-level subsystem interacting with it.

The Hamiltonians of a two-level subsystem (H_a) and an undisturbed metal (H_M),

$$H_a = \sum_{j = m, n} E_j, \qquad (2)$$

$$H_M = \sum_p E_p c_p^+ c_p, \qquad (3)$$

are expressed through the fermion operators of birth (c_j^+, c_p^+) and loss (c_j, c_p) of electrons in the atom and in the metal. Here, E_j and E_p are the energies of electron states in the atom and semi-infinite metal, respectively, and

$$U - \sum_{p, j} U_{pj} c_p^+ c_j + \text{h.c.} \qquad (4)$$

is the operator that describes the interaction between metal state p and grain state $j = m, n$. This interaction is similar to the Fano configuration interaction between the continuum and self-ionization state [16, 17]. It is supposed that the electromagnetic radiation interacts only with the atom states. This interaction is described by operator V.

QUANTUM KINETIC EQUATION

A general solution to the relevant Schrödinger equation,

$$i\hbar \partial_t \Psi = H\Psi, \qquad (5)$$

can be represented as a linear combination of the wave functions Ψ_j and Ψ_p of the stationary states for an undisturbed system with Hamiltonian $H_0 = H_a + H_M$. Since the electron spectrum of the metal is quasi-continuous, summation over states with different energy E_p can be approximated by integration:

$$\Psi = \sum_j a_j \Psi_j + \int d\omega_p a_p \Psi_p; \quad \omega_p = E_p/\hbar. \qquad (6)$$

However, the spectral characteristics of photoionization in the travelling wave field are more conveniently calculated in terms of the density matrix apparatus rather than by using a set of equations for the amplitudes $a_{j, p}$ of probabilities of states for the discrete and continuous spectra. The transition from this set of

equations to a kinetic equation for the density matrix has special features due to the electron state continuum, which are described in [16]. The quantum kinetic equation that applies to any interaction of a particle with an external field was derived elsewhere [18].

In a resonance approximation, off-diagonal density matrix element ρ_{mn} that is responsible for the Bohr frequency ω_{mn} of a radiative transition is of an oscillatory character:

$$\rho_{mn} = r_{mn} \exp[-i(\Omega t - \mathbf{k} \cdot \mathbf{r})], \quad \Omega = \omega - \omega_{mn}, \quad (7)$$

where $\omega = kc$ is the optical field frequency.

It is assumed that an atom with a ground state that lies below the Fermi level interacts with the metal much more weakly than when in the excited state. The respective matrix elements of hybridization satisfy the inequality $|U_{pm}| > |U_{pn}|$.

If the effect of radiation on lower level population ρ_{nn} is ignored, one can consider only a set of equations for r_{mn} and upper level population ρ_{mm}:

$$(\partial_t + v_z \partial_z + \Gamma - i\Omega')r_{mn} = -i(G_{mn} + \delta_{mn} + i\gamma_{mn})\rho_{nn}, \quad \Omega' = \Omega - \delta_{mm} - \mathbf{k} \cdot \mathbf{v}, \qquad (8)$$

$$(\partial_t + v_z \partial_z + \Gamma)\rho_{mm} = \text{Im}[(G_{mn} + \delta_{mn} + i\gamma_{mn})r_{nm}], \quad \Gamma = \Gamma_{mn} + \gamma_{mm}, \qquad (9)$$

$$\rho_{nn} = N. \qquad (10)$$

Here, N is the total number of atoms per unit volume, Γ_{mn} is the constant of the spontaneous decay of the excited state of the atom, $G_{mn} = E_0 d_{mn}/\hbar$, E_0 is the traveling wave amplitude, and d_{mn} is the matrix element of the electric dipole transition moment.

The parameters

$$\gamma_{mj} = \pi U_{mp} U_{pj}|_{\omega_p = \omega}, \qquad (11)$$

$$\delta_{mj} = \sum_l \frac{2G_{ml}G_{lj}\omega_l}{\omega^2 - \omega_l^2} + \frac{1}{\pi}\int \frac{\gamma_{mj}(\omega_p)d\omega_p}{\omega - \omega_p} \qquad (12)$$

take into account the relaxation processes and energy shifts that are associated with the interference effect arising from the tunnel interaction of states $j = m, n$ with the metal surface. In expression (12), the summation is over all nonresonant states and quantities γ_{mj} and δ_{mj} depend on distance z between the atom and metal surface [19].

NONLINEAR INTERFERENCE EFFECTS RELATED TO CONTACT PHOTOIONIZATION

The linear susceptibility of a medium,

$$\chi = 2\hbar|E_0|^{-2}G_{nm}\langle r_{mn}\rangle, \qquad (13)$$

and the coefficient of resonance light absorption,

$$\alpha = 4\pi k \text{Im}\chi, \qquad (14)$$

are expressed via density matrix element r_{mn} averaged over an ensemble of particles. To calculate the surface photoionization cross section,

$$\sigma = 16\pi\hbar r |E_0|^{-2} N^{-1} \langle \gamma_{mm}\rho_{mm} + 2\text{Re}(\gamma_{mn}r_{nm}) \rangle, \quad (15)$$

it is necessary to determine r_{mn} and also the population ρ_{mm} of the excited state. The solutions to Eqs. (8) and (9) have the form

$$r_{mn} = i\rho_{nn}(G_{mn} + \delta_{mn} + i\gamma_{mn})[\Gamma - i(\Omega - \delta_{mm})]^{-1} \quad (16)$$

and

$$\rho_{mm} = \rho_{nn}\gamma_{mn}^2(1 + q_{mn}^2)[\Gamma^2 + (\Omega - \delta_{mm})^2]^{-1}, \atop q_{mn} = (G_{mn} + \delta_{mn})/\gamma_{mn}, \quad (17)$$

respectively.

Parameter q_{mn} reflects the presence of two competing channels of radiation absorption: a transition to excited state m and a transition to a continuous spectrum band of width γ_{mm}, q_{mn}^2 being proportional to the ratio between the probabilities of these processes. In the limit $z \longrightarrow \infty$, where $\gamma_{mj} = 0$ and $\delta_{mj} = 0$, relationships (16) and (17) reduce to well-known results for particles that do not interact with the surface:

$$r_{mn} = i\rho_{nn}G_{mn}(\Gamma_{mn} - i\Omega)^{-1}, \qquad (18)$$

$$\rho_{mm} = \rho_{nn}G_{mn}^2(\Gamma_{mn}^2 + \Omega^2)^{-1}. \qquad (19)$$

Let us consider the resonance interaction of radiation with atoms equidistant ($z = \text{const}$) from the metal surface. This situation occurs, e.g., when absorbing atoms cover a thin insulating film that is applied on a metal [19]. Then, for the profile of the frequency dependence of the resonant absorption coefficient, we have, according to (14) and (16),

$$\alpha = 8\pi\hbar kNG_{mn}\gamma_{mn}(q_{mn} - x)|E_0|^2\Gamma(1 + x^2), \atop x = (\Omega - \delta_{mm})/\Gamma. \quad (20)$$

The asymmetry of profile $\alpha(\Omega)$ is due to the interference between the transitions to discrete state m and to the continuum that is associated with the metal surface.

According to (15)–(17), the spectrum of resonant surface photoionization is given by

$$\sigma = 16\pi\hbar|E_0|^{-2}\gamma_{mn}^2\Gamma^{-1}$$
$$\times [\theta(1 + q_{mn}^2) - 2 + 2q_{mn}x]/(1 + x^2), \qquad (21)$$
$$\theta = \gamma_{mn}/\Gamma.$$

The shape of the resonance $\sigma(x)$ of surface photoionization strongly depends on parameters q_{mn} and θ. In general, the frequency profile $\sigma(x)$ of the surface photo-

ionization cross section is similar to that of Fano self-ionization resonance [20, 21]. Parameter θ varies between 0 and 1, depending on the distance between the absorbing atoms and metal surface (specifically, $\theta \approx 1$ for $\Gamma_{mn} \ll \gamma_{mm}$).

As a rule, a decrease in relaxation constants γ_{mj} and energy shifts δ_{mj} for the atoms far removed from the metal surface is approximated by the exponential model [14, 21]:

$$\gamma_{mj} = \tilde{\gamma}_{mj}e^{-az}, \quad \delta_{mj} = \tilde{\delta}_{mj}e^{-az}. \qquad (22)$$

In this case, the asymptotic fall of the surface photoionization cross section at $z \longrightarrow \infty$ is also given by the exponential:

$$\sigma(x) \propto e^{-az}. \qquad (23)$$

Using approximation (22), we can determine the radiation-induced electron flow near the contact:

$$N_e = N\int_0^\infty W(z)dz = N\langle W \rangle. \qquad (24)$$

It is proportional to the averaged probability of charge exchange between the metal and resonantly excited grain atoms:

$$W(z) = |E_0|^2\sigma(z)/8\pi\hbar k, \qquad (25)$$

where cross section $\sigma(z)$ is given by (21).

In view of the inequalities

$$\gamma_{mj}, \delta_{mj} \gg \Gamma_{mn}, G_{mn}, \qquad (26)$$

which are usually met in a surface photoionization layer of thickness a^{-1}, the asymmetric distribution over mean probability $\langle W \rangle$ can be represented as

$$\langle W \rangle = 2[(\tilde{\delta}_{mn}^2 - \tilde{\gamma}_{mn}^2)(\cos\beta - x\arctan\varphi\cos 2\beta$$
$$+ \tilde{x}\sin 2\beta \ln r) - \gamma_{mn}\delta_{mn}(\sin\beta - \tilde{x}\arctan\varphi\sin 2\beta$$
$$- \tilde{x}\ln r\cos 2\beta)]/\gamma a, \qquad (27)$$
$$\gamma = (\tilde{\gamma}_{mm}^2 + \tilde{\delta}_{mm}^2)^{1/2}, \quad \tilde{x} = \Omega/\gamma, \quad \varphi = \tilde{\gamma}_{mm}(\Omega - \tilde{\delta}_{mm})^{-1},$$
$$r = [\tilde{\gamma}_{mm}^2 + (\Omega - \tilde{\delta}_{mm})^2]^{1/2}|\Omega|^{-1},$$
$$\beta = \arctan(\tilde{\delta}_{mm}/\tilde{\gamma}_{mm}).$$

On the frequency scale, the photoionization resonance has a width on the order of $\tilde{\gamma}_{mm}$ and the degree of its asymmetry depends on the ratio $\tilde{\delta}_{mn}/\tilde{\gamma}_{mn}$. From (25) and (27), we get a simple expression for electron flow N_e that corresponds to the absorption line center ($|\Omega| \ll \gamma$):

$$N_e = N[\tilde{\gamma}_{mm}(\tilde{\delta}_{mn}^2 - \tilde{\gamma}_{mn}^2) - 2\tilde{\gamma}_{mn}\tilde{\delta}_{mn}\tilde{\delta}_{mm}]/\gamma^2 a. \quad (28)$$

Note that such resonant tunneling of photoelectrons from the contact may give rise, in particular, to photocurrent resonances in short-period superlattices.

CONCLUSIONS

The basic result of this work is the calculation of the probability of charge exchange between atoms (in semiconductor grains or in heterogeneous semiconductor–insulator nanostructures that resonantly interact with radiation) and a metal surface. The calculation takes into account nonlinear interference effects due to the transitions to the excited state of the semiconductor and to the continuous spectrum band associated with the metal.

The spectral profiles of photoabsorption and photoionization in semiconductor grains near the metal surface are asymmetric, similarly to the Fano resonance profile [20, 21]. The asymmetry of the photoabsorption and photoionization resonances depends on the ratio between the probabilities of the radiative transition to the excited state and the transition to the metal-induced continuum. It is quite natural that the photoabsorption resonance for the atoms far removed from the metal surface becomes symmetric and the photoionization probability markedly decreases.

The above features of resonance contact photoionization may be used in devising new data-transfer and data-processing technologies.

ACKNOWLEDGMENTS

REFERENCES

1. V. V. Antsiferov, G. I. Smirnov, and G. G. Telegin, Pis'ma Zh. Tekh. Fiz. **20** (8), 74 (1994) [Tech. Phys. Lett. **20**, 338 (1994)].

2. V. V. Antsiferov, G. I. Smirnov, and G. G. Telegin, Pis'ma Zh. Tekh. Fiz. **21** (14), 43 (1995) [Tech. Phys. Lett. **21**, 556 (1995)].

3. V. V. Antsiferov and G. I. Smirnov, *Coherent Radiation Processes in Plasma* (CISP, Cambridge, 1998).

4. V. V. Antsiferov, B. P. Kashnikov, and G. I. Smirnov, Pis'ma Zh. Tekh. Fiz. **25** (3), 14 (1999) [Tech. Phys. Lett. **25**, 89 (1999)].

5. D. C. Langreth, Phys. Rev. Lett. **54**, 126 (1985).

6. D. Agassi, Phys. Rev. B **33**, 3873 (1986).

7. P. T. Leung and T. F. George, Chem. Phys. Lett. **134**, 375 (1987).

8. B. Auschwitz and K. Lacmann, Chem. Phys. Lett. **113**, 230 (1985).

9. G. F. Malyshev and G. G. Telegin, Zh. Tekh. Fiz. **56**, 1195 (1986) [Sov. Phys. Tech. Phys. **31**, 700 (1986)].

10. A. V. Chaplik, Zh. Éksp. Teor. Fiz. **54**, 332 (1968) [Sov. Phys. JETP **27**, 178 (1968)].

11. L. D. Landau and E. M. Lifshitz, *Course of Theoretical Physics*, Vol. 3: *Quantum Mechanics: Non-Relativistic Theory* (Nauka, Moscow, 1989, 4th ed.; Pergamon, New York, 1977, 3rd ed.).

12. E. M. Lifshitz and L. P. Pitaevskiĭ, *Course of Theoretical Physics*, Vol. 5: *Statistical Physics* (Nauka, Moscow, 1978; Pergamon, New York, 1980).

13. S. G. Rautian, G. I. Smirnov, and A. M. Shalagin, *Nonlinear Resonances in Atomic and Molecular Spectra* (Nauka, Novosibirsk, 1979) [in Russian].

14. P. W. Anderson, Phys. Rev. **124**, 41 (1961).

15. L. A. Bol'shov, A. P. Napartovich, A. G. Naumovets, *et al.*, Usp. Fiz. Nauk **122**, 125 (1977) [Sov. Phys. Usp. **20**, 432 (1977)].

16. Yu. I. Geller and A. K. Popov, *Laser-Induced Resonances in Continuous Spectra* (Nauka, Novosibirsk, 1981) [in Russian].

17. V. V. Antsiferov, A. S. Vartazaryan, and G. I. Smirnov, Zh. Éksp. Teor. Fiz. **93**, 762 (1987) [Sov. Phys. JETP **66**, 430 (1987)].

18. S. G. Rautian and G. I. Smirnov, Zh. Éksp. Teor. Fiz. **74**, 1295 (1978) [Sov. Phys. JETP **47**, 678 (1978)].

19. M. L. Yu and N. D. Lang, Phys. Rev. Lett. **50**, 127 (1983).

20. V. Fano, Phys. Rev. **124**, 1866 (1961).

21. S. Ravi and G. S. Agarval, Phys. Rev. A **35**, 3354 (1987).

Translated by V. Isaakyan